SCALAR AND VECTOR MULTISTATIC RADAR DATA MODELS

By

Tegan Webster

A Thesis Submitted to the Graduate

Faculty of Rensselaer Polytechnic Institute

in Partial Fulfillment of the

Requirements for the Degree of

DOCTOR OF PHILOSOPHY

Major Subject: MATHEMATICS

Approved by the
Examining Committee:

_____
Margaret Cheney, Thesis Adviser

_____
David Isaacson, Member

_____
William Siegmann, Member

_____
Eric Mokole, Member

Rensselaer Polytechnic Institute
Troy, New York

December 2012
(For Graduation December 2012)

CONTENTS

LIST OF FIGURES

ACKNOWLEDGMENT

I would like to thank my primary thesis advisor, Professor Margaret Cheney, for her guidance, support, and advice. Her enthusiasm for mathematics and cooperative research has influenced me greatly. My mentor at the Naval Research Laboratory, Dr. Eric Mokole, significantly guided the scope and subject matter of this thesis; I appreciate his generous offer of time and research resources. I would next like to thank Professor David Isaacson for his time and support as a member of my thesis committee and instructor of the many engaging courses that I took with him during my time at RPI. I would also like to thank Professor William Siegmann, for his guidance during my experiences as an undergraduate student and graduate student at Rensselaer Polytechnic Institute.

I would like to thank all of the other teachers and professors that have challenged and encouraged me including Mrs. Jonas, Mr. Hopkins, Mrs. Champagne, Mrs. Davis, Mrs. Raszewski, Professor Kovacic, and Professor Kapila. I am also extremely grateful to Dawnmarie Robens of the RPI graduate program for her continual assistance and advice.

At the Naval Research Laboratory Radar Division I have had the opportunity to work with some really exceptional people. I would like to thank my supervisor Dr. Aaron Shackelford for his mentoring and Dr. Jimmy Alatishe for his informative discussions about radar hardware. I am especially grateful to Dr. Thomas Higgins for his advice, feedback, and time consuming proofreading of this thesis.

I thank all of my talented and outrageous friends from the math department: Ashley Baer, Jessica Jones, Analee Miranda, Peter Muller, Heather Palmeri, Joseph Rosenthal, Katie Voccola, and any others that I am sure to have forgotten. Homework sessions, stress relieving workouts, and pizza are some of things that I have learned are best shared with awesome people.

I lastly thank my family for their limitless support and encouragement.

This work was supported by the Naval Research Laboratory and the National Defense Science and Engineering Graduate Fellowship.

ABSTRACT

The aim of this thesis is to further the theory for multistatic imaging of moving targets through the development and simulation of scalar and vector radar data models and accompanying imaging operations. In the first part of the thesis we investigate scalar representations of multistatic radar data. We begin by comparing two different approaches for developing a multistatic ambiguity function (MAF), a tool used to assess performance of the waveforms and geometry of a multistatic radar system jointly. One approach is deterministic in nature, originating from the scalar wave equation, and the other is statistical, relying on a Neyman-Pearson defined weighting of received data. Although the two methods are fundamentally different in formulation, they are shown to yield similar results. We then build on the data model for the existing deterministically derived MAF with the inclusion of antenna beam patterns by relating the current density on the radiating and receiving antennas to a far-field spatial weighting factor. From this model we develop an imaging formula in position and velocity that can be interpreted in terms of filtered backprojection or matched filtering and a corresponding ambiguity function or point-spread function. We use the resulting data model and MAF to examine scenarios with various geometries and transmit waveforms and we show that the performance of a multistatic system depends critically on the system geometry and transmitted waveforms.

In the second part of the thesis we develop a vector multistatic data model incorporating polarization and antenna effects from transmitters and receivers modeled as long thin dipoles. We derive the model beginning with the potential formulation of Maxwell's equations and describe radiation from a transmitting antenna, scattering from a moving target, and reception at a receiving antenna in both the time and frequency domains. This model is developed from beginning to end with the transmit waveform and scattering behavior of the target left arbitrary and we obtain physical intuition, greater understanding and control of assumptions, and the ability to carefully model the desired multistatic scenario by formulating our

data model from first principles. Following formulation of the data model we derive two imaging operations that combine the data collected at each receiver, first assuming that the contributions from all transmitters in the scene are separable and then assuming that the contributions from all transmitting antennas cannot be separated and must be treated as a unit. We then utilize the presented data model and imaging operations to simulate multiple antenna geometries and transmission schemes. Scattering behavior of the target is modeled with both a bistatic scattering matrix based on physical optics for a perfectly electrically conducting flat rectangular plate and a general complex scattering matrix. Simulations exhibit the angle and polarization dependent scattering behavior and cross-polarization of the incident electric field consistent with the scattering models. The images formed under both the separable and nonseparable assumptions are comparable when waveforms with low cross-correlation are used. We approach the multistatic radar problem by combining an electromagnetic data model with signal processing to obtain an image, but the data model can also be used to generate high-quality data for a variety of applications.

CHAPTER 1
Introduction

Multistatic radar has been an area of intense research in recent years due to the inherent flexibility and importance of radar as an all-weather electromagnetic sensor and the additional theoretical advantages of a multistatic radar system. Traditional monostatic radars radiate electromagnetic energy from an antenna, the field propagates through space and is reflected in many directions from objects in the environment, some of the reflected energy is received by the antenna of the radar, and through processing techniques information about the intercepted objects is extracted. Radar systems can be used to detect and track targets, detect moving targets in clutter rich environments, form images of stationary or moving targets or scenes, recognize meteorological conditions, and classify targets. Although for some of these applications other sensors can be used, such as electro-optical sensors, radar is functional when these sensors fail perhaps in the dark of night or behind cloud formations.

Multistatic radar systems differ from traditional monostatic systems, or bistatic systems characterized by a separated transmitter and receiver, in that they consist of multiple transmitters and/or receivers. A multistatic system consisting of multiple transmitters and one or more receivers can transmit multiple waveforms from collocated or distributed antennas, possibly illuminating a larger area than a monostatic system. The power of the transmitting antenna is a limiting factor on the extent of a radar's visibility; the use of multiple transmitting antennas to illuminate an area may help overcome the physical limitations of amplifier power and antenna aperture sizes. It is also possible to augment fielded systems with additional low-power passive components to form a multistatic system, leveraging cooperative or noncooperative signals of opportunity. These passive radar systems are well suited to a variety of situations because they can be inexpensive and unobtrusive.

The design of a multistatic system, however, requires consideration of many factors including the number, geometry, polarization of the transmitters and re-

ceivers, and the waveforms that will be transmitted from each radiating antenna. It is important to ensure that all system components are coherent in time (that there is a common clock available to all transmitters and receivers) and frequency. If either of these condition are not met there will be some loss of information. The fusion of data received from multiple sensors, whether coherent or incoherent, is another issue inherent to multistatic radar. Ongoing theoretical research is necessary to address the complexity of multistatic radar.

The aim of this thesis is to further the theory for multistatic imaging of moving targets through the development and simulation of scalar and vector radar data models and accompanying imaging operations. In the first part of the thesis we investigate scalar representations of multistatic radar data. We begin by comparing two different approaches for developing a multistatic ambiguity function (MAF), a tool used to assess performance of the waveforms and geometry of a multistatic radar system jointly. One approach is derived with a deterministic signal model from an imaging perspective and the other is derived for specific statistical target assumptions from a detection perspective. The deterministic MAF is formulated from the scalar wave equation and describes radiation of the transmitted waveforms, scattering from a distribution of moving point-like targets, and reception at the receiving antennas. The statistical MAF is developed by defining an optimal multistatic detector corresponding to a Swerling II type target with fluctuating complex reflectivity. Although the two methods are fundamentally different in formulation, the corresponding numerical simulations are shown to yield similar results.

We then build on the data model for the existing deterministically derived MAF with the inclusion of antenna beam patterns by relating the current density on the radiating and receiving antennas to a far-field spatial weighting factor. From this model we develop an imaging formula in position and velocity that can be interpreted in terms of filtered backprojection or matched filtering and a corresponding ambiguity function or point-spread function. We use the resulting data model and MAF to examine scenarios with various geometries and transmit waveforms and we show that the performance of a multistatic system depends critically on the system geometry and transmitted waveforms.

In the second part of the thesis we develop a vector multistatic data model incorporating polarization and antenna effects from transmitters and receivers modeled as long thin dipoles. We derive the model beginning with the potential formulation of Maxwell's equations and describe radiation from a transmitting antenna, scattering from a moving target, and reception at a receiving antenna in both the time and frequency domains. Following formulation of the data model we derive two imaging operations that combine the data collected at each receiver, first assuming that the contributions from all transmitters in the scene are separable and then assuming that the contributions from all transmitting antennas cannot be separated and must be treated as a unit. We then utilize the presented data model and imaging operations to simulate multiple antenna geometries and transmission schemes. Scattering behavior of the target is modeled with both a bistatic scattering matrix based on physical optics for a perfectly electrically conducting flat rectangular plate and a general complex scattering matrix. Simulations exhibit the angle and polarization dependent scattering behavior and cross-polarization of the incident electric field consistent with the scattering models. The images formed under both the separable and nonseparable assumptions are comparable when waveforms with low cross-correlation are used.

This work is novel in that the model is developed from beginning to end with the transmit waveform and scattering behavior of the target left arbitrary. We obtain physical intuition, greater understanding and control of assumptions, and the ability to model the desired multistatic scenario carefully by formulating our data model from first principles. This work is also relevant because we combine an electromagnetic data model with signal processing to obtain an image. Although electromagnetics and signal processing are rich areas of study for radar applications, the two fields are infrequently combined.

The remainder of this thesis is organized as follows. In Chapter 2 we investigate scalar representations of multistatic radar data from the perspective of the multistatic ambiguity function (MAF). In Chapter 3 we formulate a full vector model for multistatic radar data including the polarization and scattering of electromagnetic waves and two corresponding imaging operations that combine the data

collected at each receiver. In Chapter 4 we conclude with a summary of this thesis work, a description of areas left for future research, and a discussion of the specific contributions to the field of multistatic radar modeling and imaging of moving targets.

CHAPTER 2
Scalar Radar Data Model

2.1 Introduction

In this chapter we investigate scalar representations of multistatic radar data from the perspective of the multistatic ambiguity function (MAF). The classical ambiguity function (CAF) is a tool that is used to assess the performance of monostatic radar waveforms; the MAF is an analogous tool for multistatic radar systems. Multistatic radar systems are characterized by the number and geometry of transmitters and receivers, the choice of antennas, the transmitted waveforms, and the method of fusing data received by multiple sensors. The added flexibility of a multistatic radar system results in the need for developing the more complex MAF as a metric for assessing the choice of waveforms and the system geometry jointly. Although the CAF is primarily important for waveform design, we will show that the MAF can be derived as part of an imaging operation in position and velocity.

Modeling and design of multistatic radar systems has been an area of substantial research in recent years. There has been theory developed for multistatic moving target detection [1–6], multistatic imaging of a stationary scene [7–10], multistatic imaging of moving targets [11–16], and coherence of components of a multistatic system [17–19]. Multiple formulations of the multistatic ambiguity function have been presented in the literature and will be briefly described in Section 2.2.4 [4, 5, 11–14, 20–25].

In Chapter 2 we first provide some background on the electromagnetic wave equation, matched filtering, the classical ambiguity function, and the multistatic ambiguity function. The rest of the chapter is broken into two sections. In Section 2.3 we formulate two multistatic ambiguity functions that are found in the literature, one derived with a deterministic signal model from an imaging perspective and one derived for specific statistical target assumptions from a detection perspective. The deterministic MAF is formulated from the scalar wave equation and models radiation of the transmitted waveforms, scattering from a distribution of moving point-like

targets, and reception at the receiving antennas. The statistical MAF is developed by defining an optimal multistatic detector corresponding to a Swerling II type target with fluctuating complex reflectivity. After presenting both models we compare the mathematical expressions and corresponding numerical simulations. We show that although the derivations of the two MAFs are quite different, numerical results are comparable and in the case of a single transmitter both mathematical expressions can be written in terms of the classical ambiguity function. In Section 2.4 we build on the data model for the existing deterministically derived MAF with the inclusion of antenna beam patterns by relating the current density on the radiating and receiving antennas to a far-field spatial weighting factor. The formulation yields a data model that is appropriate for narrowband waveforms in the case when the targets are moving slowly relative to the speed of light. From this model we develop an imaging formula in position and velocity that can be interpreted in terms of filtered backprojection or matched filtering and a corresponding ambiguity function or point-spread function. We show through simulations how the resulting MAF can be used to investigate the impact of geometry and transmit waveforms on multistatic system performance.

2.2 Background

2.2.1 Electromagnetic Wave Equation

Maxwell's equations in the time domain

$$\nabla \cdot \boldsymbol{\mathcal{D}} = \rho$$
$$\nabla \cdot \boldsymbol{\mathcal{B}} = 0$$
$$\nabla \times \boldsymbol{\mathcal{E}} = -\frac{\partial \boldsymbol{\mathcal{B}}}{\partial t}$$
$$\nabla \times \boldsymbol{\mathcal{H}} = \boldsymbol{\mathcal{J}} + \frac{\partial \boldsymbol{\mathcal{D}}}{\partial t}$$

combined with the free space constitutive relations

$$\boldsymbol{\mathcal{D}} = \epsilon_0 \boldsymbol{\mathcal{E}}$$
$$\boldsymbol{\mathcal{B}} = \mu_0 \boldsymbol{\mathcal{H}}$$

yield

$$\nabla \cdot \boldsymbol{\mathcal{E}} = \frac{1}{\epsilon_0}\rho \tag{2.1}$$
$$\nabla \cdot \boldsymbol{\mathcal{B}} = 0 \tag{2.2}$$
$$\nabla \times \boldsymbol{\mathcal{E}} = -\frac{\partial \boldsymbol{\mathcal{B}}}{\partial t} \tag{2.3}$$
$$\nabla \times \boldsymbol{\mathcal{B}} = \mu_0 \boldsymbol{\mathcal{J}} + \mu_0 \epsilon_0 \frac{\partial \boldsymbol{\mathcal{E}}}{\partial t} \tag{2.4}$$

where $\boldsymbol{\mathcal{D}}(\boldsymbol{r}, t)$ is the electric displacement field, $\boldsymbol{\mathcal{B}}(\boldsymbol{r}, t)$ is the magnetic induction field, $\boldsymbol{\mathcal{E}}(\boldsymbol{r}, t)$ is the electric field, $\boldsymbol{\mathcal{H}}(\boldsymbol{r}, t)$ is the magnetic intensity or magnetic field, $\rho(\boldsymbol{r}, t)$ is the charge density, $\boldsymbol{\mathcal{J}}(\boldsymbol{r}, t)$ is the current density, ϵ_0 is the permittivity of free space, and μ_0 is the permeability of free space. In free space $\rho(\boldsymbol{r}, t) = 0$ and $\boldsymbol{\mathcal{J}}(\boldsymbol{r}, t) = 0$ so that (2.1) and (2.4) become

$$\nabla \cdot \boldsymbol{\mathcal{E}} = 0 \tag{2.5}$$

and

$$\nabla \times \boldsymbol{\mathcal{B}} = \mu_0 \epsilon_0 \frac{\partial \boldsymbol{\mathcal{E}}}{\partial t}, \tag{2.6}$$

respectively.

We can obtain the electromagnetic vector wave equation from Maxwell's equations under the free space assumption. We begin by taking the curl of both sides of (2.3) and substituting (2.6) to obtain

$$\nabla \times \nabla \times \boldsymbol{\mathcal{E}} = -\mu_0 \epsilon_0 \frac{\partial^2 \boldsymbol{\mathcal{E}}}{\partial t^2}. \tag{2.7}$$

We next apply the vector identity

$$\nabla \times (\nabla \times \boldsymbol{A}) = \nabla(\nabla \cdot \boldsymbol{A}) - \nabla^2 \boldsymbol{A} \tag{2.8}$$

to (2.7)

$$\nabla(\nabla \cdot \boldsymbol{\mathcal{E}}) - \nabla^2 \boldsymbol{\mathcal{E}} = -\mu_0 \epsilon_0 \frac{\partial^2 \boldsymbol{\mathcal{E}}}{\partial t^2} \tag{2.9}$$

and recall (2.5) to obtain the wave equation

$$\nabla^2 \boldsymbol{\mathcal{E}} = \mu_0 \epsilon_0 \frac{\partial^2 \boldsymbol{\mathcal{E}}}{\partial t^2} \tag{2.10}$$

or

$$\left(\nabla^2 - \frac{1}{\mathrm{c}_0^2} \frac{\partial^2}{\partial t^2} \right) \boldsymbol{\mathcal{E}}(\boldsymbol{r}, t) = 0 \tag{2.11}$$

where $\mathrm{c}_0 = (\mu_0 \epsilon_0)^{-1/2}$. We have explicitly included the temporal and spatial dependences of the electric field. Through a similar process we can obtain the vector wave equation for the magnetic field $\boldsymbol{\mathcal{H}}$. Each component of the electric field or magnetic field satisfies the scalar wave equation. In Chapter 2 we consider solutions to the scalar wave equation and in Chapter 3 we consider the vector wave equation derived from the potential formulation of Maxwell's equations.

2.2.2 Matched Filtering

The matched filter is the optimal linear filter for maximizing the signal-to-noise ratio (SNR) for a signal received in white noise. The impulse response of the matched filter is given by

$$h(t) = s^*(-t)$$

where $s(t)$ is the transmitted waveform. The signal that is transmitted, scattered from a target, and received is assumed to have the form

$$s_{\mathrm{rec}}(t) = \rho s(t - \tau) + n(t)$$

where ρ is the scattering strength of the target including range losses, $\tau = 2R/\mathrm{c}_0$ is the two-way time delay, R is the distance from the antenna to the target, and

$n(t)$ is white noise. The output of the matched filter is obtained by convolving the received signal with the impulse response

$$\eta(t) = (h * s_{\mathrm{rec}})(t) = \int_{-\infty}^{\infty} s^*(-t')s_{\mathrm{rec}}(t-t')\mathrm{d}t' = \int_{-\infty}^{\infty} s^*(t')s_{\mathrm{rec}}(t+t')\mathrm{d}t', \quad (2.12)$$

which is the correlation of $s(t)$ and $s_{\mathrm{rec}}(t)$. The matched filter output SNR, SNR_{mf}, is given by

$$SNR_{\mathrm{mf}} = \frac{2E}{N_0}$$

where E is the energy of the received signal and N_0 is the unilateral power spectral density of white noise.

2.2.3 Classical Ambiguity Function

The classical ambiguity function (CAF), or Woodard ambiguity function, is a tool that is used to assess the performance of monostatic radar waveforms [26–30]. The CAF describes the matched filter output for targets at different distances R and velocities v and is expressed as

$$\chi(\tau, f_{\mathrm{d}}) = \int_{-\infty}^{\infty} s(t)s^*(t+\tau)\mathrm{e}^{\mathrm{i}2\pi f_{\mathrm{d}}t}\mathrm{d}t \quad (2.13)$$

in terms of time delay $\tau = 2R/\mathrm{c}_0$ and Doppler frequency $f_{\mathrm{d}} = 2v/\mathrm{c}_0$ where a positive range R corresponds to a target further in range than a reference target and a positive v denotes an incoming target. Letting

$$\Psi(\tau, f_{\mathrm{d}}) = |\chi(\tau, f_{\mathrm{d}})|^2, \quad (2.14)$$

if the signal is normalized to unit energy such that

$$\int_{-\infty}^{\infty} |s(t)|^2\mathrm{d}t = 1$$

then the maximum value of (2.14) is attained at the origin

$$\Psi(\tau, f_{\mathrm{d}}) \leq \Psi(0,0) = 1 \quad (2.15)$$

and the volume under the surface of (2.14) is given by

$$\int_{-\infty}^{\infty}\int_{-\infty}^{\infty}\Psi(\tau, f_{\mathrm{d}})\mathrm{d}\tau\mathrm{d}f_{\mathrm{d}} = 1. \tag{2.16}$$

If the signal is not normalized to unit energy then (2.15) and (2.16) are equal to $(2E)^2$ where E is the energy of the signal. Sometimes (2.13) is referred to as the autocorrelation function and (2.14) the ambiguity function [28,30]. The signs of the time delay and Doppler frequency in (2.13) may be reversed.

If we assume that the received signal input for the matched filter has the form

$$s_{\mathrm{rec}}(t) = s(t)\mathrm{e}^{\mathrm{i}2\pi f_{\mathrm{d}}t}$$

with zero time delay and Doppler frequency f_{d}, then the output of the matched filter is given by

$$\eta(t) = (h * s_{\mathrm{rec}})(t) = \int_{-\infty}^{\infty} s(t')s^*(t'-t)\mathrm{e}^{\mathrm{i}2\pi f_{\mathrm{d}}t'}\mathrm{d}t' = \chi(-t, f_{\mathrm{d}}) \tag{2.17}$$

so that the matched filter output for a target with Doppler frequency f_{d} is a time-reversed version of (2.13) [30].

We will now examine the classical ambiguity functions for two standard waveforms, a linear chirp and a pseudo-random phase-coded waveform. The linear chirp has linear frequency modulation (LFM), constant amplitude, pulse width T, and bandwidth B that is swept either up or down over the duration of the pulse. The linear chirp is defined as

$$s_{\mathrm{chirp}}(t) = A\,\mathrm{rect}(t/T)\cos(2\pi f_0 t + \pi\alpha t^2) \tag{2.18}$$

where

$$\mathrm{rect}(x) = \begin{cases} 1 & |x| \le 1/2 \\ 0 & |x| > 1/2 \end{cases},$$

f_0 is the carrier frequency, A is the amplitude, and $\alpha = \pm B/T$ is the LFM slope that is positive for an up-chirp and negative for a down-chirp. The classical ambi-

guity diagram of an up-chirp waveform with 10 GHz carrier frequency, 20 μs pulse width, and 1 MHz bandwidth is plotted in power on a dB scale in Figure 2.1. We have plotted (2.14) for velocities ranging from -3 km/s to 3 km/s and time delays ranging from -20 μs to 20 μs relative to a reference target. Depending on the definition of the ambiguity function, Figure 2.1 plots either values from the ambiguity function (2.14) or the magnitude squared of values from the ambiguity function (2.13). The ridge extending from negative velocity and time delay to positive veloc-

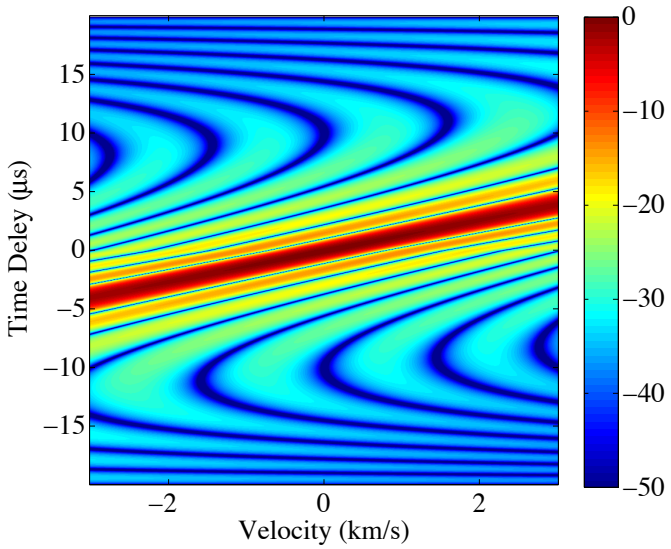

Figure 2.1: Classical ambiguity function of an up-chirp.

ity and time delay, with slope $1/\alpha = 1.33$ (km/s)/μs, reflects the Doppler tolerance of LFM waveforms. This property is beneficial for detection of fast moving targets because it is not necessary to implement multiple matched filters to cover the range of possible Doppler shifts. The time (range) sidelobes are low across all Doppler frequencies (velocities) as shown by the low ambiguity outside of the ridge in Figure 2.1. Nonlinear frequency modulated (NLFM) waveforms increase the rate of change of frequency modulation (FM) near the ends of the pulse and decrease the rate of change near the center, resulting in a waveform that does not require frequency domain weighting to reduce time sidelobes. Symmetric FM results in a thumbtack-like ambiguity function while asymmetric FM results in an ambiguity function that is more ridge-like. Nonlinear FM waveforms are less Doppler tolerant than LFM waveforms and thus are better suited to applications where the approximate target

velocity is known, such as tracking [30].

The pulse of a phase-coded waveform is subdivided into N sub-pulses, or chips, of duration $\delta = T/N$ and a phase modulation is applied to each sub-pulse. There are numerous phase modulation schemes, some resulting in ambiguity functions that resemble the ridged LFM ambiguity function and others that have a more thumbtack-like appearance. Pseudo-random phase codes, or pseudo-noise (PN) codes, are phase codes that consist of a sequence of chips with pseudo-random phases that are deterministically generated by any of a variety of mechanisms. These codes may appear random to an outside observer without prior knowledge of the code and the cross-correlation between two different codes is low compared to other types of waveforms. Pseudo-random codes are used in communications: each subscriber is assigned a unique code by the base station and is able to correctly extract the relevant signals from the collection of signals intended for all subscribers through matched filtering. The classical ambiguity diagram of a 20 chip pseudo-random phase code with 10 GHz carrier frequency, 20 μs pulse width, and 1 MHz bandwidth is plotted in power on a dB scale in Figure 2.2. We have again plotted (2.14) for velocities ranging from -3 km/s to 3 km/s and time delays ranging from -20 μs to 20 μs relative to a reference target. The thumbtack ambiguity diagram reflects the Doppler sensitiv-

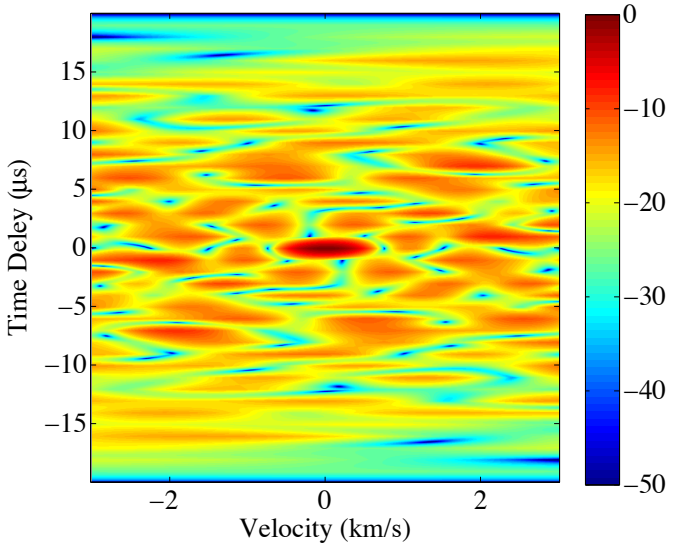

Figure 2.2: Classical ambiguity function of a 20 chip pseudo-random phase code.

ity of pseudo-random phase coded waveforms, which is beneficial for slowly moving

target applications or when knowledge of target speed is desired. It is evident from examining Figures 2.1 and 2.2 that the time (range) sidelobes are higher for the PN code than for the LFM waveform, which may hinder the detection of small targets in the sidelobes of large scatterers.

In addition to the waveforms briefly described above there are also continuous waveforms (CW) of a single amplitude and frequency. Time-frequency coded waveforms consist of a pulse train where each pulse is at a different frequency.

When modulated waveforms are matched filtered with the transmitted signal as described in Section 2.2.2, the range resolution is improved to the same level that could be achieved by a shorter pulse; this phenomenon is called pulse compression. The SNR is also increased through pulse compression, reducing the transmit power required to detect a target at a given range. Consequently, if a system is peak-power-limited, it is possible to transmit a longer waveform and increase the transmitted energy without losing range accuracy [28]. This discussion is not meant to cover the immense field of waveform design but rather to orient the reader with some terminology and concepts.

2.2.4 Multistatic Ambiguity Function

The multistatic ambiguity function (MAF), or multiple-input-multiple-output (MIMO) ambiguity function, is a tool used to assess the waveforms and geometry of a multistatic radar system jointly. The MAF is determined by the waveform choice for each transmitter, the multistatic geometry, and the method of fusing data received by multiple sensors; consequently there are numerous possible formulations.

The bistatic ambiguity function is closely related to the classical ambiguity function but considers bistatic ranges and velocities. Although there is no issue of combining information from multiple sensors as in the case of the MAF, the resulting ambiguity function is geometry dependent. The effect of system geometry on the shape of the bistatic ambiguity function has been considered in [31].

The added complexity of multiple transmitters and receivers in a multistatic radar system has led to multiple formulations of the MAF. A MAF is presented in [21] for a nonfluctuating point-like target of constant velocity and closely spaced

transmitting and receiving sensors so that the relative Doppler frequencies observed by each sensor are assumed identical. Other work has focused on developing MAFs from the perspective of determining an optimal multistatic detector corresponding to a target with statistically varying complex amplitude. An incoherent single transmitter and multiple receiver system and a moving target are considered in [4,5] and the work is extended for multiple transmitters in [20]. Coherent and incoherent processing of single transmitter and multiple receiver systems are considered in [24] and multiple transmitter and receiver systems in [23, 25]. MAFs have also been derived with deterministic signal models and a greater focus on wave propagation [11–14,22].

Although the classical and bistatic ambiguity functions are typically used for waveform design, the intrinsic dependance on geometry and fusion of information elevate the MAF to a construct that is more closely related to imaging. The MAF indicates that imaging can be thought of as a detection problem in position and velocity.

In this chapter we consider in detail the deterministically derived MAF presented in [11–14, 22] and the statistically derived MAF presented in [4, 5, 20] with multiple transmitters and receivers. We also formulate an extended deterministic MAF [16].

2.2.5 Fourier Transform Convention

Throughout this thesis we will adopt the convention that the Fourier transform is given by

$$F(\omega) = \mathcal{F}\{f(t)\} = \int_{-\infty}^{\infty} f(t)\mathrm{e}^{\mathrm{i}\omega t}\,\mathrm{d}t \tag{2.19}$$

and the inverse Fourier transform by

$$f(t) = \mathcal{F}^{-1}\{F(\omega)\} = \frac{1}{2\pi}\int_{-\infty}^{\infty} F(\omega)\mathrm{e}^{-\mathrm{i}\omega t}\,\mathrm{d}\omega. \tag{2.20}$$

2.3 Comparison of Deterministic and Statistical Multistatic Ambiguity Functions

In Section 2.3 we consider multistatic radar systems consisting of M transmitters at position $\boldsymbol{y}_m$ with $m = \{1, 2, \ldots, M\}$ and N receivers at position $\boldsymbol{z}_n$ with

$n = \{1, 2, \ldots, N\}$. We assume that all transmitters and receivers are stationary and that the target located at $\boldsymbol{x}$ may be stationary or moving with velocity $\boldsymbol{v}$. We present a deterministic signal model and corresponding MAF in Section 2.3.1 and a statistical signal model and corresponding MAF in Section 2.3.2. In Section 2.3.3 we discuss the mathematical expressions and underlying assumptions of both MAFs. We then present numerical simulations in Section 2.3.4 and conclude the section.

2.3.1 Deterministic Data Model

The multistatic ambiguity function presented in [11–14, 22] is obtained as a byproduct of an imaging method. The imaging method involves first developing a mathematical model for the scattered field, using this model in a matched filter that is applied at each receiver, and coherently summing the resulting filtered outputs with appropriate weights for each transmitter-receiver pair.

We derive the deterministic data model for a bistatic pair consisting of the m^{th} transmitter at position $\boldsymbol{y}_m$ and the n^{th} receiver at position $\boldsymbol{z}_n$. The derivations in [11, 12, 22] develop a mathematical model for data from a single isotropic source. For the transmitter source located at $\boldsymbol{y}_m$ we denote the waveform by $s_m(t)$, the transmission time by $-T_m$, and the wavefield at time t and position $\boldsymbol{x}$ by $\psi(t, \boldsymbol{x})$. We assume that away from the targets, the source wavefield satisfies the scalar wave equation

$$\left[\nabla^2 - \mathrm{c}_0^{-2}\partial_t^2\right] \psi(t, \boldsymbol{x}) = \delta(\boldsymbol{x} - \boldsymbol{y}_m) s_m(t + T_m), \tag{2.21}$$

where c_0 is the speed of light in a vacuum. We denote by $q_{\boldsymbol{v}}$ the phase-space distribution of target reflectivity. In other words, $q_{\boldsymbol{v}}(\boldsymbol{x} - \boldsymbol{v}t)$ is the reflectivity, at time t, of those scatterers moving with velocity $\boldsymbol{v}$ that, at time $t = 0$, were located at position $\boldsymbol{x}$. We write the total wavefield ψ as the sum $\psi = \psi^{\text{in}} + \psi^{\text{sc}}$ where ψ^{in} is the incident field and ψ^{sc} is the scattered field. Under the Born (single-scattering) approximation, we can think of the reflected incident field as providing a source $\int q_{\boldsymbol{v}}(\boldsymbol{x} - \boldsymbol{v}t)\mathrm{d}\boldsymbol{v}\ \psi_m^{\text{in}}(t, \boldsymbol{x})$ for the scattered field $\psi_m^{\text{sc}}(t, \boldsymbol{z}_n)$ received at $\boldsymbol{z}_n$ such that

$$[\nabla^2 - \mathrm{c}_0^{-2}\partial_t^2]\psi_m^{\text{sc}}(t, \boldsymbol{z}_n) = \int q_{\boldsymbol{v}}(\boldsymbol{x} - \boldsymbol{v}t)\mathrm{d}\boldsymbol{v}\ \psi_m^{\text{in}}(t, \boldsymbol{x}). \tag{2.22}$$

We use the free-space Green's function and several changes of variables to obtain

$$\psi_m^{\mathrm{sc}}(t, \boldsymbol{z}_n) = \int \frac{\delta(t - t' - |\boldsymbol{x} + \boldsymbol{v}t' - \boldsymbol{z}_n|/\mathrm{c}_0)}{4\pi|\boldsymbol{x} + \boldsymbol{v}t' - \boldsymbol{z}_n|} \times \int q_{\boldsymbol{v}}(\boldsymbol{x})\mathrm{d}\boldsymbol{v} \frac{s_m(t' + T_m - |\boldsymbol{x} + \boldsymbol{v}t' - \boldsymbol{y}_m|/\mathrm{c}_0)}{4\pi|\boldsymbol{x} + \boldsymbol{v}t' - \boldsymbol{y}_m|}\mathrm{d}t'\mathrm{d}\boldsymbol{x}. \tag{2.23}$$

and we write $R_{\boldsymbol{x},n} = |\boldsymbol{x} - \boldsymbol{z}_n|$, $\boldsymbol{R}_{\boldsymbol{x},n} = \boldsymbol{x} - \boldsymbol{z}_n$, and $\hat{\boldsymbol{R}}_{\boldsymbol{x},n} = \boldsymbol{R}_{\boldsymbol{x},n}/R_{\boldsymbol{x},n}$. We assume a slowly moving target (*i.e.* $|\boldsymbol{v}t| \ll |\boldsymbol{x} - \boldsymbol{z}_n|$), which allows us to carry out the t' integration in (2.23):

$$\psi_m^{\mathrm{sc}}(t, \boldsymbol{z}_n) = \int \frac{s_m(\alpha_{\boldsymbol{x},\boldsymbol{v}}(t - R_{\boldsymbol{x},n}/\mathrm{c}_0) - R_{\boldsymbol{x},m}/\mathrm{c}_0 + T_m)q_{\boldsymbol{v}}(\boldsymbol{x})}{(4\pi)^2 R_{\boldsymbol{x},n}R_{\boldsymbol{x},m}\mu_{\boldsymbol{x},\boldsymbol{v}}}\mathrm{d}\boldsymbol{x}\,\mathrm{d}\boldsymbol{v} \tag{2.24}$$

where

$$\begin{aligned}
\mu_{\boldsymbol{x},\boldsymbol{v}} =& 1 + \hat{\boldsymbol{R}}_{\boldsymbol{x},n} \cdot \boldsymbol{v}/\mathrm{c}_0, \\
\alpha_{\boldsymbol{x},\boldsymbol{v}} =& \frac{1 - \hat{\boldsymbol{R}}_{\boldsymbol{x},m} \cdot \boldsymbol{v}/\mathrm{c}_0}{1 + \hat{\boldsymbol{R}}_{\boldsymbol{x},n} \cdot \boldsymbol{v}/\mathrm{c}_0} \approx 1 - (\hat{\boldsymbol{R}}_{\boldsymbol{x},m} + \hat{\boldsymbol{R}}_{\boldsymbol{x},n}) \cdot \boldsymbol{v}/\mathrm{c}_0 \\
=& 1 + \beta_{\boldsymbol{x},\boldsymbol{v}}, \\
\beta_{\boldsymbol{x},\boldsymbol{v}} =& -(\hat{\boldsymbol{R}}_{\boldsymbol{x},m} + \hat{\boldsymbol{R}}_{\boldsymbol{x},n}) \cdot \boldsymbol{v}/\mathrm{c}_0.
\end{aligned} \tag{2.25}$$

The scattered field in (2.24) can be viewed as a sum of attenuated, time-delayed, Doppler-scaled copies of the transmitted waveform.

For the case of multiple transmitters, we assume that each of the N receivers can identify which part of the signal is from which transmitter. This identification of source transmitter could perhaps be done by separating the transmissions in frequency or code; this issue is left for the future.

We construct an image $I_{\boldsymbol{u}}(\boldsymbol{p})$ as an approximation of $q_{\boldsymbol{v}}(\boldsymbol{x})$, the true phase space distribution of scatterers moving at velocity $\boldsymbol{v}$ and located at position $\boldsymbol{x}$ at time $t = 0$. This image is formed by matched filtering the weighted scattered field with a time-delayed, Doppler-scaled version of the transmitted waveform and then

by summing over all transmitters and receivers:

$$I_{\boldsymbol{u}}(\boldsymbol{p}) = (4\pi)^2 \sum_{m=1}^{M}\sum_{n=1}^{N} R_{\boldsymbol{p},n} R_{\boldsymbol{p},m} \mu_{\boldsymbol{p},\boldsymbol{u}} \alpha_{\boldsymbol{p},\boldsymbol{u}} J_{m,n} \times \int s_m^*(\alpha_{\boldsymbol{p},\boldsymbol{u}}(t - R_{\boldsymbol{p},n}/\mathrm{c}_0) - R_{\boldsymbol{p},\boldsymbol{m}}/\mathrm{c}_0 + T_m)\, \psi_m^{\mathrm{sc}}(t, \boldsymbol{z}_n)\mathrm{d}t. \tag{2.26}$$

Here the star denotes complex conjugation, the weights $R_{\boldsymbol{p},m}, R_{\boldsymbol{p},n}$ and $\mu_{\boldsymbol{p},\boldsymbol{u}}$ are introduced to cancel the denominator of (2.24) when $\boldsymbol{p} = \boldsymbol{x}$ and $\boldsymbol{u} = \boldsymbol{v}$, and $J_{m,n}$ denotes a geometry-dependent weighting function. This weighting function is left undetermined in [12]. In the simulations below, we take $J_{m,n}$ to be equal for all pairs of transmitters and receivers.

In order to characterize the imaging system, we relate the image to the true phase-space reflectivity:

$$I_{\boldsymbol{u}}(\boldsymbol{p}) = \int K(\boldsymbol{p}, \boldsymbol{u}; \boldsymbol{x}, \boldsymbol{v}) q_{\boldsymbol{v}}(\boldsymbol{x}) \mathrm{d}\boldsymbol{x}\, \mathrm{d}\boldsymbol{v} \tag{2.27}$$

where

$$K(\boldsymbol{p}, \boldsymbol{u}; \boldsymbol{x}, \boldsymbol{v}) = \sum_{m=1}^{M}\sum_{n=1}^{N} J_{m,n} \alpha_{\boldsymbol{p},\boldsymbol{u}} \frac{R_{\boldsymbol{p},n} R_{\boldsymbol{p},m} \mu_{\boldsymbol{p},\boldsymbol{u}}}{R_{\boldsymbol{x},n} R_{\boldsymbol{x},m} \mu_{\boldsymbol{x},\boldsymbol{v}}} \times \int s_m^*(\alpha_{\boldsymbol{p},\boldsymbol{u}}(t - R_{\boldsymbol{p},n}/\mathrm{c}_0) - R_{\boldsymbol{p},m}/\mathrm{c}_0 + T_m) \times s_m(\alpha_{\boldsymbol{x},\boldsymbol{v}}(t - R_{\boldsymbol{x},n}/\mathrm{c}_0) - R_{\boldsymbol{x},m}/\mathrm{c}_0 + T_m)\mathrm{d}t \tag{2.28}$$

is the weighted multistatic ambiguity function (MAF), referred to as the point-spread function in [11,12,22]. For point-like targets ($q_{\boldsymbol{v}}(\boldsymbol{x}) = \delta(\boldsymbol{x} - \boldsymbol{x}_0)\delta(\boldsymbol{v} - \boldsymbol{v}_0)$) the weighted MAF $K(\boldsymbol{p}, \boldsymbol{u}; \boldsymbol{x}_0, \boldsymbol{v}_0)$ is the phase-space image of that target distribution.

We recall that the classical (narrowband) radar ambiguity function for the waveform radiated by the m^{th} transmitter can be written as

$$\mathcal{A}_m(\tilde{\omega}, \tau) = \mathrm{e}^{-\mathrm{i}\omega_m \tau} \int s_m(t) s_m^*(t - \tau) \mathrm{e}^{\mathrm{i}\tilde{\omega}t}\, \mathrm{d}t \tag{2.29}$$

where $\omega_m = 2\pi f_m$ and f_m is the carrier frequency of the transmitted waveform $s_m(t)$. Additionally, we write

$$\tilde{\omega} = \omega_m(\beta_{\boldsymbol{p},\boldsymbol{u}} - \beta_{\boldsymbol{x},\boldsymbol{v}}) = 2\pi f_m(\beta_{\boldsymbol{p},\boldsymbol{u}} - \beta_{\boldsymbol{x},\boldsymbol{v}})$$

where $\omega_m\beta_{\boldsymbol{p},\boldsymbol{u}}$ is the angular Doppler shift for position $\boldsymbol{p}$ and velocity $\boldsymbol{u}$. Then, in the narrowband approximation, the weighted multistatic ambiguity function (2.28) can be rewritten in the form

$$K(\boldsymbol{p},\boldsymbol{u};\boldsymbol{x},\boldsymbol{v}) = \sum_{m=1}^{M}\sum_{n=1}^{N} \mathcal{R}_{m,n}\mathcal{A}_m\left(\tilde{\omega},\tau\right) \tag{2.30}$$

where

$$\mathcal{R}_{m,n} = \frac{J_{m,n}R_{\boldsymbol{p},n}R_{\boldsymbol{p},m}\mu_{\boldsymbol{p},\boldsymbol{u}}\alpha_{\boldsymbol{p},\boldsymbol{u}}}{R_{\boldsymbol{x},n}R_{\boldsymbol{x},m}\mu_{\boldsymbol{x},\boldsymbol{v}}\alpha_{\boldsymbol{x},\boldsymbol{v}}}, \tag{2.31}$$

$$\tilde{\omega} = 2\pi f_m(\beta_{\boldsymbol{p},\boldsymbol{u}} - \beta_{\boldsymbol{x},\boldsymbol{v}}), \tag{2.32}$$

$$\tau = \frac{\alpha_{\boldsymbol{p},\boldsymbol{u}}(R_{\boldsymbol{p},n} - R_{\boldsymbol{x},n})}{\mathrm{c}_0} + \frac{R_{\boldsymbol{p},m} - R_{\boldsymbol{x},m}}{\mathrm{c}_0} + \left(1 - \frac{\alpha_{\boldsymbol{p},\boldsymbol{u}}}{\alpha_{\boldsymbol{x},\boldsymbol{v}}}\right)\left(\frac{R_{\boldsymbol{x},m}}{\mathrm{c}_0} - T_m\right). \tag{2.33}$$

Clearly, the simpler case of a single transmitter with multiple receivers reduces (2.30) to

$$K(\boldsymbol{p},\boldsymbol{u};\boldsymbol{x},\boldsymbol{v}) = \sum_{n=1}^{N} \mathcal{R}_n\mathcal{A}\left(\tilde{\omega},\tau\right)$$

with τ and $\tilde{\omega}$ defined above. In this case, there is only one transmitted waveform and the weighting $\mathcal{R}_n$ only depends on the receiver.

2.3.2 Statistical Data Model

The multistatic ambiguity function, or global ambiguity function, as presented in [4, 5, 20] determines weights for receiver contributions from the Neyman-Pearson optimal global statistic corresponding to a Swerling II target. A simple model is assumed for the received signal, weights are applied to the matched filtered output from each receiver, and the weighted contributions are added noncoherently. An overview of the derivation is presented in Section 2.3.2 and a more detailed derivation

of the global ambiguity function not readily available in the literature is given in Appendix A.

As in the deterministic model, we let $\boldsymbol{y}_m$ denote the position of the m^{th} transmitter with transmit waveform $s_m(t)$ and $\boldsymbol{z}_n$ denote the position of the n^{th} receiver. At each transmitter, we assume that a coherent processing interval (CPI) consists of a single pulse of duration T_{dm} and energy E_m so that

$$s_m(t) = \sqrt{2E_m}\Re\{f_m(t)\mathrm{e}^{\mathrm{i}\omega_c t}\}, \quad 0 \le t \le T_{dm} \tag{2.34}$$

where $f_m(t)$ is the complex envelope of the transmitted pulse, $\omega_c = 2\pi f_c$, and f_c is the carrier frequency for all transmitters. This approach does not require parts of the received signal to be separated out according to source transmitter. The input into the n^{th} receiver is given by the set of hypotheses:

$$\begin{aligned} H_0 &: r_n(t) = n_n(t) \\ H_1 &: r_n(t) = \sum_{m=1}^{M} a_{m,n}\gamma_{m,n}\tilde{s}_m(t-\tau^a_{m,n})\mathrm{e}^{\mathrm{i}\omega^a_{m,n}t} + n_n(t) \end{aligned} \tag{2.35}$$

where $n_n(t)$ is the noise at the n^{th} receiver, $\tau^a_{m,n}$ is the travel time along the propagation path from the m^{th} transmitter to the target to the n^{th} receiver, and $\gamma_{m,n} \approx (R_{\boldsymbol{x},m}R_{\boldsymbol{x},n})^{-1}$ is the propagation loss along this path for a target located at $\boldsymbol{x}$ where $R_{\boldsymbol{x},m} = |\boldsymbol{x} - \boldsymbol{y}_m|$ and $R_{\boldsymbol{x},n} = |\boldsymbol{x} - \boldsymbol{z}_n|$. The angular frequency $\omega^a_{m,n}$ is the total Doppler shift of the signal at the n^{th} receiver that originated from the m^{th} transmitter. The waveform $\tilde{s}_m(t) = \sqrt{2E_m}f_m(t)$ is the complex envelope of the transmitted signal $s_m(t)$.

The coefficient $a_{m,n}$ is the direction-dependent effective target reflectivity. We assume that $a_{1,n} = a_{2,n} = \cdots = a_{M,n} \equiv a_n$ so that the reflectivity depends only on the receiver position. This assumption may correspond to a scenario where all transmitters are isotropic; we note that bistatic range losses are taken into account elsewhere in the $\gamma_{m,n}$ term. We further assume a Swerling II target model so that the complex reflectivity is given by $a_n = A_n\mathrm{e}^{\mathrm{i}\phi_n}$ where the amplitude A_n denotes an independent Rayleigh distributed random variable with parameter A_{0n} and the

phase ϕ_n denotes an independent random variable uniformly distributed on $[0, 2\pi]$. The real and imaginary components of the noise $n_n(t)$ are zero-mean Gaussian with equal variance, unilateral power spectral density N_{0n}, and Rayleigh distributed envelope. The superscript a is used to denote a value corresponding to an actual target while the superscript h is used to denote a value corresponding to a hypothesized target.

At each receiver we perform standard matched filtering of the received data with the expected composite received waveform. The expected, normalized, and weighted composite waveform at the n^{th} receiver, $p_n(t; \vec{\tau}_n^h, \vec{\omega}_n^h)$, is specified by

$$p_n(t; \vec{\tau}_n^h, \vec{\omega}_n^h) = \frac{1}{B_n} \sum_{m=1}^{M} b_{m,n} f_m(t - \tau_{m,n}^h) \mathrm{e}^{\mathrm{i}\omega_{m,n}^h t}, \tag{2.36}$$

where

$$\begin{aligned} \vec{\tau}_n^h &= [\tau_{1,n}^h, \ldots, \tau_{M,n}^h]^T \\ \vec{\omega}_n^h &= [\omega_{1,n}^h, \ldots, \omega_{M,n}^h]^T. \end{aligned} \tag{2.37}$$

The coefficients

$$b_{m,n} = \frac{R_{\boldsymbol{p},m=1}}{R_{\boldsymbol{p},m}} \sqrt{\frac{E_m}{E_{m=1}}} \tag{2.38}$$

are derived for each transmitter-receiver pair from the bistatic radar equation, under the assumptions that $b_{1,n} = 1$ and $P_m G_m \sim E_m$ where P_m is the power of the m^{th} transmitter and G_m is the gain of the m^{th} transmitter. By inspection, $b_{m,n}$ depends only on the transmitter. The normalization constant B_n in (2.36) is chosen so that

$$\int_{-\infty}^{\infty} p_n(t; \vec{\tau}_n^h, \vec{\omega}_n^h) p_n^*(t; \vec{\tau}_n^h, \vec{\omega}_n^h) \mathrm{d}t = 1 \tag{2.39}$$

and

$$\int_{-\infty}^{\infty} p_n(t; \vec{\tau}_n^a, \vec{\omega}_n^a) p_n^*(t; \vec{\tau}_n^a, \vec{\omega}_n^a) \mathrm{d}t = 1. \tag{2.40}$$

The received signal at the n^{th} receiver can then be rewritten using (2.34), (2.36),

and (2.38) to obtain

$$\begin{aligned} r_n(t) &= \frac{a_n \mu_n}{R_{\boldsymbol{p},n}} \sum_{m=1}^{M} \frac{\sqrt{E_m}}{R_{\boldsymbol{p},m}} f_m(t - \tau_{mn}^a) \mathrm{e}^{\mathrm{i}\omega_{m,n}^a t} + n_n(t) \\ &= \frac{a_n B_n \mu_n \sqrt{E_{m=1}}}{R_{\boldsymbol{p},m=1} R_{\boldsymbol{p},n}} p_n(t; \vec{\tau}_n^a, \vec{\omega}_n^a) + n_n(t) \end{aligned} \tag{2.41}$$

where μ_n is the compensation constant [20]. The output of the matched filter at the n^{th} receiver is given by

$$d_n = \left| \int_{-\infty}^{\infty} \frac{r_n(t)}{\sqrt{N_{0n}}} p_n^*(t; \vec{\tau}_n^h, \vec{\omega}_n^h) \, \mathrm{d}t \right|. \tag{2.42}$$

By the assumptions that the envelope of the noise and the amplitude of the complex reflectivity of the target are both Rayleigh distributed, the output of the matched filter, d_n, will be Rayleigh distributed whether or not a target is present. We recall that a Rayleigh distributed random variable A with parameter A_0 will satisfy $E\{A^2\} = 2A_0^2$ and so $p(A) = R\left(A, \sqrt{\frac{1}{2}E\{A^2\}}\right)$ where R denotes the Rayleigh probability density function

$$R(A, A_0) = \frac{A}{A_0^2} \exp\left\{ -\frac{A^2}{2A_0^2} \right\}. \tag{2.43}$$

Under H_0, we have $E\{d_n^2\} = 1$, whereas under H_1, we have$E\{d_n^2\} = \frac{\rho_n}{2} + 1$ where ρ_n is the signal-to-noise ratio at the n^{th} receiver given by

$$\rho_n = \frac{4A_{0n}^2 B_n^2 \mu_n^2 E_{m=1}}{N_{0n} R_{\boldsymbol{p},m=1}^2 R_{\boldsymbol{p},n}^2}. \tag{2.44}$$

Thus, the distribution of d_n is given by

$$H_0 : p(d_n|H_0) = R\left(d_n, \sqrt{\frac{1}{2}E\{d_n^2\}}\right) = R\left(d_n, \sqrt{\frac{1}{2}}\right) \tag{2.45}$$

$$H_1 : p(d_n|H_1) = R\left(d_n, \sqrt{\frac{1}{2}E\{d_n^2\}}\right) = R\left(d_n, \sqrt{\frac{1}{2}\left(\frac{\rho_n}{2} + 1\right)}\right). \tag{2.46}$$

We treat the data from each of the receivers as N independent observations and

so the joint probability density of $\boldsymbol{d} = [d_1, \ldots, d_N]$ is the product of the individual probability densities and the likelihood ratio can be written as

$$\begin{aligned} L(\boldsymbol{d}) &= \frac{\prod_{n=1}^{N} R\left(d_n, \sqrt{\frac{1}{2}\left(\frac{\rho_n}{2}+1\right)}\right)}{\prod_{n=1}^{N} R\left(d_n, \sqrt{\frac{1}{2}}\right)} \\ &\propto \mathrm{e}^{D} \end{aligned} \tag{2.47}$$

where

$$D = \sum_{n=1}^{N} \frac{\rho_n}{\rho_n + 2} d_n^2 \tag{2.48}$$

is the optimal global statistic in the Neyman-Pearson sense.

We write the global ambiguity function [32], or multistatic ambiguity function, as

$$\Theta(T_h, T_a, \Omega_h, \Omega_a) = \sum_{n=1}^{N} c_n \Theta_n(\vec{\tau}_n^h, \vec{\tau}_n^a, \vec{\omega}_n^h, \vec{\omega}_n^a) \tag{2.49}$$

where

$$\Theta_n(\vec{\tau}_n^h, \vec{\tau}_n^a, \vec{\omega}_n^h, \vec{\omega}_n^a) = \left| \int_{-\infty}^{\infty} p_n(t; \vec{\tau}_n^a, \vec{\omega}_n^a) p_n^*(t; \vec{\tau}_n^h, \vec{\omega}_n^h)\, \mathrm{d}t \right|^2 \tag{2.50}$$

is the ambiguity function for the n^{th} receiver in terms of the composite waveforms corresponding to a true and hypothetical target and

$$\begin{aligned} T_h &= \{\tau_{m,n}^h\}_{M\times N}, & T_a &= \{\tau_{m,n}^a\}_{M\times N} \\ \Omega_h &= \{\omega_{m,n}^h\}_{M\times N}, & \Omega_a &= \{\omega_{m,n}^a\}_{M\times N}. \end{aligned}$$

The weights c_n are defined subject to $\sum_{n=1}^{N} c_n = 1$,

$$\Theta(T_a, T_a, \Omega_a, \Omega_a) = 1, \tag{2.51}$$

and

$$\Theta(T_h, T_a, \Omega_h, \Omega_a) = \frac{1}{K} E\{D_{\mathrm{s}}\} \tag{2.52}$$

where K is a normalization constant and D_{s} is the global statistic when only signal is present in the received data.

We solve for K and obtain the weights, c_n, of the individual ambiguity functions,

$$c_n = \frac{\frac{\rho_n^2}{2(\rho_n+2)}}{\sum_{k=1}^{N} \frac{\rho_k^2}{2(\rho_k+2)}},\ n = 1, ..., N. \tag{2.53}$$

It follows that the global ambiguity function, or statistically derived multistatic ambiguity function, is given by

$$\Theta(T_h, T_a, \Omega_h, \Omega_a) = \sum_{n=1}^{N} c_n \Theta_n(\vec{\tau}_n^h, \vec{\tau}_n^a, \vec{\omega}_n^h, \vec{\omega}_n^a)$$

where

$$\Theta_n(\vec{\tau}_n^h, \vec{\tau}_n^a, \vec{\omega}_n^h, \vec{\omega}_n^a) = \left| \int_{-\infty}^{\infty} p_n(t; \vec{\tau}_n^a, \vec{\omega}_n^a) p_n^*(t; \vec{\tau}_n^h, \vec{\omega}_n^h)\, \mathrm{d}t \right|^2,$$

$$c_n = \frac{\frac{\rho_n^2}{2(\rho_n+2)}}{\sum_{k=1}^{N} \frac{\rho_k^2}{2(\rho_k+2)}},$$

$$\rho_n = \frac{4A_{0n}^2 B_n^2 \mu_n^2 E_{m=1}}{N_{0n} R_{\boldsymbol{x},m=1}^2 R_{\boldsymbol{x},n}^2},$$

and $p_n(t; \vec{\tau}_n^a, \vec{\omega}_n^a)$ and $p_n(t; \vec{\tau}_n^h, \vec{\omega}_n^h)$ are the composite waveforms corresponding to a true and hypothetical target, respectively.

The global ambiguity function can be expressed in terms of actual and hypothetical ranges and velocities, as stated in [20], but for ease of comparison with the deterministic model, we write the global ambiguity function in terms of $\boldsymbol{p}, \boldsymbol{u}, \boldsymbol{x}$, and $\boldsymbol{v}$, where $\boldsymbol{x}$ and $\boldsymbol{v}$ are respectively the actual vector position and velocity of the target, and $\boldsymbol{p}$ and $\boldsymbol{u}$ correspond to a hypothetical vector position and velocity of the target. The statistically derived multistatic ambiguity function can be rewritten as

$$\Theta(\boldsymbol{p}, \boldsymbol{u}, \boldsymbol{x}, \boldsymbol{v}) = \sum_{n=1}^{N} c_n \Theta_n(\boldsymbol{p}, \boldsymbol{u}, \boldsymbol{x}, \boldsymbol{v}) \tag{2.54}$$

where

$$\tau^a_{m,n} = \frac{R_{\boldsymbol{x},m} + R_{\boldsymbol{x},n}}{\mathrm{c}_0}, \qquad \tau^h_{m,n} = \frac{R_{\boldsymbol{p},m} + R_{\boldsymbol{p},n}}{\mathrm{c}_0}$$
$$\omega^a_{m,n} = \omega_m \beta_{\boldsymbol{x},\boldsymbol{v}}, \qquad \omega^h_{m,n} = \omega_m \beta_{\boldsymbol{p},\boldsymbol{u}}$$

with

$$\beta_{\boldsymbol{x},\boldsymbol{v}} = -\left(\hat{\boldsymbol{R}}_{\boldsymbol{x},m} + \hat{\boldsymbol{R}}_{\boldsymbol{x},n}\right) \cdot \boldsymbol{v}/\mathrm{c}_0,$$
$$\beta_{\boldsymbol{p},\boldsymbol{u}} = -\left(\hat{\boldsymbol{R}}_{\boldsymbol{p},m} + \hat{\boldsymbol{R}}_{\boldsymbol{p},n}\right) \cdot \boldsymbol{u}/\mathrm{c}_0.$$

A more detailed derivation of the global ambiguity function is given in Appendix A.

For the much simplified case of a single transmitter, (2.54) can be written as

$$\begin{aligned}\Theta(\boldsymbol{p},\boldsymbol{u},\boldsymbol{x},\boldsymbol{v}) &= \sum_{n=1}^{N} c_n \tilde{\Theta}_n(\boldsymbol{p},\boldsymbol{u},\boldsymbol{x},\boldsymbol{v}) \\ &= \sum_{n=1}^{N} c_n \left| \int_{-\infty}^{\infty} f(t-\tau^a_n) f^*(t-\tau^h_n) \mathrm{e}^{\mathrm{i}(\omega^a_n - \omega^h_n)t}\, \mathrm{d}t \right|^2 \\ &= \sum_{n=1}^{N} c_n \left| \int_{-\infty}^{\infty} f(t) f^*(t-\tau) \mathrm{e}^{\mathrm{i}\tilde{\omega}t}\, \mathrm{d}t \right|^2 \end{aligned} \tag{2.55}$$

by several changes of variables and with

$$\begin{aligned}\tau &= \frac{R_{\boldsymbol{x},m=1} + R_{\boldsymbol{x},n} - (R_{\boldsymbol{p},m=1} + R_{\boldsymbol{p},n})}{\mathrm{c}_0} \\ \tilde{\omega} &= \omega_c(\beta_{\boldsymbol{p},\boldsymbol{u}} - \beta_{\boldsymbol{x},\boldsymbol{v}}) = 2\pi f_c(\beta_{\boldsymbol{p},\boldsymbol{u}} - \beta_{\boldsymbol{x},\boldsymbol{v}}),\end{aligned} \tag{2.56}$$

where $\omega_c = 2\pi f_c$ and f_c is the carrier frequency of the waveform sent from the single transmitter.

2.3.3 Discussion

Although the deterministic and statistical approaches in Sections 2.3.1 and 2.3.2 appear to have different goals (imaging versus detection), in fact these goals are closely related: both approaches provide information about target position and

velocity. In particular, plotting the detection test statistic as a function of target position and velocity produces an image [33].

The two approaches are based on fundamentally different underlying assumptions. The deterministic approach neglects multiple scattering, and uses an isotropic model for target scattering. The statistical approach assumes a Swerling II target and the resulting received signal, after processing, is assumed to be Rayleigh-distributed with zero-mean, Gaussian, equal-variance, real and imaginary components.

Both approaches, however, apply weights to the filtered data from each receiver and in the case of a single transmitter both MAFs reduce to summing ordinary bistatic narrowband radar ambiguity functions, with arguments adjusted for target locations and velocities. The weighting is done somewhat differently in the two approaches. In the deterministic approach, the weighting is due to purely geometrical factors and the data corresponding to each individual bistatic pair is weighted uniquely [34]. In the statistical approach, a statistical criterion is used to determine the appropriate weights, and the statistics are assumed to already incorporate information about the relevant geometry and target radar cross section.

The two approaches also differ in their assumptions about coherency of the system. The statistical approach assumes a noncoherent system, and consequently the summation of ambiguity functions is noncoherent. The deterministic approach can accommodate either a coherent or noncoherent system; the summation of ambiguity functions would then be coherent or noncoherent as appropriate. In our derivation and subsequent simulations we assume the deterministic approach is coherent.

2.3.4 Simulations

Simulation Parameters

In the following simulations, we use a complex up-chirp waveform of unit amplitude with 10 GHz carrier frequency, 100 MHz sampling frequency, 100 μs pulse width, and 5 MHz bandwidth. The spatial region of interest is a circle of 10 km radius.

Scenarios

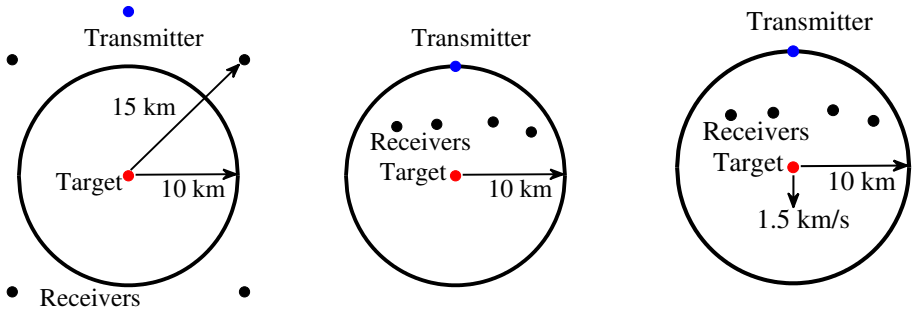

Figure 2.3: Arrangement of target, transmitter, and receivers for cases 2.3(a)-(c).

Results

Figures 2.4 and 2.5 correspond to the scene in Figure 2.3(a). Four receivers are spaced at a radius of 15 km and angles of 45°, 135°, 225°, and 315° from the center of the scene and a transmitter is placed 15 km from the center of the scene at 90°. We make an arbitrary choice to locate the target at the center of the scene to impose equal propagation loses at each receiver, and the target has constant zero velocity. The figures display the zero velocity cut and are shown with a normalized dB colorscale. The peak, identified by a white circle, is in the correct location for both models, but the ambiguity is lower for the deterministic model in Figure 2.4.

Figures 2.6 and 2.7 correspond to the scene in Figure 2.3(b). Four receivers are spaced at radius 8, 6, 5, and 7 km and angle 30°, 55°, 110°, and 140° respectively from the center of the scene and a transmitter at radius 10 km and angle 90°. The target is located at the center of the scene and has zero velocity. Due to nonuniform spacing of the receivers, the propagation loses along each path will differ. Again, the peak is in the correct location for both models but the ambiguity is lower in Figure 2.6.

Figures 2.8 and 2.9 correspond to the scene in Figure 2.3(c). This is the same scene as figures 2.6 and 2.7 except that the target has velocity 1.5 km/s in direction 270°. The figures display the zero velocity cut as before and the peak is spatially

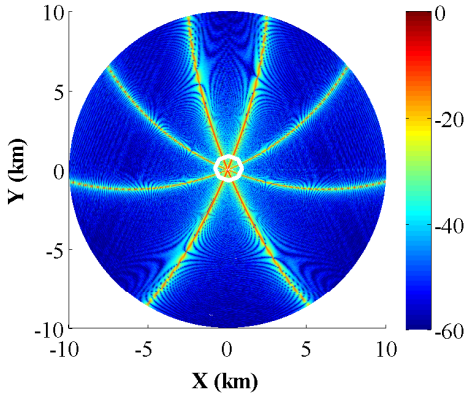

Figure 2.4: Deterministic MAF with equally spaced receivers and stationary target, zero velocity cut.

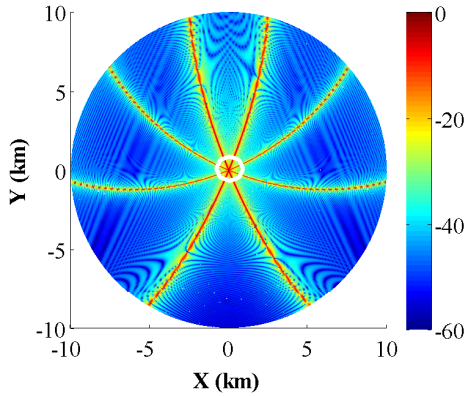

Figure 2.5: Statistical MAF with equally spaced receivers and stationary target, zero velocity cut.

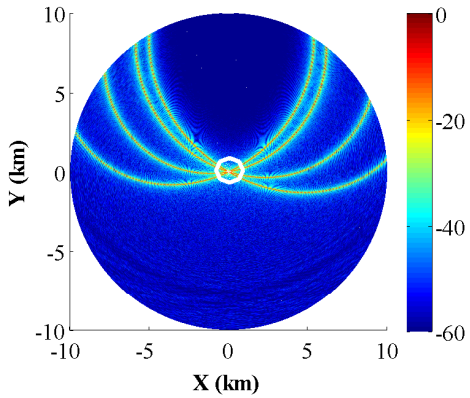

Figure 2.6: Deterministic MAF with receivers spaced in a rough line and stationary target, zero velocity cut.

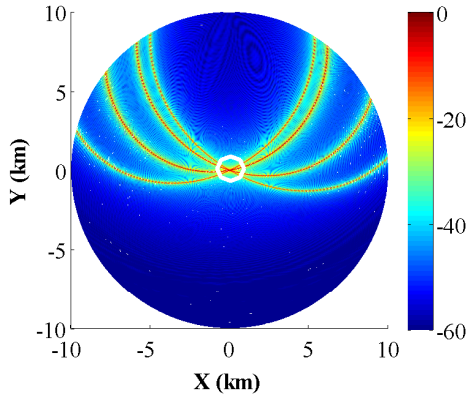

Figure 2.7: Statistical MAF with receivers spaced in a rough line and stationary target, zero velocity cut.

shifted in the direction opposite of the target velocity by about 300 m in both figures, as would be expected. As in the zero velocity cases, the ambiguity is lower in Figure 2.8.

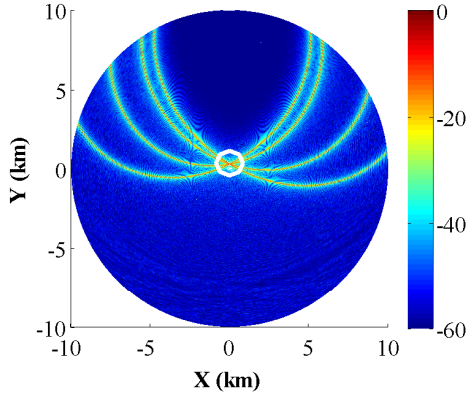

Figure 2.8: Deterministic MAF with receivers spaced in a rough line and target velocity 1.5 km/s, zero velocity cut.

2.3.5 Conclusion

Despite differences in the underlying assumptions of the deterministic and statistical models, the derived multistatic ambiguity functions and simulations are very similar. The deterministic MAF in Section 2.3.1 is derived from an imaging point of view, whereas the statistical MAF in Section 2.3.2 is derived from a detection point of view. The summations of the received data at each antenna can be either coherent or noncoherent for the deterministic MAF and are noncoherent for the

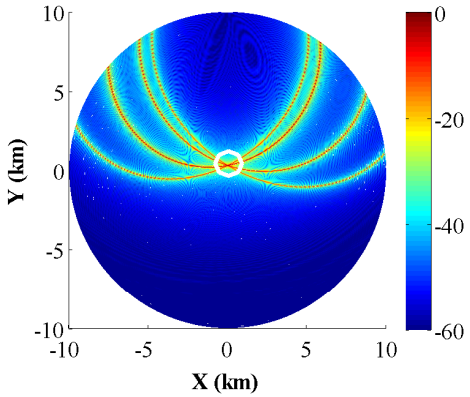

Figure 2.9: Statistical MAF with receivers spaced in a rough line and target velocity 1.5 km/s, zero velocity cut.

statistical MAF. The papers [4, 5, 20] are mainly focused on weight determination. The resulting MAFs differ yet both are modifications of the same classical ambiguity function.

The simulations show that the deterministically and statistically derived multistatic ambiguity functions provide comparable results for the zero-velocity case as well as for nonzero velocity cuts. The deterministic model has slightly more pronounced spatial localization than the statistical model, as would be predicted when comparing a coherent system to a noncoherent system.

The comparison of the resulting MAFs and corresponding simulations attests to the close relationship between detection and imaging, as observed in other works [33], and encourages thinking of imaging as a detection problem at each point in space and velocity.

2.4 Extension of the Deterministic Model

In Section 2.4 we build on the data model for the existing deterministically derived MAF from Section 2.3.1 with the inclusion of antenna beam patterns by relating the current density on the radiating and receiving antennas to a far-field spatial weighting factor. We begin in Section 2.4.1 by formulating a data model that incorporates radiation of the transmitted waveforms, scattering from a distribution of moving point-like targets, and reception at the receiving antennas. From this model we develop an imaging formula in position and velocity and a corresponding

ambiguity function or point-spread function in Sections 2.4.2 and 2.4.3. We present numerical simulations in Section 2.4.4 and then conclude.

2.4.1 Model for Data

Model for wave propagation

We model wave propagation and scattering by the scalar wave equation [35] for the wavefield $\psi(t, \boldsymbol{x})$ due to a current density $j_m(t + T_m, \boldsymbol{x} - \boldsymbol{y}_m)$ transmitted at time $-T_m$ from location $\boldsymbol{y}_m$:

$$[\nabla^2 - c^{-2}(t, \boldsymbol{x})\partial_t^2]\psi(t, \boldsymbol{x}) = \mu_0 \partial_t j_m(t + T_m, \boldsymbol{x} - \boldsymbol{y}_m)\,. \tag{2.57}$$

where μ_0 denotes the vacuum magnetic permeability.

A single scatterer moving at velocity $\boldsymbol{v}$ corresponds to an index-of-refraction distribution $n^2(\boldsymbol{x} - \boldsymbol{v}t)$:

$$c^{-2}(t, \boldsymbol{x}) = \mathrm{c}_0^{-2}[1 + n^2(\boldsymbol{x} - \boldsymbol{v}t)]\,, \tag{2.58}$$

where c_0 is the speed of light in vacuum. We write $q_{\boldsymbol{v}}(\boldsymbol{x} - \boldsymbol{v}t) = \mathrm{c}_0^{-2} n^2(\boldsymbol{x} - \boldsymbol{v}t)$. To model multiple moving scatterers, we let $q_{\boldsymbol{v}}(\boldsymbol{x} - \boldsymbol{v}t)\mathrm{d}\boldsymbol{x}\,\mathrm{d}\boldsymbol{v}$ be the corresponding quantity for the scatterers in the volume $\mathrm{d}\boldsymbol{x}\,\mathrm{d}\boldsymbol{v}$ centered at $(\boldsymbol{x}, \boldsymbol{v})$, the spatial distribution, at time $t = 0$, of scatterers moving with velocity $\boldsymbol{v}$. Consequently, the scatterers in the spatial volume $\mathrm{d}\boldsymbol{x}$ (at $\boldsymbol{x}$) give rise to

$$c^{-2}(t, \boldsymbol{x}) = \mathrm{c}_0^{-2} + \int q_{\boldsymbol{v}}(\boldsymbol{x} - \boldsymbol{v}t)\mathrm{d}\boldsymbol{v}\,. \tag{2.59}$$

We note that the physical interpretation of $q_{\boldsymbol{v}}$ involves a choice of a time origin. A choice that is particularly appropriate, in view of our assumption about linear target velocities, is a time during which the wave is interacting with targets of interest. This implies that the activation of the antenna at $\boldsymbol{y}_m$ takes place at a negative time which we have denoted in (2.57) by $-T_m$. The wave equation

corresponding to (2.59) is then

$$\left[\nabla^2 - \mathrm{c}_0^{-2}\partial_t^2 - \int q_{\boldsymbol{v}}(\boldsymbol{x} - \boldsymbol{v}t)\mathrm{d}\boldsymbol{v}\,\partial_t^2\right]\psi(t,\boldsymbol{x}) = \mu_0\partial_t j_m(t + T_m, \boldsymbol{x} - \boldsymbol{y}_m)\,. \tag{2.60}$$

Model for transmitted field

The "incident" field $\psi_m^{\mathrm{in}}(t,\boldsymbol{x})$ is the field that is generated by the transmitter at position $\boldsymbol{y}_m$ and propagates into an empty universe:

$$[\nabla^2 - \mathrm{c}_0^{-2}\partial_t^2]\psi_m^{\mathrm{in}}(t,\boldsymbol{x}) = \mu_0\partial_t j_m(t + T_m, \boldsymbol{x} - \boldsymbol{y}_m)\,. \tag{2.61}$$

We assume that the antenna is constructed to be sufficiently broadband so that the source term can be written as the product

$$\mu_0\partial_t j_m(t,\boldsymbol{x}) = s_m(t)f_m(\boldsymbol{x}) \tag{2.62}$$

where $s_m(t)$ is the waveform transmitted from the antenna located at $\boldsymbol{y}_m$ and $f_m(\boldsymbol{x})$ is a spatial factor. We recall that according to the convention adopted in (2.20), $s_m(t)$ can be written in terms of its inverse Fourier transform as

$$s_m(t) = \frac{1}{2\pi}\int \mathrm{e}^{-\mathrm{i}\omega t}S_m(\omega)\mathrm{d}\omega\,. \tag{2.63}$$

The frequency-domain version of (2.61) is then

$$[\nabla^2 + k^2]\Psi_m^{\mathrm{in}}(\omega,\boldsymbol{x}) = \mathrm{e}^{-\mathrm{i}\omega T_m}S_m(\omega)f_m(\boldsymbol{x} - \boldsymbol{y}_m), \tag{2.64}$$

where $k = \omega/c_0$ and we can solve (2.64) to obtain

$$\Psi_m^{\mathrm{in}}(\omega,\boldsymbol{x}) = \int \frac{\mathrm{e}^{\mathrm{i}k|\boldsymbol{x}-\boldsymbol{z}_n|}}{4\pi|\boldsymbol{x}-\boldsymbol{z}_n|}\mathrm{e}^{-\mathrm{i}\omega T_m}S_m(\omega)f_m(\boldsymbol{z}_n - \boldsymbol{y}_m)\mathrm{d}\boldsymbol{z}. \tag{2.65}$$

We assume that the antenna is distant from the target, so that $|\boldsymbol{x} - \boldsymbol{y}_m| \gg |\boldsymbol{z}_n - \boldsymbol{y}_m|$ and $|\boldsymbol{x} - \boldsymbol{y}_m| \gg k|\boldsymbol{z}_n - \boldsymbol{y}_m|^2$. Consequently in (2.65) we make the far-field expansion

$$\frac{\mathrm{e}^{\mathrm{i}k|\boldsymbol{x}-\boldsymbol{z}_n|}}{4\pi|\boldsymbol{x}-\boldsymbol{z}_n|} \approx \frac{\mathrm{e}^{\mathrm{i}k|\boldsymbol{x}-\boldsymbol{y}_m|}}{4\pi|\boldsymbol{x}-\boldsymbol{y}_m|}\mathrm{e}^{\mathrm{i}k\widehat{(\boldsymbol{x}-\boldsymbol{y}_m)}\cdot(\boldsymbol{y}_m-\boldsymbol{z}_n)} \tag{2.66}$$

thus obtaining

$$\begin{aligned}\Psi_m^{\mathrm{in}}(\omega,\boldsymbol{x}) &\approx \frac{\mathrm{e}^{\mathrm{i}k|\boldsymbol{x}-\boldsymbol{y}_m|}}{4\pi|\boldsymbol{x}-\boldsymbol{y}_m|}\mathrm{e}^{-\mathrm{i}\omega T_m}S_m(\omega)\int \mathrm{e}^{\mathrm{i}k(\widehat{\boldsymbol{x}-\boldsymbol{y}_m})\cdot(\boldsymbol{y}_m-\boldsymbol{z}_n)}f_m(\boldsymbol{z}_n-\boldsymbol{y}_m)\mathrm{d}\boldsymbol{z}_n \\ &= \frac{\mathrm{e}^{\mathrm{i}k|\boldsymbol{x}-\boldsymbol{y}_m|}}{4\pi|\boldsymbol{x}-\boldsymbol{y}_m|}\mathrm{e}^{-\mathrm{i}\omega T_m}S_m(\omega)F_m(k(\widehat{\boldsymbol{x}-\boldsymbol{y}_m})) \qquad (2.67)\end{aligned}$$

where F_m denotes the spatial Fourier transform of f_m. F_m represents the far-field beam pattern of the transmitting antenna as a function of frequency. We assume that the antenna is sufficiently broadband that F_m is independent of frequency over the effective support of the waveform $S_m(\omega)$. Hence, we replace $F_m(k(\widehat{\boldsymbol{x}-\boldsymbol{y}_m}))$ with $F_m(\widehat{\boldsymbol{x}-\boldsymbol{y}_m})$ to reflect the dependence of the beam pattern solely on the angle determined by the transmitter and observation positions $\boldsymbol{y}_m$ and $\boldsymbol{x}$, respectively. Consequently, the transmitted field in the time domain can be expressed as

$$\psi_m^{\mathrm{in}}(t,\boldsymbol{x}) = \frac{F_m(\widehat{\boldsymbol{x}-\boldsymbol{y}_m})}{4\pi|\boldsymbol{x}-\boldsymbol{y}_m|}s_m(t-|\boldsymbol{x}-\boldsymbol{y}_m|/\mathrm{c}_0+T_m). \qquad (2.68)$$

Model for scattered field

We can likewise model the scattered field that is received at $\boldsymbol{z}_n$ using the scalar wave equation under the Born (single-scattering) approximation with a source $\int q_{\boldsymbol{v}}(\boldsymbol{x}-\boldsymbol{v}t)\mathrm{d}\boldsymbol{v}\ \partial_t^2\psi_m^{\mathrm{in}}(t,\boldsymbol{x})$ provided by the reflected incident field:

$$[\nabla^2-\mathrm{c}_0^{-2}\partial_t^2]\psi_m^{\mathrm{sc}}(t,\boldsymbol{z}_n) = \int q_{\boldsymbol{v}}(\boldsymbol{x}-\boldsymbol{v}t)\mathrm{d}\boldsymbol{v}\partial_t^2\psi_m^{\mathrm{in}}(t,\boldsymbol{x}). \qquad (2.69)$$

Solving for the scattered field we obtain

$$\begin{aligned}\psi_m^{\mathrm{sc}}(t,\boldsymbol{z}_n) = \int &\frac{\delta(t-t'-R_{\boldsymbol{x},n}(t')/\mathrm{c}_0)}{4\pi R_{\boldsymbol{x},n}(t')}\int q_{\boldsymbol{v}}(\boldsymbol{x})\mathrm{d}\boldsymbol{v} \\ &\times F_m(\widehat{\boldsymbol{R}}_{\boldsymbol{x},m}(t'))\frac{\ddot{s}_m(t'+T_m-R_{\boldsymbol{x},m}(t')/\mathrm{c}_0)}{4\pi R_{\boldsymbol{x},m}(t')}\mathrm{d}t'\mathrm{d}\boldsymbol{x} \qquad (2.70)\end{aligned}$$

where $\boldsymbol{R}_{\boldsymbol{x},m}(t')=\boldsymbol{x}+\boldsymbol{v}t'-\boldsymbol{y}_m$, $R_{\boldsymbol{x},m}(t')=|\boldsymbol{R}_{\boldsymbol{x},m}(t')|$, and $\widehat{\boldsymbol{R}}_{\boldsymbol{x},m}(t')=\boldsymbol{R}_{\boldsymbol{x},m}(t')/R_{\boldsymbol{x},m}(t')$.

We assume that the targets are moving slowly, so that $|\boldsymbol{v}|t'$ and $k|\boldsymbol{v}|^2t'^2$ are much smaller than $|\boldsymbol{x}-\boldsymbol{y}_m|$ or $|\boldsymbol{x}-\boldsymbol{z}_n|$ where $k=\omega_{\max}/\mathrm{c}_0$ and $\omega_{\max}$ is the effective maximum angular frequency of the signal $s_m(t)$. Thus, we can replace $R_{\boldsymbol{x},m}(t')$ and

$\widehat{\boldsymbol{R}}_{\boldsymbol{x},m}(t')$ with $R_{\boldsymbol{x},m}(0)$ and $\widehat{\boldsymbol{R}}_{\boldsymbol{x},m}(0)$ such that and $\boldsymbol{R}_{\boldsymbol{x},m}(0) = \boldsymbol{x} - \boldsymbol{y}_m$, $R_{\boldsymbol{x},m}(0) = |\boldsymbol{R}_{\boldsymbol{x},m}(0)|$, and $\widehat{\boldsymbol{R}}_{\boldsymbol{x},m}(0) = \boldsymbol{R}_{\boldsymbol{x},m}(0)/R_{\boldsymbol{x},m}(0)$. The scattered field in the slow-mover case can then be written [11]

$$\psi_m^{\mathrm{sc,S}}(t, \boldsymbol{z}_n) = \int \frac{F_m(\widehat{\boldsymbol{R}}_{\boldsymbol{x},m}(0))}{(4\pi)^2 R_{\boldsymbol{x},n}(0) R_{\boldsymbol{x},m}(0) \mu_{\boldsymbol{x},\boldsymbol{v}}(0)} \ddot{s}_m \left[\phi(t, \boldsymbol{x}, \boldsymbol{v})\right] q_{\boldsymbol{v}}(\boldsymbol{x}) \mathrm{d}\boldsymbol{x}\, \mathrm{d}\boldsymbol{v} \tag{2.71}$$

where

$$\phi(t, \boldsymbol{x}, \boldsymbol{v}) = \alpha_{\boldsymbol{x},\boldsymbol{v}} \left(t - R_{\boldsymbol{x},n}(0)/\mathrm{c}_0\right) - R_{\boldsymbol{x},m}(0)/\mathrm{c}_0 + T_m \tag{2.72}$$

with Doppler scale factor

$$\alpha_{\boldsymbol{x},\boldsymbol{v}} = \frac{1 - \widehat{\boldsymbol{R}}_{\boldsymbol{x},m}(0) \cdot \boldsymbol{v}/\mathrm{c}_0}{1 + \widehat{\boldsymbol{R}}_{\boldsymbol{x},n}(0) \cdot \boldsymbol{v}/\mathrm{c}_0} \tag{2.73}$$

and

$$\mu_{\boldsymbol{x},\boldsymbol{v}}(0) = 1 + \widehat{\boldsymbol{R}}_{\boldsymbol{x},n}(0) \cdot \boldsymbol{v}/\mathrm{c}_0. \tag{2.74}$$

We assume the radar system is using a narrowband waveform of the form

$$s_m(t) = \tilde{s}_m(t)\, \mathrm{e}^{-\mathrm{i}\omega_m t} \tag{2.75}$$

where $\tilde{s}_m(t)$ is slowly varying, as a function of t, in comparison with $\exp(-\mathrm{i}\omega_m t)$ and ω_m is the carrier frequency for the transmitter at position $\boldsymbol{y}_m$. The scattered field in the narrowband case becomes

$$\psi_m^{\mathrm{sc,SN}}(t, \boldsymbol{z}_n) = \int \frac{-\omega_m^2 F_m(\widehat{\boldsymbol{R}}_{\boldsymbol{x},m}(0))}{(4\pi)^2 R_{\boldsymbol{x},n}(0) R_{\boldsymbol{x},m}(0) \mu_{\boldsymbol{x},\boldsymbol{v}}(0)} \tilde{s}_m \left[\phi(t, \boldsymbol{x}, \boldsymbol{v})\right] \mathrm{e}^{-\mathrm{i}\omega_m \phi(t,\boldsymbol{x},\boldsymbol{v})} q_{\boldsymbol{v}}(\boldsymbol{x}) \mathrm{d}\boldsymbol{x}\, \mathrm{d}\boldsymbol{v}. \tag{2.76}$$

Model for received data

By an argument similar to the one used to obtain the transmission beam pattern $F_m(\widehat{\boldsymbol{R}}_{\boldsymbol{x},m}(0))$, we obtain a receiver antenna beam pattern $F_n(\widehat{\boldsymbol{R}}_{\boldsymbol{x},n}(0))$ [35]. We observe that F_n is dependent on the angle determined by the receiver and observation positions $\boldsymbol{z}_n$ and $\boldsymbol{x}$, respectively. This factor arises from modeling the reception process that occurs at the receiving antenna, $\boldsymbol{z}_n$, as an integration of the scattered

field $\psi_m^{\mathrm{sc,SN}}(t, \boldsymbol{z}_n)$ over the antenna with an appropriate weighting function and applying the far-field expansion as before. Consequently, we express the received data as

$$d_{m,n}(t) = \int \frac{-\omega_m^2 F_m(\widehat{\boldsymbol{R}}_{\boldsymbol{x},m}(0)) F_n(\widehat{\boldsymbol{R}}_{\boldsymbol{x},n}(0))}{(4\pi)^2 R_{\boldsymbol{x},n}(0) R_{\boldsymbol{x},m}(0) \mu_{\boldsymbol{x},\boldsymbol{v}}(0)} \tilde{s}_m \left[\phi(t, \boldsymbol{x}, \boldsymbol{v})\right] \mathrm{e}^{-\mathrm{i}\omega_m \phi(t,\boldsymbol{x},\boldsymbol{v})} q_{\boldsymbol{v}}(\boldsymbol{x}) \mathrm{d}\boldsymbol{x}\, \mathrm{d}\boldsymbol{v}. \tag{2.77}$$

2.4.2 Image Formation

The corresponding imaging operation involves applying a weighted matched filter and summing over all transmitters $\boldsymbol{y}_m$ and receivers $\boldsymbol{z}_n$. The phase-space image is given by the expression

$$I_\infty(\boldsymbol{p}, \boldsymbol{u}) = \sum_m \sum_n \frac{(4\pi)^2 R_{\boldsymbol{p},n}(0) R_{\boldsymbol{p},m}(0) \mu_{\boldsymbol{p},\boldsymbol{u}}(0) \alpha_{\boldsymbol{p},\boldsymbol{u}}}{-\omega_m^2} J_{m,n}(\boldsymbol{p}, \boldsymbol{u}) \times \int \tilde{s}_m^* \left[\phi(t, \boldsymbol{p}, \boldsymbol{u})\right] \mathrm{e}^{\mathrm{i}\omega_m \phi(t,\boldsymbol{p},\boldsymbol{u})} d_{m,n}(t) \mathrm{d}t. \tag{2.78}$$

Here the star denotes complex conjugation, and $J_{m,n}$ is a geometrical factor [11] that depends on the configuration of transmitters and receivers.

2.4.3 Analysis of the Image: Ambiguity Function

We obtain the narrowband MIMO ambiguity function (point-spread function) of the imaging system, $K_\infty^{\mathrm{NB}}(\boldsymbol{p}, \boldsymbol{u}; \boldsymbol{x}, \boldsymbol{v})$, by substituting (2.77) into (2.78)

$$I_\infty(\boldsymbol{p}, \boldsymbol{u}) = \int K_\infty^{\mathrm{NB}}(\boldsymbol{p}, \boldsymbol{u}; \boldsymbol{x}, \boldsymbol{v}) q_{\boldsymbol{v}}(\boldsymbol{x}) \mathrm{d}^3x\, \mathrm{d}^3v \tag{2.79}$$

with

$$K_\infty^{\mathrm{NB}}(\boldsymbol{p}, \boldsymbol{u}; \boldsymbol{x}, \boldsymbol{v}) = \sum_m \sum_n F_m(\widehat{\boldsymbol{R}}_{\boldsymbol{x},m}(0)) F_n(\widehat{\boldsymbol{R}}_{\boldsymbol{x},n}(0)) J_{m,n}(\boldsymbol{p}, \boldsymbol{u}) \times \int \tilde{s}_m^* \left[\phi(t, \boldsymbol{p}, \boldsymbol{u})\right] \tilde{s}_m \left[\phi(t, \boldsymbol{x}, \boldsymbol{v})\right] \mathrm{e}^{\mathrm{i}\omega_m [\phi(t,\boldsymbol{p},\boldsymbol{u}) - \phi(t,\boldsymbol{x},\boldsymbol{v})]}\, \mathrm{d}t. \tag{2.80}$$

Through some manipulation the MIMO ambiguity function (MAF) reduces

to [11]

$$K_{\infty}^{\mathrm{NB}}(\boldsymbol{p},\boldsymbol{u};\boldsymbol{x},\boldsymbol{v}) = \sum_{m}\sum_{n} \mathrm{e}^{\mathrm{i}\Phi_{m,n}} F_m(\widehat{\boldsymbol{R}}_{\boldsymbol{x},m}(0)) F_n(\widehat{\boldsymbol{R}}_{\boldsymbol{x},n}(0)) \tilde{J}_{m,n}(\boldsymbol{p},\boldsymbol{u}) A_m(\tilde{\omega},\tau), \tag{2.81}$$

where $\tilde{J}_{m,n}$ is a geometrical factor closely related to $J_{m,n}$ above,

$$A_m(\tilde{\omega},\tau) = \mathrm{e}^{-\mathrm{i}\omega_m\tau} \int \tilde{s}_m^*(t-\tau)\, \tilde{s}_m(t)\, \mathrm{e}^{\mathrm{i}\tilde{\omega}t}\mathrm{d}t \tag{2.82}$$

is a version of the classical monostatic narrowband radar ambiguity function, which is defined here to include a phase, with parameters

$$\tilde{\omega} = \omega_m(\beta_{\boldsymbol{p},\boldsymbol{u}} - \beta_{\boldsymbol{x},\boldsymbol{v}}) \tag{2.83}$$

$$\tau = [(R_{\boldsymbol{p},m}(0) + R_{\boldsymbol{p},n}(0)) - (R_{\boldsymbol{x},m}(0) + R_{\boldsymbol{x},n}(0))]/\mathrm{c}_0, \tag{2.84}$$

and

$$\begin{aligned} \exp[\mathrm{i}\Phi_{m,n}] = {} & \exp[\,\mathrm{i}\omega_m(\beta_{\boldsymbol{p},\boldsymbol{u}} - \beta_{\boldsymbol{x},\boldsymbol{v}})(R_{\boldsymbol{x},m}(0)/\mathrm{c}_0 - T_m)] \\ & \times \exp[-\mathrm{i}k_m\beta_{\boldsymbol{u}}(R_{\boldsymbol{x},n}(0) - R_{\boldsymbol{p},n}(0))] \end{aligned} \tag{2.85}$$

with $k_m = \omega_m/\mathrm{c}_0$ and $\beta_{\boldsymbol{x},\boldsymbol{v}} = -\left(\widehat{\boldsymbol{R}}_{\boldsymbol{x},m}(0) + \widehat{\boldsymbol{R}}_{\boldsymbol{x},n}(0)\right)\cdot\boldsymbol{v}/\mathrm{c}_0$. The narrowband result in (2.81) clearly exhibits the importance of the bistatic bisector vectors $\widehat{\boldsymbol{R}}_{\boldsymbol{x},m}(0) + \widehat{\boldsymbol{R}}_{\boldsymbol{x},n}(0)$ and $\widehat{\boldsymbol{R}}_{\boldsymbol{p},m}(0) + \widehat{\boldsymbol{R}}_{\boldsymbol{p},n}(0)$. We observe that the MAF (2.81) is a weighted sum of classical narrowband ambiguity functions.

2.4.4 Simulations

In the following simulations, we examine multiple geometries with moving targets.

Simulation Parameters

We use a complex up-chirp and two 20-chip random polyphase codes with 10 GHz carrier frequency, 20 MHz sampling frequency, 20 μs pulse width, and 1

MHz bandwidth. The classical ambiguity functions (CAFs) for these waveforms are shown in Figures 2.10(a)-2.10(c). The ridge-like CAF with low range lobes of the up-chirp and thumbtack CAF with higher range side lobes shown in Figure 2.10 are evident in our simulations of the MAF for various geometries.

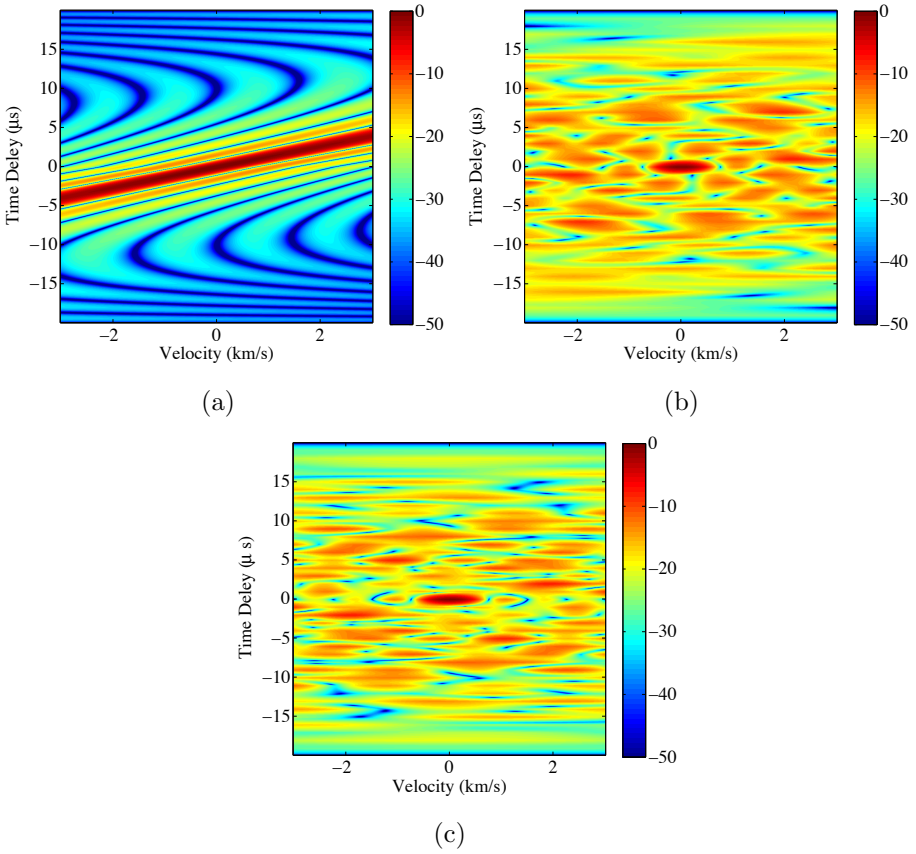

Figure 2.10: Classical ambiguity functions of an up-chirp, (a), and two 20 chip random polyphase codes, (b) and (c), plotted against velocity and time delay on a dB scale.

The beam pattern used in these simulations is based on a N-element uniform linear array with half-wavelength spacing and half-power beam width of approximately 10° for $N = 10$ and 4° for $N = 25$. It is expressed as a function of angle by

$$\tilde{F}_m(\theta) = \frac{1}{N} \frac{\sin\left(\frac{N\pi}{2}\sin(\theta)\right)}{\sin\left(\frac{\pi}{2}\sin(\theta)\right)}, \quad -\frac{\pi}{2} \leq \theta \leq \frac{\pi}{2} \tag{2.86}$$

where $\tilde{F}_m(\theta) = F_m(\widehat{\boldsymbol{R}}_{\boldsymbol{x},m}(0)) = F_n(\widehat{\boldsymbol{R}}_{\boldsymbol{x},n}(0))$ and θ is measured relative to antenna boresight. The boresight direction is assumed to be in the direction of the scene

center.

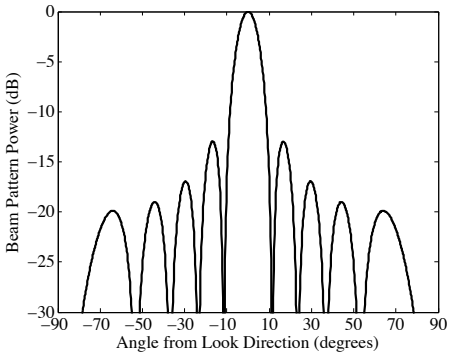

Figure 2.11: Beam Pattern Power, $\tilde{F}_m^2(\theta)$, with N=10.

Scenarios

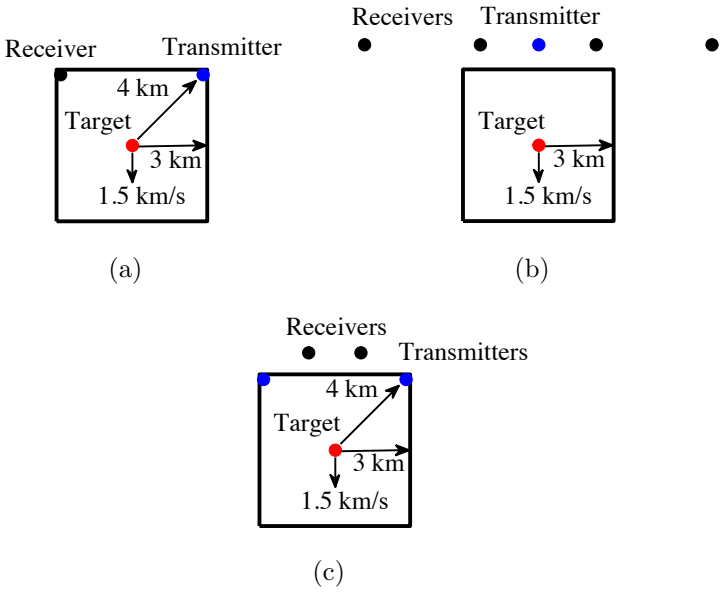

Figure 2.12: Arrangement of target, transmitters, and receivers for cases 2.12(a)-(c).

Results

Figures 2.13-2.16 display the MAF for various geometries depicted in Figure 2.12(a)-2.12(c) and are shown with a normalized dB colorscale. The region displayed is a 6 km by 6 km square. In some plots, peaks are identified by white circles. The

antenna beam patterns of the transmitters are evident in the plots of the MAF power.

Figures 2.13 and 2.14 correspond to the bistatic scene in Figure 2.12(a). A transmitter is spaced at radius 4 km and angle 50° a receiver at radius 4 km and angle 130°. The transmitted waveform is an up-chirp. We make an arbitrary choice to locate the target at the center of the scene to impose equal propagation loses at each receiver in multistatic cases described below, and the target and has velocity 1.5 km/s in direction 270°. In the corresponding velocity cut shown, the peak is in the correct location. The 10 element beam pattern in Figure 2.13 and the 25 element beam pattern in Figure 2.14 is clearly visible.

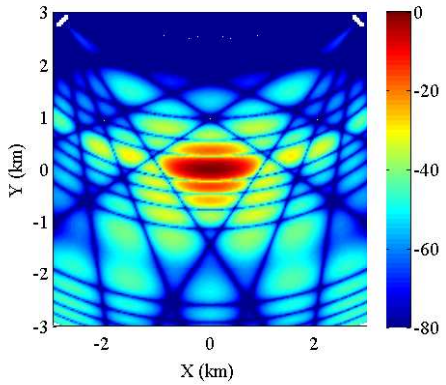

Figure 2.13: MIMO ambiguity function (MAF) for bistatic transmitter and receiver case. Each antenna has 10 elements and the transmitted waveform is an up-chirp. Cut at correct velocity.

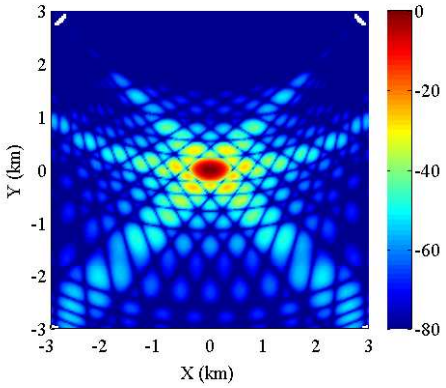

Figure 2.14: MAF for bistatic transmitter and receiver case. Each antenna has 25 elements and the transmitted waveform is an up-chirp. Cut at correct velocity.

Figures 2.15 and 2.16 correspond to the scene in Figure 2.12(b). Four receivers are spaced in a line with a transmitter in the center at radius 4 km and angle 90°. An up-chirp waveform is used in Figure 2.15 and the phase code from Figure 3.11(b) is used in Figure 2.16. The target is located at the center of the scene and has velocity 1.5 km/s in direction 270°. Figure 2.15(a) depicts the zero velocity cut in which the target is nearly in the correct location but is spatially shifted in the direction opposite of the target velocity by about 300 m, as would be expected from the up-chirp CAF in 3.11(a). Figure 2.15(b) depicts the correct velocity cut in which the target is in the correct location. Figure 2.16(a) depicts the zero velocity cut in which the target is not visible, indicative of the doppler intolerance of phase codes. Figure 2.16(b) depicts the correct velocity cut in which the target is in the correct location.

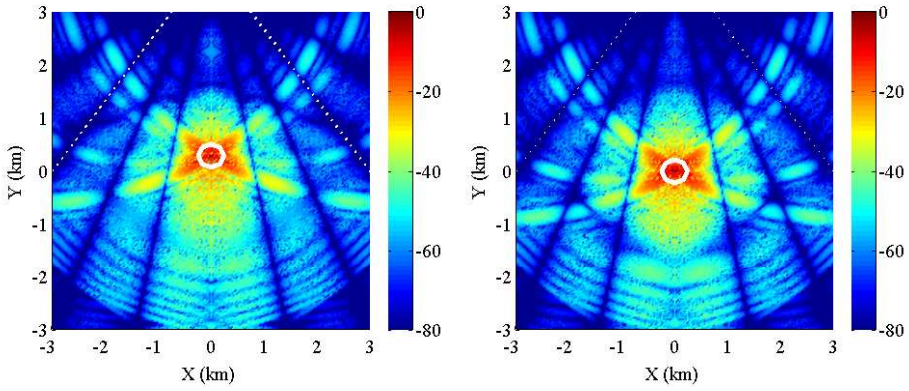

(a) (b)

Figure 2.15: MAF for one transmitter and four receiver case. Each antenna has a 10 element beam pattern and the transmitted waveform is an up-chirp, (a) zero velocity cut and (b) velocity cut at correct velocity.

Figure 2.17 corresponds to the scene in Figure 2.12(c). Two receivers are spaced at radius 4 km and angle 45° and 135° from the center of the scene and two transmitters at radius 4 km and angle 75° and 105°. The rightmost transmitter emits the random polyphase code in Figure 3.11(b) and the other the phase code in Figure 3.11(c). The target is located at the center of the scene and has velocity 1.5 km/s in direction 270°. In the corresponding velocity cut shown, the peak is in the correct location. In other velocity cuts, not presented here, the target is not visible.

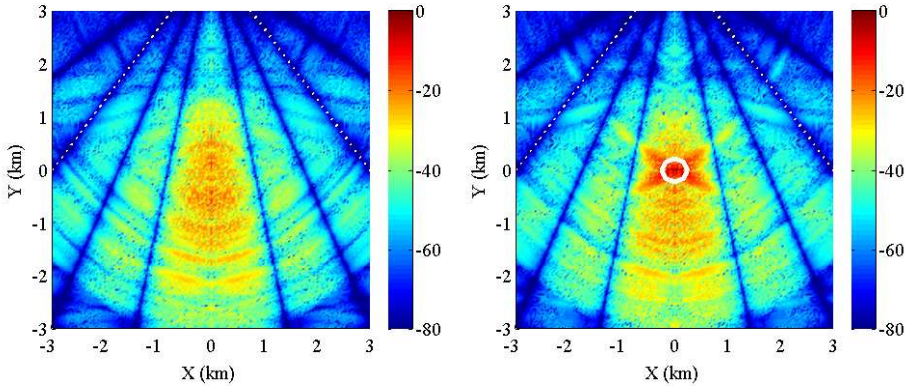

Figure 2.16: MAF for one transmitter and four receiver case. Each antenna has a 10 element beam pattern and the transmitted waveform is the phasecode in Figure 3.11(b), (a) zero velocity cut and (b) velocity cut at correct velocity.

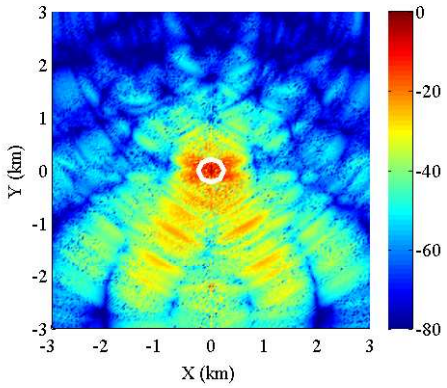

Figure 2.17: MAF for the case of two transmitters and two receivers. Each antenna has a 10 element beam pattern and each transmitter emits a distinct random polyphase code. Velocity cut at correct velocity.

2.4.5 Conclusion

We have outlined the development of a linearized imaging theory that combines the spatial, temporal, and spectral aspects of scattered waves, and also incorporates antenna beam patterns.

This imaging theory is based on the general (linearized) expression we derived for waves scattered from moving objects, which we model in terms of a distribution in phase space. The expression for the scattered waves takes the form of a superposition of weighted, time delayed, and frequency shifted versions of the incident field; consequently we form an image by applying a weighted matched filter.

The effect of incorporating a transmit beam pattern is consistent with expectations; the returns from the main lobe are greater than that from the side lobes. The derived MAF has the capability of more closely approximating reality than the previous foundational work [22].

Our simulations show that the information that can be obtained depends critically on the transmitted waveforms. In particular, the Dopper-intolerant polyphase coded waveforms produce a MAF with good localization in velocity, as expected. The up-chirp MAF, on the other hand, has low sidelobes, but can cause the target image to focus at the wrong location and wrong velocity.

CHAPTER 3
Polarimetric Radar Data Model

3.1 Introduction

In Chapter 2 we investigated scalar representations of multistatic radar data originating from the scalar wave equation. In this chapter we formulate a full vector model for multistatic radar data including the polarization and scattering of electromagnetic waves. As in the previous chapter, we must address the fusion of data from multiple transmitters and receivers, a natural consequence of considering a multistatic system. In the vector case we must also address the representation of the electromagnetic vector fields and the transformation of these fields that occurs when the waves are scattered off of a target. The possible advantages of both multistatic systems and polarimetric systems encourage the formulation of a full vector model for multistatic radar data.

As discussed in Chapter 1, multistatic systems have a number of theoretical advantages, including the ability to transmit multiple waveforms from collocated or distributed antennas, thus enabling interrogation of larger areas of interest due to the geometry of the system. It may also be possible to augment fielded systems with additional low-power passive components, forming a bistatic or multistatic system [30,36]. The performance of a multistatic system is heavily dependent upon the number, geometry, and polarization of the transmitters and receivers and the waveforms that will be transmitted. An appropriate model can be used to characterize how these parameters impact performance for a particular environment and targets of interest. A multistatic system must also ensure that all constituent antennas are coherent in time, that there is a common clock available to all transmitters and receivers, and frequency or risk a loss of information [17–19].

There has been significant work done to develop models for multistatic radar systems and to address issues related to the design of a multistatic system. There has been theory developed for multistatic moving target detection [1–6], multistatic imaging of a stationary scene [7–10], multistatic imaging of moving targets [11–16],

and coherence of a multistatic system [17–19].

Polarimetric radar systems are advantageous because more information can be collected about an environment if multiple polarizations are transmitted and received than if a single polarization is used. The polarization transformation of the field incident on a target can provide information about the shape and material of a target and can aid in target classification [37]. Receiving multiple polarizations also ensures that information is not lost due to the presence of a target that cross-polarizes the incident field. Despite the historically prohibitive cost of these systems, polarimetry is integral to weather, geoscience, and synthetic aperture radar applications [30, 37–39].

The earliest work in radar polarimetry was carried out by George Sinclair, the namesake of the Sinclair scattering matrix [40]. Other important foundational work was conducted by Edward Morton Kennaugh at the Antenna Laboratory of the Ohio State University [41] and Jean Richard Huynen [42]. There has been substantial work in measurement and interpretation of the polarization response from targets [43], decomposition of target scattering into primitive shapes [44, 45], bistatic scattering [46–51], classification of radar polarimetry according to physical scattering mechanisms [52, 53], and techniques for target detection and image contrast enhancement based on polarimetric filtering [52, 54–58]. The practicality of fully polarimetric radar systems is supported in [59, 60].

The goal of this work is to advance the theory for multistatic imaging of moving targets by incorporating polarization and considering the full vector electromagnetic fields.

In Chapter 3 we first provide some background on polarization and scattering of electromagnetic plane waves and give a detailed description of the multistatic polarimetric problem addressed in this chapter. We then formulate our data model beginning with the potential formulation of Maxwell's equations and the Green's function solution to the wave equation resulting in a far-field expression for the electric vector field. The processes of radiation from a transmitting antenna, scattering from a moving target, and reception at a receiving antenna are then described in both the time and frequency domains. Following formulation of the data model

we derive two imaging operations that weight and sum the filtered data collected at each receiver, first assuming that the contributions from each transmitter in the scene are separable and then assuming that the contributions from all transmitting antennas must be treated as a unit, an assumption that better approximates reality. We then utilize the presented data model and imaging operations to simulate multiple antenna geometries with multiple transmission schemes and a single moving target. Scattering behavior of the simulated target is modeled with both a bistatic scattering matrix based on physical optics as derived in Appendix D and a general complex scattering matrix used to investigate the effects of a scattering body that introduces cross polarization of the transmitted electric field. We end the chapter with conclusions and a summary of future work.

3.2 Background

3.2.1 Plane Wave Solution to the Wave Equation

Maxwell's equations in free space can be combined to obtain the wave equation

$$\nabla^2 \boldsymbol{\mathcal{E}}(\boldsymbol{r},t) - \frac{1}{\mathrm{c}_0^2}\frac{\partial^2 \boldsymbol{\mathcal{E}}(\boldsymbol{r},t)}{\partial t^2} = 0 \tag{3.1}$$

where

$$\mathrm{c}_0 = (\mu_0 \epsilon_0)^{-1/2}$$

is the speed of light in free space, μ_0 is the permeability of free space, and ϵ_0 is the permittivity of free space. The time dependent solution to the wave equation is the plane wave

$$\boldsymbol{\mathcal{E}}(\boldsymbol{r},t) = \boldsymbol{E}_0 \mathrm{e}^{\mathrm{i}(\boldsymbol{k}\cdot\boldsymbol{r}-\omega t)} \tag{3.2}$$

where $\boldsymbol{r}$ is the position vector to the point of interest and $\boldsymbol{k} = k\hat{\boldsymbol{k}}$ is the propagation vector with wave number $k = \omega/\mathrm{c}_0$ and direction of propagation $\hat{\boldsymbol{k}}$. The physical electric field is obtained by taking the real portion of (3.2)

$$\boldsymbol{\mathcal{E}}(\boldsymbol{r},t) = \mathrm{Re}\left\{\boldsymbol{E}_0 \mathrm{e}^{\mathrm{i}(\boldsymbol{k}\cdot\boldsymbol{r}-\omega t)}\right\}. \tag{3.3}$$

In the course of this background discussion we will refer to the physical electric field (3.3). However, we note that the electric field in the frequency domain, $\boldsymbol{E}(\boldsymbol{r}, w)$, is a complex quantity and in general when Maxwell's equations are given in the frequency domain all field quantities are assumed to be complex [61]. In later sections we will discuss the complex valued electric field in both the time and frequency domains.

3.2.2 Polarization of Electromagnetic Plane Waves

We consider a coordinate system defined by the orthonormal basis $(\hat{\boldsymbol{k}}, \hat{\boldsymbol{h}}, \hat{\boldsymbol{v}})$ and rewrite $\boldsymbol{E}_0$ as a sum of $\hat{\boldsymbol{h}}$ and $\hat{\boldsymbol{v}}$ components, perpendicular to the direction of propagation,

$$\boldsymbol{E}_0 = E_{\mathrm{h}}^0 \hat{\boldsymbol{h}} + E_{\mathrm{v}}^0 \hat{\boldsymbol{v}} \tag{3.4}$$

where $E_{\mathrm{h}}^0 = a_a \mathrm{e}^{-\mathrm{i}\delta_a}$ and $E_{\mathrm{v}}^0 = a_v \mathrm{e}^{-\mathrm{i}\delta_v}$ so that

$$\mathcal{E}_{\mathrm{h}}(\boldsymbol{r}, t) = \mathrm{Re}\left\{a_a \mathrm{e}^{\mathrm{i}(\boldsymbol{k}\cdot\boldsymbol{r} - \omega t - \delta_a)}\right\} = a_a \cos\left(\boldsymbol{k}\cdot\boldsymbol{r} - \omega t - \delta_a\right) \tag{3.5}$$

$$\mathcal{E}_{\mathrm{v}}(\boldsymbol{r}, t) = \mathrm{Re}\left\{a_v \mathrm{e}^{\mathrm{i}(\boldsymbol{k}\cdot\boldsymbol{r} - \omega t - \delta_v)}\right\} = a_v \cos\left(\boldsymbol{k}\cdot\boldsymbol{r} - \omega t - \delta_v\right) \tag{3.6}$$

with magnitudes a_a and a_v and phase angles δ_a and δ_v. We define an angle α relating these magnitudes by

$$\tan\alpha = \frac{a_a}{a_v}$$

and let $\delta = \delta_a - \delta_v$. Field quantities whose time dependence is a function of a single angular frequency, for example ω, are said to be monochromatic. A general depiction of the spatial evolution of the monochromatic plane wave components given by $\mathcal{E}_{\mathrm{h}}(\boldsymbol{r}, t)$ and $\mathcal{E}_{\mathrm{v}}(\boldsymbol{r}, t)$ is shown in Figure 3.1.

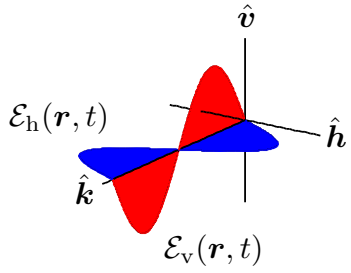

Figure 3.1: Spatial evolution of monochromatic plane wave components.

The polarization of a plane wave such as $\boldsymbol{\mathcal{E}}(\boldsymbol{r}, t)$ describes the shape and locus

of the tip of the time dependent field vector in a plane orthogonal to the direction of propagation. In general, the trace of the tip of the field vector as a function of time forms an ellipse. The polarization ellipse in the $\boldsymbol{h}$-$\boldsymbol{v}$ plane for a wave traveling into the page in the $\hat{\boldsymbol{k}}$ direction in shown in Figure 3.2.

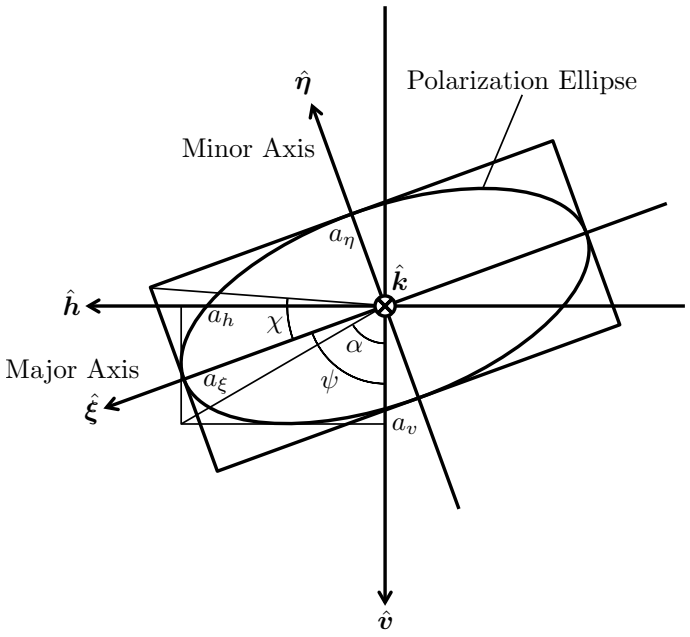

Figure 3.2: Polarization ellipse in the $\boldsymbol{h}$-$\boldsymbol{v}$ plane for a wave traveling into the page in the $\hat{\boldsymbol{k}}$ direction.

If $a_a \neq 0$, $a_v \neq 0$, and $\delta = \delta_a - \delta_v \neq 0$ then the field is elliptically polarized. The polarization is characterized by several parameters labeled in Figure 3.2. The axial ratio R is the ratio of the major axis of the ellipse, $2a_\xi$, to the minor axis of the ellipse, $2a_\eta$, and is given by

$$R = \frac{a_\xi}{a_\eta}.$$

The rotation angle ψ is the angle between the major axis and a reference direction chosen here to be $\hat{\boldsymbol{v}}$ and is given by

$$\tan 2\psi = (\tan 2\alpha)\cos\delta$$

with $-\pi/2 \leq \psi \leq \pi/2$. The ellipticity angle χ is related to the axial ratio by

$$\tan\chi = \pm\frac{1}{R} = \pm\frac{a_\eta}{a_\xi}$$

and is also given by the expression

$$\sin 2\chi = (\sin 2\alpha) \sin \delta$$

with $-\pi/4 \leq \chi \leq \pi/4$.

If the direction of rotation is clockwise in time for an observer looking in the direction of propagation then the sense of polarization of the wave is right-handed and if the direction of rotation is counterclockwise then the sense of polarization of the wave is left-handed. This is consistent with the IEEE convention but goes contrary to the definition used in classical optics [37,38,62]. With respect to Figure 3.2 the sense of rotation of the polarization is left-handed if $\chi > 0$ then and right-handed if $\chi < 0$.

The wave is linearly polarized when $\delta = 0$ and the field vector traces out a straight line in time, as shown in the first diagram of Figure 3.3. The angle α is defined above so that

$$\alpha = \arctan\left(\frac{a_a}{a_v}\right)$$

is the inclination angle. When $a_h = 0$ the inclination angle is $\alpha = 0$ and the wave is completely vertically polarized and when $a_v = 0$ the inclination angle is $\alpha = \pi/2$ and the wave is completely horizontally polarized.

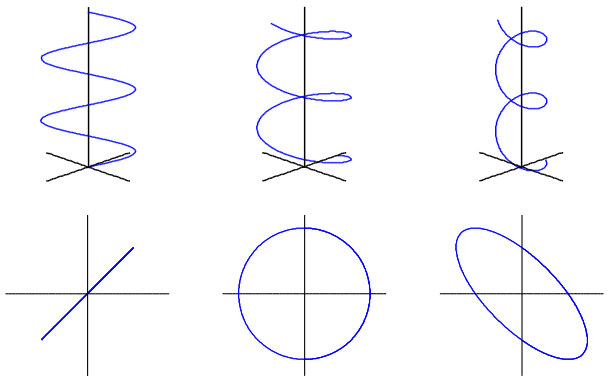

Figure 3.3: Linear, circular, and elliptical polarization states.

The wave is circularly polarized when $a_a = a_v$ and $\delta = \pm\pi/2$, as shown in the second diagram of Figure 3.3. If the sign of δ is positive then the wave has left

circular polarization and if δ is negative then the wave has right circular polarization. The third example in Figure 3.3 depicts a general elliptically polarized wave.

At this point we recall that in free space $\boldsymbol{E}_0$ and $\boldsymbol{H}_0$ are related by the expression

$$\boldsymbol{H}_0 = \frac{1}{\eta_0}\hat{\boldsymbol{k}} \times \boldsymbol{E}_0 \tag{3.7}$$

where

$$\eta_0 = \mu_0 \mathrm{c}_0 = \sqrt{\frac{\mu_0}{\epsilon_0}}$$

is the free space impedance. As a consequence of Maxwell's equations the electric field, magnetic field, and direction of propagation are mutually perpendicular and together the electric field and magnetic field constitute a transverse electromagnetic (TEM) field [38].

3.2.3 Scattering of Polarized Electromagnetic Plane Waves

The scattering of electromagnetic plane waves is usually described in either the forward scatter alignment (FSA) convention or the backward scatter (BSA) convention. Both of these conventions introduce a global coordinate system centered at the scatterer and a local coordinate system at both the transmitting and receiving antennas as shown in Figure 3.4.

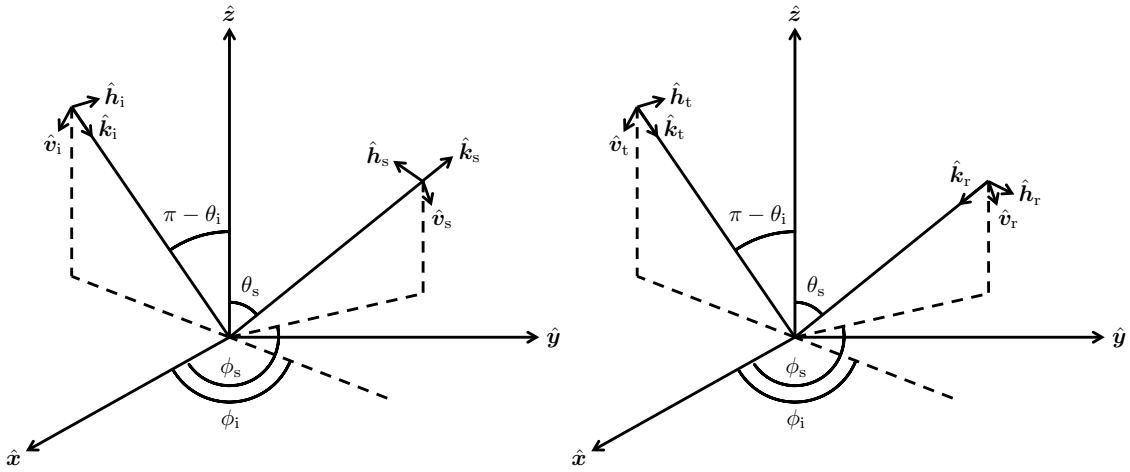

Figure 3.4: Coordinate systems corresponding to the forward scatter alignment (FSA) convention (a) and backscatter alignment (BSA) convention (b).

Forward Scatter Alignment Convention

The FSA convention depicted in Figure 3.4(a) is favored in problems involving wave scattering by particles and wave propagation in inhomogeneous media [37]. It is also the convention used to describe scattering in Sinclair's seminal work [40]. The coordinate system defined by the FSA convention is given by

$$\begin{aligned}
\hat{\boldsymbol{k}}_{\mathrm{i}} &= \cos\phi_{\mathrm{i}}\sin\theta_{\mathrm{i}}\hat{\boldsymbol{x}} + \sin\phi_{\mathrm{i}}\sin\theta_{\mathrm{i}}\hat{\boldsymbol{y}} + \cos\theta_{\mathrm{i}}\hat{\boldsymbol{z}} \\
\hat{\boldsymbol{h}}_{\mathrm{i}} &= \frac{\hat{\boldsymbol{z}} \times \hat{\boldsymbol{k}}_{\mathrm{i}}}{|\hat{\boldsymbol{z}} \times \hat{\boldsymbol{k}}_{\mathrm{i}}|} = -\sin\phi_{\mathrm{i}}\hat{\boldsymbol{x}} + \cos\phi_{\mathrm{i}}\hat{\boldsymbol{y}} \\
\hat{\boldsymbol{v}}_{\mathrm{i}} &= \hat{\boldsymbol{h}}_{\mathrm{i}} \times \hat{\boldsymbol{k}}_{\mathrm{i}} = \cos\phi_{\mathrm{i}}\cos\theta_{\mathrm{i}}\hat{\boldsymbol{x}} + \sin\phi_{\mathrm{i}}\cos\theta_{\mathrm{i}}\hat{\boldsymbol{y}} - \sin\theta_{\mathrm{i}}\hat{\boldsymbol{z}}
\end{aligned}$$

and

$$\begin{aligned}
\hat{\boldsymbol{k}}_{\mathrm{s}} &= \cos\phi_{\mathrm{s}}\sin\theta_{\mathrm{s}}\hat{\boldsymbol{x}} + \sin\phi_{\mathrm{s}}\sin\theta_{\mathrm{s}}\hat{\boldsymbol{y}} + \cos\theta_{\mathrm{s}}\hat{\boldsymbol{z}} \\
\hat{\boldsymbol{h}}_{\mathrm{s}} &= \frac{\hat{\boldsymbol{z}} \times \hat{\boldsymbol{k}}_{\mathrm{s}}}{|\hat{\boldsymbol{z}} \times \hat{\boldsymbol{k}}_{\mathrm{s}}|} = -\sin\phi_{\mathrm{s}}\hat{\boldsymbol{x}} + \cos\phi_{\mathrm{s}}\hat{\boldsymbol{y}} \\
\hat{\boldsymbol{v}}_{\mathrm{s}} &= \hat{\boldsymbol{h}}_{\mathrm{s}} \times \hat{\boldsymbol{k}}_{\mathrm{s}} = \cos\phi_{\mathrm{s}}\cos\theta_{\mathrm{s}}\hat{\boldsymbol{x}} + \sin\phi_{\mathrm{s}}\cos\theta_{\mathrm{s}}\hat{\boldsymbol{y}} - \sin\theta_{\mathrm{s}}\hat{\boldsymbol{z}}
\end{aligned}$$

where $\hat{\boldsymbol{k}}_{\mathrm{i}}$ is the direction of propagation of the incident wave and $\hat{\boldsymbol{k}}_{\mathrm{s}}$ is the direction of propagation of the scattered wave. The FSA convention ensures that the directions of the vertical and horizontal unit vectors are always defined with respect to the direction of propagation. In forward scattering $\theta_{\mathrm{s}} = \theta_{\mathrm{i}}$ and $\phi_{\mathrm{s}} = \phi_{\mathrm{i}}$, resulting in the unit vectors $\hat{\boldsymbol{k}}_{\mathrm{s}} = \hat{\boldsymbol{k}}_{\mathrm{i}}$, $\hat{\boldsymbol{h}}_{\mathrm{s}} = \hat{\boldsymbol{h}}_{\mathrm{i}}$, and $\hat{\boldsymbol{v}}_{\mathrm{s}} = \hat{\boldsymbol{v}}_{\mathrm{i}}$. In backscattering $\theta_{\mathrm{s}} = \pi - \theta_{\mathrm{i}}$ and $\phi_{\mathrm{s}} = \pi + \phi_{\mathrm{i}}$, resulting in the unit vectors $\hat{\boldsymbol{k}}_{\mathrm{s}} = -\hat{\boldsymbol{k}}_{\mathrm{i}}$, $\hat{\boldsymbol{h}}_{\mathrm{s}} = -\hat{\boldsymbol{h}}_{\mathrm{i}}$, and $\hat{\boldsymbol{v}}_{\mathrm{s}} = \hat{\boldsymbol{v}}_{\mathrm{i}}$ [37, 63].

We observe that the incident electric field can be written as a sum of components as

$$\boldsymbol{E}^{\mathrm{i}} = E_{\mathrm{h}}^{\mathrm{i}}\hat{\boldsymbol{h}} + E_{\mathrm{v}}^{\mathrm{i}}\hat{\boldsymbol{v}} \tag{3.8}$$

and likewise the scattered electric field is given by

$$\boldsymbol{E}^{\mathrm{s}} = E^{\mathrm{s}}_{\mathrm{h}}\hat{\boldsymbol{h}} + E^{\mathrm{s}}_{\mathrm{v}}\hat{\boldsymbol{v}}. \tag{3.9}$$

The scattering matrix in the FSA convention, also known as the Sinclair matrix, $[\boldsymbol{S}]^{\mathrm{FSA}}$ is defined by

$$\boldsymbol{E}^{\mathrm{s}} = \frac{\mathrm{e}^{\mathrm{i}k|\boldsymbol{r}|}}{|\boldsymbol{r}|}[\boldsymbol{S}]^{\mathrm{FSA}}\boldsymbol{E}^{\mathrm{i}} \tag{3.10}$$

or

$$\begin{bmatrix} E^{\mathrm{s}}_{\mathrm{h_s}} \\ E^{\mathrm{s}}_{\mathrm{v_s}} \end{bmatrix} = \frac{\mathrm{e}^{\mathrm{i}k|\boldsymbol{r}|}}{|\boldsymbol{r}|} \begin{bmatrix} S_{\mathrm{h_s h_i}} & S_{\mathrm{h_s v_i}} \\ S_{\mathrm{v_s h_i}} & S_{\mathrm{v_s v_i}} \end{bmatrix}^{\mathrm{FSA}} \begin{bmatrix} E^{\mathrm{i}}_{\mathrm{h_i}} \\ E^{\mathrm{i}}_{\mathrm{v_i}} \end{bmatrix} \tag{3.11}$$

where $|\boldsymbol{r}|$ is the distance between the scatterer and the receiving antenna [37, 40, 41]. The polarization of the incident field is in the basis associated with the transmitter $(\hat{\boldsymbol{k}}_{\mathrm{i}}, \hat{\boldsymbol{h}}_{\mathrm{i}}, \hat{\boldsymbol{v}}_{\mathrm{i}})$ and the polarization of the scattered field is in the basis associated with the receiver $(\hat{\boldsymbol{k}}_{\mathrm{s}}, \hat{\boldsymbol{h}}_{\mathrm{s}}, \hat{\boldsymbol{v}}_{\mathrm{s}})$.

We observe that the scattering matrix has been defined in (3.10) and (3.11) such that there is no dependence on range. The lack of range dependence is shown in more detail in Appendix D where the scattering matrix for a flat rectangular PEC plate is derived. This is the convention adopted by [37] although some references adopt a range dependent scattering matrix defined so that

$$\boldsymbol{E}^{\mathrm{s}} = [\boldsymbol{S}]^{\mathrm{FSA}}\boldsymbol{E}^{\mathrm{i}}. \tag{3.12}$$

Expression (3.12) is the definition given by [64], in which the elements of the scattering matrix are defined in terms of the radar cross section. The data model we develop in Section 3.4 will already include range dependence and so we choose to define a range independent scattering matrix.

Backscatter Alignment Convention

The BSA convention depicted in Figure 3.4(b) is favored for calculating radar backscatter from a given target or medium and in radar polarimetry. The BSA convention is also consistent with the IEEE standard which defines the polarization

state of an antenna to be the polarization of the wave radiated by the antenna even when the antenna is operating as a receiver [37]. The coordinate system defined by the BSA convention is given by

$$\hat{\boldsymbol{k}}_{\mathrm{t}} = \hat{\boldsymbol{k}}_{\mathrm{i}} = \cos\phi_{\mathrm{i}}\sin\theta_{\mathrm{i}}\hat{\boldsymbol{x}} + \sin\phi_{\mathrm{i}}\sin\theta_{\mathrm{i}}\hat{\boldsymbol{y}} + \cos\theta_{\mathrm{t}}\hat{\boldsymbol{z}}$$
$$\hat{\boldsymbol{h}}_{\mathrm{t}} = \hat{\boldsymbol{h}}_{\mathrm{i}} = -\sin\phi_{\mathrm{i}}\hat{\boldsymbol{x}} + \cos\phi_{\mathrm{i}}\hat{\boldsymbol{y}}$$
$$\hat{\boldsymbol{v}}_{\mathrm{t}} = \hat{\boldsymbol{v}}_{\mathrm{i}} = \cos\phi_{\mathrm{i}}\cos\theta_{\mathrm{i}}\hat{\boldsymbol{x}} + \sin\phi_{\mathrm{i}}\cos\theta_{\mathrm{i}}\hat{\boldsymbol{y}} - \sin\theta_{\mathrm{i}}\hat{\boldsymbol{z}}$$

and

$$\hat{\boldsymbol{k}}_{\mathrm{r}} = -\hat{\boldsymbol{k}}_{\mathrm{s}} = -\cos\phi_{\mathrm{s}}\sin\theta_{\mathrm{s}}\hat{\boldsymbol{x}} - \sin\phi_{\mathrm{s}}\sin\theta_{\mathrm{s}}\hat{\boldsymbol{y}} - \cos\theta_{\mathrm{s}}\hat{\boldsymbol{z}}$$
$$\hat{\boldsymbol{h}}_{\mathrm{r}} = -\hat{\boldsymbol{h}}_{\mathrm{s}} = \sin\phi_{\mathrm{s}}\hat{\boldsymbol{x}} - \cos\phi_{\mathrm{s}}\hat{\boldsymbol{y}}$$
$$\hat{\boldsymbol{v}}_{\mathrm{r}} = \hat{\boldsymbol{v}}_{\mathrm{s}} = \cos\phi_{\mathrm{s}}\cos\theta_{\mathrm{s}}\hat{\boldsymbol{x}} + \sin\phi_{\mathrm{s}}\cos\theta_{\mathrm{s}}\hat{\boldsymbol{y}} - \sin\theta_{\mathrm{s}}\hat{\boldsymbol{z}}$$

where $\hat{\boldsymbol{k}}_{\mathrm{t}}$ is the direction of propagation of the incident wave and $\hat{\boldsymbol{k}}_{\mathrm{r}}$ is the direction of propagation of the scattered wave. The BSA convention ensures that the coordinate systems, $(\hat{\boldsymbol{k}}_{\mathrm{t}}, \hat{\boldsymbol{h}}_{\mathrm{t}}, \hat{\boldsymbol{v}}_{\mathrm{t}})$ and $(\hat{\boldsymbol{k}}_{\mathrm{r}}, \hat{\boldsymbol{h}}_{\mathrm{r}}, \hat{\boldsymbol{v}}_{\mathrm{r}})$, are identical when the transmitting and receiving antenna are collocated. In a backscattering geometry $\theta_{\mathrm{s}} = \pi - \theta_{\mathrm{i}}$ and $\phi_{\mathrm{s}} = \pi + \phi_{\mathrm{i}}$, resulting in the unit vectors $\hat{\boldsymbol{k}}_{\mathrm{r}} = \hat{\boldsymbol{k}}_{\mathrm{t}}$, $\hat{\boldsymbol{h}}_{\mathrm{r}} = \hat{\boldsymbol{h}}_{\mathrm{t}}$, and $\hat{\boldsymbol{v}}_{\mathrm{r}} = \hat{\boldsymbol{v}}_{\mathrm{t}}$. In a forward scattering geometry $\theta_{\mathrm{s}} = \theta_{\mathrm{i}}$ and $\phi_{\mathrm{s}} = \phi_{\mathrm{i}}$, resulting in the unit vectors $\hat{\boldsymbol{k}}_{\mathrm{r}} = -\hat{\boldsymbol{k}}_{\mathrm{t}}$, $\hat{\boldsymbol{h}}_{\mathrm{r}} = -\hat{\boldsymbol{h}}_{\mathrm{t}}$, and $\hat{\boldsymbol{v}}_{\mathrm{r}} = \hat{\boldsymbol{v}}_{\mathrm{t}}$ [37, 63].

As in the FSA convention, transmitted and received electric fields in the BSA convention can be written as a sum of components as

$$\boldsymbol{E}^{\mathrm{t}} = E^{\mathrm{t}}_{\mathrm{h}}\hat{\boldsymbol{h}} + E^{\mathrm{t}}_{\mathrm{v}}\hat{\boldsymbol{v}} \tag{3.13}$$
$$\boldsymbol{E}^{\mathrm{r}} = E^{\mathrm{r}}_{\mathrm{h}}\hat{\boldsymbol{h}} + E^{\mathrm{r}}_{\mathrm{v}}\hat{\boldsymbol{v}}. \tag{3.14}$$

The scattering matrix in the BSA convention $[\boldsymbol{S}]^{\mathrm{BSA}}$ is defined by

$$\boldsymbol{E}^{\mathrm{r}} = \frac{\mathrm{e}^{\mathrm{i}k|\boldsymbol{r}|}}{|\boldsymbol{r}|}[\boldsymbol{S}]^{\mathrm{BSA}}\boldsymbol{E}^{\mathrm{t}} \tag{3.15}$$

or

$$\begin{bmatrix} E^{\mathrm{r}}_{\mathrm{h_r}} \\ E^{\mathrm{r}}_{\mathrm{v_r}} \end{bmatrix} = \frac{\mathrm{e}^{\mathrm{i}k|\boldsymbol{r}|}}{|\boldsymbol{r}|} \begin{bmatrix} S_{\mathrm{h_r h_t}} & S_{\mathrm{h_r v_t}} \\ S_{\mathrm{v_r h_t}} & S_{\mathrm{v_r v_t}} \end{bmatrix}^{\mathrm{BSA}} \begin{bmatrix} E^{\mathrm{t}}_{\mathrm{h_t}} \\ E^{\mathrm{t}}_{\mathrm{v_t}} \end{bmatrix}. \tag{3.16}$$

The polarization of the transmitted field is in the basis associated with the transmitter $(\hat{\boldsymbol{k}}_{\mathrm{t}}, \hat{\boldsymbol{h}}_{\mathrm{t}}, \hat{\boldsymbol{v}}_{\mathrm{t}})$ and the polarization of the received field is in the basis associated with the receiver $(\hat{\boldsymbol{k}}_{\mathrm{r}}, \hat{\boldsymbol{h}}_{\mathrm{r}}, \hat{\boldsymbol{v}}_{\mathrm{r}})$ [37].

Relating the FSA and BSA Conventions

From examination of the coordinate systems associated with the FSA and BSA conventions it is clear that

$$\boldsymbol{E}^{\mathrm{i}} = \boldsymbol{E}^{\mathrm{t}} \tag{3.17}$$

and

$$\boldsymbol{E}^{\mathrm{s}} = \begin{bmatrix} -1 & 0 \\ 0 & 1 \end{bmatrix} \boldsymbol{E}^{\mathrm{r}} \tag{3.18}$$

and so it follows that

$$[\boldsymbol{S}]^{\mathrm{FSA}} = \begin{bmatrix} -1 & 0 \\ 0 & 1 \end{bmatrix} [\boldsymbol{S}]^{\mathrm{BSA}} \tag{3.19}$$

or

$$[\boldsymbol{S}]^{\mathrm{BSA}} = \begin{bmatrix} -1 & 0 \\ 0 & 1 \end{bmatrix} [\boldsymbol{S}]^{\mathrm{FSA}}. \tag{3.20}$$

Throughout the rest of this chapter we will adopt the BSA convention and so for ease of notation we let $[\boldsymbol{S}] \equiv [\boldsymbol{S}]^{\mathrm{BSA}}$ denote the general scattering matrix.

3.3 Problem Set-up

We will consider a multistatic scene with $m = 1, \ldots, M$ transmitters at position $\boldsymbol{x}_{\mathrm{T},m}$, $n = 1, \ldots, N$ receivers at position $\boldsymbol{x}_{\mathrm{R},n}$, and a moving target at position $\boldsymbol{x}_a$ with velocity $\boldsymbol{v}_a$. Our data model will consider the radiation, scattering, and re-

ception processes as shown in Figure 3.5 for each bistatic pair consisting of the m^{th} transmitter and n^{th} receiver. This diagram loosely portrays the input and output parameters of each process in the frequency domain, top, and time domain, bottom. The first block entitled "Radiation" refers to the transformation from the desired

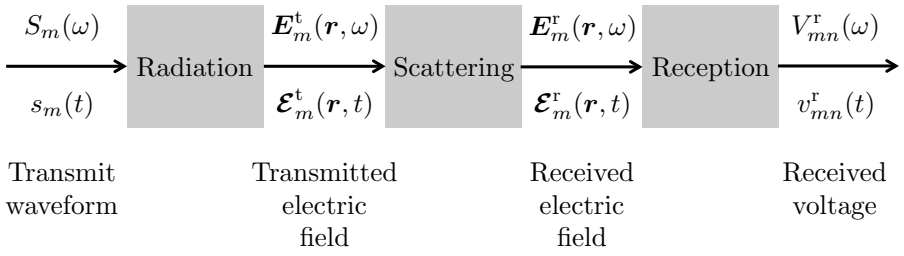

Figure 3.5: Block diagram of the polarimetric radar problem.

transmit waveform to the transmitted electric field, including antenna effects and the polarization of the transmit antenna. The "Scattering" block transforms the transmitted electric field into the received electric field by applying the scattering behavior of the target and Doppler effects from a moving target. The final "Reception" block transforms the received electric field into the received voltage, again including antenna effects and the polarization of the receiving antenna. Our data model will address each of these processes in detail.

We will assume that all antennas in the scene are dipoles of diameter $2a$ and length $2L$ as shown in Figure 3.6. In the far field the electromagnetic field radiated

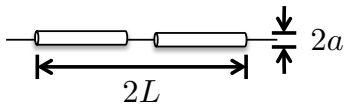

Figure 3.6: An arbitrary dipole of diameter $2a$ and length $2L$.

from a dipole antenna resembles a uniform plane wave with electric and magnetic fields in time phase, and mutually orthogonal to each other and the direction of propagation. The electric field only exists in a plane defined by the orientation of the dipole and the magnetic field exists in the plane orthogonal to both the electric field and direction of propagation satisfying (3.7) in free space [65]. Consequently, a dipole antenna is polarized in the same plane that the antenna is in, e.g., a vertically oriented dipole antenna is vertically polarized. The plane wave components radiated from a vertically polarized dipole antenna are depicted in Figure 3.7.

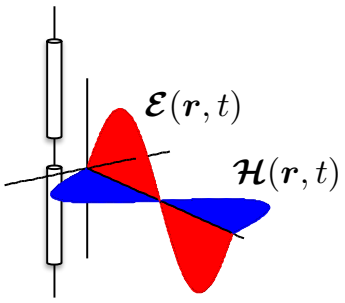

Figure 3.7: Plane wave components radiated from a vertically polarized dipole antenna.

Figure 3.8 provides a nominal example of a single bistatic pair of two dipole antennas that will be modeled in the following section. We observe that the vec-

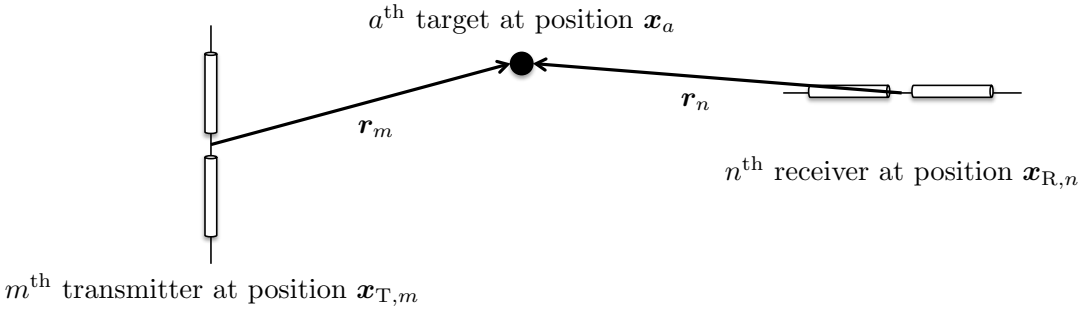

Figure 3.8: One bistatic pair of the multistatic system consisting of two dipole antennas.

tors $\boldsymbol{r}_m$ and $\boldsymbol{r}_n$ from the transmitting antenna to the target and from the receiving antenna to the target, respectively, are both oriented towards the target, as is consistent with the BSA convention described in Section 3.2.3. The global coordinate system relating the m^{th} transmitter, n^{th} receiver, and target as well as the local coordinate systems of both antennas is depicted in Figure 3.9 where

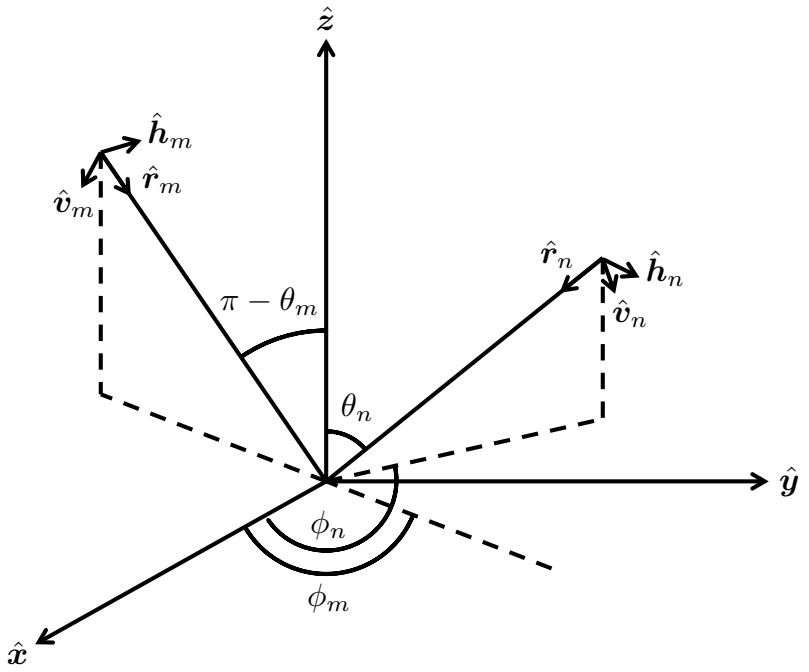

Figure 3.9: A modified BSA coordinate system where the unit vectors and angles have been renamed to better suit a multistatic geometry.

$$\hat{\boldsymbol{r}}_m = \cos\phi_m \sin\theta_m \hat{\boldsymbol{x}} + \sin\phi_m \sin\theta_m \hat{\boldsymbol{y}} + \cos\theta_m \hat{\boldsymbol{z}}$$

$$\hat{\boldsymbol{h}}_m = -\sin\phi_m \hat{\boldsymbol{x}} + \cos\phi_m \hat{\boldsymbol{y}}$$

$$\hat{\boldsymbol{v}}_m = \cos\phi_m \cos\theta_m \hat{\boldsymbol{x}} + \sin\phi_m \cos\theta_m \hat{\boldsymbol{y}} - \sin\theta_m \hat{\boldsymbol{z}}$$

$$\hat{\boldsymbol{r}}_n = -\cos\phi_n \sin\theta_n \hat{\boldsymbol{x}} - \sin\phi_n \sin\theta_n \hat{\boldsymbol{y}} - \cos\theta_n \hat{\boldsymbol{z}}$$

$$\hat{\boldsymbol{h}}_n = \sin\phi_n \hat{\boldsymbol{x}} - \cos\phi_n \hat{\boldsymbol{y}}$$

$$\hat{\boldsymbol{v}}_n = \cos\phi_n \cos\theta_n \hat{\boldsymbol{x}} + \sin\phi_n \cos\theta_n \hat{\boldsymbol{y}} - \sin\theta_n \hat{\boldsymbol{z}}$$

and the global coordinate system is centered at the target. Note that each bistatic pair will require its own coordinate system.

3.4 Data Model

3.4.1 The Potential Formulation

We begin our derivation of the vector data model with the potential formulation [66–68] . Maxwell's equations in the time domain

$$\nabla \cdot \boldsymbol{\mathcal{D}} = \rho$$
$$\nabla \cdot \boldsymbol{\mathcal{B}} = 0$$
$$\nabla \times \boldsymbol{\mathcal{E}} = -\frac{\partial \boldsymbol{\mathcal{B}}}{\partial t}$$
$$\nabla \times \boldsymbol{\mathcal{H}} = \boldsymbol{\mathcal{J}} + \frac{\partial \boldsymbol{\mathcal{D}}}{\partial t}$$

combined with the free space constitutive relations

$$\boldsymbol{\mathcal{D}} = \epsilon_0 \boldsymbol{\mathcal{E}}$$
$$\boldsymbol{\mathcal{B}} = \mu_0 \boldsymbol{\mathcal{H}}$$

yield

$$\nabla \cdot \boldsymbol{\mathcal{E}} = \frac{1}{\epsilon_0}\rho \tag{3.21}$$
$$\nabla \cdot \boldsymbol{\mathcal{B}} = 0 \tag{3.22}$$
$$\nabla \times \boldsymbol{\mathcal{E}} = -\frac{\partial \boldsymbol{\mathcal{B}}}{\partial t} \tag{3.23}$$
$$\nabla \times \boldsymbol{\mathcal{B}} = \mu_0 \boldsymbol{\mathcal{J}} + \mu_0 \epsilon_0 \frac{\partial \boldsymbol{\mathcal{E}}}{\partial t} \tag{3.24}$$

where $\boldsymbol{\mathcal{D}}(\boldsymbol{r}, t)$ is the electric displacement field, $\boldsymbol{\mathcal{B}}(\boldsymbol{r}, t)$ is the magnetic induction field, $\boldsymbol{\mathcal{E}}(\boldsymbol{r}, t)$ is the electric field, $\boldsymbol{\mathcal{H}}(\boldsymbol{r}, t)$ is the magnetic intensity or magnetic field, $\rho(\boldsymbol{r}, t)$ is the charge density, and $\boldsymbol{\mathcal{J}}(\boldsymbol{r}, t)$ is the current density. We use $\boldsymbol{\mathcal{E}}$ to denote $\boldsymbol{\mathcal{E}}(\boldsymbol{r}, t)$ for simplicity.

The divergenceless magnetic induction field can be written as the curl of a vector potential $\boldsymbol{\mathcal{A}}$

$$\boldsymbol{\mathcal{B}} = \nabla \times \boldsymbol{\mathcal{A}} \tag{3.25}$$

and then substituted into the Maxwell-Faraday equation (3.23) to obtain

$$\nabla \times \boldsymbol{\mathcal{E}} = -\frac{\partial}{\partial t}(\nabla \times \boldsymbol{\mathcal{A}}). \tag{3.26}$$

Clearly from (3.26),

$$\nabla \times \left(\boldsymbol{\mathcal{E}} + \frac{\partial \boldsymbol{\mathcal{A}}}{\partial t} \right) = 0$$

and consequently the inner sum can be written as the gradient of a scalar potential Φ

$$\boldsymbol{\mathcal{E}} + \frac{\partial \boldsymbol{\mathcal{A}}}{\partial t} = -\nabla \Phi$$

so that

$$\boldsymbol{\mathcal{E}} = -\nabla \Phi - \frac{\partial \boldsymbol{\mathcal{A}}}{\partial t}. \tag{3.27}$$

Substituting (3.27) into Gauss' law (3.21) yields

$$\nabla^2 \Phi + \frac{\partial}{\partial t} \left(\nabla \cdot \boldsymbol{\mathcal{A}} \right) = -\frac{1}{\epsilon_0} \rho. \tag{3.28}$$

and putting (3.25) and (3.27) into Ampère's law (3.24) we obtain

$$\nabla \times (\nabla \times \boldsymbol{\mathcal{A}}) = \mu_0 \boldsymbol{\mathcal{J}} - \mu_0 \epsilon_0 \nabla \left(\frac{\partial \Phi}{\partial t} \right) - \mu_0 \epsilon_0 \frac{\partial^2 \boldsymbol{\mathcal{A}}}{\partial t^2}. \tag{3.29}$$

We recall the vector identity

$$\nabla \times (\nabla \times \boldsymbol{A}) = \nabla (\nabla \cdot \boldsymbol{A}) - \nabla^2 \boldsymbol{A} \tag{3.30}$$

and rewrite (3.29)

$$\nabla (\nabla \cdot \boldsymbol{\mathcal{A}}) - \nabla^2 \boldsymbol{\mathcal{A}} = \mu_0 \boldsymbol{\mathcal{J}} - \mu_0 \epsilon_0 \nabla \left(\frac{\partial \Phi}{\partial t} \right) - \mu_0 \epsilon_0 \frac{\partial^2 \boldsymbol{\mathcal{A}}}{\partial t^2}$$

and then rearrange to obtain

$$\left(\nabla^2 \boldsymbol{\mathcal{A}} - \mu_0 \epsilon_0 \frac{\partial^2 \boldsymbol{\mathcal{A}}}{\partial t^2} \right) - \nabla \left(\nabla \cdot \boldsymbol{\mathcal{A}} + \mu_0 \epsilon_0 \frac{\partial \Phi}{\partial t} \right) = -\mu_0 \boldsymbol{\mathcal{J}}. \tag{3.31}$$

At this point we have reduced the problem of finding $\boldsymbol{\mathcal{E}}$ and $\boldsymbol{\mathcal{B}}$ from the four Maxwell's equations to finding $\boldsymbol{\mathcal{A}}$ and Φ from (3.28) and (3.31). We choose the Lorentz gauge, picking

$$\nabla \cdot \boldsymbol{\mathcal{A}} = -\mu_0 \epsilon_0 \frac{\partial \Phi}{\partial t} \tag{3.32}$$

and assuming

$$\Phi(\boldsymbol{r}) \to 0 \quad \text{as} \quad |\boldsymbol{r}| \to \infty.$$

Under the Lorentz gauge (3.28) and (3.31) reduce to

$$\nabla^2\Phi - \mu_0\epsilon_0\frac{\partial^2\Phi}{\partial t^2} = -\frac{1}{\epsilon_0}\rho \tag{3.33}$$

and

$$\nabla^2\boldsymbol{\mathcal{A}} - \mu_0\epsilon_0\frac{\partial^2\boldsymbol{\mathcal{A}}}{\partial t^2} = -\mu_0\boldsymbol{\mathcal{J}}, \tag{3.34}$$

respectively.

Expressions (3.33) and (3.34) can also be be rewritten in terms of the d'Alembertian

$$\Box^2 \equiv \nabla^2 - \mu_0\epsilon_0\frac{\partial^2}{\partial t^2} = \nabla^2 - \frac{1}{\mathrm{c}_0^2}\frac{\partial^2}{\partial t^2} \tag{3.35}$$

as

$$\Box^2\Phi = -\frac{1}{\epsilon_0}\rho \tag{3.36}$$

$$\Box^2\boldsymbol{\mathcal{A}} = -\mu_0\boldsymbol{\mathcal{J}}. \tag{3.37}$$

By taking the Fourier transform we obtain the frequency domain equivalents of (3.33) and (3.34)

$$\nabla^2\tilde{\Phi} + \mu_0\epsilon_0\omega^2\tilde{\Phi} = -\frac{1}{\epsilon_0}\tilde{\rho} \tag{3.38}$$

$$\nabla^2\boldsymbol{A} + \mu_0\epsilon_0\omega^2\boldsymbol{A} = -\mu_0\boldsymbol{J} \tag{3.39}$$

where $\boldsymbol{A}$, $\boldsymbol{J}$, $\tilde{\Phi}$, and $\tilde{\rho}$ are the Fourier transforms of $\boldsymbol{\mathcal{A}}$, $\boldsymbol{\mathcal{J}}$, Φ, and ρ, respectively, and $\boldsymbol{A}$ is used to denote $\boldsymbol{A}(\boldsymbol{r},\omega)$ for simplicity.

Recall that in free space

$$\mathrm{c}_0 = \frac{1}{\sqrt{\mu_0\epsilon_0}}$$

and

$$k = \frac{\omega}{v_\mathrm{p}}$$

where k is the wave number and v_{p} is the phase velocity of the wave and so it follows that

$$k = \frac{\omega}{\mathrm{c}_0} = \sqrt{\mu_0 \epsilon_0}\omega$$

and equations (3.38) and (3.39) become

$$\nabla^2 \tilde{\Phi} + k^2 \tilde{\Phi} = -\frac{1}{\epsilon_0}\tilde{\rho} \tag{3.40}$$

$$\nabla^2 \boldsymbol{A} + k^2 \boldsymbol{A} = -\mu_0 \boldsymbol{J}. \tag{3.41}$$

3.4.2 Green's Function Solution to the Wave Equation

We observe that (3.40) and (3.41) are both inhomogeneous Helmhotz equations that may be uniquely solved using a Green's function under the Sommerfeld radiation condition. Recall that the Sommerfeld radiation condition holds that

$$\lim_{|\boldsymbol{r}|\to\infty} |\boldsymbol{r}|^{\frac{n-1}{2}} \left(\frac{\partial}{\partial|\boldsymbol{r}|} - \mathrm{i}k\right) u(\boldsymbol{r}) = 0 \tag{3.42}$$

uniformly in all directions

$$\hat{\boldsymbol{r}} = \frac{\boldsymbol{r}}{|\boldsymbol{r}|}$$

for

$$\left(\nabla^2 + k^2\right) u = -f \quad \text{in} \quad \mathbb{R}^n \tag{3.43}$$

and that the Green's function is the solution to the inhomogeneous Helmholtz equation with a Dirac delta as the source term

$$\nabla^2 G(\boldsymbol{r}) + k^2 G(\boldsymbol{r}) = -\delta(\boldsymbol{r}), \quad \boldsymbol{r} \in \mathbb{R}^n \tag{3.44}$$

where

$$G(\boldsymbol{r}) = \frac{\mathrm{e}^{\mathrm{i}k|\boldsymbol{r}|}}{4\pi|\boldsymbol{r}|} \tag{3.45}$$

for $n = 3$. Thus, the Helmholtz equation in (3.43) has the solution

$$u(\boldsymbol{r}) = (G * f)(\boldsymbol{r}) = \int_{\mathbb{R}^n} G(\boldsymbol{r} - \boldsymbol{r}') f(\boldsymbol{r}') \mathrm{d}\boldsymbol{r}'$$

and we are now able to solve (3.40) and (3.41)for $\tilde{\Phi}$ and $\boldsymbol{A}$, respectively,

$$\tilde{\Phi}(\boldsymbol{r}) = \frac{1}{\epsilon_0}\int G(\boldsymbol{r}-\boldsymbol{r}')\tilde{\rho}(\boldsymbol{r}')\mathrm{d}\boldsymbol{r}' \tag{3.46}$$

$$\boldsymbol{A}(\boldsymbol{r}) = \mu_0\int G(\boldsymbol{r}-\boldsymbol{r}')\boldsymbol{J}(\boldsymbol{r}')\mathrm{d}\boldsymbol{r}'. \tag{3.47}$$

3.4.3 Expression for the Electric Field

We next determine an expression for $\boldsymbol{E}$, the frequency domain electric field, in terms of the vector potential $\boldsymbol{A}$. In the frequency domain, (3.27) becomes

$$\boldsymbol{E} = \mathrm{i}\omega\boldsymbol{A} - \nabla\tilde{\Phi} \tag{3.48}$$

with the corresponding Lorentz gauge

$$\nabla\cdot\boldsymbol{A} = \mathrm{i}\mu_0\epsilon_0\omega\tilde{\Phi}. \tag{3.49}$$

We solve (3.49) for $\tilde{\Phi}$

$$\tilde{\Phi} = \frac{-\mathrm{i}}{\omega\mu_0\epsilon_0}\left(\nabla\cdot\boldsymbol{A}\right) \tag{3.50}$$

and substitute (3.50) into (3.48) to obtain

$$\boldsymbol{E}(\boldsymbol{r},\omega) = \mathrm{i}\omega\left(\boldsymbol{A}(\boldsymbol{r},\omega) + \frac{1}{k^2}\nabla\left(\nabla\cdot\boldsymbol{A}(\boldsymbol{r},\omega)\right)\right). \tag{3.51}$$

Substituting our Green's function solution for $\boldsymbol{A}$ (3.47) into (3.51) we obtain

$$\begin{aligned}\boldsymbol{E}(\boldsymbol{r},\omega) = \ & \mathrm{i}\omega\mu_0\int G(\boldsymbol{r}-\boldsymbol{r}',\omega)\boldsymbol{J}(\boldsymbol{r}',\omega)\mathrm{d}\boldsymbol{r}' \\ & + \frac{\mathrm{i}\omega\mu_0}{k^2}\nabla\left(\nabla\cdot\int G(\boldsymbol{r}-\boldsymbol{r}',\omega)\boldsymbol{J}(\boldsymbol{r}',\omega)\mathrm{d}\boldsymbol{r}'\right).\end{aligned} \tag{3.52}$$

We recall from [62, 69–71] that

$$\begin{aligned}\nabla\left(\nabla\cdot\int G(\boldsymbol{r}-\boldsymbol{r}',\omega)\boldsymbol{J}(\boldsymbol{r}',\omega)\mathrm{d}\boldsymbol{r}'\right) = & \int\nabla(\nabla\cdot G(\boldsymbol{r}-\boldsymbol{r}',\omega)\boldsymbol{J}(\boldsymbol{r}',\omega))\mathrm{d}\boldsymbol{r}' \\ & - \frac{1}{3}\boldsymbol{J}(\boldsymbol{r},\omega)\end{aligned} \tag{3.53}$$

where the Green's function is defined in (3.45). A derivation of this property and an associated lemma can be found in Appendix B. We can then rewrite (3.52) as

$$\begin{aligned}\boldsymbol{E}(\boldsymbol{r},\omega) =& \mathrm{i}\omega\mu_0 \int G(\boldsymbol{r}-\boldsymbol{r}',\omega)\boldsymbol{J}(\boldsymbol{r}',\omega)\mathrm{d}\boldsymbol{r}' \\ &+ \frac{\mathrm{i}\omega\mu_0}{k^2}\int \nabla(\nabla\cdot G(\boldsymbol{r}-\boldsymbol{r}',\omega)\boldsymbol{J}(\boldsymbol{r}',\omega))\mathrm{d}\boldsymbol{r}' - \frac{\mathrm{i}\omega\mu_0}{3k^2}\boldsymbol{J}(\boldsymbol{r},\omega) \qquad (3.54)\end{aligned}$$

and further simplify to obtain

$$\begin{aligned}\boldsymbol{E}(\boldsymbol{r},\omega) =& \mathrm{i}\omega\mu_0 \left(\int \left(G(\boldsymbol{r}-\boldsymbol{r}',\omega)\boldsymbol{J}(\boldsymbol{r}',\omega) + \frac{1}{k^2}\nabla(\nabla\cdot G(\boldsymbol{r}-\boldsymbol{r}',\omega)\boldsymbol{J}(\boldsymbol{r}',\omega))\right)\mathrm{d}\boldsymbol{r}'\right. \\ &\left. -\frac{1}{3k^2}\boldsymbol{J}(\boldsymbol{r},\omega)\right) \qquad (3.55)\\ =& \mathrm{i}\omega\mu_0 \int \left(\left(\mathbf{I}+\frac{1}{k^2}\nabla\nabla\right)G(\boldsymbol{r}-\boldsymbol{r}',\omega) - \frac{1}{3k^2}\boldsymbol{\delta}(\boldsymbol{r}-\boldsymbol{r}')\right)\cdot\boldsymbol{J}(\boldsymbol{r}',\omega)\mathrm{d}\boldsymbol{r}' \qquad (3.56)\\ =& \mathrm{i}\omega\mu_0 \int \boldsymbol{G}(\boldsymbol{r}-\boldsymbol{r}',\omega)\cdot\boldsymbol{J}(\boldsymbol{r}',\omega)\mathrm{d}\boldsymbol{r}' \qquad (3.57)\end{aligned}$$

where

$$\boldsymbol{G}(\boldsymbol{r},\omega) = \left(\mathbf{I}+\frac{1}{k^2}\nabla\nabla\right)G(\boldsymbol{r},\omega) - \frac{1}{3k^2}\boldsymbol{\delta}(\boldsymbol{r}) \qquad (3.58)$$

is the dyadic Green's function [70, 71], $\boldsymbol{\delta}(\boldsymbol{r}) = \delta(\boldsymbol{r})\mathbf{I}$, and $\mathbf{I}$ is the unit dyad. We note that the delta term in (3.58) does not appear in all forms of the dyadic Green's function presented in the literature, although reputable sources acknowledge that it is necessary for (3.57) to hold. The identity

$$\nabla\left(\nabla\cdot\left(G(\boldsymbol{r}-\boldsymbol{r}',\omega)\boldsymbol{J}(\boldsymbol{r}',\omega)\right)\right) = \left(\nabla\nabla\, G(\boldsymbol{r}-\boldsymbol{r}',\omega)\right)\cdot\boldsymbol{J}(\boldsymbol{r}',\omega)$$

has been used to rewrite (3.55) as (3.56) where $\nabla\nabla\, G(\boldsymbol{r}-\boldsymbol{r}',\omega)$ is a dyadic operator. We evaluate the differentiation in (3.58) to obtain

$$\begin{aligned}\boldsymbol{G}(\boldsymbol{r},\omega) = \left(1+\frac{\mathrm{i}}{k|\boldsymbol{r}|}-\frac{1}{k^2|\boldsymbol{r}|^2}\right)\mathbf{I}G(\boldsymbol{r},\omega) + \left(-1-\frac{3\mathrm{i}}{k|\boldsymbol{r}|}+\frac{3}{k^2|\boldsymbol{r}|^2}\right)\hat{\boldsymbol{r}}\hat{\boldsymbol{r}}G(\boldsymbol{r},\omega) \\ -\frac{1}{3k^2}\boldsymbol{\delta}(\boldsymbol{r}) \qquad (3.59)\end{aligned}$$

and the dyadic Green's function can be rewritten as the sum

$$\boldsymbol{G}(\boldsymbol{r},\omega) = \boldsymbol{G}_{\mathrm{SF}}(\boldsymbol{r},\omega) + \boldsymbol{G}_{\mathrm{NF}}(\boldsymbol{r},\omega) + \boldsymbol{G}_{\mathrm{MF}}(\boldsymbol{r},\omega) + \boldsymbol{G}_{\mathrm{FF}}(\boldsymbol{r},\omega) \tag{3.60}$$

with

$$\boldsymbol{G}_{\mathrm{SF}}(\boldsymbol{r},\omega) = -\frac{1}{3k^2}\boldsymbol{\delta}(\boldsymbol{r}) \tag{3.61}$$

$$\boldsymbol{G}_{\mathrm{NF}}(\boldsymbol{r},\omega) = -\frac{\mathrm{e}^{\mathrm{i}k|\boldsymbol{r}|}}{4\pi k^2|\boldsymbol{r}|^3}\left(\mathbf{I} - 3\hat{\boldsymbol{r}}\hat{\boldsymbol{r}}\right) \tag{3.62}$$

$$\boldsymbol{G}_{\mathrm{MF}}(\boldsymbol{r},\omega) = \frac{\mathrm{i}\mathrm{e}^{\mathrm{i}k|\boldsymbol{r}|}}{4\pi k|\boldsymbol{r}|^2}\left(\mathbf{I} - 3\hat{\boldsymbol{r}}\hat{\boldsymbol{r}}\right) \tag{3.63}$$

$$\boldsymbol{G}_{\mathrm{FF}}(\boldsymbol{r},\omega) = \frac{\mathrm{e}^{\mathrm{i}k|\boldsymbol{r}|}}{4\pi k|\boldsymbol{r}|}\left(\mathbf{I} - \hat{\boldsymbol{r}}\hat{\boldsymbol{r}}\right) \tag{3.64}$$

where $\boldsymbol{G}_{\mathrm{SF}}$, $\boldsymbol{G}_{\mathrm{NF}}$, $\boldsymbol{G}_{\mathrm{MF}}$, and $\boldsymbol{G}_{\mathrm{FF}}$ correspond to the self-field, near-field, middle-field, and far-field dyadic Green's functions, respectively.

3.4.4 Radiation

We will now develop an expression for the transmitted electric field radiated by the m^{th} transmitter, denoted $\boldsymbol{E}_m^{\mathrm{t}}$ for consistency with the BSA convention. Recall the expression for the electric field in terms of the dyadic Green's function derived in section 3.4.1

$$\boldsymbol{E}_m^{\mathrm{t}}(\boldsymbol{r},\omega) = \mathrm{i}\omega\mu_0 \int \boldsymbol{G}(\boldsymbol{r}-\boldsymbol{r}',\omega)\cdot\boldsymbol{J}(\boldsymbol{r}',\omega)\mathrm{d}\boldsymbol{r}'. \tag{3.65}$$

To obtain the far-field electric field we substitute (3.64) into (3.65) to obtain

$$\begin{aligned}
\boldsymbol{E}_m^{\mathrm{t}}(\boldsymbol{r},\omega) &= \mathrm{i}\omega\mu_0 \int \boldsymbol{G}_{\mathrm{FF}}(\boldsymbol{r}-\boldsymbol{r}',\omega)\cdot\boldsymbol{J}(\boldsymbol{r}',\omega)\mathrm{d}\boldsymbol{r}' \\
&= \mathrm{i}\omega\mu_0 \int \frac{\mathrm{e}^{\mathrm{i}k|\boldsymbol{r}-\boldsymbol{r}'|}}{4\pi k|\boldsymbol{r}-\boldsymbol{r}'|}\left(\mathbf{I} - \widehat{\boldsymbol{r}-\boldsymbol{r}'}\widehat{\boldsymbol{r}-\boldsymbol{r}'}\right)\cdot\boldsymbol{J}(\boldsymbol{r}',\omega)\mathrm{d}\boldsymbol{r}' \\
&= \mathrm{i}\omega\mu_0 \int \frac{\mathrm{e}^{\mathrm{i}k|\boldsymbol{r}-\boldsymbol{r}'|}}{4\pi|\boldsymbol{r}-\boldsymbol{r}'|}\left(\boldsymbol{J}(\boldsymbol{r}',\omega) - \widehat{\boldsymbol{r}-\boldsymbol{r}'}\left(\widehat{\boldsymbol{r}-\boldsymbol{r}'}\cdot\boldsymbol{J}(\boldsymbol{r}',\omega)\right)\right)\mathrm{d}\boldsymbol{r}'.
\end{aligned} \tag{3.66}$$

For large $|\boldsymbol{r}|$ we make the far-field assumption

$$|\boldsymbol{r} - \boldsymbol{r}'| \approx |\boldsymbol{r}| - \hat{\boldsymbol{r}} \cdot \boldsymbol{r}'$$

and the expression for $\boldsymbol{E}_m^{\mathrm{t}}$ becomes

$$\boldsymbol{E}_m^{\mathrm{t}}(\boldsymbol{r}, \omega) = \mathrm{i}\omega\mu_0 \frac{\mathrm{e}^{\mathrm{i}k|\boldsymbol{r}|}}{4\pi|\boldsymbol{r}|} \left(\int \mathrm{e}^{-\mathrm{i}k\hat{\boldsymbol{r}}\cdot\boldsymbol{r}'} \boldsymbol{J}(\boldsymbol{r}', \omega) \mathrm{d}\boldsymbol{r}' - \hat{\boldsymbol{r}} \left(\hat{\boldsymbol{r}} \cdot \int \mathrm{e}^{-\mathrm{i}k\hat{\boldsymbol{r}}\cdot\boldsymbol{r}'} \boldsymbol{J}(\boldsymbol{r}', \omega) \right) \mathrm{d}\boldsymbol{r}' \right). \tag{3.67}$$

Letting

$$\boldsymbol{F}(k\hat{\boldsymbol{r}}, \omega) = \int \mathrm{e}^{-\mathrm{i}k\hat{\boldsymbol{r}}\cdot\boldsymbol{r}'} \boldsymbol{J}(\boldsymbol{r}', \omega) \mathrm{d}\boldsymbol{r}' \tag{3.68}$$

denote the radiation vector, the spatial Fourier transform of the current density $\boldsymbol{J}$, we obtain

$$\boldsymbol{E}_m^{\mathrm{t}}(\boldsymbol{r}, \omega) = \mathrm{i}\omega\mu_0 \frac{\mathrm{e}^{\mathrm{i}k|\boldsymbol{r}|}}{4\pi|\boldsymbol{r}|} \left(\boldsymbol{F}(k\hat{\boldsymbol{r}}, \omega) - \hat{\boldsymbol{r}} \left(\hat{\boldsymbol{r}} \cdot \boldsymbol{F}(k\hat{\boldsymbol{r}}, \omega) \right) \right). \tag{3.69}$$

We recall the vector identity

$$\boldsymbol{A} \times (\boldsymbol{B} \times \boldsymbol{C}) = \boldsymbol{B}(\boldsymbol{A} \cdot \boldsymbol{C}) - \boldsymbol{C}(\boldsymbol{A} \cdot \boldsymbol{B}) \tag{3.70}$$

and observe

$$\begin{aligned} \hat{\boldsymbol{r}}(\hat{\boldsymbol{r}} \cdot \boldsymbol{F}) &= \hat{\boldsymbol{r}} \times (\hat{\boldsymbol{r}} \times \boldsymbol{F}) + \boldsymbol{F}(\hat{\boldsymbol{r}} \cdot \hat{\boldsymbol{r}}) \\ &= \hat{\boldsymbol{r}} \times (\hat{\boldsymbol{r}} \times \boldsymbol{F}) + \boldsymbol{F}. \end{aligned}$$

It follows that

$$\boldsymbol{F} - \hat{\boldsymbol{r}}(\hat{\boldsymbol{r}} \cdot \boldsymbol{F}) = -\hat{\boldsymbol{r}} \times (\hat{\boldsymbol{r}} \times \boldsymbol{F})$$

and so (3.69) can be written as

$$\boldsymbol{E}_m^{\mathrm{t}}(\boldsymbol{r}, \omega) = -\mathrm{i}\omega\mu_0 \frac{\mathrm{e}^{\mathrm{i}k|\boldsymbol{r}|}}{4\pi|\boldsymbol{r}|} \left(\hat{\boldsymbol{r}} \times (\hat{\boldsymbol{r}} \times \boldsymbol{F}(k\hat{\boldsymbol{r}}, \omega)) \right). \tag{3.71}$$

Local Coordinate System

The derivation of the radiated electric field and constituent radiation vector makes use of the local coordinate system below where the center of the antenna is

located at the origin.

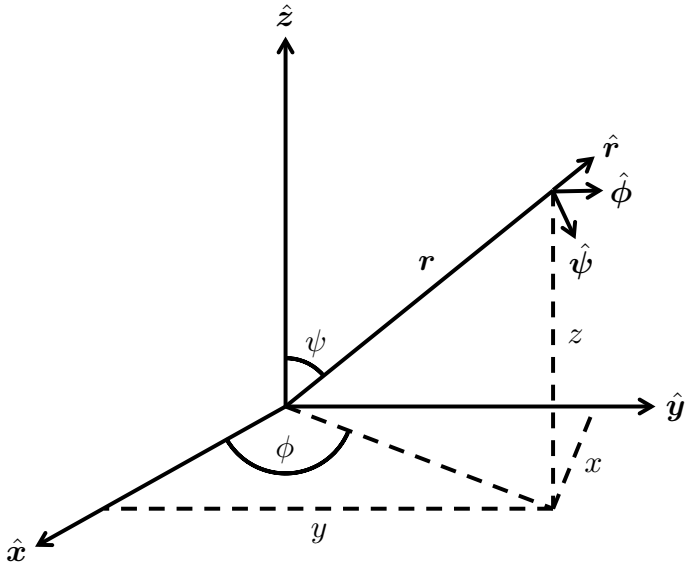

Figure 3.10: Local coordinate system used to define the radiation vector.

The coordinate system is defined as follows

$$\hat{\boldsymbol{r}} = \hat{\boldsymbol{x}}\cos\phi\sin\psi + \hat{\boldsymbol{y}}\sin\phi\sin\psi + \hat{\boldsymbol{z}}\cos\psi \tag{3.72}$$

$$\hat{\boldsymbol{\psi}} = \hat{\boldsymbol{x}}\cos\phi\cos\psi + \hat{\boldsymbol{y}}\sin\phi\cos\psi - \hat{\boldsymbol{z}}\sin\psi \tag{3.73}$$

$$\hat{\boldsymbol{\phi}} = -\hat{\boldsymbol{x}}\sin\phi + \hat{\boldsymbol{y}}\cos\phi \tag{3.74}$$

where

$$x = |\boldsymbol{r}|\cos\phi\sin\psi$$
$$y = |\boldsymbol{r}|\sin\phi\sin\psi$$
$$z = |\boldsymbol{r}|\cos\psi$$

and

$$\hat{\boldsymbol{z}} = \hat{\boldsymbol{r}}\cos\psi - \hat{\boldsymbol{\psi}}\sin\psi. \tag{3.75}$$

Decomposition of the Radiation Vector

We recall that the electric field is always parallel to the transverse portion of

the radiation vector, $\boldsymbol{F}_\perp(k\hat{\boldsymbol{r}},\omega)$, where

$$\boldsymbol{F} = \hat{\boldsymbol{r}}\boldsymbol{F}_r + \boldsymbol{F}_\perp = \hat{\boldsymbol{r}}\left(\hat{\boldsymbol{r}}\cdot\boldsymbol{F}\right) + \left(\hat{\boldsymbol{r}}\times\boldsymbol{F}\right)\times\hat{\boldsymbol{r}}$$

which can be written as spherical coordinates as

$$\boldsymbol{F} = \hat{\boldsymbol{r}}\boldsymbol{F}_r + \hat{\boldsymbol{\psi}}\boldsymbol{F}_\psi + \hat{\boldsymbol{\phi}}\boldsymbol{F}_\phi$$

and so

$$\boldsymbol{F}_\perp = \left(\hat{\boldsymbol{r}}\times\boldsymbol{F}\right)\times\hat{\boldsymbol{r}} = \hat{\boldsymbol{\psi}}\boldsymbol{F}_\psi + \hat{\boldsymbol{\phi}}\boldsymbol{F}_\phi. \tag{3.76}$$

We observe

$$\left(\hat{\boldsymbol{r}}\times\boldsymbol{F}\right)\times\hat{\boldsymbol{r}} = -\hat{\boldsymbol{r}}\times\left(\hat{\boldsymbol{r}}\times\boldsymbol{F}\right)$$

and so we can rewrite (3.71) as

$$\begin{aligned}
\boldsymbol{E}_m^{\mathrm{t}}(\boldsymbol{r},\omega) &= \mathrm{i}\omega\mu_0\frac{\mathrm{e}^{\mathrm{i}k|\boldsymbol{r}|}}{4\pi|\boldsymbol{r}|}\left(\left(\hat{\boldsymbol{r}}\times\boldsymbol{F}(k\hat{\boldsymbol{r}},\omega)\right)\times\hat{\boldsymbol{r}}\right) \\
&= \mathrm{i}\omega\mu_0\frac{\mathrm{e}^{\mathrm{i}k|\boldsymbol{r}|}}{4\pi|\boldsymbol{r}|}\boldsymbol{F}_{\perp,m}(k\hat{\boldsymbol{r}},\omega) \qquad (3.77)\\
&= \mathrm{i}\omega\mu_0\frac{\mathrm{e}^{\mathrm{i}k|\boldsymbol{r}|}}{4\pi|\boldsymbol{r}|}\left(\hat{\boldsymbol{\psi}}\boldsymbol{F}_{\psi,m}(\psi,\omega) + \hat{\boldsymbol{\phi}}\boldsymbol{F}_{\phi,m}(\phi,\omega)\right). \qquad (3.78)
\end{aligned}$$

Definition of the Radiation Vector

We will now define the radiation vector $\boldsymbol{F}(k\hat{\boldsymbol{r}},\omega)$ based on the radiator we have chosen, a thin dipole. The current density and current distribution are related by the expression

$$\boldsymbol{J}\left(x,y,z;\omega\right) = \hat{\boldsymbol{z}}I(z,\omega)\delta(x)\delta(y) \tag{3.79}$$

for linear antennas oriented along the z axis [72]. We can rewrite our expression for the radiation vector (3.68) in cartesian coordinates as

$$\boldsymbol{F}\left(\frac{kx}{|\boldsymbol{r}|},\frac{ky}{|\boldsymbol{r}|},\frac{kz}{|\boldsymbol{r}|};\omega\right) = \int \mathrm{e}^{-\mathrm{i}k(x,y,z)\cdot(x',y',z')/|\boldsymbol{r}|}\boldsymbol{J}\left(x',y',z';\omega\right)\mathrm{d}x'\mathrm{d}y'\mathrm{d}z' \tag{3.80}$$

where

$$|\boldsymbol{r}| = \sqrt{x^2+y^2+z^2}$$

and substitute (3.79) into (3.80) to obtain the radiation vector for a length $2L$ linear antenna

$$\begin{aligned}\boldsymbol{F}\left(\frac{kx}{|\boldsymbol{r}|},\frac{ky}{|\boldsymbol{r}|},\frac{kz}{|\boldsymbol{r}|};\omega\right) &= \hat{\boldsymbol{z}}\int_{-L}^{L} \mathrm{e}^{-\mathrm{i}k(x,y,z)\cdot(x',y',z')/|\boldsymbol{r}|} I(z',\omega)\delta(x')\delta(y')\mathrm{d}x'\mathrm{d}y'\mathrm{d}z' \\ &= \hat{\boldsymbol{z}}\int_{-L}^{L} I(z',\omega)\mathrm{e}^{-\mathrm{i}kzz'/|\boldsymbol{r}|}\mathrm{d}z'. \end{aligned} \tag{3.81}$$

Using (3.72) and (3.75) we can rewrite (3.81) as

$$\boldsymbol{F}(r,\psi;\omega) = \left(\hat{\boldsymbol{r}}\cos\psi - \hat{\boldsymbol{\psi}}\sin\psi\right)\int_{-L}^{L} I(z',\omega)\mathrm{e}^{-\mathrm{i}k\cos\psi\boldsymbol{z'}}\mathrm{d}z' \tag{3.82}$$

where we have left the integral in (3.82) in terms of the cartesian coordinate system along the antenna. This integral quantity is evaluated for the particular current distribution that corresponds to the chosen antenna. By (3.76) the transverse radiation vector will have only a $\hat{\boldsymbol{\psi}}$ component and the radial component can be eliminated yielding

$$\boldsymbol{F}_{\perp}(\psi,\omega) = -\hat{\boldsymbol{\psi}}\sin\psi\int_{-L}^{L} I(z',\omega)\mathrm{e}^{-\mathrm{i}k\cos\psi\boldsymbol{z'}}\mathrm{d}z'. \tag{3.83}$$

We will now consider possible choices for the current distribution of the radiating dipole.

Hertizian Dipole

For a Hertzian dipole we assume constant current distribution I_0 and infinitesimal length

$$I(z) = I_0 L\,\delta(z) \tag{3.84}$$

and substituting (3.84) into (3.83) yields the frequency independent transverse radiation vector

$$\boldsymbol{F}_{\perp}(\psi) = -\hat{\boldsymbol{\psi}}\sin\psi\, I_0 L. \tag{3.85}$$

Long Thin Dipole

We instead wish to model our radiator as a thin dipole with the length $2L$ much greater than the width $2a$. The thin standing wave antenna has approximate

current distribution

$$I(z,\omega) = I_0 \sin\left(k\left(L/2 - |z|\right)\right) \tag{3.86}$$

resulting in the transverse radiation vector

$$\boldsymbol{F}_{\perp}(\psi,\omega) = -\frac{2I_0\hat{\boldsymbol{\psi}}}{k}\left(\frac{\cos\left(kL\cos\psi\right) - \cos\left(kL\right)}{\sin\psi}\right) \tag{3.87}$$

[72]. While (3.87) is a more realistic approximation, we wish to relate the radiated electric field to the transmit waveform of the antenna.

Long Thin Dipole with Modified Current Distribution

Another model for the current distribution of a thin dipole comes from [73–77] and is related to the current distribution given by Wu and King [78, 79]. A zeroth-order approximation for the modified current distribution is given by

$$\begin{aligned} I(z,\omega) &= \frac{V^{\text{in}}(\omega)}{Z_0}\frac{\sin\left(k\left(L-|z|\right)\right)}{\alpha_{\text{r}}\sin(kL) + \text{i}\cos(kL)} \\ &= -\frac{2\text{i}V^{\text{in}}}{Z_0}\frac{\sin\left(k\left(L-|z|\right)\right)}{((1+\alpha_{\text{r}})\text{e}^{-\text{i}kL} + (1-\alpha_{\text{r}})\text{e}^{\text{i}kL})} \\ &= -\frac{\text{i}(1+\Gamma)V^{\text{in}}}{Z_0}\frac{\sin\left(k\left(L-|z|\right)\right)}{1+\Gamma\text{e}^{\text{i}2kL}}\text{e}^{\text{i}kL} \end{aligned} \tag{3.88}$$

where $V^{\text{in}}(\omega)$ is the Fourier domain input voltage, Z_0 is the characteristic impedance

$$Z_0 = \frac{\Omega\eta_0}{2\pi}$$

with free space impedance

$$\eta_0 = \mu_0 \text{c}_0$$

and

$$\Omega = 2\ln(2L/a),$$

Z_{g} is the generator impedance, assumed frequency independent, with $Z_{\text{g}} = \alpha_{\text{r}} Z_0$ and $0 < \alpha_{\text{r}} < 1$, and Γ is the reflection coefficient from the antenna to the generator

given by

$$\Gamma = \frac{(1-\alpha_{\mathrm{r}})}{(1+\alpha_{\mathrm{r}})} < 1.$$

If a system is matched then $\alpha_{\mathrm{r}} = 1$ so that $Z_{\mathrm{g}} = Z_0$ and the current distribution can be reduced to

$$I(z,\omega) = -\frac{\mathrm{i}\pi V^{\mathrm{in}}(\omega)}{\ln(2L/a)\mu_0 \mathrm{c}_0} \sin\left(k\left(L-|z|\right)\right) \mathrm{e}^{\mathrm{i}kL}. \tag{3.89}$$

We assume that $V^{\mathrm{in}}(\omega)$ is given by

$$V^{\mathrm{in}}(\omega) = V_0 S(\omega) \tag{3.90}$$

where V_0 is the amplitude of the input voltage and $S(\omega)$ is the Fourier transform of the transmit waveform. The relationship in (3.90) allows us to represent the current distribution in terms of the transmitted waveform

$$I(z,\omega) = -\frac{\mathrm{i}\pi V_0 S(\omega)}{\ln(2L/a)\mu_0 \mathrm{c}_0} \sin\left(k\left(L-|z|\right)\right) \mathrm{e}^{\mathrm{i}kL} \tag{3.91}$$

and we substitute (3.91) into (3.83) to obtain

$$\boldsymbol{F}_{\perp}(\psi,\omega) = \frac{\mathrm{i}2\pi V_0 S(\omega)\hat{\boldsymbol{\psi}}}{\ln(2L/a)\mu_0\omega} \mathrm{e}^{\mathrm{i}kL} \left(\frac{\cos\left(kL\cos\psi\right) - \cos\left(kL\right)}{\sin\psi}\right). \tag{3.92}$$

Electric Field Radiated from a Long Thin Dipole

We recall that a dipole antenna is polarized in the same plane that the antenna is in, e.g., a vertically oriented dipole antenna is vertically polarized. We let the unit vector $\hat{\boldsymbol{p}}_m$ denote the polarization of the m^{th} transmitting dipole where $\hat{\boldsymbol{p}}_m$ is given in the basis of the transmitting dipole as described under the BSA convention in Section 3.2.3. The m^{th} radiation vector can be rewritten in terms of a scalar radiation pattern that is oriented according to the antenna polarization

$$\boldsymbol{F}_{\perp,m}(\psi_m,\omega) = F_m(\psi_m,\omega)\hat{\boldsymbol{p}}_m \tag{3.93}$$

where

$$F_m(\psi_m, \omega) = \frac{\mathrm{i}2\pi V_{0,m} S_m(\omega)}{\ln(2L_m/a_m)\mu_0\omega} \mathrm{e}^{\mathrm{i}kL_m} \left(\frac{\cos\left(kL_m \cos\psi_m\right) - \cos\left(kL_m\right)}{\sin\psi_m} \right) \tag{3.94}$$

is the scalar radiation pattern for the long thin dipole with modified current distribution,

$$\psi_m = \arccos\left(|\hat{\boldsymbol{r}} \cdot \hat{\boldsymbol{e}}_m|\right), \tag{3.95}$$

and $\hat{\boldsymbol{e}}_m$ is the orientation of the dipole. Note that previously the ψ used to determine the radiation vector for a dipole was defined by the coordinate system where the antenna is oriented along the $\hat{\boldsymbol{z}}$-axis. This value of ψ corresponded to the angle between the propagation vector and the dipole orientation. In (3.95) we similarly define ψ_m as the angle between the propagation vector $\hat{\boldsymbol{r}}$ and the orientation vector $\hat{\boldsymbol{e}}_m$ of the m^{th} transmitting dipole, where the orientation of the dipole is defined in the global coordinate system of the BSA convention. In (3.95) we take the absolute value of the inner product $\hat{\boldsymbol{r}} \cdot \hat{\boldsymbol{e}}_m$ because the radiation pattern of a dipole is symmetric.

Substituting (3.93) into the radiated electric field from the m^{th} transmitter (3.77) we obtain

$$\boldsymbol{E}_m^{\mathrm{t}}(\boldsymbol{r}, \omega) = \mathrm{i}\omega\mu_0 \frac{\mathrm{e}^{\mathrm{i}k|\boldsymbol{r}|}}{4\pi|\boldsymbol{r}|} F_m(\psi_m) \hat{\boldsymbol{p}}_m. \tag{3.96}$$

Time Domain Radiated Electric Field

We can obtain a time domain version of the radiated electric field by taking the inverse Fourier transform with an appropriate contour. We have left the transmit waveform $S(\omega)$ undefined and so we assume that a contour of integration exists for a given transmit waveform so that $\mathcal{F}^{-1}\{S_m(\omega)\} = s_m(t)$

$$\begin{aligned}
\boldsymbol{\mathcal{E}}_m^{\mathrm{t}}(\boldsymbol{r}, t) =& \frac{1}{2\pi} \int \boldsymbol{E}_m^{\mathrm{t}}(\boldsymbol{r}, \omega) \mathrm{e}^{-\mathrm{i}\omega t} \mathrm{d}\omega \\
=& \mathcal{F}^{-1}\left\{ \boldsymbol{E}_m^{\mathrm{t}}(\boldsymbol{r}, \omega) \right\} \\
=& \frac{V_{0,m} \hat{\boldsymbol{p}}_m}{2|\boldsymbol{r}| \ln(2L_m/a_m) \sin\psi_m} \\
& \times \mathcal{F}^{-1}\{ S_m(\omega) \mathrm{e}^{\mathrm{i}k(|\boldsymbol{r}| + L_m)} (\cos\left(kL_m\right) - \cos\left(kL_m \cos\psi_m\right)) \}
\end{aligned}$$

$$
\begin{aligned}
=&\frac{V_{0,m}\hat{\boldsymbol{p}}_m}{2|\boldsymbol{r}|\ln(2L_m/a_m)\sin\psi_m}\,\mathcal{F}^{-1}\{S_m(\omega)\mathrm{e}^{\mathrm{i}k(|\boldsymbol{r}|+L_m)}\}\\
&*\,\mathcal{F}^{-1}\{\cos(kL_m)-\cos(kL_m\cos\psi_m)\}\\
=&\frac{V_{0,m}\hat{\boldsymbol{p}}_m}{4|\boldsymbol{r}|\ln(2L_m/a_m)\sin\psi_m}\int s_m\left(\tau-\frac{|\boldsymbol{r}|}{\mathrm{c}_0}-\frac{L_m}{\mathrm{c}_0}\right)\\
&\times\left[\delta\left(\tau-t-\frac{L_m}{\mathrm{c}_0}\right)+\delta\left(\tau-t+\frac{L_m}{\mathrm{c}_0}\right)\right.\\
&\quad\left.-\delta\left(\tau-t-\frac{L_m}{\mathrm{c}_0}\cos\psi_m\right)-\delta\left(\tau-t+\frac{L_m}{\mathrm{c}_0}\cos\psi_m\right)\right]\mathrm{d}\tau\\
=&\frac{V_{0,m}\hat{\boldsymbol{p}}_m}{4|\boldsymbol{r}|\ln(2L_m/a_m)\sin\psi_m}\left[s_m\left(t-\frac{|\boldsymbol{r}|}{\mathrm{c}_0}\right)+s_m\left(t-\frac{|\boldsymbol{r}|}{\mathrm{c}_0}-\frac{2L_m}{\mathrm{c}_0}\right)\right.\\
&\left.-s_m\left(t-\frac{|\boldsymbol{r}|}{\mathrm{c}_0}-\frac{L_m}{\mathrm{c}_0}(1-\cos\psi_m)\right)-s_m\left(t-\frac{|\boldsymbol{r}|}{\mathrm{c}_0}-\frac{L_m}{\mathrm{c}_0}(1+\cos\psi_m)\right)\right].
\end{aligned}
\tag{3.97}
$$

We observe that (3.97) is composed of four terms containing the transmitted waveform at various time delays. The first term corresponds to the field radiated from the center feed of the dipole and thus the field incident at a distance $|\boldsymbol{r}|$ away from the antenna is composed of a version of the transmit waveform that is only delayed by time $|\boldsymbol{r}|/\mathrm{c}_0$. The second term corresponds to the field radiated from the center feed but only after the current has traveled to either end of the dipole and been reflected back to the center, traveling a distance $2L_m$. Half of the second term is contributed by currents reflected from each end. The final two terms correspond to the field radiated from each end of the dipole after the current has traveled a distance L_m. This behavior results from the assumption that the field is only radiated from the discontinuities of the antenna [75], the center feed and ends. In reality there would be additional reflections of current from either end of the dipole and the center feed at decreasing amplitudes. Only the zeroth order terms result from expression (3.91) for the current distribution.

3.4.5 Scattering

The scattered electric field from a target at location $\boldsymbol{x}_a$ is given by

$$
\boldsymbol{E}_m^{\mathrm{r}}(\boldsymbol{r},\omega)=\frac{\mathrm{e}^{\mathrm{i}k|\boldsymbol{x}_a-\boldsymbol{r}|}}{4\pi|\boldsymbol{x}_a-\boldsymbol{r}|}[\boldsymbol{S}]_a\boldsymbol{E}_m^{\mathrm{t}}(\boldsymbol{r}_m,\omega)
\tag{3.98}
$$

where $\boldsymbol{E}_m^{\mathrm{r}}$ is again consistent with the BSA convention,

$$\boldsymbol{r}_m = \boldsymbol{x}_a - \boldsymbol{x}_{\mathrm{T},m}$$

is the vector from the m^{th} transmitter to the a^{th} target, and $[\boldsymbol{S}]_a$ is the scattering matrix of the a^{th} target

$$[\boldsymbol{S}]_a \equiv [\boldsymbol{S}]_a^{\mathrm{BSA}} = \begin{bmatrix} S_{\mathrm{h}_n\mathrm{h}_m} & S_{\mathrm{h}_n\mathrm{v}_m} \\ S_{\mathrm{v}_n\mathrm{h}_m} & S_{\mathrm{v}_n\mathrm{v}_m} \end{bmatrix}_a^{\mathrm{BSA}}. \tag{3.99}$$

The scattering matrix is dependent on aspect angle, frequency, and material properties of the target. The scattering matrix also completely describes the polarization transforming properties of the target and changes the basis of the polarization of the m^{th} transmitting antenna, $(\hat{\boldsymbol{r}}_m, \hat{\boldsymbol{h}}_m, \hat{\boldsymbol{v}}_m)$, into the basis of the n^{th} receiving antenna, $(\hat{\boldsymbol{r}}_n, \hat{\boldsymbol{h}}_n, \hat{\boldsymbol{v}}_n)$. The choice of receiving antenna is necessary for the definition of the scattering matrix.

In the literature most scattering matrices are given for the case of monostatic backscatter due to the extreme complexity of defining a target's scattering matrix for all possible transmitter and receiver orientations and polarizations. In the simulations presented later we will use a bistatic scattering matrix for a flat rectangular plate derived for our specific scenario in Appendix D in addition to more complex scattering matrices defined for the monostatic case.

We also observe that because we are considering a general scatterer we do not know the frequency dependence of $[\boldsymbol{S}]_a$. In subsequent sections we will assume that the scattering behavior can be sufficiently described over the bandwidth of the transmit waveform by the values of $[\boldsymbol{S}]_a$ at the carrier frequency. This is so that we may consider the scattered field in both the time and frequency domains without knowledge of the inverse Fourier transform of the scattering matrix. We will also consider the case of the flat rectangular plate where the frequency dependence is derived in Appendix D.

Let

$$\boldsymbol{p}_m^{\mathrm{r}} = [\boldsymbol{S}]_a \hat{\boldsymbol{p}}_m$$

denote the polarization vector of the incident field transformed by the scattering matrix of the a^{th} target. Observe that $\boldsymbol{p}_m^{\text{r}}$ is no longer of unit magnitude because $[\boldsymbol{S}]_a$ will be frequency dependent and include a scattering amplitude coefficient. Although we have not yet discussed the receive antenna in detail, $\boldsymbol{p}_m^{\text{r}}$ implicitly depends on the polarization basis of the receive antenna.

Substituting the radiated field (3.96) into (3.98), the scattered electric field becomes

$$\boldsymbol{E}_m^{\text{r}}(\boldsymbol{r},\omega) = \text{i}\omega\mu_0 \frac{\text{e}^{\text{i}k(|\boldsymbol{r}_m|+|\boldsymbol{x}_a-\boldsymbol{r}|)}}{(4\pi)^2|\boldsymbol{r}_m||\boldsymbol{x}_a-\boldsymbol{r}|} F_m(\psi_m)\boldsymbol{p}_m^{\text{r}}. \tag{3.100}$$

Scattered Electric Field for Moving Targets

We will next consider the case of moving targets. We first substitute (3.94) into (3.100) and Fourier transform the scattered electric field through a process similar to that used to obtain (3.97)

$$\begin{aligned}
\boldsymbol{\mathcal{E}}_m^{\text{r}}(\boldsymbol{r},t) =& \frac{1}{2\pi}\int \boldsymbol{E}_m^{\text{r}}(\boldsymbol{r},\omega)\text{e}^{-\text{i}\omega t}\text{d}\omega \\
=& \mathcal{F}^{-1}\left\{\boldsymbol{E}_m^{\text{r}}(\boldsymbol{r},\omega)\right\} \\
=& \frac{V_{0,m}\boldsymbol{p}_m^{\text{r}}}{2(4\pi)|\boldsymbol{r}_m||\boldsymbol{x}_a-\boldsymbol{r}|\ln(2L_m/a_m)\sin\psi_m} \\
& \times \mathcal{F}^{-1}\{S_m(\omega)\text{e}^{\text{i}k(|\boldsymbol{r}_m|+|\boldsymbol{x}_a-\boldsymbol{r}|+L_m)}(\cos(kL_m)-\cos(kL_m\cos\psi_m))\} \\
=& \frac{V_{0,m}\boldsymbol{p}_m^{\text{r}}}{4(4\pi)|\boldsymbol{r}_m||\boldsymbol{r}-\boldsymbol{x}_q|\ln(2L_m/a_m)\sin\psi_m} \\
& \times \left[s_m\left(t-\frac{|\boldsymbol{r}_m|}{\text{c}_0}-\frac{|\boldsymbol{x}_a-\boldsymbol{r}|}{\text{c}_0}\right)+s_m\left(t-\frac{|\boldsymbol{r}_m|}{\text{c}_0}-\frac{|\boldsymbol{x}_a-\boldsymbol{r}|}{\text{c}_0}-\frac{2L_m}{\text{c}_0}\right)\right. \\
& \quad - s_m\left(t-\frac{|\boldsymbol{r}_m|}{\text{c}_0}-\frac{|\boldsymbol{x}_a-\boldsymbol{r}|}{\text{c}_0}-\frac{L_m}{\text{c}_0}(1-\cos\psi_m)\right) \\
& \quad \left. -s_m\left(t-\frac{|\boldsymbol{r}_m|}{\text{c}_0}-\frac{|\boldsymbol{x}_a-\boldsymbol{r}|}{\text{c}_0}-\frac{L_m}{\text{c}_0}(1+\cos\psi_m)\right)\right]
\end{aligned}$$

$$
\begin{aligned}
=&\frac{V_{0,m}\boldsymbol{p}_m^{\mathrm{r}}}{4(4\pi)|\boldsymbol{x}_a-\boldsymbol{x}_{\mathrm{T},m}||\boldsymbol{r}-\boldsymbol{x}_q|\ln(2L_m/a_m)\sin\psi_m}\\
&\times\left[s_m\left(t-\frac{|\boldsymbol{x}_a-\boldsymbol{x}_{\mathrm{T},m}|}{\mathrm{c}_0}-\frac{|\boldsymbol{x}_a-\boldsymbol{r}|}{\mathrm{c}_0}\right)\right.\\
&\quad+s_m\left(t-\frac{|\boldsymbol{x}_a-\boldsymbol{x}_{\mathrm{T},m}||}{\mathrm{c}_0}-\frac{|\boldsymbol{x}_a-\boldsymbol{r}|}{\mathrm{c}_0}-\frac{2L_m}{\mathrm{c}_0}\right)\\
&\quad-s_m\left(t-\frac{|\boldsymbol{x}_a-\boldsymbol{x}_{\mathrm{T},m}|}{\mathrm{c}_0}-\frac{|\boldsymbol{x}_a-\boldsymbol{r}|}{\mathrm{c}_0}-\frac{L_m}{\mathrm{c}_0}(1-\cos\psi_m)\right)\\
&\quad\left.-s_m\left(t-\frac{|\boldsymbol{x}_a-\boldsymbol{x}_{\mathrm{T},m}|}{\mathrm{c}_0}-\frac{|\boldsymbol{x}_a-\boldsymbol{r}|}{\mathrm{c}_0}-\frac{L_m}{\mathrm{c}_0}(1+\cos\psi_m)\right)\right]. \qquad (3.101)
\end{aligned}
$$

We next substitute $\boldsymbol{x}_a-\boldsymbol{v}_at$ for the position of the a^{th} moving target to obtain

$$
\begin{aligned}
\boldsymbol{\mathcal{E}}_m^{\mathrm{r}}(\boldsymbol{r},t)=&\frac{V_{0,m}\boldsymbol{p}_m^{\mathrm{r}}}{4(4\pi)|\boldsymbol{x}_a-\boldsymbol{x}_{\mathrm{T},m}+\boldsymbol{v}_at||\boldsymbol{x}_a-\boldsymbol{r}+\boldsymbol{v}_at|\ln(2L_m/a_m)\sin\psi_m}\\
&\times\left[s_m\left(t-\frac{|\boldsymbol{x}_a-\boldsymbol{x}_{\mathrm{T},m}+\boldsymbol{v}_at|}{\mathrm{c}_0}-\frac{|\boldsymbol{x}_a-\boldsymbol{r}+\boldsymbol{v}_at|}{\mathrm{c}_0}\right)\right.\\
&\quad+s_m\left(t-\frac{|\boldsymbol{x}_a-\boldsymbol{x}_{\mathrm{T},m}+\boldsymbol{v}_at||}{\mathrm{c}_0}-\frac{|\boldsymbol{x}_a-\boldsymbol{r}+\boldsymbol{v}_at|}{\mathrm{c}_0}-\frac{2L_m}{\mathrm{c}_0}\right)\\
&\quad-s_m\left(t-\frac{|\boldsymbol{x}_a-\boldsymbol{x}_{\mathrm{T},m}+\boldsymbol{v}_at|}{\mathrm{c}_0}-\frac{|\boldsymbol{x}_a-\boldsymbol{r}+\boldsymbol{v}_at|}{\mathrm{c}_0}-\frac{L_m}{\mathrm{c}_0}(1-\cos\psi_m)\right)\\
&\quad\left.-s_m\left(t-\frac{|\boldsymbol{x}_a-\boldsymbol{x}_{\mathrm{T},m}+\boldsymbol{v}_at|}{\mathrm{c}_0}-\frac{|\boldsymbol{x}_a-\boldsymbol{r}+\boldsymbol{v}_at|}{\mathrm{c}_0}-\frac{L_m}{\mathrm{c}_0}(1+\cos\psi_m)\right)\right] \qquad (3.102)
\end{aligned}
$$

and assume that the target is slowly moving with respect to c_0, $|\boldsymbol{v}_a|\ll\mathrm{c}_0$. For large distances $|\boldsymbol{x}_a-\boldsymbol{x}_{\mathrm{T},m}|$ and $|\boldsymbol{x}_a-\boldsymbol{r}|$ we assume

$$
|\boldsymbol{x}_a-\boldsymbol{x}_{\mathrm{T},m}+\boldsymbol{v}_at|\approx|\boldsymbol{x}_a-\boldsymbol{x}_{\mathrm{T},m}|+\widehat{\boldsymbol{x}_a-\boldsymbol{x}_{\mathrm{T},m}}\cdot\boldsymbol{v}_at
$$

and

$$
|\boldsymbol{x}_a-\boldsymbol{r}+\boldsymbol{v}_at|\approx|\boldsymbol{x}_a-\boldsymbol{r}|+\widehat{\boldsymbol{x}_a-\boldsymbol{r}}\cdot\boldsymbol{v}_at
$$

so that our expression for the time domain scattered electric field becomes

$$
\begin{aligned}
\boldsymbol{\mathcal{E}}_m^{\mathrm{r}}(\boldsymbol{r},t) =& \frac{V_{0,m}\boldsymbol{p}_m^{\mathrm{r}}}{4(4\pi)|\boldsymbol{x}_a-\boldsymbol{x}_{\mathrm{T},m}||\boldsymbol{x}_a-\boldsymbol{r}|\ln(2L_m/a_m)\sin\psi_m} \\
&\times\Bigg[s_m\left(t-\frac{|\boldsymbol{x}_a-\boldsymbol{x}_{\mathrm{T},m}|}{\mathrm{c}_0}-\frac{\widehat{\boldsymbol{x}_a-\boldsymbol{x}_{\mathrm{T},m}}\cdot\boldsymbol{v}_a t}{\mathrm{c}_0}-\frac{|\boldsymbol{x}_a-\boldsymbol{r}|}{\mathrm{c}_0}-\frac{\widehat{\boldsymbol{x}_a-\boldsymbol{r}}\cdot\boldsymbol{v}_a t}{\mathrm{c}_0}\right) \\
&\quad+s_m\left(t-\frac{|\boldsymbol{x}_a-\boldsymbol{x}_{\mathrm{T},m}|}{\mathrm{c}_0}-\frac{\widehat{\boldsymbol{x}_a-\boldsymbol{x}_{\mathrm{T},m}}\cdot\boldsymbol{v}_a t}{\mathrm{c}_0}-\frac{|\boldsymbol{x}_a-\boldsymbol{r}|}{\mathrm{c}_0}\right. \\
&\qquad\left.-\frac{\widehat{\boldsymbol{x}_a-\boldsymbol{r}}\cdot\boldsymbol{v}_a t}{\mathrm{c}_0}-\frac{2L_m}{\mathrm{c}_0}\right) \\
&\quad-s_m\left(t-\frac{|\boldsymbol{x}_a-\boldsymbol{x}_{\mathrm{T},m}|}{\mathrm{c}_0}-\frac{\widehat{\boldsymbol{x}_a-\boldsymbol{x}_{\mathrm{T},m}}\cdot\boldsymbol{v}_a t}{\mathrm{c}_0}-\frac{|\boldsymbol{x}_a-\boldsymbol{r}|}{\mathrm{c}_0}\right. \\
&\qquad\left.-\frac{\widehat{\boldsymbol{x}_a-\boldsymbol{r}}\cdot\boldsymbol{v}_a t}{\mathrm{c}_0}-\frac{L_m}{\mathrm{c}_0}(1-\cos\psi_m)\right) \\
&\quad-s_m\left(t-\frac{|\boldsymbol{x}_a-\boldsymbol{x}_{\mathrm{T},m}|}{\mathrm{c}_0}-\frac{\widehat{\boldsymbol{x}_a-\boldsymbol{x}_{\mathrm{T},m}}\cdot\boldsymbol{v}_a t}{\mathrm{c}_0}-\frac{|\boldsymbol{x}_a-\boldsymbol{r}|}{\mathrm{c}_0}\right. \\
&\qquad\left.-\frac{\widehat{\boldsymbol{x}_a-\boldsymbol{r}}\cdot\boldsymbol{v}_a t}{\mathrm{c}_0}-\frac{L_m}{\mathrm{c}_0}(1+\cos\psi_m)\right)\Bigg] \\
=& \frac{V_{0,m}\boldsymbol{p}_m^{\mathrm{r}}}{4(4\pi)|\boldsymbol{r}_m||\boldsymbol{x}_a-\boldsymbol{r}|\ln(2L_m/a_m)\sin\psi_m} \\
&\times\Bigg[s_m\left(t-\frac{|\boldsymbol{r}_m|}{\mathrm{c}_0}-\frac{\hat{\boldsymbol{r}}_m\cdot\boldsymbol{v}_a t}{\mathrm{c}_0}-\frac{|\boldsymbol{x}_a-\boldsymbol{r}|}{\mathrm{c}_0}-\frac{\widehat{\boldsymbol{x}_a-\boldsymbol{r}}\cdot\boldsymbol{v}_a t}{\mathrm{c}_0}\right) \\
&\quad+s_m\left(t-\frac{|\boldsymbol{r}_m|}{\mathrm{c}_0}-\frac{\hat{\boldsymbol{r}}_m\cdot\boldsymbol{v}_a t}{\mathrm{c}_0}-\frac{|\boldsymbol{x}_a-\boldsymbol{r}|}{\mathrm{c}_0}\right. \\
&\qquad\left.-\frac{\widehat{\boldsymbol{x}_a-\boldsymbol{r}}\cdot\boldsymbol{v}_a t}{\mathrm{c}_0}-\frac{2L_m}{\mathrm{c}_0}\right) \\
&\quad-s_m\left(t-\frac{|\boldsymbol{r}_m|}{\mathrm{c}_0}-\frac{\hat{\boldsymbol{r}}_m\cdot\boldsymbol{v}_a t}{\mathrm{c}_0}-\frac{|\boldsymbol{x}_a-\boldsymbol{r}|}{\mathrm{c}_0}\right. \\
&\qquad\left.-\frac{\widehat{\boldsymbol{x}_a-\boldsymbol{r}}\cdot\boldsymbol{v}_a t}{\mathrm{c}_0}-\frac{L_m}{\mathrm{c}_0}(1-\cos\psi_m)\right) \\
&\quad-s_m\left(t-\frac{|\boldsymbol{r}_m|}{\mathrm{c}_0}-\frac{\hat{\boldsymbol{r}}_m\cdot\boldsymbol{v}_a t}{\mathrm{c}_0}-\frac{|\boldsymbol{x}_a-\boldsymbol{r}|}{\mathrm{c}_0}\right. \\
&\qquad\left.-\frac{\widehat{\boldsymbol{x}_a-\boldsymbol{r}}\cdot\boldsymbol{v}_a t}{\mathrm{c}_0}-\frac{L_m}{\mathrm{c}_0}(1+\cos\psi_m)\right)\Bigg]. \qquad (3.103)
\end{aligned}
$$

Frequency Domain Scattered Electric Field for Moving Targets

We obtain the frequency domain scattered field for a moving target by Fourier transforming (3.103)

$$
\begin{aligned}
\boldsymbol{E}_m^{\mathrm{r}}(\boldsymbol{r},\omega) =& \int \boldsymbol{\mathcal{E}}_m^{\mathrm{r}}(\boldsymbol{r},t)\mathrm{e}^{\mathrm{i}\omega t}\mathrm{d}t \\
=& \mathcal{F}\left\{\boldsymbol{\mathcal{E}}_m^{\mathrm{r}}(\boldsymbol{r},t)\right\} \\
=& \frac{V_{0,m}\boldsymbol{p}_m^{\mathrm{r}}}{4(4\pi)|\boldsymbol{r}_m||\boldsymbol{x}_a-\boldsymbol{r}|\ln(2L_m/a_m)\sin\psi_m} \\
& \times \mathcal{F}\left\{ s_m\left(t-\frac{|\boldsymbol{r}_m|}{\mathrm{c}_0}-\frac{\hat{\boldsymbol{r}}_m\cdot\boldsymbol{v}_a t}{\mathrm{c}_0}-\frac{|\boldsymbol{x}_a-\boldsymbol{r}|}{\mathrm{c}_0}-\frac{\widehat{\boldsymbol{x}_a-\boldsymbol{r}}\cdot\boldsymbol{v}_a t}{\mathrm{c}_0}\right)\right. \\
& \quad + s_m\left(t-\frac{|\boldsymbol{r}_m|}{\mathrm{c}_0}-\frac{\hat{\boldsymbol{r}}_m\cdot\boldsymbol{v}_a t}{\mathrm{c}_0}-\frac{|\boldsymbol{x}_a-\boldsymbol{r}|}{\mathrm{c}_0}-\frac{\widehat{\boldsymbol{x}_a-\boldsymbol{r}}\cdot\boldsymbol{v}_a t}{\mathrm{c}_0}-\frac{2L_m}{\mathrm{c}_0}\right) \\
& \quad - s_m\left(t-\frac{|\boldsymbol{r}_m|}{\mathrm{c}_0}-\frac{\hat{\boldsymbol{r}}_m\cdot\boldsymbol{v}_a t}{\mathrm{c}_0}-\frac{|\boldsymbol{x}_a-\boldsymbol{r}|}{\mathrm{c}_0}\right. \\
& \qquad \left.-\frac{\widehat{\boldsymbol{x}_a-\boldsymbol{r}}\cdot\boldsymbol{v}_a t}{\mathrm{c}_0}-\frac{L_m}{\mathrm{c}_0}(1-\cos\psi_m)\right) \\
& \quad - s_m\left(t-\frac{|\boldsymbol{r}_m|}{\mathrm{c}_0}-\frac{\hat{\boldsymbol{r}}_m\cdot\boldsymbol{v}_a t}{\mathrm{c}_0}-\frac{|\boldsymbol{x}_a-\boldsymbol{r}|}{\mathrm{c}_0}\right. \\
& \qquad \left.\left.-\frac{\widehat{\boldsymbol{x}_a-\boldsymbol{r}}\cdot\boldsymbol{v}_a t}{\mathrm{c}_0}-\frac{L_m}{\mathrm{c}_0}(1+\cos\psi_m)\right)\right\} \\
=& \frac{V_{0,m}\boldsymbol{p}_m^{\mathrm{r}}}{4(4\pi)|\boldsymbol{r}_m||\boldsymbol{x}_a-\boldsymbol{r}|\ln(2L_m/a_m)\sin\psi_m} \\
& \times \mathcal{F}\left\{\int s_m\left(\tau-\frac{|\boldsymbol{r}_m|}{\mathrm{c}_0}-\frac{\hat{\boldsymbol{r}}_m\cdot\boldsymbol{v}_a t}{\mathrm{c}_0}-\frac{|\boldsymbol{x}_a-\boldsymbol{r}|}{\mathrm{c}_0}-\frac{\widehat{\boldsymbol{x}_a-\boldsymbol{r}}\cdot\boldsymbol{v}_a t}{\mathrm{c}_0}-\frac{L_m}{\mathrm{c}_0}\right)\right. \\
& \quad \times\left[\delta\left(\tau-t-\frac{L_m}{\mathrm{c}_0}\right)+\delta\left(\tau-t+\frac{L_m}{\mathrm{c}_0}\right)\right. \\
& \qquad \left.\left.-\delta\left(\tau-t-\frac{L_m\cos\psi_m}{\mathrm{c}_0}\right)-\delta\left(\tau-t+\frac{L_m\cos\psi_m}{\mathrm{c}_0}\right)\right]\mathrm{d}\tau\right\}
\end{aligned}
$$

$$
\begin{aligned}
=&\frac{V_{0,m}\boldsymbol{p}_m^{\mathrm{r}}}{4(4\pi)|\boldsymbol{r}_m||\boldsymbol{x}_a-\boldsymbol{r}|\ln(2L_m/a_m)\sin\psi_m}\\
&\times\mathcal{F}\left\{s_m\left(t-\frac{|\boldsymbol{r}_m|}{\mathrm{c}_0}-\frac{\hat{\boldsymbol{r}}_m\cdot\boldsymbol{v}_a t}{\mathrm{c}_0}-\frac{|\boldsymbol{x}_a-\boldsymbol{r}|}{\mathrm{c}_0}-\frac{\widehat{\boldsymbol{x}_a-\boldsymbol{r}}\cdot\boldsymbol{v}_a t}{\mathrm{c}_0}-\frac{L_m}{\mathrm{c}_0}\right)\right.\\
&\qquad *\left[\delta\left(t+\frac{L_m}{\mathrm{c}_0}\right)+\delta\left(t-\frac{L_m}{\mathrm{c}_0}\right)-\delta\left(t+\frac{L_m\cos\psi_m}{\mathrm{c}_0}\right)\right.\\
&\qquad\left.\left.-\delta\left(t-\frac{L_m\cos\psi_m}{\mathrm{c}_0}\right)\right]\right\}\\
=&\frac{V_{0,m}\boldsymbol{p}_m^{\mathrm{r}}}{2(4\pi)|\boldsymbol{r}_m||\boldsymbol{x}_a-\boldsymbol{r}|\ln(2L_m/a_m)\sin\psi_m}\left(\cos\left(kL_m\right)-\cos\left(kL_m\cos\psi_m\right)\right)\\
&\times\mathcal{F}\left\{s_m\left(t-\frac{|\boldsymbol{r}_m|}{\mathrm{c}_0}-\frac{\hat{\boldsymbol{r}}_m\cdot\boldsymbol{v}_a t}{\mathrm{c}_0}-\frac{|\boldsymbol{x}_a-\boldsymbol{r}|}{\mathrm{c}_0}-\frac{\widehat{\boldsymbol{x}_a-\boldsymbol{r}}\cdot\boldsymbol{v}_a t}{\mathrm{c}_0}-\frac{L_m}{\mathrm{c}_0}\right)\right\}.
\end{aligned}
\tag{3.104}
$$

To obtain the $\mathcal{F}\{s_m(\cdot)\}$ we first rewrite the expression

$$
\begin{aligned}
\mathcal{F}\{s_m(\cdot)\}=&\mathcal{F}\left\{s_m\left(t-\frac{|\boldsymbol{r}_m|}{\mathrm{c}_0}-\frac{\hat{\boldsymbol{r}}_m\cdot\boldsymbol{v}_a t}{\mathrm{c}_0}-\frac{|\boldsymbol{x}_a-\boldsymbol{r}|}{\mathrm{c}_0}-\frac{\widehat{\boldsymbol{x}_a-\boldsymbol{r}}\cdot\boldsymbol{v}_a t}{\mathrm{c}_0}-\frac{L_m}{\mathrm{c}_0}\right)\right\}\\
=&\mathcal{F}\left\{s_m\left(\left(1-\frac{(\hat{\boldsymbol{r}}_m+\widehat{\boldsymbol{x}_a-\boldsymbol{r}})\cdot\boldsymbol{v}_a}{\mathrm{c}_0}\right)t-\frac{|\boldsymbol{r}_m|}{\mathrm{c}_0}-\frac{|\boldsymbol{x}_a-\boldsymbol{r}|}{\mathrm{c}_0}-\frac{L_m}{\mathrm{c}_0}\right)\right\}\\
=&\mathcal{F}\left\{s_m\left(\alpha t-\frac{|\boldsymbol{r}_m|}{\mathrm{c}_0}-\frac{|\boldsymbol{x}_a-\boldsymbol{r}|}{\mathrm{c}_0}-\frac{L_m}{\mathrm{c}_0}\right)\right\}
\end{aligned}
\tag{3.105}
$$

where

$$
\alpha=1-\frac{(\hat{\boldsymbol{r}}_m+\widehat{\boldsymbol{x}_a-\boldsymbol{r}})\cdot\boldsymbol{v}_a}{\mathrm{c}_0}=1-\beta
$$

and through the change of variables $\tau=\alpha t$ (3.105) becomes

$$
\mathcal{F}\{s_m(\cdot)\}=\int\frac{1}{\alpha}s_m\left(\tau-\frac{|\boldsymbol{r}_m|}{\mathrm{c}_0}-\frac{|\boldsymbol{x}_a-\boldsymbol{r}|}{\mathrm{c}_0}-\frac{L_m}{\mathrm{c}_0}\right)\mathrm{e}^{\mathrm{i}\omega\tau/\alpha}\mathrm{d}\tau. \tag{3.106}
$$

We observe that the quantity β is very small and so we are able to Taylor expand

$$
\frac{1}{\alpha}\approx 1+\beta=1+\frac{(\hat{\boldsymbol{r}}_m+\widehat{\boldsymbol{x}_a-\boldsymbol{r}})\cdot\boldsymbol{v}_a}{\mathrm{c}_0}
$$

and we can rewrite (3.106)

$$\begin{aligned}\mathcal{F}\{s_m(\cdot)\} =& \int s_m\left(\tau - \frac{|\boldsymbol{r}_m|}{\mathrm{c}_0} - \frac{|\boldsymbol{x}_a - \boldsymbol{r}|}{\mathrm{c}_0} - \frac{L_m}{\mathrm{c}_0}\right) \mathrm{e}^{\mathrm{i}(1+\beta)\omega\tau}\mathrm{d}\tau \\ =& S_m\left((1+\beta)\omega\right) \mathrm{e}^{\mathrm{i}(1+\beta)\omega\left(\frac{|\boldsymbol{r}_m|}{\mathrm{c}_0} + \frac{|\boldsymbol{x}_a - \boldsymbol{r}|}{\mathrm{c}_0} + \frac{L_m}{\mathrm{c}_0}\right)} \end{aligned} \tag{3.107}$$

where

$$\beta = \frac{(\hat{\boldsymbol{r}}_m + \widehat{\boldsymbol{x}_a - \boldsymbol{r}}) \cdot \boldsymbol{v}_a}{\mathrm{c}_0}.$$

The frequency domain scattered field for a moving target can now be written by substituting (3.107) into (3.104)

$$\begin{aligned}\boldsymbol{E}_m^{\mathrm{r}}(\boldsymbol{r},\omega) =& \frac{V_{0,m}\boldsymbol{p}_m^{\mathrm{r}} S_m\left((1+\beta)\omega\right)}{2(4\pi)|\boldsymbol{r}_m||\boldsymbol{x}_a - \boldsymbol{r}|\ln(2L_m/a_m)\sin\psi_m} \mathrm{e}^{\mathrm{i}(1+\beta)\omega\left(\frac{|\boldsymbol{r}_m|}{\mathrm{c}_0} + \frac{|\boldsymbol{x}_a - \boldsymbol{r}|}{\mathrm{c}_0} + \frac{L_m}{\mathrm{c}_0}\right)} \\ & \times \left(\cos\left(kL_m\right) - \cos\left(kL_m\cos\psi_m\right)\right). \end{aligned} \tag{3.108}$$

Narrowband Assumption

As an aside we recall from [80] the definition of a narrowband signal. We define the upper and lower frequencies of the passband of the power spectral density of a signal as f_{U} and f_{L}. A signal is considered narrowband if the fractional bandwidth

$$B_{\mathrm{F}} = \frac{f_{\mathrm{U}} - f_{\mathrm{L}}}{(f_{\mathrm{U}} + f_{\mathrm{L}})/2}$$

is between 0 and 0.01. We observe that in simulations utilizing an X-band waveform with 10GHz carrier frequency can have a fractional bandwidth of nearly 100 MHz and still be considered narrowband.

We can alternately obtain the frequency domain version of (3.105) after making the narrowband assumption. We assume that the transmit waveform $s_m(\cdot)$ is narrowband and can be rewritten as

$$s_m(t) = \tilde{s}_m(t)\mathrm{e}^{-\mathrm{i}\omega_m t}$$

where $\tilde{s}_m(t)$ is slowly varying with respect to t and ω_m is the carrier frequency of

the transmit waveform. Then (3.105) becomes

$$\begin{aligned}\mathcal{F}\{s_m(\cdot)\} =&\mathcal{F}\left\{\tilde{s}_m\left(t-\frac{|\boldsymbol{r}_m|}{\mathrm{c}_0}-\frac{|\boldsymbol{x}_a-\boldsymbol{r}|}{\mathrm{c}_0}-\frac{L_m}{\mathrm{c}_0}\right)\mathrm{e}^{-\mathrm{i}\omega_m\left(\alpha t-\frac{|\boldsymbol{r}_m|}{\mathrm{c}_0}-\frac{|\boldsymbol{x}_a-\boldsymbol{r}|}{\mathrm{c}_0}-\frac{L_m}{\mathrm{c}_0}\right)}\right\}\\ =&\tilde{S}_m\left(\omega-\alpha\omega_m\right)\mathrm{e}^{\mathrm{i}(\omega+(1-\alpha)\omega_m)\left(\frac{|\boldsymbol{r}_m|}{\mathrm{c}_0}+\frac{|\boldsymbol{x}_a-\boldsymbol{r}|}{\mathrm{c}_0}+\frac{L_m}{\mathrm{c}_0}\right)}\end{aligned} \tag{3.109}$$

If we make the narrowband assumption the expression for the scattered field becomes

$$\begin{aligned}\boldsymbol{E}_m^{\mathrm{r}}(\boldsymbol{r},\omega) =&\frac{V_{0,m}\boldsymbol{p}_m^{\mathrm{r}}\tilde{S}_m\left(\omega-\alpha\omega_m\right)}{2(4\pi)|\boldsymbol{r}_m||\boldsymbol{x}_a-\boldsymbol{r}|\ln(2L_m/a_m)\sin\psi_m}\mathrm{e}^{\mathrm{i}(\omega+(1-\alpha)\omega_m)\left(\frac{|\boldsymbol{r}_m|}{\mathrm{c}_0}+\frac{|\boldsymbol{x}_a-\boldsymbol{r}|}{\mathrm{c}_0}+\frac{L_m}{\mathrm{c}_0}\right)}\\ &\times\left(\cos\left(kL_m\right)-\cos\left(kL_m\cos\psi_m\right)\right).\end{aligned} \tag{3.110}$$

3.4.6 Reception

We will now model reception of the scattered electric field on the n^{th} dipole receiver located at $\boldsymbol{x}_{\mathrm{R},n}$ and with polarization $\hat{\boldsymbol{p}}_n$ given in the basis of the receive antenna. By the general Lorentz reciprocity theorem, the open current received voltage at the n^{th} receiver is given by

$$V_{mn}^{\mathrm{r}}(\omega)=\boldsymbol{E}_m^{\mathrm{r}}\left(\boldsymbol{x}_{\mathrm{R},n},\omega\right)\cdot\boldsymbol{H}_{\perp,n} \tag{3.111}$$

where $\boldsymbol{H}_{\perp,n}$ is the perpendicular component of the effective vector height of the n^{th} dipole $\boldsymbol{H}_n$ [66, 72, 81].

The effective vector height is related to the radiation vector, previously defined for a thin dipole in section 3.4.4, by

$$\boldsymbol{H}_{\perp}=-\frac{\boldsymbol{F}_{\perp}}{I_{\mathrm{in}}} \tag{3.112}$$

where I_{in} is the input current to the antenna terminals [40, 72, 82]. We again assume a matched antenna system and define the input current of the n^{th} dipole by substituting $z=0$ into the modified current distribution for a long thin dipole (3.91)

$$I_{\mathrm{in},n}=-\frac{\mathrm{i}\pi V_{0,n}S_n\left(\omega\right)}{\ln(2L_n/a_n)\mu_0\mathrm{c}_0}\sin(kL_n)\mathrm{e}^{\mathrm{i}kL_n}. \tag{3.113}$$

We can write the transverse radiation vector, $\boldsymbol{H}_{\perp,n}$, in terms of a scalar reception pattern and the polarization of the dipole just as was done with the radiation vector in (3.93)

$$\boldsymbol{H}_{\perp,n}(\psi_n,\omega) = H_n(\psi_n,\omega)\hat{\boldsymbol{p}}_n \tag{3.114}$$

where

$$H_n(\psi_n,\omega) = \frac{2}{k\sin(kL_n)}\left(\frac{\cos(kL_n)-\cos(kL_n\cos\psi_n)}{\sin\psi_n}\right) \tag{3.115}$$

is the scalar reception pattern obtained by substituting (3.92) and (3.113) into (3.112) and taking the scalar portion,

$$\psi_n = \arccos\left(|\hat{\boldsymbol{r}}_n\cdot\hat{\boldsymbol{e}}_n|\right),$$

and $\hat{\boldsymbol{e}}_n$ is the orientation of the receive dipole. Substituting (3.114) into (3.111) we obtain

$$V^{\mathrm{r}}_{mn}(\omega) = \frac{2}{k\sin(kL_n)}\left(\frac{\cos(kL_n)-\cos(kL_n\cos\psi_n)}{\sin\psi_n}\right)\hat{\boldsymbol{p}}_n\cdot\boldsymbol{E}^{\mathrm{r}}_m\left(\boldsymbol{x}_{\mathrm{R},n},\omega\right). \tag{3.116}$$

Time Domain Received Voltage as a Function of $\boldsymbol{\mathcal{E}}^{\mathrm{r}}_m(\boldsymbol{r},t)$

We can obtain the time domain received voltage in terms of the scattered electric field, $\boldsymbol{\mathcal{E}}^{\mathrm{r}}_m(\boldsymbol{r},t)$, in (3.103) by inverse Fourier transform using $\mathcal{F}^{-1}\{\boldsymbol{E}^{\mathrm{r}}_m\left(\boldsymbol{x}_{\mathrm{R},n},\omega\right)\} = \boldsymbol{\mathcal{E}}^{\mathrm{r}}_m(\boldsymbol{r},t)$

$$\begin{aligned} v^{\mathrm{r}}_{mn}(t) =& \frac{1}{2\pi}\int V^{\mathrm{r}}_{mn}(\omega)\mathrm{e}^{-\mathrm{i}\omega t}\mathrm{d}\omega \\ =& \mathcal{F}^{-1}\left\{V^{\mathrm{r}}_{mn}(\omega)\right\} \\ =& \frac{2\mathrm{c}_0\hat{\boldsymbol{p}}_n}{\sin\psi_n}\cdot\mathcal{F}^{-1}\left\{\boldsymbol{E}^{\mathrm{r}}_m\left(\boldsymbol{x}_{\mathrm{R},n},\omega\right)\frac{1}{\omega\sin(kL_n)}\left(\cos(kL_n)-\cos(kL_n\cos\psi_n)\right)\right\}. \end{aligned} \tag{3.117}$$

We continue the derivation of the time domain received voltage by writing the inverse Fourier transform term as a convolution of two inverse Fourier transformed

terms, one known and one to be determined,

$$\begin{aligned} v^{\mathrm{r}}_{mn}(t) =& \frac{2\mathrm{c}_0\hat{\boldsymbol{p}}_n}{\sin\psi_n} \cdot \left[\mathcal{F}^{-1}\left\{ \boldsymbol{E}^{\mathrm{r}}_m\left(\boldsymbol{x}_{\mathrm{R},n},\omega\right)\right\} * \mathcal{F}^{-1}\left\{ \frac{\cos\left(kL_n\right) - \cos\left(kL_n\cos\psi_n\right)}{\omega\sin(kL_n)} \right\} \right] \\ =& \frac{2\mathrm{c}_0\hat{\boldsymbol{p}}_n}{\sin\psi_n} \cdot \left[\boldsymbol{\mathcal{E}}^{\mathrm{r}}_m(\boldsymbol{x}_{\mathrm{R},n},t) * \mathcal{F}^{-1}\left\{ \frac{\cos\left(kL_n\right) - \cos\left(kL_n\cos\psi_n\right)}{\omega\sin(kL_n)} \right\} \right]. \end{aligned} \tag{3.118}$$

Observe that in (3.118) we have written the time domain received voltage as a convolution of the scattered electric field incident at $\boldsymbol{x}_{\mathrm{R},n}$, $\boldsymbol{\mathcal{E}}^{\mathrm{r}}_m(\boldsymbol{x}_{\mathrm{R},n},t)$, with the time dependent portion of the impulse response of the reception process. This impulse response is the inverse Fourier transform of the frequency dependent terms of the transfer function for the reception process. The frequency independent portion of the transfer function is still present in the impulse response and can be seen at the beginning of (3.118).

We find the inverse Fourier transform term in (3.118) using the residue theorem and Jordan's lemma. We take the real line indented below the simple poles from the denominator as the line of integration resulting in

$$\mathcal{F}^{-1}\left\{ \frac{\cos\left(kL_n\right) - \cos\left(kL_n\cos\psi_n\right)}{\omega\sin(kL_n)} \right\} = \frac{1}{2\pi\mathrm{i}} \sum_{\substack{p=-\infty \\ p\neq 0}}^{\infty} \frac{1}{p}\, \mathrm{e}^{-\mathrm{i}p\pi t\frac{\mathrm{c}_0}{L_n}} \left(1-(-1)^p\cos\left(p\pi\cos\psi_n\right)\right). \tag{3.119}$$

The details of this procedure can be found in Appendix C. Substituting our solution from (3.119) into (3.118) we obtain

$$v^{\mathrm{r}}_{mn}(t) = \frac{2\mathrm{c}_0\hat{\boldsymbol{p}}_n}{\sin\psi_n} \cdot \left[\boldsymbol{\mathcal{E}}^{\mathrm{r}}_m(\boldsymbol{x}_{\mathrm{R},n},t) * \frac{1}{2\pi\mathrm{i}} \sum_{\substack{p=-\infty \\ p\neq 0}}^{\infty} \frac{1}{p}\, \mathrm{e}^{-\mathrm{i}p\pi t\frac{\mathrm{c}_0}{L_n}} \left(1-(-1)^p\cos\left(p\pi\cos\psi_n\right)\right) \right]. \tag{3.120}$$

We now substitute our expression for $\boldsymbol{\mathcal{E}}^{\mathrm{r}}_m(\boldsymbol{r},t)$ from (3.103) with $\boldsymbol{r} = \boldsymbol{x}_{\mathrm{R},n}$ into

(3.120)

$$
\begin{aligned}
v^{\mathrm{r}}_{mn}(t) =& \frac{\mathrm{c}_0 \hat{\boldsymbol{p}}_n}{\pi \mathrm{i} \sin\psi_n} \cdot \Bigg[\frac{V_{0,m} \boldsymbol{p}^{\mathrm{r}}_m}{4(4\pi)|\boldsymbol{r}_m||\boldsymbol{r}_n| \ln(2L_m/a_m) \sin\psi_m} \\
& \times \Bigg[s_m \left(t - \frac{|\boldsymbol{r}_m|}{\mathrm{c}_0} - \frac{\hat{\boldsymbol{r}}_m \cdot \boldsymbol{v}_a t}{\mathrm{c}_0} - \frac{|\boldsymbol{r}_n|}{\mathrm{c}_0} - \frac{\hat{\boldsymbol{r}}_n \cdot \boldsymbol{v}_a t}{\mathrm{c}_0} \right) \\
& \quad + s_m \left(t - \frac{|\boldsymbol{r}_m|}{\mathrm{c}_0} - \frac{\hat{\boldsymbol{r}}_m \cdot \boldsymbol{v}_a t}{\mathrm{c}_0} - \frac{|\boldsymbol{r}_n|}{\mathrm{c}_0} \right. \\
& \qquad \left. - \frac{\hat{\boldsymbol{r}}_n \cdot \boldsymbol{v}_a t}{\mathrm{c}_0} - \frac{2L_m}{\mathrm{c}_0} \right) \\
& \quad - s_m \left(t - \frac{|\boldsymbol{r}_m|}{\mathrm{c}_0} - \frac{\hat{\boldsymbol{r}}_m \cdot \boldsymbol{v}_a t}{\mathrm{c}_0} - \frac{|\boldsymbol{r}_n|}{\mathrm{c}_0} \right. \\
& \qquad \left. - \frac{\hat{\boldsymbol{r}}_n \cdot \boldsymbol{v}_a t}{\mathrm{c}_0} - \frac{L_m}{\mathrm{c}_0}(1 - \cos\psi_m) \right) \\
& \quad - s_m \left(t - \frac{|\boldsymbol{r}_m|}{\mathrm{c}_0} - \frac{\hat{\boldsymbol{r}}_m \cdot \boldsymbol{v}_a t}{\mathrm{c}_0} - \frac{|\boldsymbol{r}_n|}{\mathrm{c}_0} \right. \\
& \qquad \left. - \frac{\hat{\boldsymbol{r}}_n \cdot \boldsymbol{v}_a t}{\mathrm{c}_0} - \frac{L_m}{\mathrm{c}_0}(1 + \cos\psi_m) \right) \Bigg] \\
& * \sum_{\substack{p=-\infty \\ p\neq 0}}^{\infty} \frac{1}{p} \, \mathrm{e}^{-\mathrm{i}p\pi t \frac{\mathrm{c}_0}{L_n}} \left(1 - (-1)^p \cos\left(p\pi \cos\psi_n\right)\right) \Bigg].
\end{aligned} \tag{3.121}
$$

We let

$$
\beta = \frac{(\hat{\boldsymbol{r}}_m + \hat{\boldsymbol{r}}_n) \cdot \boldsymbol{v}_a}{\mathrm{c}_0},
$$

$$
\gamma = \frac{|\boldsymbol{r}_m|}{\mathrm{c}_0} + \frac{|\boldsymbol{r}_n|}{\mathrm{c}_0},
$$

and $\boldsymbol{r}_n = \boldsymbol{x}_a - \boldsymbol{x}_{\mathrm{R},n}$ for the receiving dipole located at $\boldsymbol{x}_{\mathrm{R},n}$. We note that this β is the same as defined in Section 3.4.5 but with the position $\boldsymbol{x}_{\mathrm{R},n}$ substituted for $\boldsymbol{r}$ so that $\widehat{\boldsymbol{x}_a - \boldsymbol{r}}$ becomes $\hat{\boldsymbol{r}}_n = \widehat{\boldsymbol{x}_a - \boldsymbol{x}_{\mathrm{R},n}}$. We rewrite the sum of delayed transmit waveforms as a single delayed transmit waveform convolved with a sum of delta functions

$$
\begin{aligned}
v_{mn}^{\mathrm{r}}(t) =& \frac{\mathrm{c}_0 V_{0,m} \boldsymbol{p}_m^{\mathrm{r}} \cdot \hat{\boldsymbol{p}}_n}{(4\pi\mathrm{i})(4\pi)|\boldsymbol{r}_m||\boldsymbol{x}_a - \boldsymbol{r}| \ln(2L_m/a_m) \sin\psi_m \sin\psi_n} \\
& \times s_m\left((1-\beta)t - \gamma - \frac{L_m}{\mathrm{c}_0}\right) * \left[\delta\left(t + \frac{L_m}{\mathrm{c}_0}\right) + \delta\left(t - \frac{L_m}{\mathrm{c}_0}\right)\right. \\
& \left. -\delta\left(t + \frac{L_m}{\mathrm{c}_0}\cos\psi_m\right) - \delta\left(t - \frac{L_m}{\mathrm{c}_0}\cos\psi_m\right)\right] \\
& * \sum_{\substack{p=-\infty \\ p\neq 0}}^{\infty} \frac{1}{p} \mathrm{e}^{-\mathrm{i}p\pi t \frac{\mathrm{c}_0}{L_n}} \left(1 - (-1)^p \cos\left(p\pi\cos\psi_n\right)\right) \\
=& \frac{\mathrm{c}_0 V_{0,m} \boldsymbol{p}_m^{\mathrm{r}} \cdot \hat{\boldsymbol{p}}_n}{(4\pi\mathrm{i})(4\pi)|\boldsymbol{r}_m||\boldsymbol{x}_a - \boldsymbol{r}| \ln(2L_m/a_m) \sin\psi_m \sin\psi_n} \\
& \times s_m\left((1-\beta)t - \gamma - \frac{L_m}{\mathrm{c}_0}\right) \\
& * \sum_{\substack{p=-\infty \\ p\neq 0}}^{\infty} \frac{1}{p} \mathrm{e}^{-\mathrm{i}p\pi t \frac{\mathrm{c}_0}{L_n}} \left(1 - (-1)^p \cos\left(p\pi\cos\psi_n\right)\right) \\
& \times \left[\mathrm{e}^{-\mathrm{i}p\pi\frac{L_m}{L_n}} + \mathrm{e}^{\mathrm{i}p\pi\frac{L_m}{L_n}} - \mathrm{e}^{-\mathrm{i}p\pi\frac{L_m}{L_n}\cos\psi_m} - \mathrm{e}^{\mathrm{i}p\pi\frac{L_m}{L_n}\cos\psi_m}\right] \\
=& \frac{\mathrm{c}_0 V_{0,m} \boldsymbol{p}_m^{\mathrm{r}} \cdot \hat{\boldsymbol{p}}_n}{(2\pi\mathrm{i})(4\pi)|\boldsymbol{r}_m||\boldsymbol{x}_a - \boldsymbol{r}| \ln(2L_m/a_m) \sin\psi_m \sin\psi_n} \\
& \times s_m\left((1-\beta)t - \gamma - \frac{L_m}{\mathrm{c}_0}\right) \\
& * \sum_{\substack{p=-\infty \\ p\neq 0}}^{\infty} \frac{1}{p} \mathrm{e}^{-\mathrm{i}p\pi t \frac{\mathrm{c}_0}{L_n}} \left[\left(1 - (-1)^p \cos\left(p\pi\cos\psi_n\right)\right)\right. \\
& \left. \times \left(\cos\left(p\pi\frac{L_m}{L_n}\right) - \cos\left(p\pi\frac{L_m}{L_n}\cos\psi_m\right)\right)\right] \\
=& \frac{\mathrm{c}_0 V_{0,m} \boldsymbol{p}_m^{\mathrm{r}} \cdot \hat{\boldsymbol{p}}_n}{(2\pi\mathrm{i})(4\pi)|\boldsymbol{r}_m||\boldsymbol{x}_a - \boldsymbol{r}| \ln(2L_m/a_m) \sin\psi_m \sin\psi_n} \\
& \times \int_{-\infty}^{\infty} s_m\left((1-\beta)\tau - \gamma - \frac{L_m}{\mathrm{c}_0}\right) \\
& \times \sum_{\substack{p=-\infty \\ p\neq 0}}^{\infty} \frac{1}{p} \mathrm{e}^{-\mathrm{i}p\pi(t-\tau) \frac{\mathrm{c}_0}{L_n}} \left[\left(1 - (-1)^p \cos\left(p\pi\cos\psi_n\right)\right)\right. \\
& \left. \times \left(\cos\left(p\pi\frac{L_m}{L_n}\right) - \cos\left(p\pi\frac{L_m}{L_n}\cos\psi_m\right)\right)\right] \mathrm{d}\tau. \qquad (3.122)
\end{aligned}
$$

The physical significance of (3.122) can be partially understood by examining the

above derivation, particularly (3.121). It is clear that four time delayed versions of the transmit waveform are incident on the receive antenna. However, the reception process of the dipole, which is expected to mirror the radiation process by reciprocity, is hidden in this formulation. The physical interpretation of the received voltage will be explained in an aside in the next section.

Time Domain Received Voltage by Substituting $\boldsymbol{E}_m^{\mathrm{r}}(\boldsymbol{r},\omega)$

Alternatively we can obtain the frequency domain received voltage (3.122) by substituting the expression for the frequency domain scattered electric field, $\boldsymbol{E}_m^{\mathrm{r}}(\boldsymbol{r},\omega)$ (3.116), into (3.108). We choose not to make the narrowband assumption for generality and $V_{mn}^{\mathrm{r}}(\omega)$ becomes

$$\begin{aligned} V_{mn}^{\mathrm{r}}(\omega) =& \frac{V_{0,m} S_m\left((1+\beta)\omega\right) \boldsymbol{p}_m^{\mathrm{r}} \cdot \hat{\boldsymbol{p}}_n}{(4\pi) k |\boldsymbol{r}_m||\boldsymbol{r}_n| \ln(2L_m/a_m)} \mathrm{e}^{\mathrm{i}(1+\beta)\omega\left(\gamma+\frac{L_m}{\mathrm{c}_0}\right)} \frac{1}{\sin(kL_n)} \\ & \times \left(\frac{\cos\left(kL_m\right) - \cos\left(kL_m\cos\psi_m\right)}{\sin\psi_m}\right)\left(\frac{\cos\left(kL_n\right) - \cos\left(kL_n\cos\psi_n\right)}{\sin\psi_n}\right). \end{aligned} \tag{3.123}$$

We again obtain the time domain received voltage by inverse Fourier transform

$$\begin{aligned} v_{mn}^{\mathrm{r}}(t) =& \frac{1}{2\pi}\int V_{mn}^{\mathrm{r}}(\omega)\mathrm{e}^{-\mathrm{i}\omega t}\mathrm{d}\omega \\ =& \mathcal{F}^{-1}\left\{V_{mn}^{\mathrm{r}}(\omega)\right\} \\ =& \frac{\mathrm{c}_0 V_{0,m}\, \boldsymbol{p}_m^{\mathrm{r}} \cdot \hat{\boldsymbol{p}}_n}{(4\pi)|\boldsymbol{r}_m||\boldsymbol{r}_n| \ln(2L_m/a_m)\sin\psi_m \sin\psi_n} \mathcal{F}^{-1}\left\{\frac{1}{\omega} S_m\left((1+\beta)\omega\right) \mathrm{e}^{\mathrm{i}\omega(1+\beta)\left(\gamma+\frac{L_m}{\mathrm{c}_0}\right)}\right. \\ & \left. \times \frac{1}{\sin(kL_n)}\left(\cos\left(kL_m\right) - \cos\left(kL_m\cos\psi_m\right)\right)\left(\cos\left(kL_n\right) - \cos\left(kL_n\cos\psi_n\right)\right)\right\} \\ =& \frac{\mathrm{c}_0 V_{0,m}\, \boldsymbol{p}_m^{\mathrm{r}} \cdot \hat{\boldsymbol{p}}_n}{(4\pi)|\boldsymbol{r}_m||\boldsymbol{r}_n| \ln(2L_m/a_m)\sin\psi_m \sin\psi_n} \mathcal{F}^{-1}\left\{S_m\left((1+\beta)\omega\right) \mathrm{e}^{\mathrm{i}\omega(1+\beta)\left(\gamma+\frac{L_m}{\mathrm{c}_0}\right)}\right\} \\ & * \mathcal{F}^{-1}\left\{\frac{\left(\cos\left(kL_m\right) - \cos\left(kL_m\cos\psi_m\right)\right)\left(\cos\left(kL_n\right) - \cos\left(kL_n\cos\psi_n\right)\right)}{\omega\sin(kL_n)}\right\}. \end{aligned} \tag{3.124}$$

We next make a change of variables to find the first inverse Fourier transform term

$$\begin{aligned}\mathcal{F}^{-1}\left\{S_m\left((1+\beta)\omega\right)\mathrm{e}^{\mathrm{i}\omega(1+\beta)\left(\gamma+\frac{L_m}{\mathrm{c}_0}\right)}\right\} &= \frac{1}{1+\beta}s_m\left(\frac{t}{1+\beta}-\gamma-\frac{L_m}{\mathrm{c}_0}\right)\\ &\approx (1-\beta)s_m\left((1-\beta)t-\gamma-\frac{L_m}{\mathrm{c}_0}\right)\\ &\approx s_m\left((1-\beta)t-\gamma-\frac{L_m}{\mathrm{c}_0}\right)\end{aligned}$$

for small β and continue the derivation of $v_{mn}^{\mathrm{r}}(t)$

$$\begin{aligned}v_{mn}^{\mathrm{r}}(t) =& \frac{\mathrm{c}_0 V_{0,m}\,\boldsymbol{p}_m^{\mathrm{r}}\cdot\hat{\boldsymbol{p}}_n}{(4\pi)|\boldsymbol{r}_m||\boldsymbol{r}_n|\ln(2L_m/a_m)\sin\psi_m\sin\psi_n}s_m\left((1-\beta)t-\gamma-\frac{L_m}{\mathrm{c}_0}\right)\\ &* \mathcal{F}^{-1}\left\{\frac{\left(\cos\left(kL_m\right)-\cos\left(kL_m\cos\psi_m\right)\right)\left(\cos\left(kL_n\right)-\cos\left(kL_n\cos\psi_n\right)\right)}{\omega\sin(kL_n)}\right\}.\end{aligned} \tag{3.125}$$

Observe that in (3.125) we have again written the received voltage as a convolution, here a convolution of the time delayed transmit waveform $s_m(\cdot)$ with the time dependent portion of the impulse response of the combined radiation and reception processes. This impulse response is the inverse Fourier transform of the frequency dependent terms of the corresponding transfer function. We note that this impulse response does not completely relate the original transmit waveform $s_m(t)$ with the received voltage because the waveform in (3.125) is time delayed.

As an aside, we examine the physical interpretation of (3.125). We rewrite (3.125)

$$\begin{aligned}v_{mn}^{\mathrm{r}}(t) =& \frac{\mathrm{c}_0 V_{0,m}\,\boldsymbol{p}_m^{\mathrm{r}}\cdot\hat{\boldsymbol{p}}_n}{2(4\pi)|\boldsymbol{r}_m||\boldsymbol{r}_n|\ln(2L_m/a_m)\sin\psi_m\sin\psi_n}s_m\left((1-\beta)t-\gamma-\frac{L_m}{\mathrm{c}_0}\right)\\ &* \mathcal{F}^{-1}\Bigg\{\frac{\mathrm{i}}{\omega\left(\mathrm{e}^{\mathrm{i}\omega\frac{L_n}{\mathrm{c}_0}}-\mathrm{e}^{-\mathrm{i}\omega\frac{L_n}{\mathrm{c}_0}}\right)}\\ &\qquad\times\left(\mathrm{e}^{\mathrm{i}\omega\frac{L_m}{\mathrm{c}_0}}+\mathrm{e}^{-\mathrm{i}\omega\frac{L_m}{\mathrm{c}_0}}-\mathrm{e}^{\mathrm{i}\omega\frac{L_m}{\mathrm{c}_0}\cos\psi_m}-\mathrm{e}^{-\mathrm{i}\omega\frac{L_m}{\mathrm{c}_0}\cos\psi_m}\right)\\ &\qquad\times\left(\mathrm{e}^{\mathrm{i}\omega\frac{L_n}{\mathrm{c}_0}}+\mathrm{e}^{-\mathrm{i}\omega\frac{L_n}{\mathrm{c}_0}}-\mathrm{e}^{\mathrm{i}\omega\frac{L_n}{\mathrm{c}_0}\cos\psi_n}-\mathrm{e}^{-\mathrm{i}\omega\frac{L_n}{\mathrm{c}_0}\cos\psi_n}\right)\Bigg\}\end{aligned}$$

$$
\begin{aligned}
=&\frac{\mathrm{c}_0 V_{0,m}\,\boldsymbol{p}_m^{\mathrm{r}}\cdot\hat{\boldsymbol{p}}_n}{2(4\pi)|\boldsymbol{r}_m||\boldsymbol{r}_n|\ln(2L_m/a_m)\sin\psi_m\sin\psi_n}s_m\left((1-\beta)t-\gamma-\frac{L_m}{\mathrm{c}_0}\right)\\
&*\mathcal{F}^{-1}\Bigg\{\mathrm{e}^{\mathrm{i}\omega\frac{(L_m+L_n)}{\mathrm{c}_0}}+\mathrm{e}^{-\mathrm{i}\omega\frac{(L_m+L_n)}{\mathrm{c}_0}}+\mathrm{e}^{\mathrm{i}\omega\frac{(L_m-L_n)}{\mathrm{c}_0}}+\mathrm{e}^{\mathrm{i}\omega\frac{(-L_m+L_n)}{\mathrm{c}_0}}\\
&\qquad+\mathrm{e}^{\mathrm{i}\omega\frac{(L_m\cos\psi_m+L_n\cos\psi_n)}{\mathrm{c}_0}}+\mathrm{e}^{-\mathrm{i}\omega\frac{(L_m\cos\psi_m+L_n\cos\psi_n)}{\mathrm{c}_0}}\\
&\qquad+\mathrm{e}^{\mathrm{i}\omega\frac{(L_m\cos\psi_m-L_n\cos\psi_n)}{\mathrm{c}_0}}+\mathrm{e}^{\mathrm{i}\omega\frac{(-L_m\cos\psi_m+L_n\cos\psi_n)}{\mathrm{c}_0}}\\
&\qquad-\mathrm{e}^{\mathrm{i}\omega\frac{(L_m+L_n\cos\psi_n)}{\mathrm{c}_0}}-\mathrm{e}^{-\mathrm{i}\omega\frac{(L_m+L_n\cos\psi_n)}{\mathrm{c}_0}}-\mathrm{e}^{\mathrm{i}\omega\frac{(L_m-L_n\cos\psi_n)}{\mathrm{c}_0}}\\
&\qquad-\mathrm{e}^{\mathrm{i}\omega\frac{(-L_m+L_n\cos\psi_n)}{\mathrm{c}_0}}-\mathrm{e}^{\mathrm{i}\omega\frac{(L_m\cos\psi_m+L_n)}{\mathrm{c}_0}}-\mathrm{e}^{-\mathrm{i}\omega\frac{(L_m\cos\psi_m+L_n)}{\mathrm{c}_0}}\\
&\qquad-\mathrm{e}^{\mathrm{i}\omega\frac{(L_m\cos\psi_m-L_n)}{\mathrm{c}_0}}-\mathrm{e}^{\mathrm{i}\omega\frac{(-L_m\cos\psi_m+L_n)}{\mathrm{c}_0}}\Bigg\}\\
&*\mathcal{F}^{-1}\left\{\frac{\mathrm{i}}{\omega\left(\mathrm{e}^{\mathrm{i}\omega\frac{L_n}{\mathrm{c}_0}}-\mathrm{e}^{-\mathrm{i}\omega\frac{L_n}{\mathrm{c}_0}}\right)}\right\}\\
=&\frac{\mathrm{c}_0 V_{0,m}\,\boldsymbol{p}_m^{\mathrm{r}}\cdot\hat{\boldsymbol{p}}_n}{2(4\pi)|\boldsymbol{r}_m||\boldsymbol{r}_n|\ln(2L_m/a_m)\sin\psi_m\sin\psi_n}\int s_m\left((1-\beta)\tau-\gamma-\frac{L_m}{\mathrm{c}_0}\right)\\
&\times\Bigg[\delta\left(\tau-t+\frac{L_m}{\mathrm{c}_0}+\frac{L_n}{\mathrm{c}_0}\right)+\delta\left(\tau-t-\frac{L_m}{\mathrm{c}_0}-\frac{L_n}{\mathrm{c}_0}\right)\\
&\quad+\delta\left(\tau-t+\frac{L_m}{\mathrm{c}_0}-\frac{L_n}{\mathrm{c}_0}\right)+\delta\left(\tau-t-\frac{L_m}{\mathrm{c}_0}+\frac{L_n}{\mathrm{c}_0}\right)\\
&\quad+\delta\left(\tau-t+\frac{L_m}{\mathrm{c}_0}\cos\psi_m+\frac{L_n}{\mathrm{c}_0}\cos\psi_n\right)\\
&\quad+\delta\left(\tau-t-\frac{L_m}{\mathrm{c}_0}\cos\psi_m-\frac{L_n}{\mathrm{c}_0}\cos\psi_n\right)\\
&\quad+\delta\left(\tau-t+\frac{L_m}{\mathrm{c}_0}\cos\psi_m-\frac{L_n}{\mathrm{c}_0}\cos\psi_n\right)\\
&\quad+\delta\left(\tau-t-\frac{L_m}{\mathrm{c}_0}\cos\psi_m+\frac{L_n}{\mathrm{c}_0}\cos\psi_n\right)\\
&\quad-\delta\left(\tau-t+\frac{L_m}{\mathrm{c}_0}\cos\psi_m+\frac{L_n}{\mathrm{c}_0}\right)-\delta\left(\tau-t-\frac{L_m}{\mathrm{c}_0}\cos\psi_m-\frac{L_n}{\mathrm{c}_0}\right)\\
&\quad-\delta\left(\tau-t+\frac{L_m}{\mathrm{c}_0}\cos\psi_m-\frac{L_n}{\mathrm{c}_0}\right)-\delta\left(\tau-t-\frac{L_m}{\mathrm{c}_0}\cos\psi_m+\frac{L_n}{\mathrm{c}_0}\right)\\
&\quad-\delta\left(\tau-t+\frac{L_m}{\mathrm{c}_0}+\frac{L_n}{\mathrm{c}_0}\cos\psi_n\right)-\delta\left(\tau-t-\frac{L_m}{\mathrm{c}_0}-\frac{L_n}{\mathrm{c}_0}\cos\psi_n\right)\\
&\quad-\delta\left(\tau-t+\frac{L_m}{\mathrm{c}_0}-\frac{L_n}{\mathrm{c}_0}\cos\psi_n\right)-\delta\left(\tau-t-\frac{L_m}{\mathrm{c}_0}+\frac{L_n}{\mathrm{c}_0}\cos\psi_n\right)\Bigg]\mathrm{d}\tau
\end{aligned}
$$

$$
\begin{aligned}
&* \mathcal{F}^{-1}\left\{\frac{\mathrm{i}}{\omega\left(\mathrm{e}^{\mathrm{i}\omega\frac{L_n}{\mathrm{c}_0}}-\mathrm{e}^{-\mathrm{i}\omega\frac{L_n}{\mathrm{c}_0}}\right)}\right\}\\
=&\frac{\mathrm{c}_0 V_{0,m}\,\hat{\boldsymbol{p}}_n\cdot\boldsymbol{p}_m^{\mathrm{r}}}{(4\pi)^3|\boldsymbol{r}_m||\boldsymbol{r}_n|\ln(2L_m/a_m)\sin\psi_m\sin\psi_n}\left(s_m\left((1-\beta)t_1-\gamma-\frac{L_m}{\mathrm{c}_0}\right)+\ldots\right.\\
&+s_m\left((1-\beta)t_8-\gamma-\frac{L_m}{\mathrm{c}_0}\right)-s_m\left((1-\beta)t_9-\gamma-\frac{L_m}{\mathrm{c}_0}\right)-\ldots\\
&\left.-s_m\left((1-\beta)t_{16}-\gamma-\frac{L_m}{\mathrm{c}_0}\right)\right)\\
&* \mathcal{F}^{-1}\left\{\frac{\mathrm{i}}{\omega\left(\mathrm{e}^{\mathrm{i}\omega\frac{L_n}{\mathrm{c}_0}}-\mathrm{e}^{-\mathrm{i}\omega\frac{L_n}{\mathrm{c}_0}}\right)}\right\}
\end{aligned}
\tag{3.126}
$$

where

$$
\begin{aligned}
t_1&=t-\frac{L_m}{\mathrm{c}_0}-\frac{L_n}{\mathrm{c}_0} & t_9&=t-\frac{L_m}{\mathrm{c}_0}\cos\psi_m-\frac{L_n}{\mathrm{c}_0}\\
t_2&=t+\frac{L_m}{\mathrm{c}_0}+\frac{L_n}{\mathrm{c}_0} & t_{10}&=t+\frac{L_m}{\mathrm{c}_0}\cos\psi_m+\frac{L_n}{\mathrm{c}_0}\\
t_3&=t-\frac{L_m}{\mathrm{c}_0}+\frac{L_n}{\mathrm{c}_0} & t_{11}&=t-\frac{L_m}{\mathrm{c}_0}\cos\psi_m+\frac{L_n}{\mathrm{c}_0}\\
t_4&=t+\frac{L_m}{\mathrm{c}_0}-\frac{L_n}{\mathrm{c}_0} & t_{12}&=t+\frac{L_m}{\mathrm{c}_0}\cos\psi_m-\frac{L_n}{\mathrm{c}_0}\\
t_5&=t-\frac{L_m}{\mathrm{c}_0}\cos\psi_m-\frac{L_n}{\mathrm{c}_0}\cos\psi_n & t_{13}&=t-\frac{L_m}{\mathrm{c}_0}-\frac{L_n}{\mathrm{c}_0}\cos\psi_n\\
t_6&=t+\frac{L_m}{\mathrm{c}_0}\cos\psi_m+\frac{L_n}{\mathrm{c}_0}\cos\psi_n & t_{14}&=t+\frac{L_m}{\mathrm{c}_0}+\frac{L_n}{\mathrm{c}_0}\cos\psi_n\\
t_7&=t-\frac{L_m}{\mathrm{c}_0}\cos\psi_m+\frac{L_n}{\mathrm{c}_0}\cos\psi_n & t_{15}&=t-\frac{L_m}{\mathrm{c}_0}+\frac{L_n}{\mathrm{c}_0}\cos\psi_n\\
t_8&=t+\frac{L_m}{\mathrm{c}_0}\cos\psi_m-\frac{L_n}{\mathrm{c}_0}\cos\psi_n & t_{16}&=t+\frac{L_m}{\mathrm{c}_0}-\frac{L_n}{\mathrm{c}_0}\cos\psi_n,
\end{aligned}
\tag{3.127}
$$

$$
\beta=\frac{(\hat{\boldsymbol{r}}_m+\hat{\boldsymbol{r}}_n)\cdot\boldsymbol{v}_a}{\mathrm{c}_0},
$$

and

$$
\gamma=\frac{|\boldsymbol{r}_m|}{\mathrm{c}_0}+\frac{|\boldsymbol{r}_n|}{\mathrm{c}_0}.
$$

We leave the remaining inverse Fourier transform term in (3.126) in its current form. Examining this term, we observe that the complex inverse Fourier transform will have a double pole at $\omega=0$. This singularity is order 2 due to the $\sin(kL_n)$ term in

our choice of input current, I_{in}, in (3.112) in addition to the $1/\omega$ from $\boldsymbol{E}_m^{\text{r}}(\boldsymbol{x}_{\text{R},n},\omega)$. As in Appendix C, we can indent below this pole and find the contribution from the small arc of radius ϵ. We find that in the limit as $\epsilon \to 0$, the contribution goes to infinity and so we cannot continue to solve for the time domain received voltage. The complete time domain received voltage will be derived shortly in a more tractable formulation. However, the point of this aside has been to obtain a formulation of $v_{mn}^{\text{r}}(t)$ that can be interpreted physically. We observe that we obtain a summation of sixteen time delayed versions of the transmitted waveform. This intuitively makes sense for the chosen radiator, a long thin dipole, because, as we have shown in Section 3.4.4, using the zeroth order model for the current distribution on a long thin dipole results in the radiation of four distinct time delayed versions of the transmit waveform emanating from the feed point, an end of the dipole, or the feed point after reflection at one end of the dipole. After undergoing the scattering process described by the scattering matrix $[\boldsymbol{S}]_a$, each of these signals may be incident on either end of the receive dipole, the feed point, or may enter the feed point, travel to an end of the dipole and back to the feed, resulting in four received voltages from each radiated signal for a total of sixteen received voltages. The time delay of each term in (3.126) corresponds to one of the scenarios just described.

Now that we have developed some understanding of the physical significance of the received voltage we will continue our derivation. We find the remaining inverse Fourier transform term in (3.125) using the residue theorem and Jordan's lemma. As in (3.119), we take the real line indented below the simple poles from the denominator as the line of integration

$$\begin{aligned}
&\mathcal{F}^{-1}\left\{\frac{\left(\cos\left(kL_m\right)-\cos\left(kL_m\cos\psi_m\right)\right)\left(\cos\left(kL_n\right)-\cos\left(kL_n\cos\psi_n\right)\right)}{\omega\sin(kL_n)}\right\}\\
&=\frac{1}{2\pi\mathrm{i}}\sum_{\substack{p=-\infty\\p\neq 0}}^{\infty}\frac{1}{p}\,\mathrm{e}^{-\mathrm{i}p\pi t\frac{c_0}{L_n}}\Bigg[\left(1-(-1)^p\cos\left(p\pi\cos\psi_n\right)\right)\\
&\qquad\qquad\times\left(\cos\left(p\pi\frac{L_m}{L_n}\right)-\cos\left(p\pi\frac{L_m}{L_n}\cos\psi_m\right)\right)\Bigg].
\end{aligned}\tag{3.128}$$

The details of this procedure can also be found in Appendix C. Substituting our

solution from (3.128) into (3.125) we obtain

$$
\begin{aligned}
v^{\mathrm{r}}_{mn}(t) =& \frac{\mathrm{c}_0 V_{0,m}\, \boldsymbol{p}^{\mathrm{r}}_m \cdot \hat{\boldsymbol{p}}_n}{(4\pi)|\boldsymbol{r}_m||\boldsymbol{r}_n| \ln(2L_m/a_m) \sin\psi_m \sin\psi_n} s_m\left((1-\beta)t - \gamma - \frac{L_m}{\mathrm{c}_0}\right) \\
& * \frac{1}{2\pi \mathrm{i}} \sum_{\substack{p=-\infty \\ p\neq 0}}^{\infty} \frac{1}{p}\, \mathrm{e}^{-\mathrm{i}p\pi t \frac{\mathrm{c}_0}{L_n}} \Bigg[(1-(-1)^p \cos(p\pi \cos\psi_n)) \\
& \qquad \times \left(\cos\left(p\pi \frac{L_m}{L_n}\right) - \cos\left(p\pi \frac{L_m}{L_n}\cos\psi_m\right)\right)\Bigg] \\
=& \frac{\mathrm{c}_0 V_{0,m} \boldsymbol{p}^{\mathrm{r}}_m \cdot \hat{\boldsymbol{p}}_n}{(2\pi\mathrm{i})(4\pi)|\boldsymbol{r}_m||\boldsymbol{r}_n| \ln(2L_m/a_m) \sin\psi_m \sin\psi_n} \\
& \times \int_{-\infty}^{\infty} s_m\left((1-\beta)\tau - \gamma - \frac{L_m}{\mathrm{c}_0}\right) \\
& \qquad \times \sum_{\substack{p=-\infty \\ p\neq 0}}^{\infty} \frac{1}{p}\, \mathrm{e}^{-\mathrm{i}p\pi(t-\tau)\frac{\mathrm{c}_0}{L_n}} \Bigg[(1-(-1)^p \cos(p\pi \cos\psi_n)) \\
& \qquad\qquad \times \left(\cos\left(p\pi \frac{L_m}{L_n}\right) - \cos\left(p\pi \frac{L_m}{L_n}\cos\psi_m\right)\right)\Bigg] \mathrm{d}\tau
\end{aligned} \tag{3.129}
$$

with

$$\beta = \frac{(\hat{\boldsymbol{r}}_m + \hat{\boldsymbol{r}}_n)\cdot \boldsymbol{v}_a}{\mathrm{c}_0}$$

and

$$\gamma = \frac{|\boldsymbol{r}_m|}{\mathrm{c}_0} + \frac{|\boldsymbol{r}_n|}{\mathrm{c}_0}.$$

We observe that (3.129) is identical to (3.122), as expected.

Narrowband Assumption

We next rewrite expression (3.129) under the narrowband assumption. As in section 3.4.5 we assume that the transmit waveform $s_m(\cdot)$ is narrowband and can be rewritten as

$$s_m(t) = \tilde{s}_m(t)\mathrm{e}^{-\mathrm{i}\omega_m t}$$

where $\tilde{s}_m(t)$ is slowly varying with respect to t and ω_m is the carrier frequency of the transmit waveform. Then (3.129) becomes

$$\begin{aligned} v_{mn}^{\mathrm{r,\,NB}}(t) = & \frac{\mathrm{c}_0 V_{0,m} \boldsymbol{p}_m^{\mathrm{r}} \cdot \hat{\boldsymbol{p}}_n}{(2\pi\mathrm{i})(4\pi)|\boldsymbol{r}_m||\boldsymbol{r}_n| \ln(2L_m/a_m) \sin\psi_m \sin\psi_n} \\ & \times \int_{-\infty}^{\infty} \tilde{s}_m \left(\tau - \gamma - \frac{L_m}{\mathrm{c}_0} \right) \mathrm{e}^{-\mathrm{i}\omega_m \left((1-\beta)\tau - \gamma - \frac{L_m}{\mathrm{c}_0} \right)} \\ & \quad \times \sum_{\substack{p=-\infty \\ p\neq 0}}^{\infty} \frac{1}{p} \mathrm{e}^{-\mathrm{i}p\pi(t-\tau)\frac{\mathrm{c}_0}{L_n}} \Bigg[\left(1 - (-1)^p \cos\left(p\pi \cos\psi_n\right)\right) \\ & \quad\quad \times \left(\cos\left(p\pi \frac{L_m}{L_n} \right) - \cos\left(p\pi \frac{L_m}{L_n} \cos\psi_m \right) \right) \Bigg] \mathrm{d}\tau. \end{aligned} \tag{3.130}$$

3.5 Image Formation

The goal of the imaging operation is to determine the distribution of three-dimensional positions and three-dimensional velocities corresponding to targets in the scene. Consequently, the full dimensional case image is formed in six-dimensional phase space. The resulting image will also allow us to examine the angle dependent scattering response of these targets and the transformation of transmit waveforms caused by the chosen radiators.

We let $\boldsymbol{x}_h$ and $\boldsymbol{v}_h$ denote a hypothetical position and velocity, respectively, and the a subscripts in $\boldsymbol{x}_a$ and $\boldsymbol{v}_a$ now denote a true location and velocity. Then time domain received voltage, as given by (3.129), from the n^{th} receiver corresponding to the signal radiated from the m^{th} transmitter and scattered by a true target at position $\boldsymbol{x}_a$ with velocity $\boldsymbol{v}_a$ and angle dependent scattering matrix $[\boldsymbol{S}]_a$ can be

rewritten

$$\begin{aligned} v^{\mathrm{r}}_{mn}(t,\boldsymbol{x}_a,\boldsymbol{v}_a) =& \frac{([\boldsymbol{S}]_a\hat{\boldsymbol{p}}_m)\cdot\hat{\boldsymbol{p}}_n}{\ln(2L_m/a_m)\sin\psi_m\sin\psi_n}\frac{\mathrm{c}_0 V_{0,m}}{(2\pi\mathrm{i})(4\pi)|\boldsymbol{r}^a_m||\boldsymbol{r}^a_n|} \\ &\times\int_{-\infty}^{\infty} s_m\left((1-\beta^a)\tau-\gamma^a-\frac{L_m}{\mathrm{c}_0}\right) \\ &\quad\times\sum_{\substack{p=-\infty\\ p\neq 0}}^{\infty}\frac{1}{p}\,\mathrm{e}^{-\mathrm{i}p\pi(t-\tau)\frac{\mathrm{c}_0}{L_n}}\Bigg[(1-(-1)^p\cos(p\pi\cos\psi_n)) \\ &\qquad\times\left(\cos\left(p\pi\frac{L_m}{L_n}\right)-\cos\left(p\pi\frac{L_m}{L_n}\cos\psi_m\right)\right)\Bigg]\mathrm{d}\tau \\ =& R^a_{mn}Q_{mn}(t,\boldsymbol{x}_a,\boldsymbol{v}_a) \end{aligned} \tag{3.131}$$

where

$$R^a_{mn}=\frac{V_{0,m}}{(4\pi)|\boldsymbol{r}^a_m||\boldsymbol{r}^a_n|\ln(2L_m/a_m)\sin\psi_m\sin\psi_n}$$

and

$$\begin{aligned} Q_{mn}(t,\boldsymbol{x}_a,\boldsymbol{v}_a) =& \frac{([\boldsymbol{S}]_a\hat{\boldsymbol{p}}_m)^{\mathrm{T}}\hat{\boldsymbol{p}}_n}{2\pi\mathrm{i}}\int_{-\infty}^{\infty} s_m\left((1-\beta^a)\tau-\gamma^a-\frac{L_m}{\mathrm{c}_0}\right) \\ &\times\sum_{\substack{p=-\infty\\ p\neq 0}}^{\infty}\frac{\mathrm{c}_0}{p}\,\mathrm{e}^{-\mathrm{i}p\pi(t-\tau)\frac{\mathrm{c}_0}{L_n}}\Bigg[(1-(-1)^p\cos(p\pi\cos\psi_n)) \\ &\times\left(\cos\left(p\pi\frac{L_m}{L_n}\right)-\cos\left(p\pi\frac{L_m}{L_n}\cos\psi_m\right)\right)\Bigg]\mathrm{d}\tau. \end{aligned} \tag{3.132}$$

We note that we will now explicitly include the parameters $\boldsymbol{x}_a$ and $\boldsymbol{v}_a$ in $v^{\mathrm{r}}_{mn}(t,\boldsymbol{x}_a,\boldsymbol{v}_a)$ so that it may be distinguished from $v^{\mathrm{r}}_{mn}(t,\boldsymbol{x}_h,\boldsymbol{v}_h)$. Likewise we add the superscript h to $\boldsymbol{r}^a_m=\boldsymbol{x}_a-\boldsymbol{x}_{\mathrm{T},m}$ and $\boldsymbol{r}^a_n=\boldsymbol{x}_a-\boldsymbol{x}_{\mathrm{R},n}$ to distinguish the quantities from $\boldsymbol{r}^h_m=\boldsymbol{x}_h-\boldsymbol{x}_{\mathrm{T},m}$ and $\boldsymbol{r}^h_n=\boldsymbol{x}_h-\boldsymbol{x}_{\mathrm{R},n}$ and

$$\beta^a=\frac{(\hat{\boldsymbol{r}}^a_m+\hat{\boldsymbol{r}}^a_n)\cdot\boldsymbol{v}_a}{\mathrm{c}_0}$$

and

$$\gamma^a=\frac{|\boldsymbol{r}^a_m|}{\mathrm{c}_0}+\frac{|\boldsymbol{r}^a_n|}{\mathrm{c}_0}.$$

At this time we will also define $s_{mn}(t, \boldsymbol{x}_h, \boldsymbol{v}_h)$, the time-delayed, Doppler-scaled version of the transmitted waveform corresponding to a target at position $\boldsymbol{x}_h$ with velocity $\boldsymbol{v}_h$ so that

$$s_{mn}(t, \boldsymbol{x}_h, \boldsymbol{v}_h) = s_m\left((1-\beta^h)t - \gamma^h\right) \tag{3.133}$$

where $s_m(t)$ is the waveform emitted by the m^{th} transmitter. Observe that this waveform does not have the L_m/c_0 delay present in the waveform in (3.132). This delay corresponds to the time that it takes for the signal to travel from the feed point of the antenna to either end and is specific to the chosen radiator. We will use this notation in the following description of the imaging process.

We let $q(\boldsymbol{x}_a, \boldsymbol{v}_a)$ denote the true distribution of point-like scatterers in position and velocity and as in [11–16], we construct an image $I(\boldsymbol{x}_h, \boldsymbol{v}_h)$ as an approximation to $q(\boldsymbol{x}_a, \boldsymbol{v}_a)$. The scattering matrix $[\boldsymbol{S}]_a$ describes the scattering behavior for a point-like target at position $\boldsymbol{x}_a$ and velocity $\boldsymbol{v}_a$ in the distribution $q(\boldsymbol{x}_a, \boldsymbol{v}_a)$.

We will approach image formation under two sets of assumptions: first the received data is assumed separable so that the contributions emanating from each transmitter can be distinguished and next the total received data at each receiver must be treated as a unit. While the former scenario is more desirable, because the contribution from each bistatic pair of a transmitter and receiver can be examined independently and weighted, the later scenario more closely approximates reality. In general, a receiver in a multistatic system will receive a superposition of transformed versions of the waveforms from each transmitter and would only be able to deal with individual bistatic pairs if the signals can be separated through preprocessing, which may not be possible. However, if the transmitted waveforms are distributed in frequency or are coded in a way that makes the signals separable, then the first approach may be possible and the added flexibility of dealing with bistatic pairs makes this approach worthy of investigation.

Narrowband Assumption

If the narrowband assumption is made and we use the expression for the time

domain received voltage in (3.130) then

$$v_{mn}^{\mathrm{r,\,NB}}(t,\boldsymbol{x}_a,\boldsymbol{v}_a) = R_{mn}^{a} Q_{mn}^{\mathrm{NB}}(t,\boldsymbol{x}_a,\boldsymbol{v}_a) \tag{3.134}$$

with

$$\begin{aligned} Q_{mn}^{\mathrm{NB}}(t,\boldsymbol{x}_a,\boldsymbol{v}_a) = \frac{([\boldsymbol{S}]_a\hat{\boldsymbol{p}}_m)^{\mathrm{T}}\hat{\boldsymbol{p}}_n}{2\pi\mathrm{i}} \int_{-\infty}^{\infty} \tilde{s}_m\left(\tau-\gamma^a-\frac{L_m}{\mathrm{c}_0}\right) \mathrm{e}^{-\mathrm{i}\omega_m\left((1-\beta^a)\tau-\gamma^a-\frac{L_m}{\mathrm{c}_0}\right)} \\ \times \sum_{\substack{p=-\infty \\ p\neq 0}}^{\infty} \frac{\mathrm{c}_0}{p}\,\mathrm{e}^{-\mathrm{i}p\pi(t-\tau)\frac{\mathrm{c}_0}{L_n}} \Bigg[\left(1-(-1)^p\cos\left(p\pi\cos\psi_n\right)\right) \\ \times \left(\cos\left(p\pi\frac{L_m}{L_n}\right)-\cos\left(p\pi\frac{L_m}{L_n}\cos\psi_m\right)\right)\Bigg]\mathrm{d}\tau. \end{aligned} \tag{3.135}$$

Frequency Sensitive Scattering Matrix

If the scattering behavior of the target varies over the bandwidth of the transmitted waveform then we cannot take the term $([\boldsymbol{S}]_a\hat{\boldsymbol{p}}_m)^{\mathrm{T}}\hat{\boldsymbol{p}}_n$ outside the inverse Fourier transform to find the time domain received voltage as in Section 3.4.6. The expression for the time domain received voltage is then given by

$$v_{mn}^{\mathrm{r,FS}}(t,\boldsymbol{x}_a,\boldsymbol{v}_a) = R_{mn}^{a} Q_{mn}^{\mathrm{FS}}(t,\boldsymbol{x}_a,\boldsymbol{v}_a) \tag{3.136}$$

with

$$\begin{aligned} Q_{mn}^{\mathrm{FS}}(t,\boldsymbol{x}_a,\boldsymbol{v}_a) = \mathcal{F}^{-1}\Bigg\{ \frac{([\boldsymbol{S}]_a\hat{\boldsymbol{p}}_m)^{\mathrm{T}}\hat{\boldsymbol{p}}_n}{k\sin(kL_n)} S_m\left((1+\beta^a)\omega\right)\mathrm{e}^{\mathrm{i}\omega(1+\beta^a)\left(\gamma^a+\frac{L_m}{\mathrm{c}_0}\right)} \\ \times \Bigg[\left(\cos\left(kL_m\right)-\cos\left(kL_m\cos\psi_m\right)\right) \\ \times \left(\cos\left(kL_n\right)-\cos\left(kL_n\cos\psi_n\right)\right)\Bigg]\Bigg\}. \end{aligned} \tag{3.137}$$

In this case (3.137) cannot be further simplified without knowledge of the specific frequency dependence of the scattering matrix $[\boldsymbol{S}]_a$.

3.5.1 Contributions from each Transmitter Assumed Separable

In this section we assume that some preprocessing has been done to the data from each receiver so that the contributions from each transmitter are known. As discussed above, the transmit waveforms would need to be specially designed in this scenario and knowledge of the transmit waveforms and positions of each transmit and receive antenna would be beneficial if not necessary. This is the assumption made in [11–16].

The time domain data from the n^{th} receiver corresponding to the signal radiated from the m^{th} transmitter and scattered by a true target at position $\boldsymbol{x}_a$ with velocity $\boldsymbol{v}_a$ and angle dependent scattering matrix $[\boldsymbol{S}]_a$ is written in terms of the time domain received voltage as

$$\begin{aligned} d_{mn}(t, \boldsymbol{x}_a, \boldsymbol{v}_a) &= \int v^{\text{r}}_{mn}(t, \boldsymbol{x}_a, \boldsymbol{v}_a) q(\boldsymbol{x}_a, \boldsymbol{v}_a) \, \mathrm{d}\boldsymbol{x}_a \mathrm{d}\boldsymbol{v}_a \\ &= \int R^a_{mn} Q_{mn}(t, \boldsymbol{x}_a, \boldsymbol{v}_a) q(\boldsymbol{x}_a, \boldsymbol{v}_a) \, \mathrm{d}\boldsymbol{x}_a \mathrm{d}\boldsymbol{v}_a. \end{aligned}$$

We can then write the data in terms of a forward operator

$$\mathcal{P} : (q(\boldsymbol{x}_a, \boldsymbol{v}_a), [\boldsymbol{S}]_a) \rightarrow d_{mn}(t, \boldsymbol{x}_a, \boldsymbol{v}_a) \tag{3.138}$$

that describes the transformation from the distribution of targets $q(\boldsymbol{x}_a, \boldsymbol{v}_a)$ and corresponding scattering matrices $[\boldsymbol{S}]_a$ to the received data $d_{mn}(t, \boldsymbol{x}_a, \boldsymbol{v}_a)$. Image formation involves applying an approximate inverse of the forward operator to the received data

$$\mathcal{P}^{-1} : d_{mn}(t, \boldsymbol{x}_a, \boldsymbol{v}_a) \rightarrow I(\boldsymbol{x}_h, \boldsymbol{v}_h). \tag{3.139}$$

As in [11–14, 35], this is done by taking the inner product of the received data, $d_{mn}(t, \boldsymbol{x}_a, \boldsymbol{v}_a)$, with a version of the transmit waveform $s_{mn}(t, \boldsymbol{x}_h, \boldsymbol{v}_h)$ corresponding to a hypothetical location and velocity. We recall that the complex inner product, $< \cdot, \cdot >$, is given by

$$< f, g >= \int f(x) g^*(x) \, \mathrm{d}x.$$

The output from each bistatic pair is then weighted and summed under the as-

sumption that the system is coherent, that there is a common clock available to all transmitters and receivers.

We write the resulting image as

$$\begin{aligned} I(\boldsymbol{x}_h, \boldsymbol{v}_h) &= \sum_m \sum_n W_{mn} \int s^*_{mn}(t, \boldsymbol{x}_h, \boldsymbol{v}_h) d_{mn}(t, \boldsymbol{x}_a, \boldsymbol{v}_a)\, \mathrm{d}t \\ &= \sum_m \sum_n W_{mn} \int s^*_{mn}(t, \boldsymbol{x}_h, \boldsymbol{v}_h) \int R^a_{mn} Q_{mn}(t, \boldsymbol{x}_a, \boldsymbol{v}_a) q(\boldsymbol{x}_a, \boldsymbol{v}_a)\, \mathrm{d}\boldsymbol{x}_a \mathrm{d}\boldsymbol{v}_a\, \mathrm{d}t \\ &= \int \left[\sum_m \sum_n W_{mn} R^a_{mn} \int Q_{mn}(t, \boldsymbol{x}_a, \boldsymbol{v}_a) s^*_{mn}(t, \boldsymbol{x}_h, \boldsymbol{v}_h)\, \mathrm{d}t \right] \\ &\qquad \times q(\boldsymbol{x}_a, \boldsymbol{v}_a)\, \mathrm{d}\boldsymbol{x}_a \mathrm{d}\boldsymbol{v}_a \\ &= \int K(\boldsymbol{x}_h, \boldsymbol{v}_h; \boldsymbol{x}_a, \boldsymbol{v}_a) q(\boldsymbol{x}_a, \boldsymbol{v}_a)\, \mathrm{d}\boldsymbol{x}_a \mathrm{d}\boldsymbol{v}_a \end{aligned} \tag{3.140}$$

where the point-spread function, $K(\cdot)$, is given by

$$\begin{aligned} K(\boldsymbol{x}_h, \boldsymbol{v}_h; \boldsymbol{x}_a, \boldsymbol{v}_a) &= \sum_m \sum_n W_{mn} R^a_{mn} \int Q_{mn}(t, \boldsymbol{x}_a, \boldsymbol{v}_a) s^*_{mn}(t, \boldsymbol{x}_h, \boldsymbol{v}_h)\, \mathrm{d}t \\ &= \sum_m \sum_n W_{mn} R^a_{mn} \mathcal{A}_{mn}(\boldsymbol{x}_h, \boldsymbol{v}_h; \boldsymbol{x}_a, \boldsymbol{v}_a) \end{aligned} \tag{3.141}$$

and as in Chapter 2 $\mathcal{A}_{mn}(\cdot)$ is an analog to the ambiguity function given by

$$\mathcal{A}_{mn}(\boldsymbol{x}_h, \boldsymbol{v}_h; \boldsymbol{x}_a, \boldsymbol{v}_a) = \int Q_{mn}(t, \boldsymbol{x}_a, \boldsymbol{v}_a) s^*_{mn}(t, \boldsymbol{x}_h, \boldsymbol{v}_h)\, \mathrm{d}t. \tag{3.142}$$

The image formed in (3.140) is the total image created by combining contributions from all transmit and receive polarizations, equivalent to adding the HH, HV, VH, and VV components from each receiver. We recall that the linear basis that defines the polarization of each transmitter and receiver is dependent on the location of the antenna. If there are multiple transmitters or receivers then it no longer makes sense to talk about the HH, for example, component of the image because there may be multiple contributions with horizontal transmit and receive polarization where horizontal polarization is defined differently at each antenna. If we wish to examine the HH, HV, VH, and VV components of an image individually then we use (3.140) but consider only the received data that has a single transmit and receive

polarization. Considering these components is more intuitive when there is a single transmitter and receiver.

If the system is not coherent, the magnitude must be taken of the output from each pair before summation, phase information will be lost, and (3.142) becomes

$$\mathcal{A}_{mn}(\boldsymbol{x}_h, \boldsymbol{v}_h; \boldsymbol{x}_a, \boldsymbol{v}_a) = \left| \int Q_{mn}(t, \boldsymbol{x}_a, \boldsymbol{v}_a) s^*_{mn}(t, \boldsymbol{x}_h, \boldsymbol{v}_h) \, \mathrm{d}t \right|. \tag{3.143}$$

3.5.2 Contributions from each Transmitter Assumed Nonseparable

In this section we assume that no preprocessing has been done to the data from each receiver so that the total received data at each receiver must be treated as a unit. This is the assumption made in the statistical MAF presented in Chapter 2 and in [4, 5, 15, 20, 83–85].

The total time domain data from the n^{th} receiver corresponding to the signal radiated from all transmitters and scattered by a true target at position $\boldsymbol{x}_a$ with velocity $\boldsymbol{v}_a$ and angle dependent scattering matrix $[\boldsymbol{S}]_a$ is written in terms of the time domain received voltage as

$$\begin{aligned} d_n(t, \boldsymbol{x}_a, \boldsymbol{v}_a) &= \int \sum_m v^{\mathrm{r}}_{mn}(t, \boldsymbol{x}_a, \boldsymbol{v}_a) q(\boldsymbol{x}_a, \boldsymbol{v}_a) \, \mathrm{d}\boldsymbol{x}_a \mathrm{d}\boldsymbol{v}_a \\ &= \int \sum_m R^a_{mn} Q_{mn}(t, \boldsymbol{x}_a, \boldsymbol{v}_a) q(\boldsymbol{x}_a, \boldsymbol{v}_a) \, \mathrm{d}\boldsymbol{x}_a \mathrm{d}\boldsymbol{v}_a. \end{aligned}$$

We can then write the data in terms of a forward operator similar to the operator defined in (3.138)

$$\tilde{\mathcal{P}} : (q(\boldsymbol{x}_a, \boldsymbol{v}_a), [\boldsymbol{S}]_a) \to d_n(t, \boldsymbol{x}_a, \boldsymbol{v}_a) \tag{3.144}$$

that describes the transformation from the distribution of targets $q(\boldsymbol{x}_a, \boldsymbol{v}_a)$ and corresponding scattering matrices $[\boldsymbol{S}]_a$ to the total received data $d_n(t, \boldsymbol{x}_a, \boldsymbol{v}_a)$. We again find an approximate inverse of the forward operator to the received data

$$\tilde{\mathcal{P}}^{-1} : d_n(t, \boldsymbol{x}_a, \boldsymbol{v}_a) \to \tilde{I}(\boldsymbol{x}_h, \boldsymbol{v}_h). \tag{3.145}$$

Observe the assumption that the transmitted signals are nonseparable results in a

slightly different image, denoted by $\tilde{I}(\boldsymbol{x}_h, \boldsymbol{v}_h)$. Under this assumption the image is formed by taking the inner product of the received data, $d_n(t, \boldsymbol{x}_a, \boldsymbol{v}_a)$, with a summation of versions of the transmit waveform from each transmitter $\sum_m s_{mn}(t, \boldsymbol{x}_h, \boldsymbol{v}_h)$ corresponding to a hypothetical location and velocity. The output from each receiver is then weighted and coherently summed. Note that it will now only be possible to weight the data from the individual receivers.

We write the resulting image as

$$\begin{aligned}
\tilde{I}(\boldsymbol{x}_h, \boldsymbol{v}_h) &= \sum_n W_n \int \left(\sum_m s_{mn}(t, \boldsymbol{x}_h, \boldsymbol{v}_h) \right)^* d_n(t, \boldsymbol{x}_a, \boldsymbol{v}_a) \, \mathrm{d}t \\
&= \sum_n W_n \int \left(\sum_m s_{mn}(t, \boldsymbol{x}_h, \boldsymbol{v}_h) \right)^* \\
&\qquad \times \int \sum_m R^a_{mn} Q_{mn}(t, \boldsymbol{x}_a, \boldsymbol{v}_a) q(\boldsymbol{x}_a, \boldsymbol{v}_a) \, \mathrm{d}\boldsymbol{x}_a \mathrm{d}\boldsymbol{v}_a \mathrm{d}t \\
&= \int \left[\sum_n W_n \int \left(\sum_m s_{mn}(t, \boldsymbol{x}_h, \boldsymbol{v}_h) \right)^* \right. \\
&\qquad \left. \times \left(\sum_m R^a_{mn} Q_{mn}(t, \boldsymbol{x}_a, \boldsymbol{v}_a) \right) \mathrm{d}t \right] q(\boldsymbol{x}_a, \boldsymbol{v}_a) \, \mathrm{d}\boldsymbol{x}_a \mathrm{d}\boldsymbol{v}_a \\
&= \int \tilde{K}(\boldsymbol{x}_h, \boldsymbol{v}_h; \boldsymbol{x}_a, \boldsymbol{v}_a) q(\boldsymbol{x}_a, \boldsymbol{v}_a) \, \mathrm{d}\boldsymbol{x}_a \mathrm{d}\boldsymbol{v}_a
\end{aligned} \tag{3.146}$$

where the point-spread function, $\tilde{K}(\cdot)$, is given by

$$\begin{aligned}
\tilde{K}(\boldsymbol{x}_h, \boldsymbol{v}_h; \boldsymbol{x}_a, \boldsymbol{v}_a) &= \sum_n W_n \int \left(\sum_m s_{mn}(t, \boldsymbol{x}_h, \boldsymbol{v}_h) \right)^* \left(\sum_m R^a_{mn} Q_{mn}(t, \boldsymbol{x}_a, \boldsymbol{v}_a) \right) \mathrm{d}t \\
&= \sum_n W_n \, \tilde{\mathcal{A}}_n(\boldsymbol{x}_h, \boldsymbol{v}_h; \boldsymbol{x}_a, \boldsymbol{v}_a)
\end{aligned} \tag{3.147}$$

and as in Chapter 2 $\tilde{\mathcal{A}}_n(\cdot)$ is an analog to the ambiguity function given by

$$\tilde{\mathcal{A}}_n(\boldsymbol{x}_h, \boldsymbol{v}_h; \boldsymbol{x}_a, \boldsymbol{v}_a) = \int \left(\sum_m s_{mn}(t, \boldsymbol{x}_h, \boldsymbol{v}_h) \right)^* \left(\sum_m R^a_{mn} Q_{mn}(t, \boldsymbol{x}_a, \boldsymbol{v}_a) \right) \mathrm{d}t. \tag{3.148}$$

The image formed in (3.146) is again the total image created by combining contri-

butions from all transmit and receive polarizations, equivalent to adding the HH, HV, VH, and VV components from each receiver.

If the system is not coherent (3.148) becomes

$$\tilde{\mathcal{A}}_n(\boldsymbol{x}_h, \boldsymbol{v}_h; \boldsymbol{x}_a, \boldsymbol{v}_a) = \left| \int \left(\sum_m s_{mn}(t, \boldsymbol{x}_h, \boldsymbol{v}_h) \right)^* \left(\sum_m R^a_{mn} Q_{mn}(t, \boldsymbol{x}_a, \boldsymbol{v}_a) \right) \mathrm{d}t \right|. \tag{3.149}$$

3.6 Simulations

In the following simulations we examine a scene of interest with a moving target under multiple transmitter and receiver configurations and polarization schemes. The simulation parameters, scenarios considered, and results for both separable and nonseparable transmitter contributions are offered in this section.

3.6.1 Simulation Parameters

We use a complex up-chirp and two 20-chip random polyphase codes with 10 GHz carrier frequency, 20 MHz sampling frequency, 50 μs pulse width, and 1 MHz bandwidth. The classical ambiguity functions (CAFs) for these waveforms are shown in Figures 3.11(a)-3.11(c). The ridge-like CAF with low range lobes of the up-chirp and thumbtack CAF with higher range side lobes shown in Figure 3.11 are evident in our simulations of the MAF for various geometries. We recall that these waveforms may be considered narrowband by the definition cited in section 3.4.5 and so in the following simulations we make the narrowband assumption and we use the time domain received voltage given by expression (3.134).

We assume that the antennas are half-wavelength dipoles with total length $2L = \lambda/2$. For a 10 GHz carrier frequency $\lambda = 3$ cm and so $L = 0.75$ cm and the total length is 1.5cm. We assume that that diameter of the dipole antenna is 0.75 mm, or $a = 0.375$ mm where the diameter is $2a$ and so the length of the dipole is 20 times its diameter. This roughly corresponds to 21 AWG wire.

Figure 3.12 shows the CAF of an up-chirp waveform with 10 GHz center frequency and 1 Mhz of bandwidth in 3.12(a), the CAF of this waveform after it has been radiated from the long thin dipole of half-wavelength length 1.5 cm in 3.12(b),

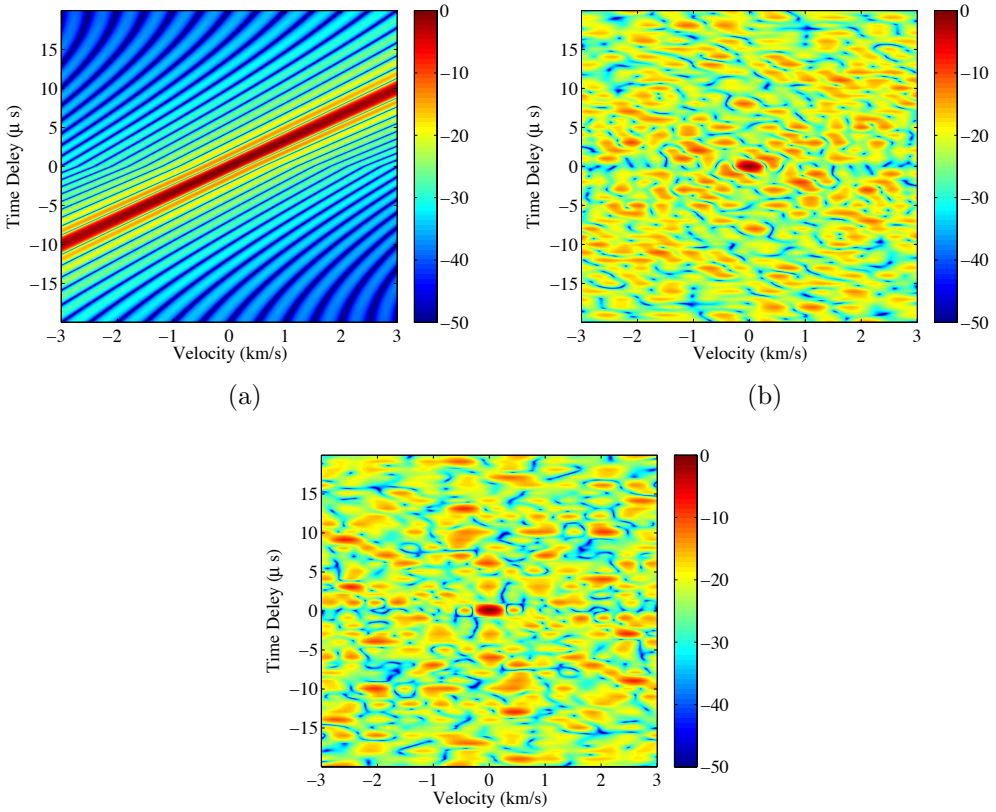

Figure 3.11: Classical ambiguity functions of an up-chirp, (a), and two 20 chip random polyphase codes, (b) and (c), plotted against velocity and time delay on a dB scale.

and the CAF of this waveform after it has been radiated and received on the same dipole in a monostatic set-up in 3.12(c). This corresponds to the same waveform shown in 3.11(a) and it is one of the waveforms used in simulations in this section. Clearly there is very little distortion from either radiation or radiation and reception of this narrowband waveform at this center frequency.

Figure 3.13 shows the CAF of an up-chirp waveform with 100 MHz center frequency and 1 Mhz of bandwidth in 3.13(a), the CAF of this waveform after it has been radiated from the long thin dipole of half-wavelength length 1.5 m in 3.13(b), and the CAF of this waveform after it has been radiated and received on the same dipole in a monostatic set-up in3.13(c). This waveform is just outside the limit of the narrowband definition given in Section 3.4.5 with a fractional bandwidth

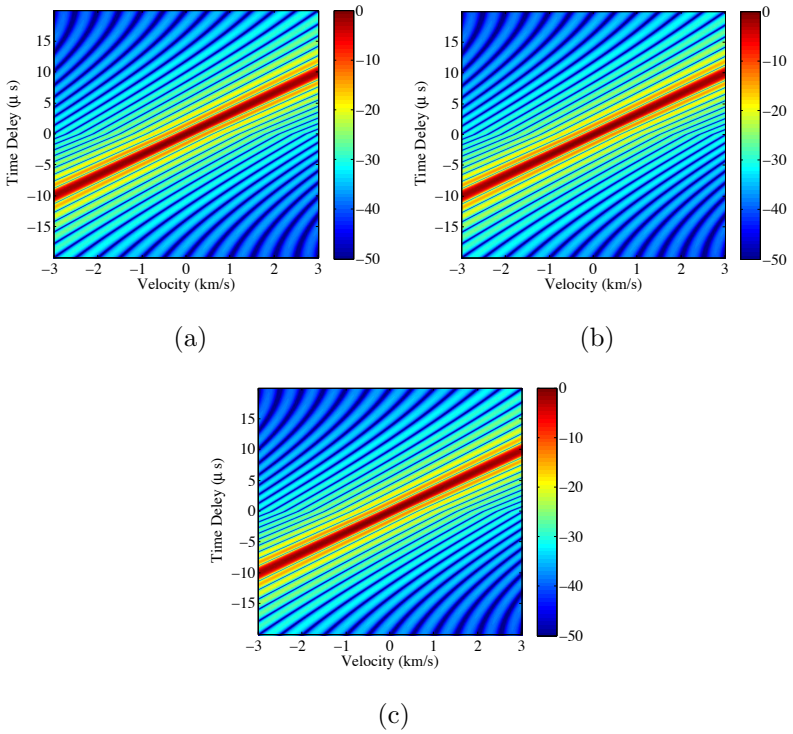

Figure 3.12: Classical ambiguity functions of an up-chirp with 10 GHz center frequency and 1 MHz bandwidth (a), the up-chirp after it has been radiated from a long thin dipole (b), and after radiation and reception on the same dipole (c).

of 0.01. There is little distortion from radiation alone resulting in a CAF 3.13(b) that looks nearly identical to 3.13(a) but with slightly less dynamic range near the prominent diagonal ridge. However, the distortion from radiation and reception is much greater as seen in 3.13(c), especially away from the range-Doppler ridge. This distortion encourages the use of a data model that includes antenna effects like the one presented in Section 3.4. We will not use waveforms with a lower center frequency or larger fractional bandwidth, as shown here, in the following simulations because we wish to make the narrowband approximation and use a physical optics approximation for some of our scatterers, requiring λ much smaller than the length of the target.

3.6.2 Scenarios

The simulations in this section correspond to the arrangement of target, transmitters, and receivers for the cases depicted in Figure 3.14(a)-(e). Figure 3.14(a)

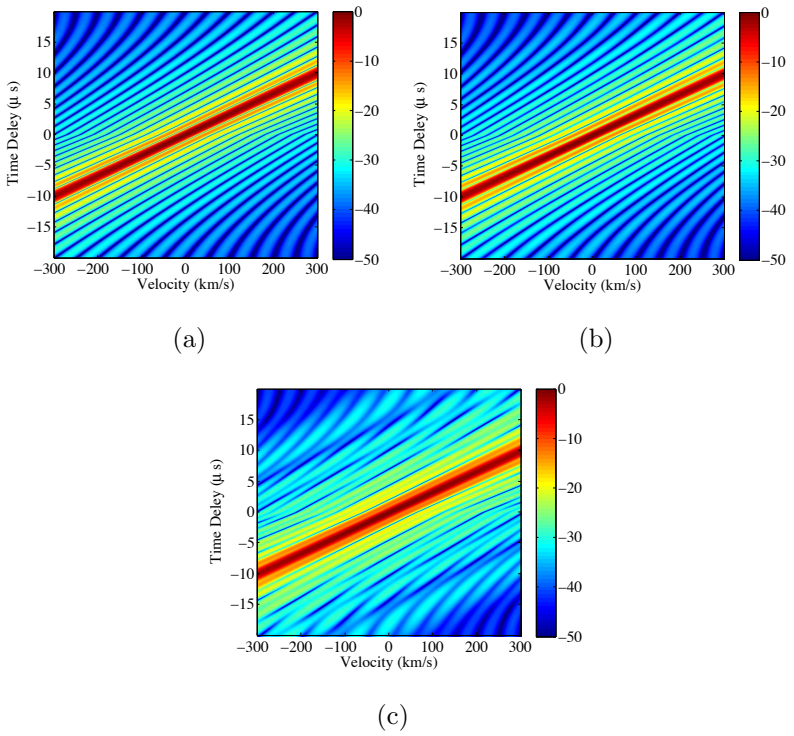

Figure 3.13: Classical ambiguity functions of an up-chirp with 100 MHz center frequency and 1 MHz bandwidth (a), the up-chirp after it has been radiated from a long thin dipole (b), and after radiation and reception on the same dipole (c).

is a standard monostatic backscatter scenario that is used to verify the data model and provide a baseline that simulations from other geometries can be compared to and Figure 3.14(b) is a bistatic scenario with a bistatic angle of 60^o that is used to illustrate the effect of incidence angle on scattering behavior. Figures 3.14(c) and 3.14(d) incorporate two receivers with a single transmitter between the receivers and Figure 3.14(e) is a more complicated scenario with two transmitters and two receivers. Figures 3.14(c) - (e) require data from multiple receivers to be fused and Figure 3.14(e) introduces the additional problem of multiple transmit waveforms. Although the data model addresses a six-dimensional position and velocity space, the center of the scatterer and the feed points of the transmitters and receivers are assumed to be in the same $\boldsymbol{x}$-$\boldsymbol{y}$ plane for the cases shown. This is so that the six-dimensional space can be presented in two dimensions by taking a cut in the $\hat{\boldsymbol{z}}$-direction of position and a single velocity cut. Unless specified the velocity cut is always the velocity cut corresponding to the moving target. However, the scattering

body and antennas may be oriented out of the $\boldsymbol{x}$-$\boldsymbol{y}$ plane.

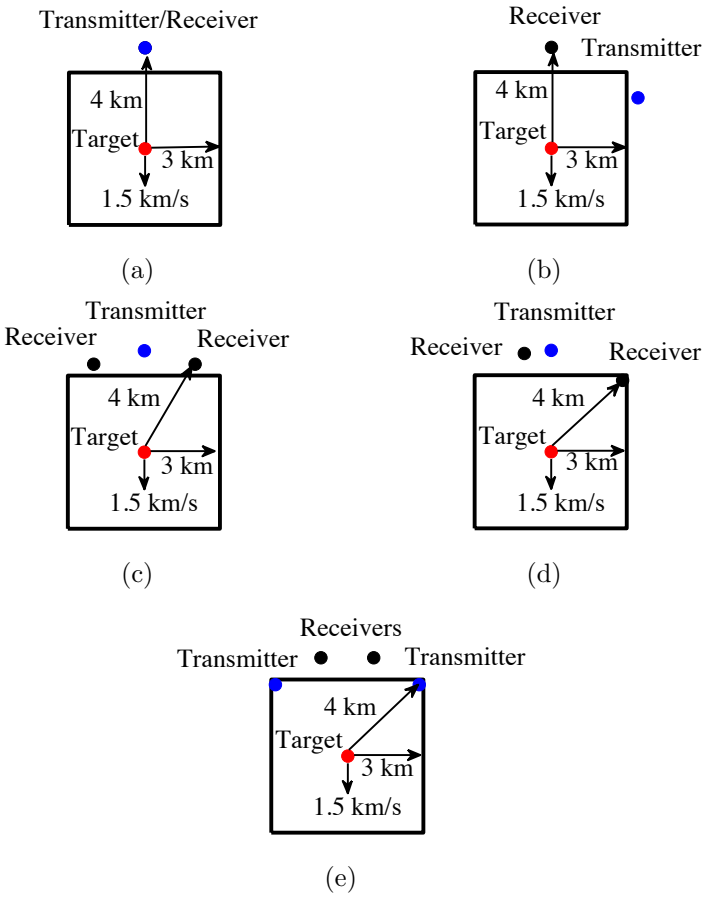

Figure 3.14: Arrangement of target, transmitters, and receivers for cases 3.14(a)-(e).

The scene of interest is a 6 km by 6 km square. In all cases we assume a single target in the center of the scene moving at a speed of 1.5 km/s in the 270^o direction. We make an arbitrary choice to locate the target at the center of the scene to impose equal propagation loses at each receiver in multistatic cases. We also assume that all transmitters and receivers are oriented so that boresight is towards the center of the scene and coincides with the direction of propagation for a target located at scene center. All plots in this section are shown of power on a dB scale.

3.6.3 Results

Separable Transmitter Contributions

The first set of results we will examine were obtained assuming that the con-

tributions from each transmitter are known. The images are formed using the first process described in Section 3.5.

Figures 3.15 through 3.27 consider a perfectly electrically conducting flat rectangular plate of length $L = 1$ m and height $H = 1$ m that is oriented along the $\boldsymbol{x}$-$\boldsymbol{z}$ plane with normal pointing in the $\hat{\boldsymbol{y}}$ direction. With respect to the diagrams of the simulation scenarios given in Figure 3.14, the plate is located in the center of the scenes and each of the scenes depict the orientation of scatterer, transmitters, and receivers in the $\boldsymbol{x}$-$\boldsymbol{y}$ plane with the $\hat{\boldsymbol{z}}$ direction pointing out of the page. The BSA scattering matrix used to model this plate is derived in Appendix D

$$\begin{aligned}[\boldsymbol{S}]_{\text{plate}} = &-\frac{\mathrm{i}k}{2\pi}LH\operatorname{sinc}\left(k\frac{L}{2}(\cos\phi_m\sin\theta_m-\cos\phi_n\sin\theta_n)\right)\\ &\times\operatorname{sinc}\left(k\frac{H}{2}(\cos\theta_m-\cos\theta_n)\right)\\ &\times\begin{bmatrix}-\sin\phi_n\sin\theta_m & 0\\ \cos\phi_m\cos\theta_m\sin\theta_n-\cos\phi_n\cos\theta_n\sin\theta_m & \sin\phi_m\sin\theta_n\end{bmatrix}\end{aligned} \tag{3.150}$$

where angles ϕ_m, ϕ_n, θ_m and θ_n are given by Figure 3.9. Due to our specific scenarios where the scatterer, transmitters, and receivers are all located in the same $\boldsymbol{x}$-$\boldsymbol{y}$ plane, $\theta_m = \theta_n = \pi/2$ and

$$[\boldsymbol{S}]_{\text{plate}} = -\frac{\mathrm{i}k}{2\pi}LH\operatorname{sinc}\left(k\frac{L}{2}(\cos\phi_m-\cos\phi_n)\right)\begin{bmatrix}-\sin\phi_n & 0\\ 0 & \sin\phi_m\end{bmatrix}. \tag{3.151}$$

In Figures 3.15 and 3.16 we consider the simple monostatic scenario described in Figure 3.14(a) and the scattering matrix reduces to

$$[\boldsymbol{S}]_{\text{plate}} = \frac{\mathrm{i}k}{2\pi}LH\begin{bmatrix}1 & 0\\ 0 & 1\end{bmatrix} \tag{3.152}$$

for normal incidence with $\theta_n = \pi - \theta_m = \pi/2$ and $\phi_n = \pi + \phi_m = \pi/2$. This is the same scattering matrix that is found in the literature [37, 38, 42, 51, 64] and the matrix portion of (3.152) is consistent with the monoscatic backscatter response from a sphere, plate, or trihedral [38].

Due to the symmetric nature of (3.152) we assume that the single transmit and receive dipole is horizontally polarized in Figures 3.15 and 3.16 for simplicity. In Figure 3.15 the transmit waveform is the chirp with CAF shown in 3.11(a) and in Figure 3.16 the transmit waveform is the phase code with CAF shown in 3.11(b). These baseline images are consistent with the behavior of these waveforms as discussed in Chapter 2. The Doppler tolerance of linearly modulated frequency waveforms and Doppler intolerance of phase codes is evident in Figures 3.15 and 3.16, respectively. The range rings visible in 3.15 and 3.16 are consistent with the monostatic geometry.

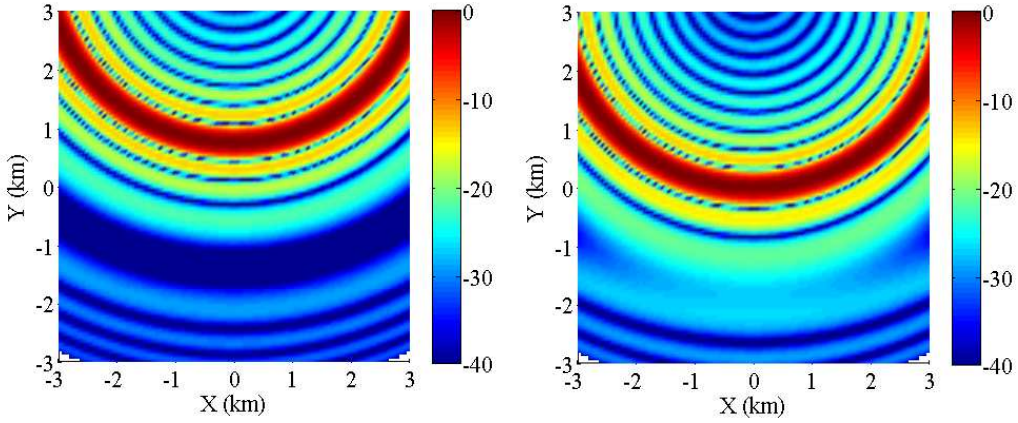

Figure 3.15: Chirp waveform, for scene Figure 3.14(a), flat rectangular scatterer, (a) zero velocity cut and (b) velocity cut at correct velocity.

Figures 3.17 through 3.20 correspond to the simple bistatic case described in Figure3.14(b). The scattering matrix now reduces to

$$[\boldsymbol{S}]_{\text{plate}} = \frac{ik}{2\pi} LH \text{sinc}\left(k\frac{\sqrt{3}L}{4}\right)\begin{bmatrix} 1 & 0 \\ 0 & \frac{1}{2} \end{bmatrix} \tag{3.153}$$

and we assume that the transmitter and receiver both consist of a horizontally polarized dipole and a vertically polarized dipole. In Figures 3.17 and 3.18 the transmit waveform is the chirp with CAF shown in 3.11(a) and in Figures 3.19 and 3.20 the transmit waveform is the phase code with CAF shown in 3.11(b). The total images are shown in Figures 3.17 and 3.19 and the HH and VV components

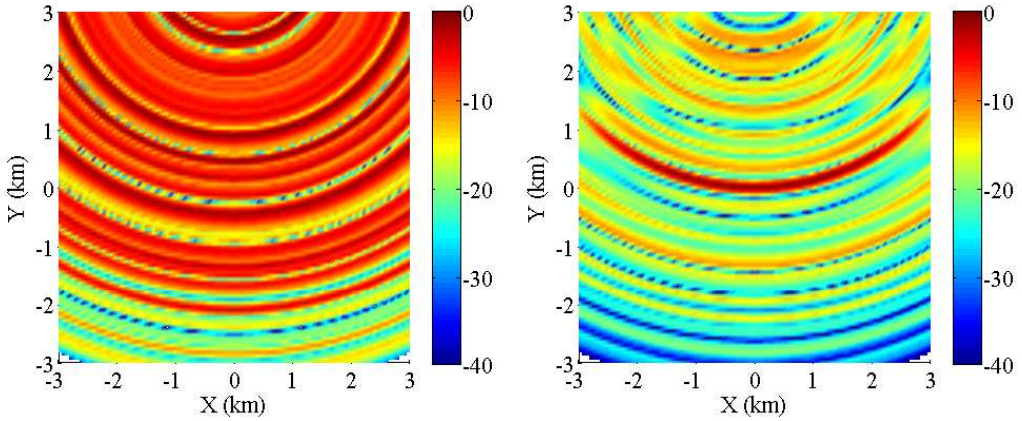

Figure 3.16: Phase coded waveform, for scene Figure 3.14(a), flat rectangular scatterer, (a) zero velocity cut and (b) velocity cut at correct velocity.

are shown in Figures 3.18 and 3.20. Figures 3.18(a) and (b) are normalized to Figure 3.17 and Figures 3.20(a) and (b) are normalized to Figure 3.19. It is clear from Figures 3.18 and 3.20 that the magnitude of the horizontal component of the scattered electric field is greater than the vertical component, as expected from (3.153). We note that the first "H" in HH denotes the receive polarization and the second denotes the transmit polarization. These polarizations are given in the bases associated with the transmit and receive dipoles as defined in Figure 3.9.

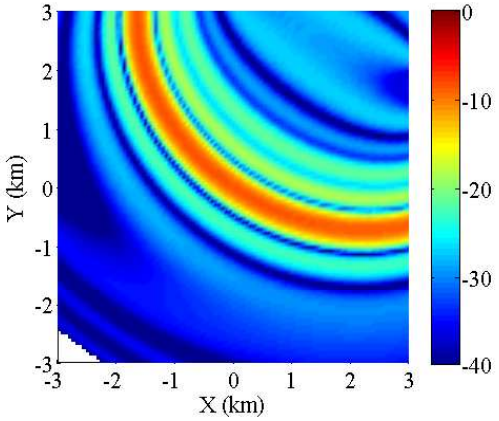

Figure 3.17: Chirp waveform, for scene Figure 3.14(b), flat rectangular scatterer, total image.

Figures 3.21 and 3.22 correspond to the multistatic scenario described in Figure

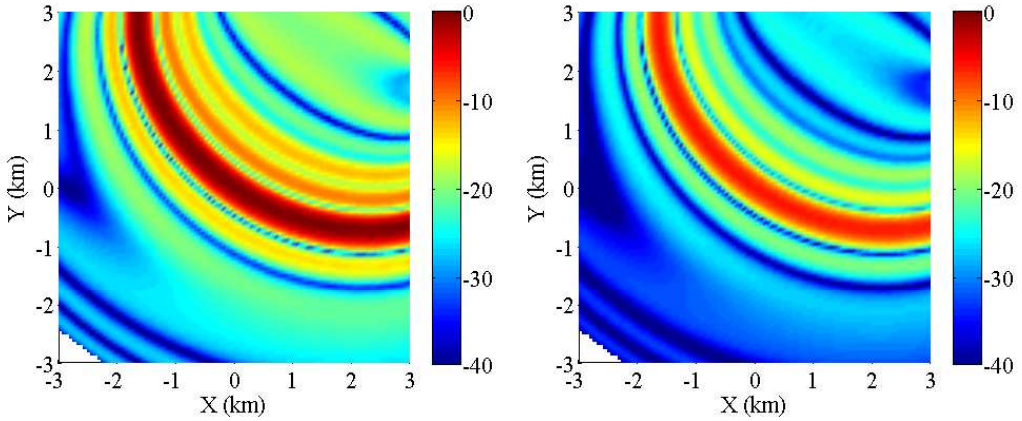

Figure 3.18: Chirp waveform, for scene Figure 3.14(b), flat rectangular scatterer, HH image (a) and VV image (b).

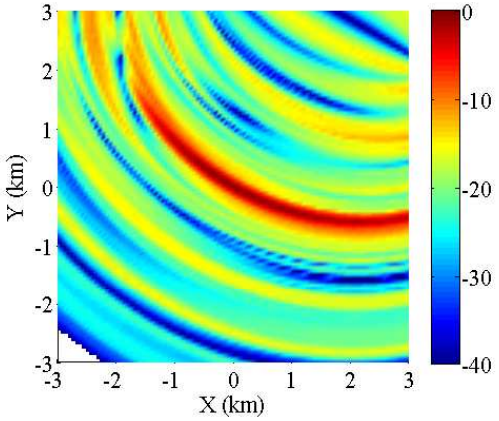

Figure 3.19: Phase coded waveform, for scene Figure 3.14(b), flat rectangular scatterer, total image.

3.14(c). We assume the transmitting antenna consists of two orthogonal dipoles, one horizontally polarized and the other vertical, and that the receiver to the right of the transmitter at 30^o is horizontally polarized and the receiver to the left of the transmitter and 150^o is vertically polarized. The scattering matrix associated with both bistatic pairs is given by

$$[\boldsymbol{S}]_{\text{plate}} = \frac{\mathrm{i}k}{2\pi} LH \operatorname{sinc}\left(k\frac{\sqrt{3}L}{4}\right) \begin{bmatrix} \frac{1}{2} & 0 \\ 0 & 1 \end{bmatrix}. \tag{3.154}$$

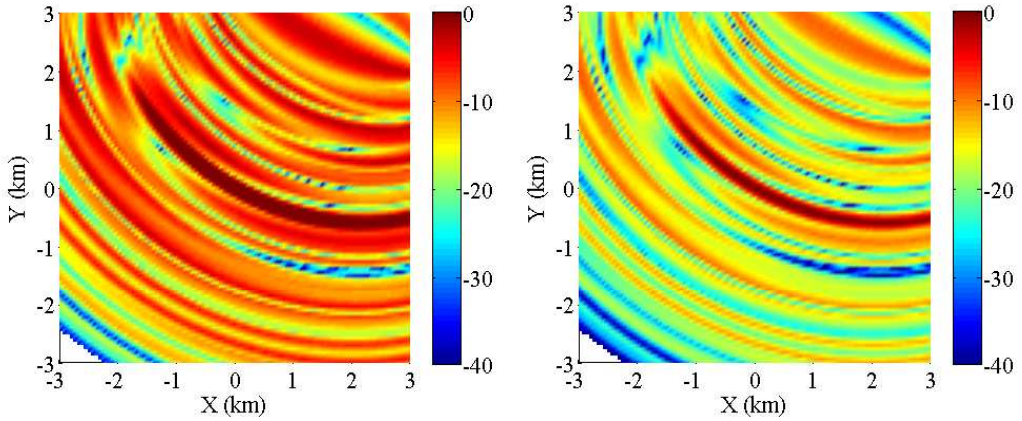

Figure 3.20: Phase coded waveform, for scene Figure 3.14(b), flat rectangular scatterer, HH image (a) and VV image (b).

In Figure 3.21 the transmit waveform is the chirp with CAF shown in 3.11(a) and in Figure 3.22 the transmit waveform is the phase code with CAF shown in 3.11(b). The peaks of the plots are denoted with white circles. Only the total images are shown because it makes little sense to compare the components from different bistatic pairs. The scattering matrix given in (3.154) corresponds to both bistatic pairs but this is due to the symmetry of the receivers about the transmitter and in general a different scattering matrix will reflect the polarization and amplitude transformation by the scatterer for each bistatic pair. The contribution from the bistatic pair consisting of the transmitter and leftmost receiver with vertical polarizations is greater than the contribution from the bistatic pair consisting of the transmitter and rightmost receiver with horizontal polarizations, as again would be expected from the scattering matrix in (3.154).

Figures 3.23 and 3.24 correspond to the multistatic scenario described in Figure 3.14(d). This scenario is very similar to Figure 3.14(c) but now the receivers are no longer symmetric about the transmitter and so we will obtain a different scattering matrix for each bistatic pair. We assume the transmitting antenna and both receiving antennas, located at 45^o and 105^o are horizontally polarized. The scattering matrix associated with the bistatic pair consisting of the transmit antenna and

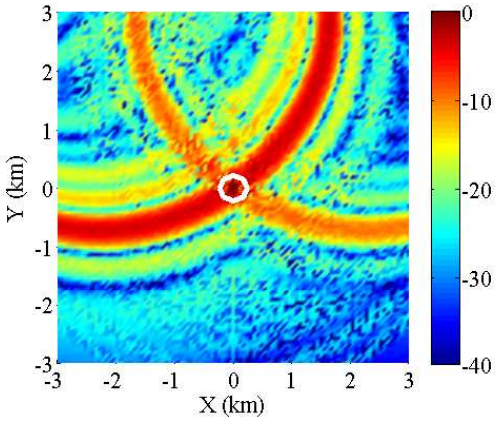

Figure 3.21: Chirp waveform, for scene Figure 3.14(c), flat rectangular scatterer, total image.

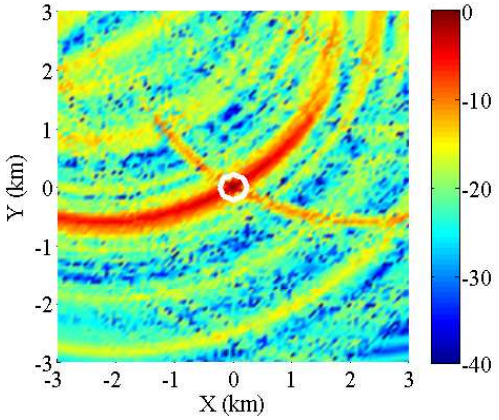

Figure 3.22: Phase coded waveform, for scene Figure 3.14(c), flat rectangular scatterer, total image.

the rightmost antenna is given by

$$
\begin{aligned}
[\boldsymbol{S}]_{\text{plate, }45^o} =& \frac{\mathrm{i}k}{2\pi} LH \operatorname{sinc}\left(k\frac{\sqrt{2}L}{4}\right)\begin{bmatrix} \frac{\sqrt{2}}{2} & 0 \\ 0 & 1 \end{bmatrix} \\
\approx& \frac{\mathrm{i}k}{2\pi} LH \operatorname{sinc}\left(0.3536\,kL\right)\begin{bmatrix} 0.7071 & 0 \\ 0 & 1 \end{bmatrix}
\end{aligned} \tag{3.155}
$$

and the scattering matrix associated with the bistatic pair consisting of the transmit

antenna and the leftmost antenna is given by

$$[\boldsymbol{S}]_{\text{plate},\,105^o} = \frac{\mathrm{i}k}{2\pi} LH \operatorname{sinc}\left(k\frac{\sqrt{2}(\sqrt{3}-1)L}{8}\right)\begin{bmatrix} \frac{\sqrt{2}(\sqrt{3}+1)}{4} & 0 \\ 0 & 1 \end{bmatrix}$$
$$\approx \frac{\mathrm{i}k}{2\pi} LH \operatorname{sinc}\left(0.1294\,kL\right)\begin{bmatrix} 0.9659 & 0 \\ 0 & 1 \end{bmatrix}. \tag{3.156}$$

The contribution from the horizontally polarized bistatic pair consisting of the transmitter and leftmost receiver is much greater than the contribution from the horizontally polarized bistatic pair consisting of the transmitter and rightmost receiver, which correspond to the first elements in (3.156) and (3.155), respectively. Figures 3.23 and 3.24 illustrate angle dependent scattering strength.

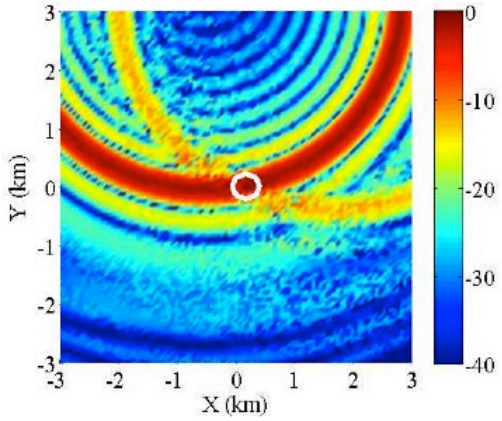

Figure 3.23: Chirp waveform, for scene Figure 3.14(d), flat rectangular scatterer, total image.

In Figures 3.25 through 3.27 we consider the multistatic scenario with multiple transmitters shown in Figure 3.14(e). In Figure 3.25 the transmit waveform is the chirp with CAF shown in 3.11(a) and in Figures 3.26 and 3.27 the transmit waveform for the transmitter at 45^o is the phase code with CAF shown in 3.11(b) and transmit waveform for the transmitter at 135^o is the phase code with CAF shown in 3.11(c). The scattering matrix associated with each bistatic pair is defined from (3.151) as we have done previously.

In Figures 3.25 and 3.26 we assume the transmitting antenna at 45^o is horizontally polarized, the transmitter at 135^o is vertically polarized, the receiver at 75^o

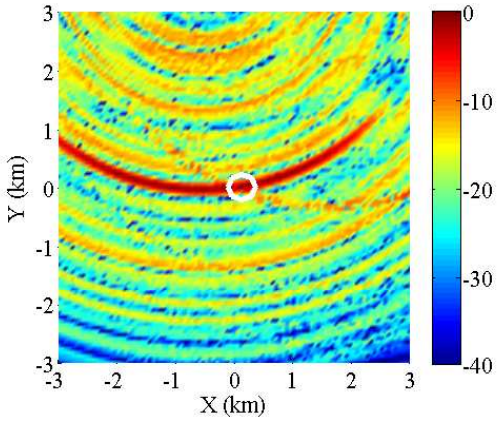

Figure 3.24: Phase coded waveform, for scene Figure 3.14(d), flat rectangular scatterer, total image.

is vertically polarized, and the receiver at 105^o is horizontally polarized. The total images show bistatic range rings for the contribution from each bistatic pair. We observe that although we transmit the same waveform from both transmitters in Figure 3.25, the chirps are transmitted from two different polarizations. In Figure 3.26, the phase codes are different and the waveforms are transmitted from two different polarizations. The positions of the transmitters and receivers are symmetric about the normal of the scattering plate, resulting in the same scattering matrix for each bistatic pair. However, the contribution from the vertically polarized bistatic pair consisting of the leftmost transmitter and rightmost receiver is less than the contribution from the horizontally polarized bistatic pair consisting of the rightmost transmitter and leftmost receiver, because the "HH" term is larger than the "VV" term in the scattering matrix that corresponds to both bistatic pairs. Figures 3.25 and 3.26 illustrate polarization dependent scattering strength.

In Figure 3.27 we assume the transmitting antennas at 45^o and 135^o consist of both a vertically polarized dipole and a horizontally polarized dipole, the receiver at 75^o is vertically polarized, and the receiver at 105^o is horizontally polarized. The scattering strength corresponding to each bistatic pair varies according to both angle and polarization, and is consistent with the scattering matrices that arise for each pair.

Although in Figures 3.25 through 3.27 we have assumed that some prepro-

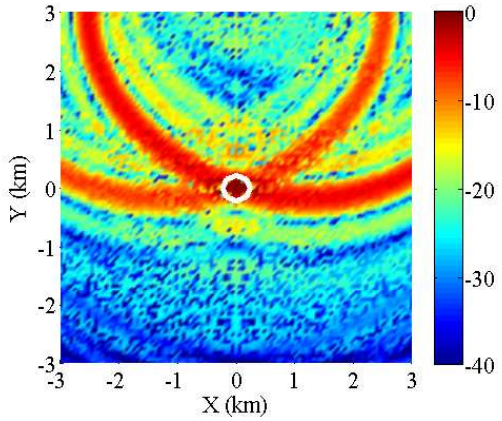

Figure 3.25: Chirp waveform, for scene Figure 3.14(e), flat rectangular scatterer, total image.

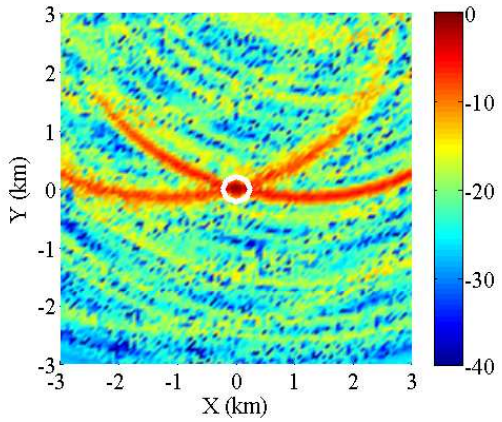

Figure 3.26: Phase coded waveform, for scene Figure 3.14(e), flat rectangular scatterer, total image.

cessing has been done on the received data so that the contributions from each transmitter are separable, we will later consider a similar case where the contributions are nonseparable.

In Figures 3.28 through 3.31 we again consider the bistatic case described in Figure 3.14(b) and we assume that the transmitter and receiver both consist of a horizontally polarized dipole and a vertically polarized dipole. We will now consider a complex target with corresponding scattering matrix

$$[\boldsymbol{S}]_{\text{complex}} = \begin{bmatrix} \frac{3}{2} & 1 - \frac{\mathrm{i}}{2} \\ 1 - \frac{\mathrm{i}}{2} & \frac{1}{2} \end{bmatrix}. \tag{3.157}$$

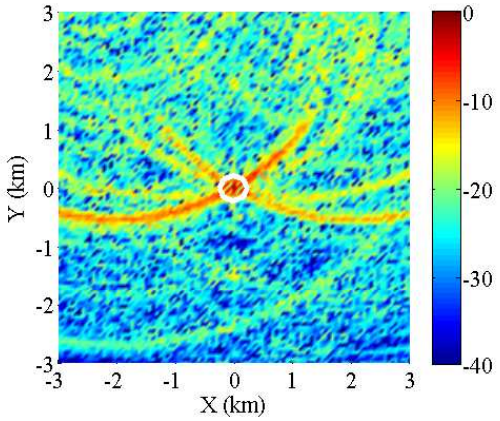

Figure 3.27: Phase coded waveform, for scene Figure 3.14(e), flat rectangular scatterer, total image. Transmitter composed of both a horizontally polarized dipole and vertically polarized dipole.

The scattering matrix in (3.157) does not correspond to a known scatterer and it is not defined based on the orientation of the scatterer, transmitter, and receiver. However, we are only considering a single transmitter and receiver so we can assume that (3.157) corresponds to this scenario for some unspecified scatterer in some orientation.

As an aside we observe that in a purely monostatic configuration the matrix (3.157) could decomposed into the following

$$\begin{bmatrix} \frac{3}{2} & 1-\frac{\mathrm{i}}{2} \\ 1-\frac{\mathrm{i}}{2} & \frac{1}{2} \end{bmatrix} = \begin{bmatrix} 1 & 0 \\ 0 & 1 \end{bmatrix} + \begin{bmatrix} 0 & 1 \\ 1 & 0 \end{bmatrix} + \frac{1}{2}\begin{bmatrix} 1 & -\mathrm{i} \\ -\mathrm{i} & -1 \end{bmatrix} \tag{3.158}$$

where the first matrix on the right hand side may correspond to a sphere, plate, or trihedral, the second matrix may correspond to a dihedral, and the third may correspond to a helix [38, 42]. Note that the above dihedral scattering matrix completely cross-polarizes an incident linearly polarized wave. This behavior is only observed in the unique case when the dihedral is tilted 45^o relative to the incident wave polarization. Although we are not considering a monostatic scenario in the following simulations, the images that result from using this scattering matrix give insight into the effect of a complex scatterer that introduces cross polarization.

In Figures 3.28 and 3.29 the transmit waveform is the chirp with CAF shown

in 3.11(a) and in Figures 3.30 and 3.31 the transmit waveform is the phase code with CAF shown in 3.11(b). The total images are shown in Figures 3.28 and 3.30 and the HH, HV, VH, and VV components are shown in Figures 3.29 and 3.31. In Figures 3.18 and 3.20 we only had HH and VV components because the scattering matrix for the flat plate (3.153) does not have cross terms but in Figures 3.29 and 3.31 we have all four components due to the cross terms in (3.157). We again note that the first "H" in HH denotes the receive polarization and the second denotes the transmit polarization. Figures 3.29(a)-(d) are normalized to Figure 3.28 and Figures 3.31(a)-(d) are normalized to Figure 3.30.

In Figures 3.29 and 3.31 the magnitudes of the HH, HV, and VH components are noticeably larger than the magnitude of the VV component and the magnitudes of the HH and HV components are somewhat larger than the magnitude of the VH component. From (3.157) we expect the magnitude of the HH component to be larger than the magnitude of the VV component but any discussion of the HV and VH components would benefit from examination of the real and imaginary parts of each component of the received data.

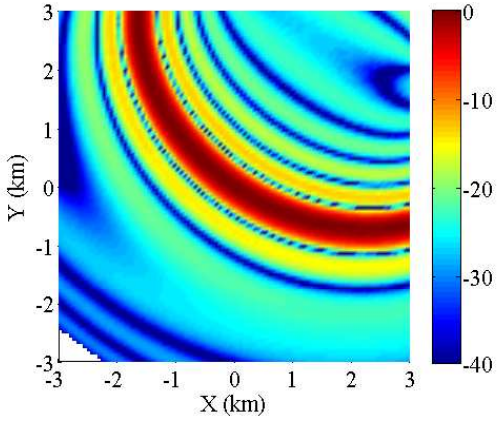

Figure 3.28: Chirp waveform, for scene Figure 3.14(b), complex scatterer, total image.

Nonseparable Transmitter Contributions

The next set of results we will examine were obtained assuming that the contributions received from all transmitters must be treated as a unit and consequently

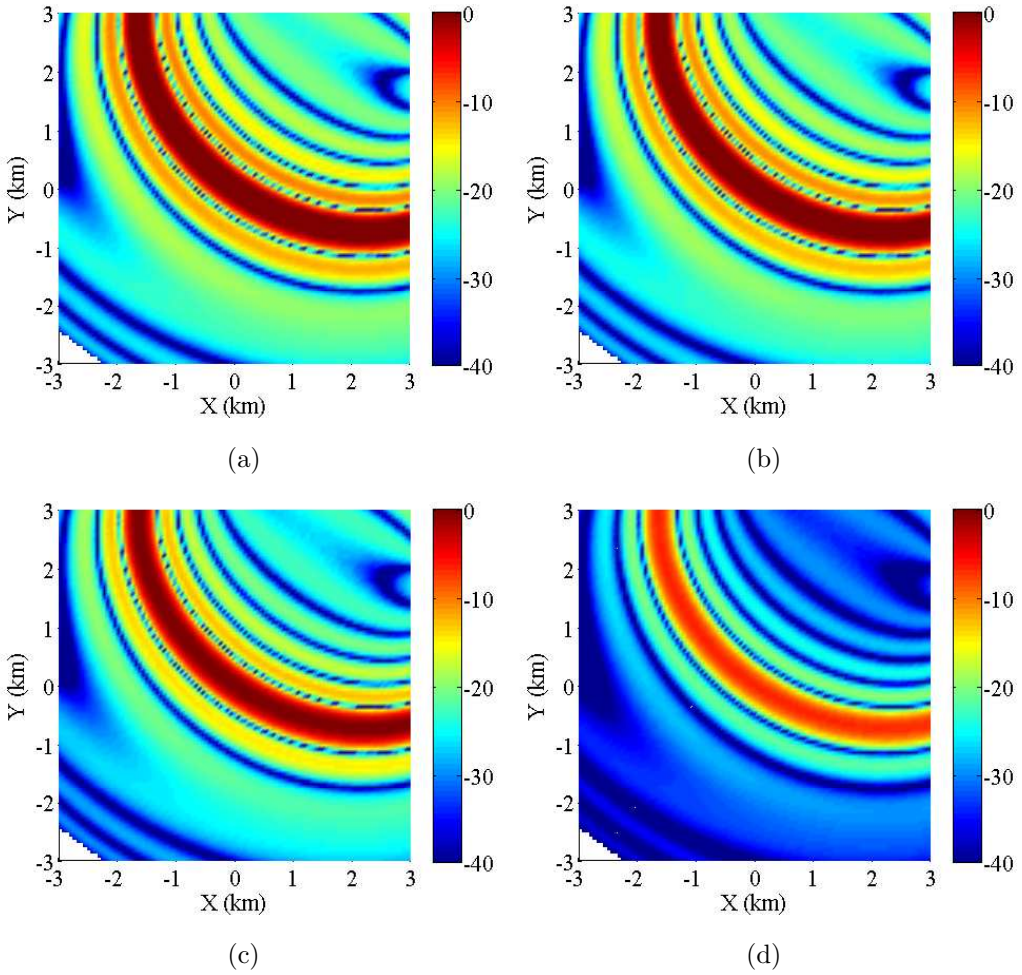

Figure 3.29: Chirp waveform, for scene Figure 3.14(b), complex scatterer, HH image (a), HV image (b), VH image (c), and VV image (d).

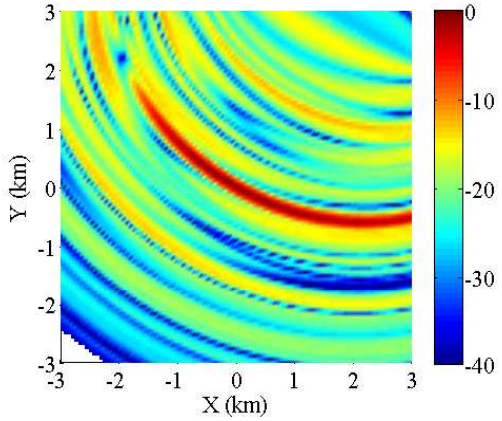

Figure 3.30: Phase coded waveform, for scene Figure 3.14(b), complex scatterer, total image.

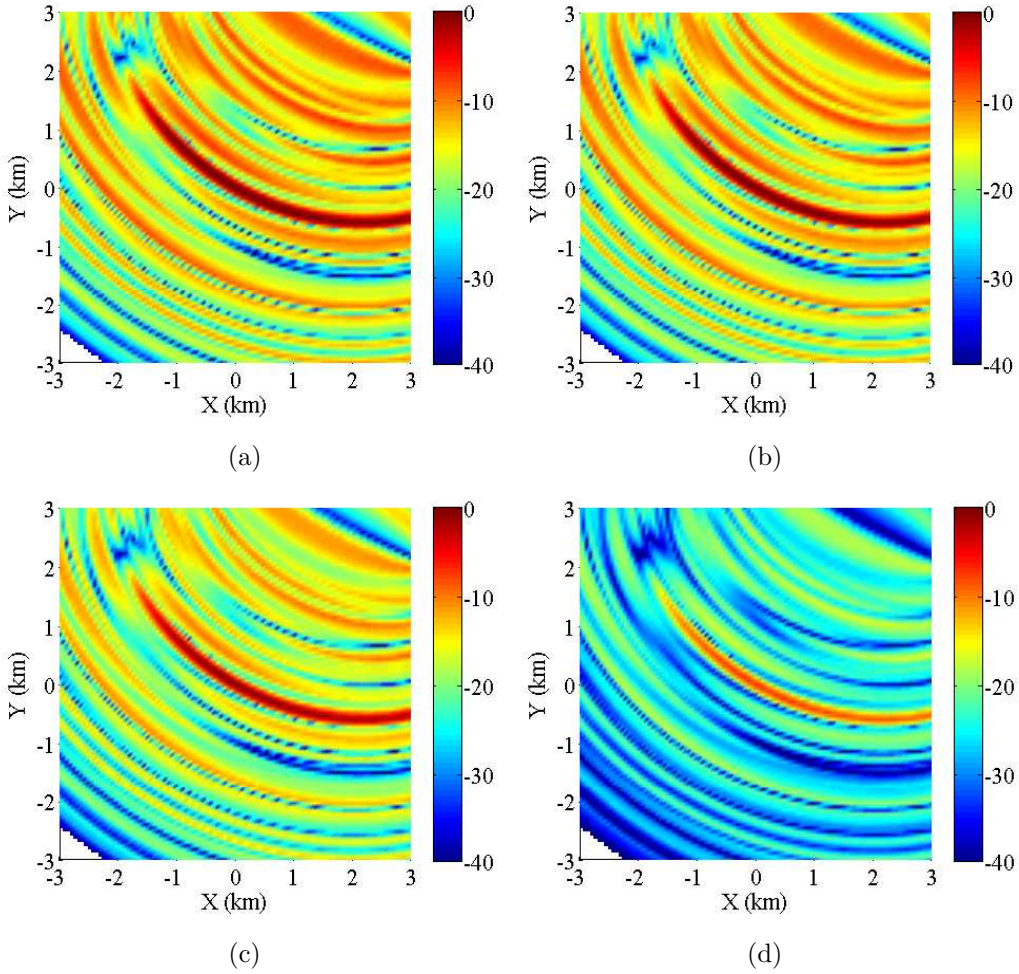

Figure 3.31: Phase coded waveform, for scene Figure 3.14(b), complex scatterer, HH image (a), HV image (b), VH image (c), and VV image (d).

the images are formed using the second process described in Section 3.5.

In Figures 3.32 through 3.34 we again consider the multistatic scenario with multiple transmitters shown in Figure 3.14(e). The scattering matrix associated with each bistatic pair is defined from (3.151) as in the previous section.

In Figures 3.32 and 3.33 we assume the transmitting antenna at 45^o is horizontally polarized, the transmitter at 135^o is vertically polarized, the receiver at 75^o is vertically polarized, and the receiver at 105^o is horizontally polarized. The total images show bistatic range rings for the contribution from each bistatic pair.

In Figure 3.32 the transmit waveform for the transmitter at 45^o is the phase code with CAF shown in 3.11(b) and transmit waveform for the transmitter at 135^o is

the phase code with CAF shown in 3.11(c) so that the two transmitted phase codes are different and the waveforms are transmitted from two different polarizations. However, unlike the previous section in which we treated the contributions from each transmitter as separable, now the contributions are added prior to image formation and are treated as a unit. The total received data at each receiver is convolved with the sum of the time-delayed and Doppler-scaled transmit waveforms. As a result, we observe cross-correlation residue in Figure 3.32 that is not present in Figure 3.26. The peak and prominent range rings are visible in both the figure obtained assuming separable transmitter contributions and the figure obtained assuming nonseparable contributions because the two transmitted phase codes have low cross-correlation.

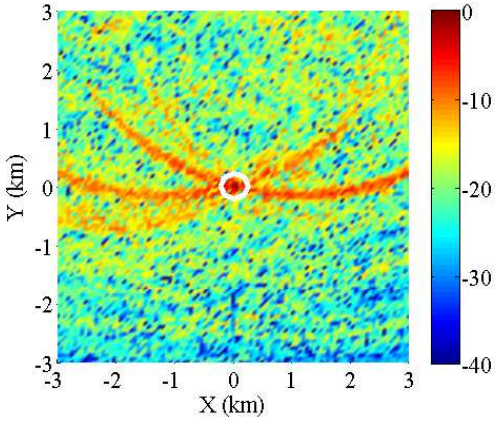

Figure 3.32: Phase coded waveform, for scene Figure 3.14(e), flat rectangular scatterer, total image formed assuming the transmitter contributions are nonseparable.

We will next examine a case where the nonseparable image formation method is not ideal. In Figure 3.33 the transmit waveform from both transmitters is the chirp with CAF shown in 3.11(a). Although the chirp is transmitted at a different polarization from each transmitter, the received data is convolved with the sum of time-delayed and Doppler-shifted waveforms from both transmitters, regardless of the polarization of the transmitting antenna. The correlation of the transmitting chirp with itself is much higher than the cross-correlation of the two phase codes, resulting in much more residue in the resulting image. Clearly, the transmission scheme corresponding to Figure 3.32 is not desirable when the contributions from all transmitters can not be separated prior to image formation.

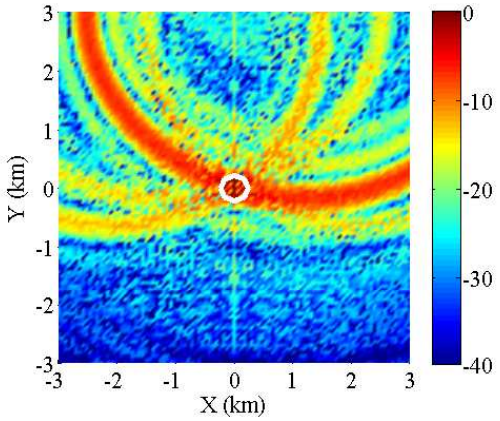

Figure 3.33: Chirp waveform, for scene Figure 3.14(e), flat rectangular scatterer, total image formed assuming the transmitter contributions are nonseparable.

In Figure 3.34 we assume the transmitting antennas at 45^o and 135^o consist of both a vertically polarized dipole and a horizontally polarized dipole, the receiver at 75^o is vertically polarized, and the receiver at 105^o is horizontally polarized. As in Figure 3.32 the transmit waveform for the transmitter at 45^o is the phase code with CAF shown in 3.11(b) and transmit waveform for the transmitter at 135^o is the phase code with CAF shown in 3.11(c). The transmitter contributions are nonseparable, in contrast to Figure 3.27 where the contributions were separated. Examining both Figures 3.27 and 3.34 we observe that the range rings are much less pronounced in Figure 3.34 but that the shapes of the bistatic range rings are similar for both and the peaks are in the correct location. As in Figure 3.32, we observe cross-correlation residue in Figure 3.34 but the correct image is obtained because the two transmitted phase codes have low cross-correlation.

We note that we have considered only a scene with multiple transmitters and receivers in simulations where the transmitter contributions are assumed nonseparable. In the case of a single transmitter, the resulting images are identical whether the transmitter contributions are assumed separable or nonseparable.

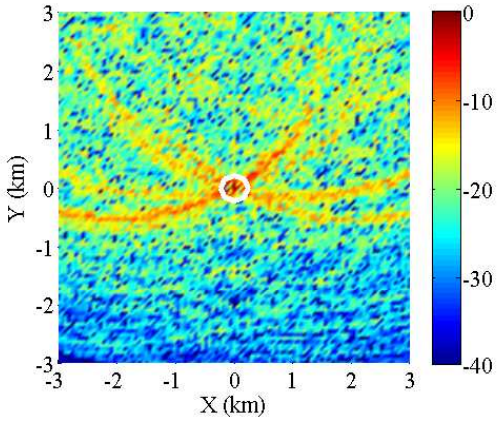

Figure 3.34: Phase coded waveform, for scene Figure 3.14(e), flat rectangular scatterer, total image formed assuming the transmitter contributions are nonseparable. Transmitter composed of both a horizontally polarized dipole and vertically polarized dipole.

3.7 Conclusions

In Chapter 3 we provided some background on polarization and scattering of electromagnetic plane waves and described the specific multistatic polarimetric problem addressed in the chapter. We then formulated a full vector data model incorporating propagation and scattering of the electric vector field and realistic antenna effects. Following formulation of the data model we described two imaging operations, first assuming that the contributions from each transmitter in the scene are separable and then assuming that the contributions from all transmitting antennas must be treated as a unit. The presented data model and imaging operations were then utilized to simulate multiple antenna geometries with multiple transmission and polarization schemes and a single moving target.

The data model was formulated by examining analytic expressions for the transmit waveform, transmitted electric field, scattered electric field, and received voltage in both the time and frequency domains. In the time domain, a summation of time-delayed versions of the transmit waveform is present in expressions for the transmitted field and the received voltage. These summations are consistent with radiation and reception of the electric field at the discontinuities of a long thin dipole under the zeroth order approximation for the current distribution on the dipole. Antenna effects from the dipole that are incorporated into the data model were

shown through simulation to be negligible for a small fractional bandwidth and more evident for a larger fractional bandwidth. Inclusion of both the scattering matrix and fast-time Doppler effects from a moving target is achieved by considering both the time and frequency domains. We obtain physical intuition, greater understanding and control of assumptions, and the ability to model the desired multistatic scenario carefully by formulating our data model from first principles. This work is novel in that the model is developed from beginning to end with the transmit waveform and scattering behavior of the target left arbitrary.

Simulations that employed the bistatic scattering matrix for a PEC flat rectangular plate demonstrated the model's ability to accurately depict angle and polarization dependent scattering behavior. The simulations that incorporated the scattering matrix consistent with a cross-polarizing complex scatterer illustrated the transformation of each component of the incident electric field in polarization, magnitude, and phase. Fast-time Doppler effects of a moving target were also discernible; as in Chapter 2 the target was visible in the correct velocity cut in all cases and the Doppler tolerance of the chirp waveforms and Doppler sensitivity of the phase coded waveforms was demonstrated.

Separable and nonseparable imaging operations were employed to form images of the simulated data. The separable image formation was successful regardless of the transmit waveforms and provides the opportunity to incorporate bistatic weighting schemes that could improve the performance of a multistatic system. The more realistic nonseparable image formation relied on low cross-correlation of the transmit waveforms if multiple transmitters were included. When two different phase coded waveforms were transmitted from two locations, the images formed under both assumptions were comparable.

Future work may consider bistatic scattering from other physical objects, time-varying scattering behavior, non-free-space propagation, and alternative transmitting and receiving antennas. Multiple targets can be easily modeled with a superposition of the received data corresponding to each scatterer. The data model can also be tailored for other applications, including moving target indication and synthetic aperture radar with one or more bistatic pairs.

CHAPTER 4
Conclusions and Future Work

In this thesis we have extended the theory for multistatic imaging of moving targets through the development and simulation of scalar and vector radar data models and accompanying imaging operations. In the first part of this work, we investigated scalar representations of multistatic radar data from the perspective of the multistatic ambiguity function. We began by examining two different MAFs from the literature, one approach deterministic in nature, originating from the scalar wave equation, and the other statistical, relying on a Neyman-Pearson defined weighting of received data. Despite differences in the underlying assumptions of the deterministic and statistical models, the mathematical expressions for the MAFs in the case of a single transmitter and multiple receivers can both be written in terms of the classical ambiguity function. Simulations show that the deterministically and statistically derived multistatic ambiguity functions provide comparable results for both stationary and moving targets. The comparison of the resulting MAFs and corresponding simulations attests to the close relationship between detection and imaging, encouraging the view of imaging as a detection problem at each point in space and velocity.

We then extended the data model for the existing deterministically derived MAF with the inclusion of antenna beam patterns by relating the current density on the radiating and receiving antennas to a far-field spatial weighting factor. The resulting data model is appropriate for narrowband waveforms in the case when the targets are moving slowly relative to the speed of light. From this model we developed an imaging formula in position and velocity that can be interpreted in terms of filtered backprojection or matched filtering and a corresponding ambiguity function or point-spread function. We used the resulting data model and MAF to examine scenarios with various geometries and transmit waveforms and showed that the performance of a multistatic system depends critically on the transmitted waveforms.

In second part of this thesis, we developed a vector multistatic data model, incorporating polarization and antenna effects from transmitters and receivers modeled as long thin dipoles. The derived data model describes radiation from a transmitting antenna, scattering from a moving target, and reception at a receiving antenna in both the time and frequency domains. Scattering from a moving target is modeled by including both the target scattering matrix and fast-time Doppler effects. Following formulation of the data model we described two imaging operations, first assuming that the contributions from each transmitter in the scene are separable and then assuming that the contributions from all transmitting antennas must be treated as a unit. The presented data model and imaging operations were then used to simulate multiple antenna geometries with multiple transmission and polarization schemes and a single moving target. The simulations that employed the bistatic scattering matrix for a perfectly electrically conducting flat rectangular plate exhibited the expected angle and polarization dependent scattering behavior. The simulations that incorporated the scattering matrix consistent with a cross-polarizing complex scatterer illustrated the transformation of each component of the incident electric field. The two imaging operations were employed to form images of the simulated data. While the more realistic nonseparable image formation relied on low cross-correlation of the transmit waveforms if multiple transmitters were included, the separable image formation was successful regardless of the transmit waveforms.

This work is novel in that the model is developed from beginning to end with the transmit waveform and scattering behavior of the target left arbitrary. The derivation of the received data relates the desired transmit waveform to the transmitted field, scattered field, and received voltage, describing transformations that are sometimes simplified without knowledge of what assumptions are necessary or have already been made. We obtain physical intuition, greater understanding and control of assumptions, and the ability to model the desired multistatic scenario carefully by formulating our data model from first principles. Although electromagnetics and signal processing are rich areas of study for radar applications, the two fields are infrequently combined. Without a high-fidelity data model, it is difficult

to predict how signal processing techniques will perform with real data. In this work we combine an electromagnetic data model with signal processing to obtain an image, but the data model can also be used to generate high-quality data for a variety of applications.

Future work would likely build upon the vector multistatic data model and corresponding imaging operations. This more complete model is especially relevant for multistatic scenarios because the polarization of the radiated electromagnetic field is inherently linked to the orientation and geometry of antennas in the scene. Modeling the full vector electromagnetic field is advantageous even in the case of a single polarization monostatic radar system because the polarization dependent scattering behavior of objects in the environment can result in a loss of information if the polarization of the incident field is cross-polarized by scatterers. Future work may consider analytically and through simulations: bistatic scattering from other physical objects, time-varying scattering behavior, non-free-space propagation, and alternative transmitting and receiving antennas. Multiple targets can be easily modeled with a superposition of the received data corresponding to each scatterer. The data model can also be tailored for other applications, including moving target indication and synthetic aperture radar with one or more bistatic pairs.

LITERATURE CITED

[1] B. Himed, H. Bascom, J. Clancy, and M. C. Wicks, "Tomography of moving targets (tmt)," in *Proc. SPIE*, vol. 4540, Dec. 2001, pp. 608–619.

[2] R. S. Adve, R. A. Schneible, M. C. Wicks, and R. McMillan, "Adaptive processing for distributed aperture radars," in *2004 Int. Waveform Diversity and Design Conf.*, Edinburgh, UK, Nov. 2004.

[3] R. S. Adve, R. A. Schneible, G. Genello, and P. Antonik, "Waveform-space-time adaptive processing for distributed aperture radars," in *2005 IEEE Int. Radar Conf.*, Arlington, VA, USA, May 2005, pp. 93–97.

[4] I. Bradaric, G. Capraro, D. Weiner, and M. Wicks, "Multistatic radar systems signal processing," in *2006 IEEE Radar Conf.*, Verona, New York, USA, Apr. 2006, p. 22.

[5] I. Bradaric, G. Capraro, and M. Wicks, "Waveform diversity for different multistatic radar configurations," in *Conf. Record 41st Asilomar Conf. Signals, Systems and Computers*, Nov. 2007, pp. 2038–2042.

[6] L. Landi and R. S. Adve, "Time-orthogonal-waveform-space-time adaptive processing for distributed aperture radars," in *2007 Int. Waveform Diversity and Design Conf.*, Pisa, IT, Jun. 2007, pp. 13–17.

[7] A. J. Devaney, "Inversion formula for inverse scattering within the Born approximation," *Optics Letters*, vol. 7, pp. 111–112, 1982.

[8] ——, "A filtered backpropagation algorithm for diffraction tomography," *Ultrasonic Imaging*, vol. 4, pp. 336–350, 1982.

[9] D. Colton and R. Kress, *Inverse Acoustic and Electromagnetic Scattering Theory*, 2nd ed. Berlin: Springer, 1998.

[10] T. Varsolt, B. Yazici, and M. Cheney, "Wide-band pulse-echo imaging with distributed apertures in multi-path environments," *Inverse Problems*, vol. 24, no. 4, p. 045013, Aug. 2008.

[11] M. Cheney and B. Borden, "Imaging moving targets from scattered waves," *Inverse Problems*, vol. 24, p. 22, Oct. 2008.

[12] L. Wang, M. Cheney, and B. Borden, "Multistatic radar imaging of moving targets," in *2010 IEEE Radar Conf.*, Washington, DC, USA, May 2010, pp. 391–396.

[13] ——, "Multistatic radar waveforms for imaging of moving targets," in *Proc. FFT 2011*, Feb. 2011.

[14] ——, "Multistatic radar imaging of moving targets," *IEEE Trans. Aerosp. Electron. Syst.*, Nov. 2010.

[15] T. Webster, J. Kim, I. Bradaric, and M. Cheney, "Deterministic and statistical models for multistatic ambiguity functions," in *2012 IEEE Radar Conf.*, Atlanta, GA, USA, May 2012, pp. 208–213.

[16] T. Webster, L. Xu, and M. Cheney, "Antenna beam patterns in MIMO radar," in *2012 IEEE Radar Conf.*, Atlanta, GA, USA, May 2012, pp. 332–337.

[17] M. Weiß, "Synchronisation of bistatic radar systems," in *Proc. 2004 IEEE Int. Geoscience and Remote Sensing Symp.*, vol. 3, Sep. 2004, pp. 1750–1753.

[18] I. Walterscheid, T. Espeter, A. R. Brenner, J. Klare, J. H. G. Ender, H. Nies, R. Wang, and O. Loffeld, "Bistatic SAR experiments with PAMIR and TerraSAR-X–setup, processing, and image results," *IEEE Trans. Geosci. Remote Sens.*, vol. 48, no. 8, pp. 3268–3279, Aug. 2010.

[19] J. S. Sandenbergh, M. R. Inggs, and W. A. Al-Ashwal, "Evaluation of coherent netted radar carrier stability while synchronised with gps-disciplined oscillators," in *2011 IEEE Radar Conf.*, Kansas City, MO, USA, May 2011, pp. 1100–1105.

[20] I. Bradaric, G. Capraro, D. Weiner, and M. Wicks, "A framework for the analysis of multistatic radar systems with multiple transmitters," in *Int. Conf. Electromagnetics Advanced Applications*, Sep. 2007, pp. 443–446.

[21] G. San Antonio, D. R. Fuhrmann, and F. C. Robey, "MIMO radar ambiguity functions," *IEEE J. Sel. Topics Signal Process.*, vol. 1, no. 1, pp. 167–177, Jun. 2007.

[22] M. Cheney, L. Wang, and B. Borden, "Spatial, temporal, and spectral aspects of radar data," in *2009 IEEE Radar Conf.*, Pasadena, CA, USA, May 2009, pp. 1–5.

[23] T. Derham, S. Doughty, C. Baker, and K. Woodbridge, "Ambiguity functions for spatially coherent and incoherent multistatic radar," *IEEE Trans. Aerosp. Electron. Syst.*, vol. 46, no. 1, pp. 230–245, Jan. 2010.

[24] M. Adjrad and K. Woodbridge, "Analysis of the multistatic ambiguity function for coherent and incoherent detectors," in *2011 IEEE Radar Conf.*, Kansas City, MO, USA, May 2011, pp. 1096–1099.

[25] A. Guruswamy and R. Blum, "On a definition of the ambiguity function for non-coherent radars," in *2012 IEEE 7th Sensor Array and Multichannel Signal Processing Workshop*, Hoboken, NJ, USA, Jun. 2012, pp. 141–144.

[26] C. E. Cook and M. Bernfeld, *Radar Signals*. New York: Academic, 1965.

[27] P. M. Woodward, *Probability and Information Theory, with Applications to Radar*. New York: McGraw-Hill, 1953.

[28] H. L. V. Trees, *Detection, Estimation, and Modulation Theory, Part III*, 1st ed. New York: John Wiley and Sons, Inc., 1971.

[29] N. Levanon, *Radar Principles*. New York: Wiley, 1998.

[30] M. Skolnik, *Radar Handbook*, 3rd ed. New York: The McGraw-Hill Companies, 2008.

[31] T. Tsao, M. Slamani, P. Varshney, D. Weiner, H. Schwarzlander, and S. Borek, "Ambiguity function for a bistatic radar," *IEEE Trans. Aerosp. Electron. Syst.*, vol. 33, no. 3, pp. 1041–1051, Jul. 1997.

[32] D. Weiner, M. Wicks, and G. Capraro, "Waveform diversity and sensors as robots in advanced military systems," in *2004 Int. Waveform Diversity and Design Conf.*, Edinburgh, UK, Nov. 2004.

[33] K. Voccola, B. Yazici, M. Ferrara, and M. Cheney, "On the relationship between the generalized likelihood ratio test and backprojection for synthetic aperture radar imaging," in *Proc. SPIE*, vol. 7335, May 2009.

[34] Y. Fang, M. Cheney, and S. Roecker, "Imaging from sparse measurements," *Geophysical Journal International*, vol. 180, pp. 1289–1302, 2010.

[35] M. Cheney and B. Borden, *Fundamentals of Radar Imaging*. SIAM, 2009.

[36] N. J. Willis and H. D. Griffiths, Eds., *Advances in Bistatic Radar*. Raleigh, NC: SciTech Publishing, 2007.

[37] F. T. Ulaby and C. Elachi, Eds., *Radar Polarimetry*. Norwood, MA: Artech House, Inc., 1990.

[38] E. Krogager, "Aspects of polarimetric radar imaging," Ph.D. dissertation, Tech. Univ. Denmark, Copenhagen, Denmark, 1993.

[39] K. Voccola, "Statistical and analytical techniques in synthetic aperture radar imaging," Ph.D. dissertation, Dept. Math. Sciences, Rensselaer Polytechnic Inst., Troy, NY, 2011.

[40] G. Sinclair, "The transmission and reception of elliptically polarized waves," in *Proc. IRE*, vol. 38, no. 2, Feb. 1950, pp. 148–151.

[41] E. M. Kennaugh, "Effects of type of polarization on echo characteristics," Antenna Lab., Ohio State Univ., Columbus, Rep. 381-1 to 394-24, 1949-1954.

[42] J. R. Huynen, "Phenomenological theory of radar targets," Ph.D. dissertation, Delft Univ. Technol., Delft, The Netherlands, 1970.

[43] H. A. Zebker and L. Norikane, "Radar polarimeter measures orientation of calibration corner reflectors," *Proc. IEEE*, vol. 75, pp. 1686–1688, 1987.

[44] S. R. Cloude and E. Pottier, "Review of target decomposition theorems in radar polarimetry," *IEEE Trans. Geosci. Remote Sens.*, vol. 34, no. 2, pp. 498–518, Mar. 1996.

[45] W. L. Cameron, N. N. Youssef, and L. K. Leung, "Simulated polarimetric signatures of primitive geometrical shapes," *IEEE Trans. Geosci. Remote Sens.*, vol. 34, no. 3, pp. 793–803, May 1996.

[46] G. Heath, "Bistatic scattering reflection asymmetry, polarization reversal asymmetry, and polarization reversal reflection symmetry," *IEEE Trans. Antennas Propag.*, vol. 29, no. 3, pp. 429–434, May 1981.

[47] S. Chaudhuri and W. Boerner, "A polarimetric model for the recovery of the high-frequency scattering centers from bistatic-monostatic scattering matrix data," *IEEE Trans. Antennas Propag.*, vol. 35, no. 1, pp. 87–93, Jan. 1987.

[48] A.-L. Germond, E. Pottier, and J. Saillard, "Foundations of bistatic radar polarimetry theory," in *Radar 97*, no. 449, Oct. 1997, pp. 833–837.

[49] E. Lüneburg and S. R. Cloude, "Bistatic scattering," in *Proc. SPIE*, vol. 3120, Dec. 1997, pp. 56–68.

[50] A.-L. Germond, E. Pottier, and J. Saillard, "Two bistatic target signatures: the bistatic equations and the bistatic polarisation fork," in *12th Int. Conf. Microwaves and Radar*, vol. 1, May 1998, pp. 123–127.

[51] J. A. Jackson, "Three-dimensional feature models for synthetic aperture radar and experiments in feature extraction," Ph.D. dissertation, Dept. Elect. and Comp. Eng., Ohio State Univ., Columbus, 2009.

[52] J. J. van Zyl, "On the importance of polarization in radar scattering problems," Ph.D. dissertation, Dept. Elect. Eng., California Inst. Technol., Pasadena, 1985.

[53] H. H. Lim, A. A. Swartz, H. A. Yueh, J. A. Kong, R. T. Shin, and J. J. van Zyl, "Classification of earth terrain using polarimetric synthetic aperture radar images," *Journal of Geophysical Research*, vol. 94, 1989.

[54] G. A. Ioannidis and D. E. Hammers, "Optimum antenna polarizations for target discrimination in clutter," *IEEE Trans. Antennas Propag.*, vol. AP-27, pp. 357–363, 1979.

[55] A. A. Swartz, H. A. Yueh, J. A. Kong, L. M. Novak, and R. T. Shin, "Optimum polarizations for achieving maximum contrast in radar images," *Journal of Geophysical Research*, vol. 93, no. B12, pp. 15 252–15 260, 1988.

[56] L. M. Novak, M. B. Sechtin, and M. J. Cardullo, "Studies of target detection algorithms that use polarimetric radar data," *IEEE Trans. Aerosp. Electron. Syst.*, vol. 25, no. 2, 1989.

[57] R. Chaney, M. Burl, and L. Novak, "On the performance of polarimetric target detection algorithms," in *1990 IEEE Int. Radar Conf.*, Arlington, VA, USA, May 1990, pp. 520–525.

[58] L. M. Novak, M. C. Burl, and W. W. Irving, "Optimal polarimetric processing for enhanced target detection," *IEEE Trans. Aerosp. Electron. Syst.*, vol. 29, no. 1, 1993.

[59] W.-M. Boerner, Ed., *Inverse Methods in Electromagnetic Imaging: (Proc. NATO Advanced Research Workshop, Bad Windsheim, 18-24 September 1983)*, ser. NATO ASI series. Series C, Mathematical and physical sciences. Dordrecht: Reidel, 1985.

[60] D. Giuli, "Polarization diversity in radars," *Proc. IEEE*, vol. 74, no. 2, pp. 245–269, Feb. 1986.

[61] J. A. Kong, *Theory of Electromagnetic Waves*. New York: John Wiley and Sons, Inc., 1975.

[62] M. Born and E. Wolf, *Principles of Optics*, 6th ed. Oxford: Pergamon Press, 1984.

[63] N. Trouvé, E. C. Koeniguer, P. Fargette, and A. De Martino, "Influence of geometrical configurations and polarization basis definitions on the analysis of bistatic polarimetric measurements," *IEEE Trans. Geosci. Remote Sens.*, vol. 49, no. 6, pp. 2238–2250, June 2011.

[64] E. F. Knott, J. F. Schaeffer, and M. T. Tuley, *Radar Cross Section*, 1st ed. Norwood, MA: Artech House, Inc., 1985.

[65] F. T. Ulaby, R. K. Moore, and A. K. Fung, Eds., *Microwave Remote Sensing: Active and Passive*. Norwood, MA: Artech House, Inc., 1981.

[66] J. A. Stratton, *Electromagnetic Theory*. New York: McGraw-Hill Book Company, 1941.

[67] D. J. Griffiths, *Introduction to Electrodynamics*, 3rd ed. Upper Saddle River: Prentice Hall, 1999.

[68] J. D. Jackson, *Classical Electrodynamics*, 3rd ed. Hoboken: John Wiley and Sons, Inc., 1998.

[69] J. Van Kranendonk and J. E. Sipe, "Foundations of the macroscopic electromagnetic theory of dielectric media," in *Progress in Optics*, E. Wolf, Ed. Amsterdam: North-Holland Publishing Company, 1977, vol. 15, ch. 5, pp. 245–350.

[70] A. D. Yaghjian, "Electric dyadic Greens functions in the source region," *Proc. IEEE*, vol. 68, no. 2, pp. 248–263, Feb. 1980.

[71] H. F. Arnoldus, "Transverse and longitudinal components of the optical self-, near-, middle- and far-field," *Journal of Modern Optics*, vol. 50, no. 5, pp. 755–770, 2003.

[72] S. J. Orfanidis. (2012, Mar. 5) *Electromagnetic Waves and Antennas*. [Online]. Available: www.ece.rutgers.edu/∼orfanidi/ewa

[73] G. Franceschetti and C. H. Papas, "Pulsed antennas," *IEEE Trans. Antennas Propag.*, vol. AP-22, no. 5, pp. 651–661, Sep. 1974.

[74] S. N. Samaddar, "Radiated field from a thin half-wave dipole excited by a single-cycle sinusoid," Naval Res. Lab., Washington, DC, NRL Memorandum Rep. 6465, Oct. 1989.

[75] ——, "Transient radiation of a single-cycle sinusoidal pulse from a thin dipole," *Journal of the Franklin Institute*, vol. 329, no. 2, pp. 259–271, Mar. 1992.

[76] E. L. Mokole, A. K. Choudhury, and S. N. Samaddar, "Transient radiation from thin, half-wave, orthogonal dipoles," *Radio Science*, vol. 33, no. 2, pp. 219–229, March-April 1998.

[77] S. N. Samaddar and E. L. Mokole, "Transient behavior of radiated and received fields associated with a resistively loaded dipole," in *Ultra-Wideband Short-Pulse Electromagnetics 4*, E. Heyman, B. Mandelbaum, and J. Shiloh, Eds. New York: Kluwer Academic Publishers, 2002, pp. 165–180.

[78] R. W. P. King, *Theory of Linear Antennas*. Cambridge, MA: Harvard University Press, 1956.

[79] T. T. Wu and R. W. P. King, "The cylindrical antenna with nonreflecting resistive loading," *IEEE Trans. Antennas Propag.*, vol. 13, no. 3, pp. 369–373, May 1965.

[80] E. L. Mokole, "Behavior of ultrawideband-radar array antennas," in *IEEE Int. Symp. Phased Array Systems and Technology*, Oct. 1996, pp. 113–118.

[81] D. L. Sengupta and C.-T. Tai, "Radiation and reception of transients by linear antennas," in *Transient Electromagnetic Fields*, L. B. Felsen, Ed. Berlin: Springer-Verlag, 1976, ch. 4, pp. 181–235.

[82] S. N. Samaddar, "Behavior of a received pulse radiated by half-wave dipole excited by a single-cycle sinusoidal voltage," *Journal of the Franklin Institute*, vol. 330, no. 1, pp. 17–28, Jan. 1993.

[83] J. V. DiFranco and W. L. Rubin, *Radar Detection*, 1st ed. Englewood Cliffs: Prentice-Hall, Inc., 1968.

[84] E. Conte, E. D'Addio, A. Farina, and M. Longo, "Multistatic radar detection: synthesis and comparison of optimum and suboptimum receivers," *IEE Proc.*, vol. 130, no. 6, pp. 484–494, Oct. 1983.

[85] E. D'Addio, A. Farina, E. Conte, and M. Longo, "Multistatic detection of radar signals for swerling models of the target," *Rivista Tecnica Selenia*, vol. 9, no. 4, pp. 11–17, 1985.

[86] D. Baumgarten, "Optimum detection and receiver performance for multistatic radar configurations," in *IEEE Int. Conf. Acoustics, Speech, and Signal Processing*, vol. 7, May 1982, pp. 359–362.

[87] A. Papoulis, *Probability, Random Variables, and Stochastic Processes*, 2nd ed. New York: McGraw-Hill Book Company, 1984.

[88] H. L. V. Trees, *Detection, Estimation, and Modulation Theory, Part I*, 1st ed. New York: John Wiley and Sons, Inc., 1968.

APPENDIX A
Derivation of the Global Ambiguity Function

The goal of this appendix is to derive the global ambiguity function, or statistically derived multistatic ambiguity function, described in Section 2.3.2. This derivation determines weights for the matched filter output of each receiver from the Neyman-Pearson optimal global statistic, which is found from the likelihood ratio. The derivation originates from a construct developed to determine the optimal detector for a pulsed monostatic system [83]. The concept was later extended to weight receiver contributions from a multistatic system utilizing a single pulse with multiple receivers and either a single transmitter [4, 5, 84–86] or multiple transmitters [20]. The weighted contributions from each multistatic receiver can be used to determine the optimal detector or can be combined to form a multistatic ambiguity function.

We first provide some relevant background and then recall the model for the received data and the matched filtered output from each receiver described in Section 2.3.2. From the matched filtered output we determine the probability density functions corresponding to the assumptions that the received data is completely noise and that the received data is composed of noise and a target return. The likelihood ratio and optimal global statistic are found from the two pdfs and then the weighting on each receiver's output is computed and applied. The weighted receiver contributions are added non-coherently to obtain the multistatic ambiguity function.

A.1 Background

A.1.1 Rayleigh Distribution

The probability density function for a Rayleigh distributed random variable x with parameter σ is given by

$$p(x) = R(x, \sigma) = \frac{x}{\sigma^2} e^{\frac{-x^2}{2\sigma^2}} \tag{A.1}$$

with variance $\frac{4-\pi}{2}\sigma^2$ and mean $\sigma\sqrt{\frac{\pi}{2}}$. Recall the relationship

$$E\{x^2\} = \text{var}\{x\} + (E\{x\})^2. \tag{A.2}$$

Substituting a Rayleigh distributed RV x with parameter σ into (A.2) we obtain

$$E\{x^2\} = \frac{4-\pi}{2}\sigma^2 + \left(\sigma\sqrt{\frac{\pi}{2}}\right)^2 = 2\sigma^2 \tag{A.3}$$

and so

$$\sigma = \sqrt{\frac{1}{2}E\{x^2\}}$$

and the pdf of x is given by

$$p(x) = R\left(x, \sqrt{\frac{1}{2}E\{x^2\}}\right). \tag{A.4}$$

We also recall that if two random variables x and y are Gaussian and independent with zero mean and equal variance then the random variable $z = \sqrt{x^2+y^2}$ has a Rayleigh density [87]. In the following derivation we will assume that the in-phase and quadrature components of the noise from each of the N receivers, $n_n(t)$, are zero-mean Gaussian with equal variance such that the envelope of the noise is Rayleigh distributed.

A.1.2 Swerling II Target Model

Swerling target models describe the fluctuations in radar cross section (RCS) of a target as observed by a pulsed radar system that may illuminate the same target during multiple scans. The RCS varies according to the probability density function of a chi-squared distribution with a given number of degrees of freedom.

The Swerling II target model specifically describes a target with an RCS that is independent from pulse to pulse. The RCS is given by a chi-squared pdf with 2 degrees of freedom

$$p(x) = \frac{1}{\bar{x}}\mathrm{e}^{-\frac{x}{\bar{x}}}, \tag{A.5}$$

with $\bar{x} = E\{x\}$, which is consistent with a target that is made up of multiple

independent scatterers of roughly equal areas. The complex gain of a Swerling II type target corresponding to the n^{th} pulse is given by $a_n = A_n e^{i\phi_n}$ where the amplitude A_n denotes an independent Rayleigh distributed random variable with parameter A_{0n} so that $p(A_n) = R(A_n, A_{0n})$ and the phase ϕ_n denotes an independent random variable uniformly distributed on $[0, 2\pi]$ [83]. In the following derivation we will assume a Swerling II type target where the RCS associated with the look direction of each receiver is independent.

A.2 Output of the Matched Filter

We recall from Section 2.3.2 that at each transmitter, we assume that a coherent processing interval consists of a single pulse of duration T_{dm} and energy E_m:

$$s_m(t) = \sqrt{2E_m}\Re\{f_m(t)\mathrm{e}^{\mathrm{i}\omega_c t}\}, \quad 0 \le t \le T_{dm} \tag{A.6}$$

where $f_m(t)$ is the complex envelope of the transmitted pulse, $\omega_c = 2\pi f_c$, and it is assumed that the carrier frequency f_c is the same for all transmitters.

The input into the n^{th} receiver is given by the set of hypotheses:

$$\begin{aligned} H_0 &: r_n(t) = n_n(t) \\ H_1 &: r_n(t) = \sum_{m=1}^{M} a_{m,n}\gamma_{m,n}\tilde{s}_m(t - \tau^a_{m,n})\mathrm{e}^{\mathrm{i}\omega^a_{m,n}t} + n_n(t) \end{aligned} \tag{A.7}$$

where $n_n(t)$ is the noise at the n^{th} receiver, $\tau^a_{m,n}$ is the travel time along the propagation path from the m^{th} transmitter to the target and from there to the n^{th} receiver, and $\gamma_{m,n} \approx (R_{\boldsymbol{x},m}R_{\boldsymbol{x},n})^{-1}$ is the propagation loss along this path for a target located at $\boldsymbol{x}$ where $R_{\boldsymbol{x},m}$ is the distance between the target and m^{th} transmitter located at $\boldsymbol{y}_m$ and $R_{\boldsymbol{x},n}$ is the distance between the target and n^{th} receiver located at $\boldsymbol{z}_n$. The angular frequency $\omega^a_{m,n}$ is the total Doppler shift of the signal at the n^{th} receiver that originated from the m^{th} transmitter. The superscript a denotes a value that corresponds to a true target, and so $\tau^a_{m,n}$ and $\omega^a_{m,n}$ correspond to the travel time and Doppler shift, respectively, of a true target. The relationship between the travel time and angular frequency and the target position and velocity will be explicitly

stated later. The waveform $\tilde{s}_m(t) = \sqrt{2E_m} f_m(t)$ is the complex envelope of the transmitted signal $s_m(t)$. The coefficient $a_{m,n}$ is the direction-dependent effective target reflectivity. We assume that $a_{1,n} = a_{2,n} = \cdots = a_{M,n} \equiv a_n$. In addition, we assume a Swerling II target model with complex reflectivity given by $a_n = A_n e^{i\phi_n}$ where the amplitude A_n denotes an independent Rayleigh distributed random variable with parameter A_{0n} and the phase ϕ_n denotes an independent random variable uniformly distributed on $[0, 2\pi]$. The real and imaginary components of the noise $n_n(t)$ are zero-mean Gaussian with equal variance, unilateral power spectral density N_{0n}, and Rayleigh distributed envelope.

At each receiver we perform standard matched filtering of the received data corresponding to a true target at position $\boldsymbol{x}$ and with velocity $\boldsymbol{v}$ with the expected composite received waveform corresponding to a hypothetical target at position $\boldsymbol{p}$ and with velocity $\boldsymbol{u}$. The expected, normalized, and weighted composite waveform at the n^{th} receiver $p_n(t; \vec{\tau}_n^h, \vec{\omega}_n^h)$ is specified by

$$p_n(t; \vec{\tau}_n^h, \vec{\omega}_n^h) = \frac{1}{B_n} \sum_{m=1}^{M} b_{m,n} f_m(t - \tau_{m,n}^h) e^{i\omega_{m,n}^h t}, \tag{A.8}$$

where

$$\begin{aligned} \vec{\tau}_n^h &= [\tau_{1,n}^h, \ldots, \tau_{M,n}^h]^T \\ \vec{\omega}_n^h &= [\omega_{1,n}^h, \ldots, \omega_{M,n}^h]^T \end{aligned} \tag{A.9}$$

and the superscript h denotes that this composite waveform corresponds to a hypothetical target. The coefficients

$$b_{m,n} = \frac{R_{\boldsymbol{p},m=1}}{R_{\boldsymbol{p},m}} \sqrt{\frac{E_m}{E_{m=1}}} \tag{A.10}$$

are derived for each transmitter-receiver pair from the bistatic radar equation, under the assumptions that $b_{1,n} = 1$ and $P_m G_m \sim E_m$ where P_m is the power of the m^{th} transmitter and G_m is the gain of the m^{th} transmitter. By inspection, $b_{m,n}$ depends only on the transmitter. The composite waveform corresponding to a true target $p_n(t; \vec{\tau}_n^a, \vec{\omega}_n^a)$ is defined the same way with subscript $\boldsymbol{p}$ replaced with $\boldsymbol{x}$ and superscript

h replaced with a. The normalization constant B_n is chosen so that

$$\int_{-\infty}^{\infty} p_n(t;\vec{\tau}_n^h,\vec{\omega}_n^h)p_n^*(t;\vec{\tau}_n^h,\vec{\omega}_n^h)\mathrm{d}t = 1 \tag{A.11}$$

and

$$\int_{-\infty}^{\infty} p_n(t;\vec{\tau}_n^a,\vec{\omega}_n^a)p_n^*(t;\vec{\tau}_n^a,\vec{\omega}_n^a)\mathrm{d}t = 1. \tag{A.12}$$

The received signal at the n^{th} receiver under hypothesis H_1 can be rewritten in terms of the composite waveform yielding

$$r_n(t) = \frac{a_n B_n \mu_n \sqrt{E_{m=1}}}{R_{\boldsymbol{x},m=1}R_{\boldsymbol{x},n}} p_n(t;\vec{\tau}_n^a,\vec{\omega}_n^a) + n_n(t) \tag{A.13}$$

where μ_n is the compensation constant [20]. Then the output of the matched filter at the n^{th} receiver is given by

$$d_n = \left| \int_{-\infty}^{\infty} \frac{r_n(t)}{\sqrt{N_{0n}}} p_n^*(t;\vec{\tau}_n^h,\vec{\omega}_n^h)\,\mathrm{d}t \right|. \tag{A.14}$$

A.3 Derivation of the Optimal Global Statistic

To derive the likelihood ratio and corresponding optimal global statistic we must first determine the pdfs of the output of the matched filter for each receiver, d_n, under hypotheses H_0 and H_1. We find $E\{d_n^2|H_0\}$ and $E\{d_n^2|H_1\}$ under the assumption that the output of the matched filter is Rayleigh under both hypotheses.

A.3.1 Probability Density Under H_0

Under H_0 the received data at the n^{th} receiver is $r_n(t) = n_n(t)$ and so the output of the matched filter is given by

$$d_n = \left| \int_{-\infty}^{\infty} \frac{n_n(t)}{\sqrt{N_{0n}}} p_n^*(t;\vec{\tau}_n^h,\vec{\omega}_n^h)\,\mathrm{d}t \right|. \tag{A.15}$$

We recall that the envelope of the white Gaussian noise is Rayleigh distributed so under hypothesis H_0, the matched filter output d_n is also Rayleigh distributed. The

desired expectation is then given by

$$\begin{aligned}
E\{d_n^2|H_0\} &= E\left\{\left|\int_{-\infty}^{\infty}\frac{n_n(t)}{\sqrt{N_{0n}}}p_n^*(t;\vec{\tau}_n^h,\vec{\omega}_n^h)\,\mathrm{d}t\right|^2\right\} \\
&= E\left\{\left[\int_{-\infty}^{\infty}\frac{n_n(t)}{\sqrt{N_{0n}}}p_n^*(t;\vec{\tau}_n^h,\vec{\omega}_n^h)\,\mathrm{d}t\right]\left[\int_{-\infty}^{\infty}\frac{n_n(\alpha)}{\sqrt{N_{0n}}}p_n^*(\alpha;\vec{\tau}_n^h,\vec{\omega}_n^h)\,\mathrm{d}\alpha\right]^*\right\} \\
&= E\left\{\left[\int_{-\infty}^{\infty}\frac{n_n(t)}{\sqrt{N_{0n}}}p_n^*(t;\vec{\tau}_n^h,\vec{\omega}_n^h)\,\mathrm{d}t\right]\left[\int_{-\infty}^{\infty}\frac{n_n^*(\alpha)}{\sqrt{N_{0n}}}p_n(\alpha;\vec{\tau}_n^h,\vec{\omega}_n^h)\,\mathrm{d}\alpha\right]\right\} \\
&= E\left\{\int_{-\infty}^{\infty}\int_{-\infty}^{\infty}\frac{1}{N_{0n}}n_n(t)n_n^*(\alpha)p_n^*(t;\vec{\tau}_n^h,\vec{\omega}_n^h)p_n(\alpha;\vec{\tau}_n^h,\vec{\omega}_n^h)\,\mathrm{d}t\mathrm{d}\alpha\right\} \\
&= \int_{-\infty}^{\infty}\int_{-\infty}^{\infty}E\left\{\frac{1}{N_{0n}}n_n(t)n_n^*(\alpha)p_n^*(t;\vec{\tau}_n^h,\vec{\omega}_n^h)p_n(\alpha;\vec{\tau}_n^h,\vec{\omega}_n^h)\right\}\mathrm{d}t\mathrm{d}\alpha \\
&= \frac{1}{N_{0n}}\int_{-\infty}^{\infty}\int_{-\infty}^{\infty}E\left\{n_n(t)n_n^*(\alpha)\right\}E\left\{p_n^*(t;\vec{\tau}_n^h,\vec{\omega}_n^h)p_n(\alpha;\vec{\tau}_n^h,\vec{\omega}_n^h)\right\}\mathrm{d}t\mathrm{d}\alpha.
\end{aligned}$$

We next recall that white noise has unilateral power spectral density $S(\omega) = N_{0n}$ (in contrast to the more familiar bilateral power spectral density given by $S(\omega) = N_{0n}/2$) and corresponding autocorrelation

$$E\{n_n(t)n_n^*(\alpha)\} = N_{0n}\delta(t-\alpha) \tag{A.16}$$

so that

$$\begin{aligned}
E\{d_n^2|H_0\} &= \frac{1}{N_{0n}}\int_{-\infty}^{\infty}\int_{-\infty}^{\infty}N_{0n}\delta(t-\alpha)E\left\{p_n^*(t;\vec{\tau}_n^h,\vec{\omega}_n^h)p_n(\alpha;\vec{\tau}_n^h,\vec{\omega}_n^h)\right\}\mathrm{d}t\mathrm{d}\alpha \\
&= \int_{-\infty}^{\infty}E\left\{p_n^*(t;\vec{\tau}_n^h,\vec{\omega}_n^h)p_n(t;\vec{\tau}_n^h,\vec{\omega}_n^h)\right\}\mathrm{d}t \\
&= E\left\{\int_{-\infty}^{\infty}p_n^*(t;\vec{\tau}_n^h,\vec{\omega}_n^h)p_n(t;\vec{\tau}_n^h,\vec{\omega}_n^h)\right\} \\
&= 1
\end{aligned}$$

by (A.11). We recall (A.4) and write the probability density function for the Rayleigh distributed matched filter output under hypothesis H_0 as

$$p(d_n|H_0) = R\left(d_n,\sqrt{\frac{1}{2}E\{d_n^2|H_0\}}\right) = R\left(d_n,\sqrt{\frac{1}{2}}\right). \tag{A.17}$$

A.3.2 Probability Density Under H_1

Under H_1 the received data at the n^{th} receiver is

$$r_n(t) = \frac{a_n B_n \mu_n \sqrt{E_{m=1}}}{R_{\boldsymbol{x},m=1} R_{\boldsymbol{x},n}} p_n(t; \vec{\tau}_n^a, \vec{\omega}_n^a) + n_n(t) \tag{A.18}$$

and so the output of the matched filter is given by

$$d_n = \left| \int_{-\infty}^{\infty} \left(\frac{a_n B_n \mu_n \sqrt{E_{m=1}}}{R_{\boldsymbol{x},m=1} R_{\boldsymbol{x},n}} p_n(t; \vec{\tau}_n^a, \vec{\omega}_n^a) + n_n(t) \right) \frac{1}{\sqrt{N_{0n}}} p_n^*(t; \vec{\tau}_n^h, \vec{\omega}_n^h) \, \mathrm{d}t \right|. \tag{A.19}$$

We recall that the amplitude A_n of the complex gain a_n is Rayleigh distributed, as is the envelope of the noise, and so under hypothesis H_1 the matched filter output d_n is also Rayleigh distributed. We let

$$\tilde{p}_n^a(t) = \frac{a_n B_n \mu_n \sqrt{E_{m=1}}}{R_{\boldsymbol{x},m=1} R_{\boldsymbol{x},n}} p_n(t; \vec{\tau}_n^a, \vec{\omega}_n^a) \tag{A.20}$$

denote the portion of the received data that corresponds to the scaled, time-delayed, and Doppler-shifted composite transmit waveform scattered from a true target so that (A.18) can be written in terms of (A.20) as

$$r_n(t) = \tilde{p}_n^a(t) + n_n(t). \tag{A.21}$$

We choose

$$E\{\tilde{p}_n^a(t) \tilde{p}_n^{a*}(\alpha)\} = \frac{2A_{0n}^2 B_n^2 \mu_n^2 E_{m=1}}{R_{\boldsymbol{x},m=1}^2 R_{\boldsymbol{x},n}^2} \delta(t - \alpha), \tag{A.22}$$

recalling $E\{A_n^2\} = 2A_{0n}^2$ from (A.3), and so

$$E\{r_n(t) r_n^*(\alpha)\} = \left(\frac{2A_{0n}^2 B_n^2 \mu_n^2 E_{m=1}}{R_{\boldsymbol{x},m=1}^2 R_{\boldsymbol{x},n}^2} + N_{0n} \right) \delta(t - \alpha) \tag{A.23}$$

from (A.16). The desired expectation is then given by

$$\begin{aligned}
E\{d_n^2|H_1\} &= \frac{1}{N_{0n}}\int_{-\infty}^{\infty}\int_{-\infty}^{\infty} E\left\{r_n(t)r_n^*(\alpha)\right\} E\left\{p_n^*(t;\vec{\tau}_n^h,\vec{\omega}_n^h)p_n(\alpha;\vec{\tau}_n^h,\vec{\omega}_n^h)\right\}\mathrm{d}t\mathrm{d}\alpha \\
&= \frac{1}{N_{0n}}\int_{-\infty}^{\infty}\int_{-\infty}^{\infty}\left(\frac{2A_{0n}^2B_n^2\mu_n^2E_{m=1}}{R_{\boldsymbol{x},m=1}^2R_{\boldsymbol{x},n}^2}+N_{0n}\right)\delta(t-\alpha) \\
&\qquad\qquad \times E\left\{p_n^*(t;\vec{\tau}_n^h,\vec{\omega}_n^h)p_n(\alpha;\vec{\tau}_n^h,\vec{\omega}_n^h)\right\}\mathrm{d}t\mathrm{d}\alpha \\
&= \left(\frac{2A_{0n}^2B_n^2\mu_n^2E_{m=1}}{N_{0n}R_{\boldsymbol{x},m=1}^2R_{\boldsymbol{x},n}^2}+1\right)\int_{-\infty}^{\infty} E\left\{p_n^*(t;\vec{\tau}_n^h,\vec{\omega}_n^h)p_n(t;\vec{\tau}_n^h,\vec{\omega}_n^h)\right\}\mathrm{d}t \\
&= \left(\frac{2A_{0n}^2B_n^2\mu_n^2E_{m=1}}{N_{0n}R_{\boldsymbol{x},m=1}^2R_{\boldsymbol{x},n}^2}+1\right) E\left\{\int_{-\infty}^{\infty} p_n^*(t;\vec{\tau}_n^h,\vec{\omega}_n^h)p_n(t;\vec{\tau}_n^h,\vec{\omega}_n^h)\mathrm{d}t\right\} \\
&= \frac{2A_{0n}^2B_n^2\mu_n^2E_{m=1}}{N_{0n}R_{\boldsymbol{x},m=1}^2R_{\boldsymbol{x},n}^2}+1. \qquad \text{(A.24)}
\end{aligned}$$

We let

$$\rho_n = \frac{4A_{0n}^2B_n^2\mu_n^2E_{m=1}}{N_{0n}R_{\boldsymbol{x},m=1}^2R_{\boldsymbol{x},n}^2} \qquad \text{(A.25)}$$

denote the signal-to-noise ratio at the n^{th} receiver and rewrite (A.24) as

$$E\{d_n^2|H_1\} = \frac{\rho_n}{2}+1. \qquad \text{(A.26)}$$

We again recall (A.4) and write the probability density function for the Rayleigh distributed matched filter output under hypothesis H_1 as

$$p(d_n|H_1) = R\left(d_n,\sqrt{\frac{1}{2}E\{d_n^2|H_1\}}\right) = R\left(d_n,\sqrt{\frac{1}{2}\left(\frac{\rho_n}{2}+1\right)}\right). \qquad \text{(A.27)}$$

A.3.3 Likelihood Ratio

The likelihood ratio test with threshold η is expressed

$$L(x) \underset{H_0}{\overset{H_1}{\gtrless}} \eta \qquad \text{(A.28)}$$

where the likelihood ratio $L(x)$ is given by

$$L(x) \equiv \frac{p(x|H_1)}{p(x|H_0)} \qquad \text{(A.29)}$$

[88].

We have derived the probability density function of the Rayleigh distributed d_n under H_0 and H_1

$$H_0 : p(d_n|H_0) = R\left(d_n, \sqrt{\frac{1}{2}}\right) = 2d_n \exp\left\{-d_n^2\right\} \tag{A.30}$$

$$H_1 : p(d_n|H_1) = R\left(d_n, \sqrt{\frac{1}{2}\left(\frac{\rho_n}{2}+1\right)}\right) = \frac{2d_n}{\frac{\rho_n}{2}+1}\exp\left\{\frac{-d_n^2}{\frac{\rho_n}{2}+1}\right\}. \tag{A.31}$$

We treat the data from each of the receivers as N independent observations and so the joint probability density of $\boldsymbol{d} = [d_1, \ldots, d_N]$ is the product of the individual probability densities and the likelihood ratio can be written as

$$\begin{aligned}
L(\boldsymbol{d}) &= \frac{\prod_{n=1}^{N} R\left(d_n, \sqrt{\frac{1}{2}\left(\frac{\rho_n}{2}+1\right)}\right)}{\prod_{n=1}^{N} R\left(d_n, \sqrt{\frac{1}{2}}\right)} \\
&= \frac{\prod_{n=1}^{N} \frac{2d_n}{\frac{\rho_n}{2}+1}\exp\left\{\frac{-d_n^2}{\frac{\rho_n}{2}+1}\right\}}{\prod_{n=1}^{N} 2d_n \exp\left\{-d_n^2\right\}} \\
&= \prod_{n=1}^{N}\left(\frac{1}{\frac{\rho_n}{2}+1}\right)\frac{\exp\left\{\frac{-d_n^2}{\frac{\rho_n}{2}+1}\right\}}{\exp\left\{-d_n^2\right\}} \\
&= \left(\prod_{n=1}^{N}\frac{1}{\frac{\rho_n}{2}+1}\right)\frac{\exp\left\{\sum_{n=1}^{N}\frac{-d_n^2}{\frac{\rho_n}{2}+1}\right\}}{\exp\left\{\sum_{n=1}^{N}-d_n^2\right\}} \\
&= \left(\prod_{n=1}^{N}\frac{1}{\frac{\rho_n}{2}+1}\right)\exp\left\{\sum_{n=1}^{N}\frac{-d_n^2}{\frac{\rho_n}{2}+1} - \sum_{n=1}^{N}-d_n^2\right\} \\
&= \left(\prod_{n=1}^{N}\frac{1}{\frac{\rho_n}{2}+1}\right)\exp\left\{\sum_{n=1}^{N}\frac{-d_n^2}{\frac{\rho_n}{2}+1} + d_n^2\right\} \\
&= \left(\prod_{2=1}^{N}\frac{1}{\frac{\rho_n}{2}+1}\right)\exp\left\{\sum_{n=1}^{N}\frac{\frac{\rho_n}{2}d_n^2}{\frac{\rho_n}{2}+1}\right\} \\
&= \underbrace{\left(\prod_{n=1}^{N}\frac{1}{\frac{\rho_n}{2}+1}\right)}_{C}\exp\left\{\sum_{n=1}^{N}\frac{\rho_n}{\rho_n+2}d_n^2\right\}.
\end{aligned} \tag{A.32}$$

Moving the quantity C into the threshold of the likelihood ratio we obtain

$$\tilde{L}(\boldsymbol{d}) = \exp\left\{\sum_{n=1}^{N} \frac{\rho_n}{\rho_n + 2} d_n^2\right\} \tag{A.33}$$

and we arrive at a sufficient statistic by taking the logarithm of both sides

$$\tilde{l}(\boldsymbol{d}) = \sum_{n=1}^{N} \frac{\rho_n}{\rho_n + 2} d_n^2. \tag{A.34}$$

A.3.4 Optimal Global Statistic

We define the optimal global statistic D in the Neyman-Pearson sense as

$$D = \sum_{n=1}^{N} w_n d_n^2 \tag{A.35}$$

with weight

$$w_n = \frac{\rho_n}{\rho_n + 2} \tag{A.36}$$

and signal-to-noise ratio

$$\rho_n = \frac{4A_{0n}^2 B_n^2 \mu_n^2 E_{m=1}}{N_{0n} R_{\boldsymbol{x},m=1}^2 R_{\boldsymbol{x},n}^2}. \tag{A.37}$$

These weights are used to optimally weight the matched filtered outputs from the individual receivers with the goal of maximizing the probability of detection for a given probability of false alarm.

A.4 Global Ambiguity Function

We write the global ambiguity function, or multistatic ambiguity function, as

$$\Theta(T_h, T_a, \Omega_h, \Omega_a) = \sum_{n=1}^{N} c_n \Theta_n(\vec{\tau}_n^h, \vec{\tau}_n^a, \vec{\omega}_n^h, \vec{\omega}_n^a) \tag{A.38}$$

where

$$\Theta_n(\vec{\tau}_n^h, \vec{\tau}_n^a, \vec{\omega}_n^h, \vec{\omega}_n^a) = \left| \int_{-\infty}^{\infty} p_n(t; \vec{\tau}_n^a, \vec{\omega}_n^a) p_n^*(t; \vec{\tau}_n^h, \vec{\omega}_n^h)\, \mathrm{d}t \right|^2 \tag{A.39}$$

is the ambiguity function for the n^{th} receiver in terms of the composite waveforms corresponding to a true and hypothetical target and

$$T_h = \{\tau^h_{m,n}\}_{M\times N}, \qquad T_a = \{\tau^a_{m,n}\}_{M\times N}$$
$$\Omega_h = \{\omega^h_{m,n}\}_{M\times N}, \qquad \Omega_a = \{\omega^a_{m,n}\}_{M\times N}.$$

The weights c_n are defined subject to $\sum_{n=1}^{N} c_n = 1$,

$$\Theta(T_a, T_a, \Omega_a, \Omega_a) = 1, \tag{A.40}$$

and

$$\Theta(T_h, T_a, \Omega_h, \Omega_a) = \frac{1}{K} E\{D_{\mathrm{s}}\} \tag{A.41}$$

where K is a normalization constant and D_{s} is the global statistic when only signal is present in the received data. We observe that the global ambiguity function (A.38) is a weighted sum of the output of the matched filter (A.15) squared.

We next solve for K and obtain the weights, c_n, of the individual ambiguity functions. We let d_{sn} denote the output of the matched filter when only signal is present in the received data

$$d_{sn} = \left| \int_{-\infty}^{\infty} \frac{a_n B_n \mu_n \sqrt{E_{m=1}}}{\sqrt{N_{0n}} R_{\boldsymbol{x},m=1} R_{\boldsymbol{x},n}} p_n(t; \vec{\tau}^a_n, \vec{\omega}^a_n) p^*_n(t; \vec{\tau}^h_n, \vec{\omega}^h_n)\, \mathrm{d}t \right| \tag{A.42}$$

so that

$$\begin{aligned} E\left\{d^2_{sn}\right\} &= E\left\{ \left| \int_{-\infty}^{\infty} \frac{a_n B_n \mu_n \sqrt{E_{m=1}}}{\sqrt{N_{0n}} R_{\boldsymbol{x},m=1} R_{\boldsymbol{x},n}} p_n(t; \vec{\tau}^a_n, \vec{\omega}^a_n) p^*_n(t; \vec{\tau}^h_n, \vec{\omega}^h_n)\, \mathrm{d}t \right|^2 \right\} \\ &= E\left\{ \left| \frac{a_n B_n \mu_n \sqrt{E_{m=1}}}{\sqrt{N_{0n}} R_{\boldsymbol{x},m=1} R_{\boldsymbol{x},n}} \right|^2 \right\} \left| \int_{-\infty}^{\infty} p_n(t; \vec{\tau}^a_n, \vec{\omega}^a_n) p^*_n(t; \vec{\tau}^h_n, \vec{\omega}^h_n)\, \mathrm{d}t \right|^2 \\ &= \frac{2A^2_{0n} B^2_n \mu^2_n E_{m=1}}{N_{0n} R^2_{\boldsymbol{x},m=1} R^2_{\boldsymbol{x},n}} \Theta_n(\vec{\tau}^h_n, \vec{\tau}^a_n, \vec{\omega}^h_n, \vec{\omega}^a_n) \\ &= \frac{\rho_n}{2} \Theta_n(\vec{\tau}^h_n, \vec{\tau}^a_n, \vec{\omega}^h_n, \vec{\omega}^a_n). \end{aligned} \tag{A.43}$$

It follows that

$$\begin{aligned} E\{D_{\mathrm{s}}\} &= E\left\{\sum_{n=1}^{N} w_n d_{\mathrm{s}n}^2\right\} \\ &= \sum_{n=1}^{N} w_n E\{d_{\mathrm{s}n}^2\} \\ &= \sum_{n=1}^{N} w_n \frac{\rho_n}{2} \Theta_n(\vec{\tau}_n^h, \vec{\tau}_n^a, \vec{\omega}_n^h, \vec{\omega}_n^a) \\ &= \sum_{n=1}^{N} \frac{\rho_n^2}{2\left(\rho_n+2\right)} \Theta_n(\vec{\tau}_n^h, \vec{\tau}_n^a, \vec{\omega}_n^h, \vec{\omega}_n^a) \end{aligned}$$

and by (A.41)

$$\begin{aligned} \Theta(T_a, T_a, \Omega_a, \Omega_a) &= \frac{1}{K} E\{D_{\mathrm{s}}\}\Big|_{T_h=T_a, \Omega_h=\Omega_a} \\ &= \frac{1}{K} \sum_{n=1}^{N} \frac{\rho_n^2}{2\left(\rho_n+2\right)} \Theta_n(\vec{\tau}_n^a, \vec{\tau}_n^a, \vec{\omega}_n^a, \vec{\omega}_n^a) \\ &= \frac{1}{K} \sum_{n=1}^{N} \frac{\rho_n^2}{2\left(\rho_n+2\right)}. \end{aligned} \tag{A.44}$$

We recall (A.40) and solve (A.44) for K to obtain

$$K = \sum_{n=1}^{N} \frac{\rho_n^2}{2\left(\rho_n+2\right)} \tag{A.45}$$

and the normalized weight c_n of the ambiguity function of the n^{th} receiver becomes

$$c_n = \frac{\frac{\rho_n^2}{2(\rho_n+2)}}{\sum_{k=1}^{N} \frac{\rho_k^2}{2(\rho_k+2)}}, \ n = 1, ..., N. \tag{A.46}$$

It follows that the global ambiguity function, or statistically derived multistatic ambiguity function, is given by

$$\Theta(T_h, T_a, \Omega_h, \Omega_a) = \sum_{n=1}^{N} c_n \Theta_n(\vec{\tau}_n^h, \vec{\tau}_n^a, \vec{\omega}_n^h, \vec{\omega}_n^a)$$

where

$$\Theta_n(\vec{\tau}_n^h, \vec{\tau}_n^a, \vec{\omega}_n^h, \vec{\omega}_n^a) = \left| \int_{-\infty}^{\infty} p_n(t; \vec{\tau}_n^a, \vec{\omega}_n^a) p_n^*(t; \vec{\tau}_n^h, \vec{\omega}_n^h)\, \mathrm{d}t \right|^2,$$

$$c_n = \frac{\frac{\rho_n^2}{2(\rho_n+2)}}{\sum_{k=1}^{N} \frac{\rho_k^2}{2(\rho_k+2)}},$$

$$\rho_n = \frac{4A_{0n}^2 B_n^2 \mu_n^2 E_{m=1}}{N_{0n} R_{\boldsymbol{x},m=1}^2 R_{\boldsymbol{x},n}^2},$$

and $p_n(t; \vec{\tau}_n^a, \vec{\omega}_n^a)$ and $p_n(t; \vec{\tau}_n^h, \vec{\omega}_n^h)$ are the composite waveforms corresponding to a true and hypothetical target, respectively.

We can also write the global ambiguity function in terms of $\boldsymbol{x}$, $\boldsymbol{v}$, $\boldsymbol{p}$, and $\boldsymbol{u}$, where $\boldsymbol{x}$ and $\boldsymbol{v}$ are respectively the actual vector position and velocity of the target, and $\boldsymbol{p}$ and $\boldsymbol{u}$ correspond to a hypothetical vector position and velocity of the target so that

$$\Theta(\boldsymbol{p}, \boldsymbol{u}, \boldsymbol{x}, \boldsymbol{v}) = \sum_{n=1}^{N} c_n \Theta_n(\boldsymbol{p}, \boldsymbol{u}, \boldsymbol{x}, \boldsymbol{v}) \tag{A.47}$$

where

$$\tau_{m,n}^a = \frac{R_{\boldsymbol{x},m} + R_{\boldsymbol{x},n}}{\mathrm{c}_0}, \qquad \tau_{m,n}^h = \frac{R_{\boldsymbol{p},m} + R_{\boldsymbol{p},n}}{\mathrm{c}_0},$$

$$\omega_{m,n}^a = \omega_m \beta_{\boldsymbol{x},\boldsymbol{v}}, \qquad \omega_{m,n}^h = \omega_m \beta_{\boldsymbol{p},\boldsymbol{u}},$$

with

$$\beta_{\boldsymbol{x},\boldsymbol{v}} = -(\hat{R}_{\boldsymbol{x},m} + \hat{R}_{\boldsymbol{x},n}) \cdot \boldsymbol{v}/\mathrm{c}_0,$$
$$\beta_{\boldsymbol{p},\boldsymbol{u}} = -(\hat{R}_{\boldsymbol{p},m} + \hat{R}_{\boldsymbol{p},n}) \cdot \boldsymbol{u}/\mathrm{c}_0.$$

APPENDIX B
Properties Concerning Differentiation of Certain Spatial Integrals

B.1 Motivation

The derivation of the expression for the electric field $\boldsymbol{E}$ in Section 3.4.3 makes use of the property

$$\nabla\left(\nabla\cdot\int_{\epsilon(\boldsymbol{r})}^{V}G(\boldsymbol{r}-\boldsymbol{r}')\boldsymbol{F}(\boldsymbol{r}')\mathrm{d}\boldsymbol{r}'\right)=\int_{\epsilon(\boldsymbol{r})}^{V}\nabla(\nabla\cdot G(\boldsymbol{r}-\boldsymbol{r}')\boldsymbol{F}(\boldsymbol{r}'))\mathrm{d}\boldsymbol{r}' - \frac{1}{3}\boldsymbol{F}(\boldsymbol{r}). \tag{B.1}$$

The proof of this property is achieved alongside the derivation of

$$\nabla\times\nabla\times\int_{\epsilon(\boldsymbol{r})}^{V}G(\boldsymbol{r}-\boldsymbol{r}')\boldsymbol{F}(\boldsymbol{r}')\mathrm{d}\boldsymbol{r}'=\int_{\epsilon(\boldsymbol{r})}^{V}\nabla\times\nabla\times G(\boldsymbol{r}-\boldsymbol{r}')\boldsymbol{F}(\boldsymbol{r}'))\mathrm{d}\boldsymbol{r}' + \frac{2}{3}\boldsymbol{F}(\boldsymbol{r}) \tag{B.2}$$

[62, 69] with Green's function

$$G(\boldsymbol{r})=\frac{\mathrm{e}^{\mathrm{i}k|\boldsymbol{r}|}}{4\pi|\boldsymbol{r}|}. \tag{B.3}$$

In (B.1) and (B.2) V is a volume enclosed by a regular closed surface Σ and $\epsilon(\boldsymbol{r})$ is an infinitesimal sphere centered at $\boldsymbol{r}$. Lemma B.2 is used in the theory of dispersion and specifically the derivation of the Lorentz-Lorenz law.

B.2 Problem Set-up

We assume $\boldsymbol{F}(\boldsymbol{r})$ is an arbitrary continuous vector field and has continuous derivatives of a sufficiently high order. Likewise, we assume $G(\boldsymbol{r}-\boldsymbol{r}')$ is continuous in $\boldsymbol{r}$ and $\boldsymbol{r}'$ with continuous derivatives except at $\boldsymbol{r}=\boldsymbol{r}'$ where $G(\boldsymbol{r}-\boldsymbol{r}')$ may have a singularity of the form $|\boldsymbol{r}-\boldsymbol{r}'|$. Throughout the derivation we will consider the

integral

$$\boldsymbol{I}(\boldsymbol{r}) = \int_{v_s(\boldsymbol{r})}^{V} G(\boldsymbol{r}, \boldsymbol{r}')\boldsymbol{F}(\boldsymbol{r}')\mathrm{d}\boldsymbol{r}' \tag{B.4}$$

where $v_s(\boldsymbol{r})$ is a small volume element completely contained within V that surrounds a point $\boldsymbol{r} \in V$ lying a sufficient distance within Σ. All volume elements $v_s(\boldsymbol{r})$ are spheres of radius s with surface $\sigma_s(\boldsymbol{r})$. The notation used to define the bounds in (B.4) indicates that the integrand is integrated within the entire volume V excluding the small sphere $v_s(\boldsymbol{r})$. In our derivation we wish to examine what happens as $v_s(\boldsymbol{r})$ shrinks to $\boldsymbol{r}$, or the limit as the radius $s \to 0$.

B.3 Relation for Scalar Functions

We will first derive the expression

Lemma.

$$\begin{aligned}\frac{\partial}{\partial\alpha}\int_{v_s(\boldsymbol{r})}^{V} G(\boldsymbol{r}, \boldsymbol{r}')F_j(\boldsymbol{r}')\,d\boldsymbol{r}' = &\int_{v_s(\boldsymbol{r})}^{V} \frac{\partial}{\partial\alpha}G(\boldsymbol{r}, \boldsymbol{r}')F_j(\boldsymbol{r}')\,d\boldsymbol{r}' \\ &- \int^{\sigma_s(\boldsymbol{r})} G(\boldsymbol{r}, \boldsymbol{r}')F_j(\boldsymbol{r}')n_\alpha\,dS'\end{aligned} \tag{B.5}$$

where α is one component of an arbitrary coordinate system, $F_j(\boldsymbol{r})$ is a scalar component of the vector field $\boldsymbol{F}(\boldsymbol{r})$, n_α is the α component of the unit radial vector $\hat{\boldsymbol{n}}$ pointing outward from $\boldsymbol{r}$ towards the surface $\sigma_s(\boldsymbol{r})$, and $\mathrm{d}S'$ is the surface element.

Proof. [62] Without loss of generality we consider the x-component in a Cartesian coordinate system and let $H = G(\boldsymbol{r}, \boldsymbol{r}')F_j(\boldsymbol{r}')$. We will also let $\mathrm{d}V' = \mathrm{d}\boldsymbol{r}'$ denote the volume element and the expression we wish to derive, (B.5), becomes

$$\frac{\partial}{\partial x}\int_{v_s(\boldsymbol{r})}^{V} H\mathrm{d}V' = \int_{v_s(\boldsymbol{r})}^{V} \frac{\partial H}{\partial x}\mathrm{d}V' - \int^{\sigma_s(\boldsymbol{r})} Hn_x\mathrm{d}S'. \tag{B.6}$$

From Leibniz's rule for differentiation under the integral, for a differentiable scalar function H we can write

$$\frac{\partial}{\partial x}\int_{v_s(\boldsymbol{r}_1)}^{V} H\mathrm{d}V' = \int_{v_s(\boldsymbol{r}_1)}^{V} \frac{\partial H}{\partial x}\mathrm{d}V' + \lim_{\delta x\to 0}\left[\int_{v_s(\boldsymbol{r}_2)}^{V} H\mathrm{d}V' - \int_{v_s(\boldsymbol{r}_1)}^{V} H\mathrm{d}V'\right] \tag{B.7}$$

where $\boldsymbol{r}_1 = (x, y, z)$ and $\boldsymbol{r}_2 = (x + \delta x, y, z)$ denote the centers of spheres $v(\boldsymbol{r}_1)$ and $v(\boldsymbol{r}_1)$ with surfaces $\sigma_s(\boldsymbol{r}_1)$ and $\sigma_s(\boldsymbol{r}_2)$. Consider Figure B.1 and observe that the difference of the two integrals in (B.7) is equivalent to the contribution from the two shaded regions.

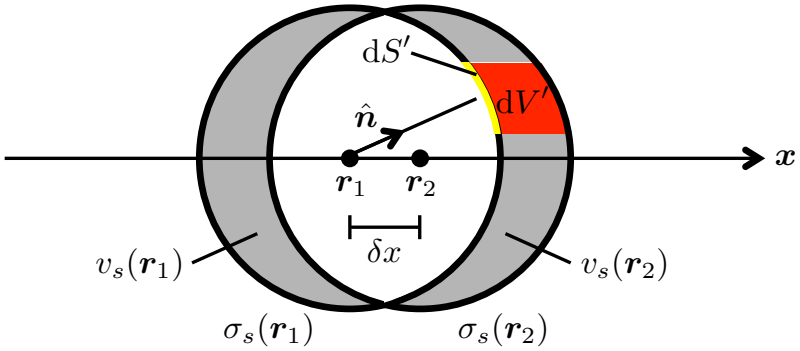

Figure B.1: Spheres $v_s(\boldsymbol{r}_1)$ and $v_s(\boldsymbol{r}_2)$ with surfaces $\sigma_s(\boldsymbol{r}_1)$ and $\sigma_s(\boldsymbol{r}_2)$, respectively.

The volume element $\mathrm{d}V'$ can be rewritten in terms of the surface element $\mathrm{d}S'$, the x-component of the outward normal n_x, and the small distance δx

$$\mathrm{d}V' = -\mathrm{d}S' n_x \delta x$$

and (B.7) reduces to

$$\frac{\partial}{\partial x}\int_{v_s(\boldsymbol{r}_1)}^{V} H \mathrm{d}V' = \int_{v_s(\boldsymbol{r}_1)}^{V} \frac{\partial H}{\partial x}\mathrm{d}V' - \int^{\sigma(\boldsymbol{r}_1)} H n_x \mathrm{d}S'. \tag{B.8}$$

Substituting $H = G(\boldsymbol{r}, \boldsymbol{r}')F_j(\boldsymbol{r}')$ and $\mathrm{d}V' = \mathrm{d}\boldsymbol{r}'$ back into (B.8) and writing the partial derivatives in terms of an arbitrary component α we obtain the desired relation (B.5).

We observe that the last term in (B.5)

$$\int^{\sigma_s(\boldsymbol{r})} G(\boldsymbol{r}, \boldsymbol{r}')F_j(\boldsymbol{r}')n_\alpha \mathrm{d}S'$$

is a surface integral that will vanish as $s \to 0$. In the limit (B.5) becomes

$$\frac{\partial}{\partial \alpha}\int_{\epsilon(\boldsymbol{r})}^{V} G(\boldsymbol{r}, \boldsymbol{r}')F_j(\boldsymbol{r}')\mathrm{d}\boldsymbol{r}' = \int_{\epsilon(\boldsymbol{r})}^{V} \frac{\partial}{\partial \alpha} G(\boldsymbol{r}, \boldsymbol{r}')F_j(\boldsymbol{r}')\mathrm{d}\boldsymbol{r}'. \tag{B.9}$$

B.4 Higher Order Derivatives

We next examine the result of repeated application of the property given by (B.5). We first consider the second partial with respect to the arbitrary component α

$$\begin{aligned}\frac{\partial^2}{\partial\alpha^2}\int_{v_s(\boldsymbol{r})}^{V} G(\boldsymbol{r},\boldsymbol{r}')F_j(\boldsymbol{r}')\mathrm{d}\boldsymbol{r}' =&\frac{\partial}{\partial\alpha}\left(\int_{v_s(\boldsymbol{r})}^{V}\frac{\partial}{\partial\alpha}G(\boldsymbol{r},\boldsymbol{r}')F_j(\boldsymbol{r}')\mathrm{d}\boldsymbol{r}'\right.\\ &\left.-\int^{\sigma_s(\boldsymbol{r})} G(\boldsymbol{r},\boldsymbol{r}')F_j(\boldsymbol{r}')n_\alpha\mathrm{d}S'\right)\\ =&\int_{v_s(\boldsymbol{r})}^{V}\frac{\partial^2}{\partial\alpha^2}G(\boldsymbol{r},\boldsymbol{r}')F_j(\boldsymbol{r}')\mathrm{d}\boldsymbol{r}'\\ &-\int^{\sigma_s(\boldsymbol{r})}\frac{\partial}{\partial\alpha}\left(G(\boldsymbol{r},\boldsymbol{r}')F_j(\boldsymbol{r}')\right)n_\alpha\mathrm{d}S'\\ &-\frac{\partial}{\partial\alpha}\int^{\sigma_s(\boldsymbol{r})} G(\boldsymbol{r},\boldsymbol{r}')F_j(\boldsymbol{r}')n_\alpha\mathrm{d}S'. \qquad \text{(B.10)}\end{aligned}$$

As $s\to 0$ the last term will vanish as discussed in Section B.3. We observe

$$\frac{\partial G}{\partial\alpha}=\frac{\mathrm{d}G}{\mathrm{d}r}\frac{\partial r}{\partial\alpha}=-n_\alpha\frac{\mathrm{d}}{\mathrm{d}r}\frac{\mathrm{e}^{\mathrm{i}kr}}{4\pi r}=-n_\alpha\frac{\mathrm{e}^{\mathrm{i}kr}}{4\pi r}\left(\mathrm{i}k-\frac{1}{r}\right)=n_\alpha\frac{\mathrm{e}^{\mathrm{i}kr}}{4\pi r}\left(\frac{1}{r}-\mathrm{i}k\right)$$

where $r=|\boldsymbol{r}-\boldsymbol{r}'|$ and the surface element of a sphere can be rewritten in terms of the solid angle element $\mathrm{d}\Omega'$ as $\mathrm{d}S'=s^2\mathrm{d}\Omega'$. It follows that the middle term of (B.10) can be rewritten

$$\begin{aligned}\int^{\sigma_s(\boldsymbol{r})}\frac{\partial}{\partial\alpha}\left(G(\boldsymbol{r},\boldsymbol{r}')F_j(\boldsymbol{r}')\right)n_\alpha\mathrm{d}S' =&\int^{\Omega}F_j(\boldsymbol{r}')\frac{\partial G(\boldsymbol{r},\boldsymbol{r}')}{\partial\alpha}n_\alpha s^2\mathrm{d}\Omega'\\ =&\frac{1}{4\pi}\int^{\Omega}F_j(\boldsymbol{r}')n_\alpha^2\mathrm{e}^{\mathrm{i}ks}\left(1-\mathrm{i}ks\right)\mathrm{d}\Omega' \qquad \text{(B.11)}\end{aligned}$$

where Ω is the surface of the unit sphere. We recall that the average value of two components, α and β, of the unit vector $\hat{\boldsymbol{n}}$ over the surface of the unit sphere is

given by the expression

$$< n_\alpha n_\beta >= \frac{\int_0^{2\pi}\int_0^{\pi} n_\alpha n_\beta \sin\phi \, \mathrm{d}\phi \mathrm{d}\theta}{\int_0^{2\pi}\int_0^{\pi} \sin\phi \, \mathrm{d}\phi \mathrm{d}\theta} \tag{B.12}$$

$$= \frac{1}{3}\delta_{\alpha\beta} \tag{B.13}$$

where $\delta_{\alpha\beta}$ is the Kronecker delta. This expression is easily obtained by substituting the x, y, and z components of $\hat{\boldsymbol{n}}$ in spherical coordinates

$$\hat{\boldsymbol{n}} = \begin{bmatrix} \cos\theta \sin\phi \\ \sin\theta \sin\phi \\ \cos\phi \end{bmatrix} \tag{B.14}$$

into the numerator of (B.12) as n_α and n_β. We also note that the surface area of the unit sphere is 4π and this quantity cancels out from the numerator and denominator of (B.12). As $s \to 0$ expression (B.11) becomes

$$\int^{\sigma_s(\boldsymbol{r})} \frac{\partial}{\partial\alpha} \left(G(\boldsymbol{r}, \boldsymbol{r}') F_j(\boldsymbol{r}') \right) n_\alpha \mathrm{d}S' = \frac{1}{3} F_j(\boldsymbol{r})$$

where $F_j(\boldsymbol{r}')$ has gone to $F_j(\boldsymbol{r})$ in the limit. As $s \to 0$, $v_s(\boldsymbol{r}) \to \epsilon(\boldsymbol{r})$ and the second partial of (B.4) with respect to α reduces to

$$\frac{\partial^2}{\partial\alpha^2} \int_{\epsilon(\boldsymbol{r})}^{V} G(\boldsymbol{r}, \boldsymbol{r}') F_j(\boldsymbol{r}') \mathrm{d}\boldsymbol{r}' = \int_{\epsilon(\boldsymbol{r})}^{V} \frac{\partial^2}{\partial\alpha^2} G(\boldsymbol{r}, \boldsymbol{r}') F_j(\boldsymbol{r}') \mathrm{d}\boldsymbol{r}' - \frac{1}{3} F_j(\boldsymbol{r}). \tag{B.15}$$

We next consider the second mixed partial derivative of (B.4) and let β denote

a component different from α

$$\begin{aligned}\frac{\partial^2}{\partial\beta\partial\alpha}\int_{v_s(\boldsymbol{r})}^{V} G(\boldsymbol{r},\boldsymbol{r}')F_j(\boldsymbol{r}')\mathrm{d}\boldsymbol{r}' =& \frac{\partial}{\partial\beta}\left(\int_{v_s(\boldsymbol{r})}^{V}\frac{\partial}{\partial\alpha}G(\boldsymbol{r},\boldsymbol{r}')F_j(\boldsymbol{r}')\mathrm{d}\boldsymbol{r}'\right.\\ &\left.-\int^{\sigma_s(\boldsymbol{r})} G(\boldsymbol{r},\boldsymbol{r}')F_j(\boldsymbol{r}')n_\alpha \mathrm{d}S'\right)\\ =&\int_{v_s(\boldsymbol{r})}^{V}\frac{\partial^2}{\partial\beta\partial\alpha}G(\boldsymbol{r},\boldsymbol{r}')F_j(\boldsymbol{r}')\mathrm{d}\boldsymbol{r}'\\ &-\int^{\sigma_s(\boldsymbol{r})}\frac{\partial}{\partial\alpha}\left(G(\boldsymbol{r},\boldsymbol{r}')F_j(\boldsymbol{r}')\right)n_\beta\mathrm{d}S'\\ &-\frac{\partial}{\partial\beta}\int^{\sigma_s(\boldsymbol{r})} G(\boldsymbol{r},\boldsymbol{r}')F_j(\boldsymbol{r}')n_\alpha\mathrm{d}S'. \end{aligned}\tag{B.16}$$

As in (B.10) the last term tends to zero as $s\to 0$ and the middle term which can be rewritten

$$\begin{aligned}\int^{\sigma_s(\boldsymbol{r})}\frac{\partial}{\partial\alpha}\left(G(\boldsymbol{r},\boldsymbol{r}')F_j(\boldsymbol{r}')\right)n_\beta\mathrm{d}S' =& \int^{\sigma_s(\boldsymbol{r})} F_j(\boldsymbol{r}')\frac{\partial G(\boldsymbol{r},\boldsymbol{r}')}{\partial\alpha}n_\beta s^2\mathrm{d}\Omega'\\ =&\frac{1}{4\pi}\int^{\sigma_s(\boldsymbol{r})} F_j(\boldsymbol{r}')n_\alpha n_\beta \mathrm{e}^{\mathrm{i}ks}\left(1-\mathrm{i}ks\right)\mathrm{d}\Omega'\end{aligned}$$

also goes to zero as $s\to 0$ due to (B.13). The mixed partial derivative reduces to a single term as $s\to 0$

$$\frac{\partial^2}{\partial\beta\partial\alpha}\int_{\epsilon(\boldsymbol{r})}^{V} G(\boldsymbol{r},\boldsymbol{r}')F_j(\boldsymbol{r}')\mathrm{d}\boldsymbol{r}' = \int_{\epsilon(\boldsymbol{r})}^{V}\frac{\partial^2}{\partial\beta\partial\alpha}G(\boldsymbol{r},\boldsymbol{r}')F_j(\boldsymbol{r}')\mathrm{d}\boldsymbol{r}'.\tag{B.17}$$

B.5 Derivation of (B.1)

Lemma.

$$\begin{aligned}\nabla\left(\nabla\cdot\int_{\epsilon(\boldsymbol{r})}^{V} G(\boldsymbol{r}-\boldsymbol{r}')\boldsymbol{F}(\boldsymbol{r}')\,d\boldsymbol{r}'\right) =& \int_{\epsilon(\boldsymbol{r})}^{V}\nabla(\nabla\cdot G(\boldsymbol{r}-\boldsymbol{r}')\boldsymbol{F}(\boldsymbol{r}'))\,d\boldsymbol{r}'\\ &-\frac{1}{3}\boldsymbol{F}(\boldsymbol{r}).\end{aligned}\tag{B.18}$$

Proof. We first recall that in Cartesian coordinates (x, y, z) the gradient of the divergence of a vector field $\boldsymbol{F}$ yields

$$\nabla\left(\nabla\cdot\boldsymbol{F}\right)=\left(\frac{\partial^2F_x}{\partial x^2}+\frac{\partial^2F_y}{\partial x\partial y}+\frac{\partial^2F_z}{\partial x\partial z}\,,\frac{\partial^2F_x}{\partial y\partial x}+\frac{\partial^2F_y}{\partial y^2}+\frac{\partial^2F_z}{\partial y\partial z},\right.$$
$$\left.\frac{\partial^2F_x}{\partial z\partial x}+\frac{\partial^2F_y}{\partial z\partial y}+\frac{\partial^2F_z}{\partial z^2}\right). \tag{B.19}$$

We use (B.19) to consider the x-component of (B.18)

$$\begin{aligned}\left[\nabla\left(\nabla\cdot\int_{\epsilon(\boldsymbol{r})}^{V}G(\boldsymbol{r}-\boldsymbol{r}')\boldsymbol{F}(\boldsymbol{r}')\mathrm{d}\boldsymbol{r}'\right)\right]_x=&\frac{\partial^2}{\partial x^2}\int_{\epsilon(\boldsymbol{r})}^{V}G(\boldsymbol{r}-\boldsymbol{r}')F_x(\boldsymbol{r}')\mathrm{d}\boldsymbol{r}'\\&+\frac{\partial^2}{\partial x\partial y}\int_{\epsilon(\boldsymbol{r})}^{V}G(\boldsymbol{r}-\boldsymbol{r}')F_y(\boldsymbol{r}')\mathrm{d}\boldsymbol{r}'\\&+\frac{\partial^2}{\partial x\partial z}\int_{\epsilon(\boldsymbol{r})}^{V}G(\boldsymbol{r}-\boldsymbol{r}')F_z(\boldsymbol{r}')\mathrm{d}\boldsymbol{r}'\end{aligned} \tag{B.20}$$

and using the derived second order partial derivative properties from (B.15) and (B.17) we obtain

$$\begin{aligned}\left[\nabla\left(\nabla\cdot\int_{\epsilon(\boldsymbol{r})}^{V}G(\boldsymbol{r}-\boldsymbol{r}')\boldsymbol{F}(\boldsymbol{r}')\mathrm{d}\boldsymbol{r}'\right)\right]_x=&\int_{\epsilon(\boldsymbol{r})}^{V}\frac{\partial^2}{\partial x^2}G(\boldsymbol{r},\boldsymbol{r}')F_x(\boldsymbol{r}')\mathrm{d}\boldsymbol{r}'-\frac{1}{3}F_x(\boldsymbol{r})\\&+\int_{\epsilon(\boldsymbol{r})}^{V}\frac{\partial^2}{\partial x\partial y}G(\boldsymbol{r},\boldsymbol{r}')F_y(\boldsymbol{r}')\mathrm{d}\boldsymbol{r}'\\&+\int_{\epsilon(\boldsymbol{r})}^{V}\frac{\partial^2}{\partial x\partial z}G(\boldsymbol{r},\boldsymbol{r}')F_z(\boldsymbol{r}')\mathrm{d}\boldsymbol{r}'.\end{aligned} \tag{B.21}$$

Similarly, the y- and z-components have the form

$$\begin{aligned}\left[\nabla\left(\nabla\cdot\int_{\epsilon(\boldsymbol{r})}^{V}G(\boldsymbol{r}-\boldsymbol{r}')\boldsymbol{F}(\boldsymbol{r}')\mathrm{d}\boldsymbol{r}'\right)\right]_y=&\int_{\epsilon(\boldsymbol{r})}^{V}\frac{\partial^2}{\partial y\partial x}G(\boldsymbol{r},\boldsymbol{r}')F_x(\boldsymbol{r}')\mathrm{d}\boldsymbol{r}'\\&+\int_{\epsilon(\boldsymbol{r})}^{V}\frac{\partial^2}{\partial y^2}G(\boldsymbol{r},\boldsymbol{r}')F_y(\boldsymbol{r}')\mathrm{d}\boldsymbol{r}'-\frac{1}{3}F_y(\boldsymbol{r})\\&+\int_{\epsilon(\boldsymbol{r})}^{V}\frac{\partial^2}{\partial y\partial z}G(\boldsymbol{r},\boldsymbol{r}')F_z(\boldsymbol{r}')\mathrm{d}\boldsymbol{r}'\end{aligned} \tag{B.22}$$

$$\left[\nabla\left(\nabla\cdot\int_{\epsilon(\boldsymbol{r})}^{V}G(\boldsymbol{r}-\boldsymbol{r}')\boldsymbol{F}(\boldsymbol{r}')\mathrm{d}\boldsymbol{r}'\right)\right]_z = \int_{\epsilon(\boldsymbol{r})}^{V}\frac{\partial^2}{\partial z\partial x}G(\boldsymbol{r},\boldsymbol{r}')F_x(\boldsymbol{r}')\mathrm{d}\boldsymbol{r}' + \int_{\epsilon(\boldsymbol{r})}^{V}\frac{\partial^2}{\partial z\partial y}G(\boldsymbol{r},\boldsymbol{r}')F_y(\boldsymbol{r}')\mathrm{d}\boldsymbol{r}' + \int_{\epsilon(\boldsymbol{r})}^{V}\frac{\partial^2}{\partial z^2}G(\boldsymbol{r},\boldsymbol{r}')F_z(\boldsymbol{r}')\mathrm{d}\boldsymbol{r}' - \frac{1}{3}F_z(\boldsymbol{r}) \tag{B.23}$$

and by combining the results for the individual components we obtain (B.18).

B.6 Derivation of (B.2)

Lemma.

$$\nabla\times\nabla\times\int_{\epsilon(\boldsymbol{r})}^{V}G(\boldsymbol{r}-\boldsymbol{r}')\boldsymbol{F}(\boldsymbol{r}')\,d\boldsymbol{r}' = \int_{\epsilon(\boldsymbol{r})}^{V}\nabla\times\nabla\times G(\boldsymbol{r}-\boldsymbol{r}')\boldsymbol{F}(\boldsymbol{r}'))\,d\boldsymbol{r}' + \frac{2}{3}\boldsymbol{F}(\boldsymbol{r}) \tag{B.24}$$

Proof. As in the previous section we begin by recalling a vector identity; the curl of the curl of a vector field $\boldsymbol{F}$ yields

$$\nabla\times\nabla\times\boldsymbol{F} = \begin{pmatrix} \dfrac{\partial^2 F_y}{\partial y\partial x} + \dfrac{\partial^2 F_z}{\partial z\partial x} - \left(\dfrac{\partial^2}{\partial y^2}+\dfrac{\partial^2}{\partial z^2}\right)F_x, \\ \dfrac{\partial^2 F_x}{\partial x\partial y} + \dfrac{\partial^2 F_z}{\partial z\partial y} - \left(\dfrac{\partial^2}{\partial x^2}+\dfrac{\partial^2}{\partial z^2}\right)F_y, \\ \dfrac{\partial^2 F_x}{\partial x\partial z} + \dfrac{\partial^2 F_y}{\partial y\partial z} - \left(\dfrac{\partial^2}{\partial x^2}+\dfrac{\partial^2}{\partial y^2}\right)F_z \end{pmatrix}. \tag{B.25}$$

We use (B.25) to consider the x-component of (B.24)

$$\begin{aligned}\left[\nabla\times\nabla\times\int_{\epsilon(\boldsymbol{r})}^{V}G(\boldsymbol{r}-\boldsymbol{r}')\boldsymbol{F}(\boldsymbol{r}')\mathrm{d}\boldsymbol{r}'\right]_x =&\frac{\partial^2}{\partial y\partial x}\int_{\epsilon(\boldsymbol{r})}^{V}G(\boldsymbol{r}-\boldsymbol{r}')F_y(\boldsymbol{r}')\mathrm{d}\boldsymbol{r}'\\&+\frac{\partial^2}{\partial z\partial x}\int_{\epsilon(\boldsymbol{r})}^{V}G(\boldsymbol{r}-\boldsymbol{r}')F_z(\boldsymbol{r}')\mathrm{d}\boldsymbol{r}'\\&-\frac{\partial^2}{\partial y^2}\int_{\epsilon(\boldsymbol{r})}^{V}G(\boldsymbol{r}-\boldsymbol{r}')F_x(\boldsymbol{r}')\mathrm{d}\boldsymbol{r}'\\&-\frac{\partial^2}{\partial z^2}\int_{\epsilon(\boldsymbol{r})}^{V}G(\boldsymbol{r}-\boldsymbol{r}')F_x(\boldsymbol{r}')\mathrm{d}\boldsymbol{r}'\end{aligned}\tag{B.26}$$

and again using the derived second order partial derivative properties from (B.15) and (B.17) we obtain

$$\begin{aligned}\left[\nabla\times\nabla\times\int_{\epsilon(\boldsymbol{r})}^{V}G(\boldsymbol{r}-\boldsymbol{r}')\boldsymbol{F}(\boldsymbol{r}')\mathrm{d}\boldsymbol{r}'\right]_x =&\int_{\epsilon(\boldsymbol{r})}^{V}\frac{\partial^2}{\partial y\partial x}G(\boldsymbol{r},\boldsymbol{r}')F_y(\boldsymbol{r}')\mathrm{d}\boldsymbol{r}'\\&+\int_{\epsilon(\boldsymbol{r})}^{V}\frac{\partial^2}{\partial z\partial x}G(\boldsymbol{r},\boldsymbol{r}')F_z(\boldsymbol{r}')\mathrm{d}\boldsymbol{r}'\\&-\int_{\epsilon(\boldsymbol{r})}^{V}\frac{\partial^2}{\partial y^2}G(\boldsymbol{r},\boldsymbol{r}')F_x(\boldsymbol{r}')\mathrm{d}\boldsymbol{r}'\\&-\int_{\epsilon(\boldsymbol{r})}^{V}\frac{\partial^2}{\partial z^2}G(\boldsymbol{r},\boldsymbol{r}')F_x(\boldsymbol{r}')\mathrm{d}\boldsymbol{r}'+\frac{2}{3}F_x(\boldsymbol{r}).\end{aligned}\tag{B.27}$$

Similarly, the y- and z-components have the form

$$\begin{aligned}\left[\nabla\times\nabla\times\int_{\epsilon(\boldsymbol{r})}^{V}G(\boldsymbol{r}-\boldsymbol{r}')\boldsymbol{F}(\boldsymbol{r}')\mathrm{d}\boldsymbol{r}'\right]_y =&\int_{\epsilon(\boldsymbol{r})}^{V}\frac{\partial^2}{\partial x\partial y}G(\boldsymbol{r},\boldsymbol{r}')F_x(\boldsymbol{r}')\mathrm{d}\boldsymbol{r}'\\&+\int_{\epsilon(\boldsymbol{r})}^{V}\frac{\partial^2}{\partial z\partial y}G(\boldsymbol{r},\boldsymbol{r}')F_z(\boldsymbol{r}')\mathrm{d}\boldsymbol{r}'\\&-\int_{\epsilon(\boldsymbol{r})}^{V}\frac{\partial^2}{\partial x^2}G(\boldsymbol{r},\boldsymbol{r}')F_y(\boldsymbol{r}')\mathrm{d}\boldsymbol{r}'\\&-\int_{\epsilon(\boldsymbol{r})}^{V}\frac{\partial^2}{\partial z^2}G(\boldsymbol{r},\boldsymbol{r}')F_y(\boldsymbol{r}')\mathrm{d}\boldsymbol{r}'+\frac{2}{3}F_y(\boldsymbol{r})\end{aligned}\tag{B.28}$$

$$\left[\nabla\times\nabla\times\int_{\epsilon(\boldsymbol{r})}^{V}G(\boldsymbol{r}-\boldsymbol{r}')\boldsymbol{F}(\boldsymbol{r}')\mathrm{d}\boldsymbol{r}'\right]_z=\int_{\epsilon(\boldsymbol{r})}^{V}\frac{\partial^2}{\partial x\partial z}G(\boldsymbol{r},\boldsymbol{r}')F_x(\boldsymbol{r}')\mathrm{d}\boldsymbol{r}'+\int_{\epsilon(\boldsymbol{r})}^{V}\frac{\partial^2}{\partial y\partial z}G(\boldsymbol{r},\boldsymbol{r}')F_y(\boldsymbol{r}')\mathrm{d}\boldsymbol{r}'-\int_{\epsilon(\boldsymbol{r})}^{V}\frac{\partial^2}{\partial x^2}G(\boldsymbol{r},\boldsymbol{r}')F_z(\boldsymbol{r}')\mathrm{d}\boldsymbol{r}'-\int_{\epsilon(\boldsymbol{r})}^{V}\frac{\partial^2}{\partial y^2}G(\boldsymbol{r},\boldsymbol{r}')F_z(\boldsymbol{r}')\mathrm{d}\boldsymbol{r}'+\frac{2}{3}F_z(\boldsymbol{r}) \tag{B.29}$$

and by combining the results for the individual components we obtain (B.24).

APPENDIX C
Complex Inverse Fourier Transform of Certain Quantities

In this appendix we will provide a detailed explanation of the process used to find the complex inverse Fourier transforms given in (3.119) and (3.128).

C.1 Derivation of (3.119)

Equation (3.119) gives the inverse Fourier transform of the expression

$$\begin{aligned} F(\omega) &= \frac{\cos(kL_n) - \cos(kL_n\cos\theta_n)}{\omega\sin(kL_n)} \\ &= \mathrm{i}\frac{\mathrm{e}^{\mathrm{i}\omega\frac{L_n}{c_0}} + \mathrm{e}^{-\mathrm{i}\omega\frac{L_n}{c_0}} - \mathrm{e}^{\mathrm{i}\omega\frac{L_n}{c_0}\cos\theta_n} - \mathrm{e}^{-\mathrm{i}\omega\frac{L_n}{c_0}\cos\theta_n}}{\omega\left(\mathrm{e}^{\mathrm{i}\omega\frac{L_n}{c_0}} - \mathrm{e}^{-\mathrm{i}\omega\frac{L_n}{c_0}}\right)} \\ &= \mathrm{i}\frac{\mathrm{e}^{2\mathrm{i}\omega\frac{L_n}{c_0}} + 1 - \mathrm{e}^{\mathrm{i}\omega\frac{L_n}{c_0}(1+\cos\theta_n)} - \mathrm{e}^{\mathrm{i}\omega\frac{L_n}{c_0}(1-\cos\theta_n)}}{\omega\left(\mathrm{e}^{2\mathrm{i}\omega\frac{L_n}{c_0}} - 1\right)}. \end{aligned} \tag{C.1}$$

The desired transform is

$$f(t)_L = \frac{\mathrm{i}}{2\pi}\int_L \frac{\mathrm{e}^{-\mathrm{i}\omega t}\left(\mathrm{e}^{2\mathrm{i}\omega\frac{L_n}{c_0}} + 1 - \mathrm{e}^{\mathrm{i}\omega\frac{L_n}{c_0}(1+\cos\theta_n)} - \mathrm{e}^{\mathrm{i}\omega\frac{L_n}{c_0}(1-\cos\theta_n)}\right)}{\omega\left(\mathrm{e}^{2\mathrm{i}\omega\frac{L_n}{c_0}} - 1\right)}\mathrm{d}\omega \tag{C.2}$$

with the real line indented below the simple poles from the denominator as the line of integration. We observe that the singularity at $\omega = 0$ is once removable and so the only singularities are simple poles located at

$$\omega_p = \frac{p\pi c_0}{L_n}, \;\; p \in \mathbb{Z}.$$

Figure C.1 displays the simple poles and the closed contour in the lower half plane. We choose to perform the integration in the lower half plane to obtain the solution for positive t, as directed by the form we take of the inverse Fourier transform.

We denote the closed contour by C_n and observe that it is composed of the large arc Γ_n, the infinite sum of smaller arcs γ_p, and the line L along the real axis

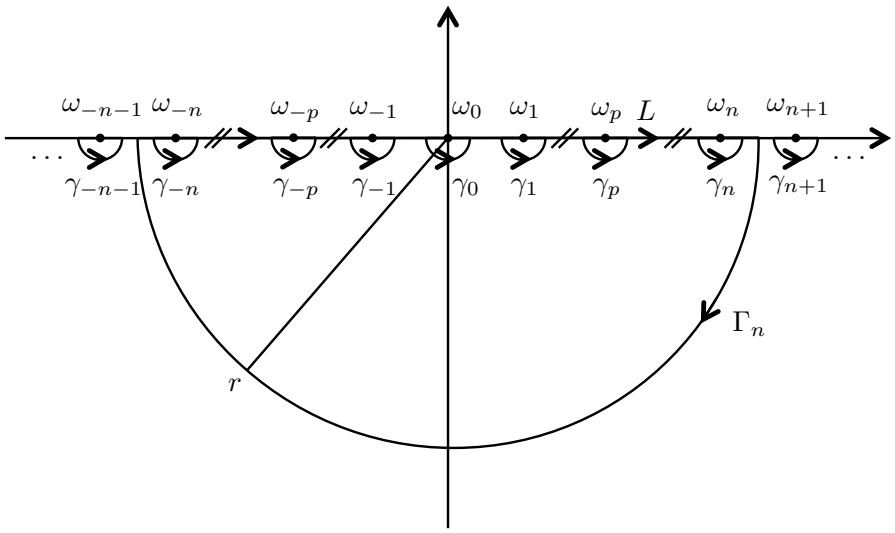

Figure C.1: Contour of integration used to derive (3.119).

so that

$$C_n = \Gamma_n + \sum_{p=-\infty}^{\infty} \gamma_p + L.$$

The arc Γ_n is chosen so that the radius r tends to infinity as $n \to \infty$ and so that the arc does not intersect any of the poles along the real axis. The carefully treatment of Γ_n is necessary so that we may apply Jordan's lemma in this case of infinitely many poles. The smaller arc's, γ_p for $p \in \mathbb{Z}$, indent below each simple pole and exclude these singularities from the closed contour, resulting in integration around C_n that equals zero. These small arcs are of radius ϵ and we determine the contribution of the integration along each γ_p as $\epsilon \to 0$. The line L spans the real axis between the poles and becomes the whole real axis as $r \to \infty$ and $\epsilon \to 0$. We denote the contribution from integrating along each segment of the path by $f(t)_{(\cdot)}$ where $(\cdot)$ is a placeholder for the segment so that

$$f(t)_{C_n} = f(t)_{\Gamma_n} + \sum_{p=-\infty}^{\infty} f(t)_{\gamma_p} + f(t)_L.$$

There are no singularities within the closed contour C_n and so by Cauchy's formula and the calculus of residues it is clear that $f(t)_{C_n} = 0$. As discussed briefly above, the large arc Γ_n is chosen so that we may apply Jordan's lemma. The $F(\omega)$ in the

integrand tends to zero as $\omega \to 0$ and so $f(t)_{\Gamma_n} \to 0$ as $n \to \infty$. We are left with the expression

$$f(t)_L = -\sum_{p=-\infty}^{\infty} f(t)_{\gamma_p}.$$

we must determine the contribution from along each arc γ_p as $\epsilon \to 0$ to obtain the desired inverse Fourier transform $f(t)_L$.

We begin by considering the special case of $\omega_0 = 0$ by letting $\omega = \epsilon \mathrm{e}^{\mathrm{i}\theta}$ with $\mathrm{d}\omega = \mathrm{i}\epsilon \mathrm{e}^{\mathrm{i}\theta}\mathrm{d}\theta$ and taking θ from π to 2π

$$\begin{aligned}
f(t)_{\gamma_0} &= \lim_{\epsilon\to 0} \frac{\mathrm{i}}{2\pi} \int_{\pi}^{2\pi} \frac{\mathrm{e}^{-\mathrm{i}\epsilon\mathrm{e}^{\mathrm{i}\theta}t}\left(\mathrm{e}^{2\mathrm{i}\epsilon\mathrm{e}^{\mathrm{i}\theta}\frac{L_n}{\mathrm{c}_0}} + 1 - \mathrm{e}^{\mathrm{i}\epsilon\mathrm{e}^{\mathrm{i}\theta}\frac{L_n}{\mathrm{c}_0}(1+\cos\theta_n)} - \mathrm{e}^{\mathrm{i}\epsilon\mathrm{e}^{\mathrm{i}\theta}\frac{L_n}{\mathrm{c}_0}(1-\cos\theta_n)}\right)}{\epsilon\mathrm{e}^{\mathrm{i}\theta}\left(\mathrm{e}^{2\mathrm{i}\epsilon\mathrm{e}^{\mathrm{i}\theta}\frac{L_n}{\mathrm{c}_0}} - 1\right)} \mathrm{i}\epsilon\mathrm{e}^{\mathrm{i}\theta}\mathrm{d}\theta \\
&= \lim_{\epsilon\to 0} \frac{1}{2\pi} \int_{\pi}^{2\pi} \frac{\alpha\epsilon\mathrm{e}^{\mathrm{i}\theta}\left(1 - \mathrm{i}\epsilon\mathrm{e}^{\mathrm{i}\theta}t\right)}{2\mathrm{i} - \alpha\epsilon\mathrm{e}^{\mathrm{i}\theta}}\mathrm{d}\theta \\
&= \frac{1}{2\pi}\int_{\pi}^{2\pi} \lim_{\epsilon\to 0} \frac{\mathcal{O}(\epsilon)}{2\mathrm{i} - \mathcal{O}(\epsilon)}\mathrm{d}\theta \\
&= 0.
\end{aligned} \tag{C.3}$$

We next consider the case of $\omega_p = p\pi\mathrm{c}_0/L_n$ with $p \in \mathbb{Z}/\{0\}$ by letting $\omega = \epsilon\mathrm{e}^{\mathrm{i}\theta} + p\pi\mathrm{c}_0/L_n$ with $\mathrm{d}\omega = \mathrm{i}\epsilon\mathrm{e}^{\mathrm{i}\theta}\mathrm{d}\theta$ and taking θ from π to 2π

$$\begin{aligned}
f(t)_{\gamma_p} =& \lim_{\epsilon\to 0} \frac{\mathrm{i}}{2\pi} \int_{\pi}^{2\pi} \left[\frac{\mathrm{e}^{-\mathrm{i}\left(\epsilon\mathrm{e}^{\mathrm{i}\theta} + \frac{p\pi\mathrm{c}_0}{L_n}\right)t}\left(\mathrm{e}^{2\mathrm{i}\left(\epsilon\mathrm{e}^{\mathrm{i}\theta} + \frac{p\pi\mathrm{c}_0}{L_n}\right)\frac{L_n}{\mathrm{c}_0}} + 1 - \mathrm{e}^{\mathrm{i}\left(\epsilon\mathrm{e}^{\mathrm{i}\theta} + \frac{p\pi\mathrm{c}_0}{L_n}\right)\frac{L_n}{\mathrm{c}_0}(1+\cos\theta_n)}\right)}{\left(\epsilon\mathrm{e}^{\mathrm{i}\theta} + \frac{p\pi\mathrm{c}_0}{L_n}\right)\left(\mathrm{e}^{2\mathrm{i}\left(\epsilon\mathrm{e}^{\mathrm{i}\theta} + \frac{p\pi\mathrm{c}_0}{L_n}\right)\frac{L_n}{\mathrm{c}_0}} - 1\right)} \right. \\
&\left. + \frac{\mathrm{e}^{-\mathrm{i}\left(\epsilon\mathrm{e}^{\mathrm{i}\theta} + \frac{p\pi\mathrm{c}_0}{L_n}\right)t}\left(-\mathrm{e}^{\mathrm{i}\left(\epsilon\mathrm{e}^{\mathrm{i}\theta} + \frac{p\pi\mathrm{c}_0}{L_n}\right)\frac{L_n}{\mathrm{c}_0}(1-\cos\theta_n)}\right)}{\left(\epsilon\mathrm{e}^{\mathrm{i}\theta} + \frac{p\pi\mathrm{c}_0}{L_n}\right)\left(\mathrm{e}^{2\mathrm{i}\left(\epsilon\mathrm{e}^{\mathrm{i}\theta} + \frac{p\pi\mathrm{c}_0}{L_n}\right)\frac{L_n}{\mathrm{c}_0}} - 1\right)} \right] \mathrm{i}\epsilon\mathrm{e}^{\mathrm{i}\theta}\mathrm{d}\theta \\
=& \lim_{\epsilon\to 0} \frac{-1}{(2\pi\mathrm{i})(2p\pi)} \left[\frac{\mathrm{e}^{-\mathrm{i}p\pi t\frac{\mathrm{c}_0}{L_n}}\left(2 - (-1)^p\left(\mathrm{e}^{\mathrm{i}p\pi\cos\theta_n} + \mathrm{e}^{-\mathrm{i}p\pi\cos\theta_n}\right) + \mathcal{O}(\epsilon)\right)}{1 + \mathcal{O}(\epsilon)} \right] \\
&\times \int_{\pi}^{2\pi} \mathrm{d}\theta \\
=& \frac{-1}{(2\pi\mathrm{i})(p\pi)} \left[\lim_{\epsilon\to 0} \frac{\mathrm{e}^{-\mathrm{i}p\pi t\frac{\mathrm{c}_0}{L_n}}\left(1 - (-1)^p\cos\left(p\pi\cos\theta_n\right) + \mathcal{O}(\epsilon)\right)}{1 + \mathcal{O}(\epsilon)} \right] \int_{\pi}^{2\pi} \mathrm{d}\theta \\
=& \frac{-1}{(2\pi\mathrm{i})}\frac{1}{p}\mathrm{e}^{-\mathrm{i}p\pi t\frac{\mathrm{c}_0}{L_n}}\left(1 - (-1)^p\cos\left(p\pi\cos\theta_n\right)\right).
\end{aligned} \tag{C.4}$$

It follows that the desired inverse Fourier transform has the form

$$\begin{aligned} f(t)_L &= -\sum_{p=-\infty}^{\infty} f(t)_{\gamma_p} \\ &= -\sum_{\substack{p=-\infty \\ p\neq 0}}^{\infty} \frac{-1}{(2\pi \mathrm{i})} \frac{1}{p} \mathrm{e}^{-\mathrm{i}p\pi t \frac{\mathrm{c}_0}{L_n}} \left(1-(-1)^p \cos\left(p\pi \cos\theta_n\right)\right) \\ &= \frac{1}{(2\pi \mathrm{i})} \sum_{\substack{p=-\infty \\ p\neq 0}}^{\infty} \frac{1}{p} \mathrm{e}^{-\mathrm{i}p\pi t \frac{\mathrm{c}_0}{L_n}} \left(1-(-1)^p \cos\left(p\pi \cos\theta_n\right)\right) \end{aligned} \tag{C.5}$$

and we have obtained (3.119).

C.2 Derivation of (3.128)

Equation (3.128) gives the inverse Fourier transform of the expression

$$\begin{aligned} F(\omega) &= \frac{\left(\cos\left(kL_m\right)-\cos\left(kL_m\cos\theta_m\right)\right)\left(\cos\left(kL_n\right)-\cos\left(kL_n\cos\theta_n\right)\right)}{\omega \sin(kL_n)} \\ &= \frac{\mathrm{i}}{\omega\left(\mathrm{e}^{\mathrm{i}\omega\frac{L_n}{\mathrm{c}_0}}-\mathrm{e}^{-\mathrm{i}\omega\frac{L_n}{\mathrm{c}_0}}\right)} \left(\mathrm{e}^{\mathrm{i}\omega\frac{L_m}{\mathrm{c}_0}}+\mathrm{e}^{-\mathrm{i}\omega\frac{L_m}{\mathrm{c}_0}}-\mathrm{e}^{\mathrm{i}\omega\frac{L_m}{\mathrm{c}_0}\cos\theta_m}-\mathrm{e}^{-\mathrm{i}\omega\frac{L_m}{\mathrm{c}_0}\cos\theta_m}\right) \\ &\quad \times \left(\mathrm{e}^{\mathrm{i}\omega\frac{L_n}{\mathrm{c}_0}}+\mathrm{e}^{-\mathrm{i}\omega\frac{L_n}{\mathrm{c}_0}}-\mathrm{e}^{\mathrm{i}\omega\frac{L_n}{\mathrm{c}_0}\cos\theta_n}-\mathrm{e}^{-\mathrm{i}\omega\frac{L_n}{\mathrm{c}_0}\cos\theta_n}\right) \\ &= \frac{\mathrm{i}}{\omega\left(\mathrm{e}^{2\mathrm{i}\omega\frac{L_n}{\mathrm{c}_0}}-1\right)} \left(\mathrm{e}^{\mathrm{i}\omega\frac{L_m}{\mathrm{c}_0}}+\mathrm{e}^{-\mathrm{i}\omega\frac{L_m}{\mathrm{c}_0}}-\mathrm{e}^{\mathrm{i}\omega\frac{L_m}{\mathrm{c}_0}\cos\theta_m}-\mathrm{e}^{-\mathrm{i}\omega\frac{L_m}{\mathrm{c}_0}\cos\theta_m}\right) \\ &\quad \times \left(\mathrm{e}^{2\mathrm{i}\omega\frac{L_n}{\mathrm{c}_0}}+1-\mathrm{e}^{\mathrm{i}\omega\frac{L_n}{\mathrm{c}_0}(1+\cos\theta_n)}-\mathrm{e}^{\mathrm{i}\omega\frac{L_n}{\mathrm{c}_0}(1-\cos\theta_n)}\right). \end{aligned} \tag{C.6}$$

The desired transform is

$$\begin{aligned} f(t)_L = \frac{\mathrm{i}}{2\pi}\int_L \frac{\mathrm{e}^{-\mathrm{i}\omega t}}{\omega\left(\mathrm{e}^{2\mathrm{i}\omega\frac{L_n}{\mathrm{c}_0}}-1\right)} &\left(\mathrm{e}^{\mathrm{i}\omega\frac{L_m}{\mathrm{c}_0}}+\mathrm{e}^{-\mathrm{i}\omega\frac{L_m}{\mathrm{c}_0}}-\mathrm{e}^{\mathrm{i}\omega\frac{L_m}{\mathrm{c}_0}\cos\theta_m}-\mathrm{e}^{-\mathrm{i}\omega\frac{L_m}{\mathrm{c}_0}\cos\theta_m}\right) \\ &\times \left(\mathrm{e}^{2\mathrm{i}\omega\frac{L_n}{\mathrm{c}_0}}+1-\mathrm{e}^{\mathrm{i}\omega\frac{L_n}{\mathrm{c}_0}(1+\cos\theta_n)}-\mathrm{e}^{\mathrm{i}\omega\frac{L_n}{\mathrm{c}_0}(1-\cos\theta_n)}\right)\mathrm{d}\omega \end{aligned} \tag{C.7}$$

with the real line indented below the simple poles from the denominator as the line of integration. We observe that the singularity at $\omega = 0$ is now twice removable and

so the only singularities are simple poles located at

$$\omega_p = \frac{p\pi c_0}{L_n}, \;\; p \in \mathbb{Z}/\{0\}.$$

Figure C.2 displays the simple poles and the closed contour in the lower half plane. We again choose to perform the integration in the lower half plane to obtain the solution for positive t.

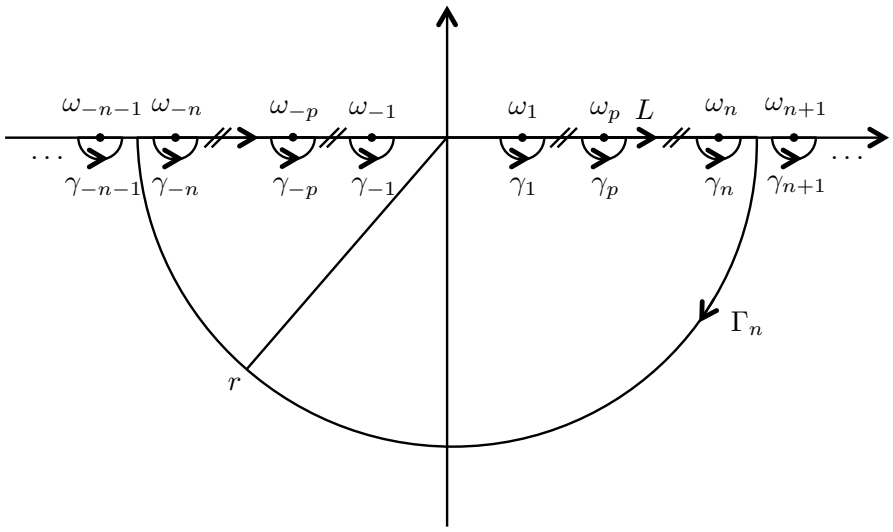

Figure C.2: Contour of integration used to derive (3.128).

As in Section C.1, we denote the closed contour by C_n and observe that it is composed of the large arc Γ_n, the infinite sum of smaller arcs γ_p, and the line L along the real axis so that

$$C_n = \Gamma_n + \sum_{\substack{p=-\infty \\ p\neq 0}}^{\infty} \gamma_p + L.$$

We also denote the contribution from integrating along each segment of the path by $f(t)_{(\cdot)}$ where $(\cdot)$ is a placeholder for the segment so that

$$f(t)_{C_n} = f(t)_{\Gamma_n} + \sum_{\substack{p=-\infty \\ p\neq 0}}^{\infty} f(t)_{\gamma_p} + f(t)_L.$$

By the same arguments presented in the previous section $f(t)_{C_n} = 0$ and $f(t)_{\Gamma_n} \to 0$ as $n \to \infty$. We are left with the expression

$$f(t)_L = -\sum_{\substack{p=-\infty \\ p\neq 0}}^{\infty} f(t)_{\gamma_p}.$$

we must determine the contribution from along each arc γ_p as $\epsilon \to 0$ to obtain the desired inverse Fourier transform $f(t)_L$.

We consider only the case of $\omega_p = p\pi c_0/L_n$ with $p \in \mathbb{Z}/\{0\}$ by again letting $\omega = \epsilon e^{i\theta} + p\pi c_0/L_n$ with $d\omega = i\epsilon e^{i\theta} d\theta$ and taking θ from π to 2π

$$\begin{aligned}
f(t)_{\gamma_p} = \lim_{\epsilon\to 0} \frac{i}{2\pi} \int_{\pi}^{2\pi} \Bigg[& \frac{e^{-i\left(\epsilon e^{i\theta} + \frac{p\pi c_0}{L_n}\right)t}}{\left(\epsilon e^{i\theta} + \frac{p\pi c_0}{L_n}\right)\left(e^{2i\left(\epsilon e^{i\theta} + \frac{p\pi c_0}{L_n}\right)\frac{L_n}{c_0}} - 1\right)} \\
& \times \left(e^{i\left(\epsilon e^{i\theta} + \frac{p\pi c_0}{L_n}\right)\frac{L_m}{c_0}} + e^{-i\left(\epsilon e^{i\theta} + \frac{p\pi c_0}{L_n}\right)\frac{L_m}{c_0}} - e^{i\left(\epsilon e^{i\theta} + \frac{p\pi c_0}{L_n}\right)\frac{L_m}{c_0}\cos\theta_m}\right. \\
& \quad \left. - e^{-i\left(\epsilon e^{i\theta} + \frac{p\pi c_0}{L_n}\right)\frac{L_m}{c_0}\cos\theta_m}\right) \\
& \times \left(e^{2i\left(\epsilon e^{i\theta} + \frac{p\pi c_0}{L_n}\right)\frac{L_n}{c_0}} + 1 - e^{i\left(\epsilon e^{i\theta} + \frac{p\pi c_0}{L_n}\right)\frac{L_n}{c_0}(1+\cos\theta_n)}\right. \\
& \quad \left. - e^{i\left(\epsilon e^{i\theta} + \frac{p\pi c_0}{L_n}\right)\frac{L_n}{c_0}(1-\cos\theta_n)}\right) \Bigg] i\epsilon e^{i\theta} d\theta \\
= \lim_{\epsilon\to 0} \frac{-1}{(2\pi i)(2p\pi)} \Bigg[& \frac{e^{-ip\pi t\frac{c_0}{L_n}}(1+\mathcal{O}(\epsilon))}{1+\mathcal{O}(\epsilon)} \\
& \times \left(\left(e^{ip\pi\frac{L_m}{L_n}} + e^{-ip\pi\frac{L_m}{L_n}}\right) - \left(e^{ip\pi\frac{L_m}{L_n}\cos\theta_m} + e^{-ip\pi\frac{L_m}{L_n}\cos\theta_m}\right) + \mathcal{O}(\epsilon)\right) \\
& \times \left(2 - (-1)^p\left(e^{ip\pi\cos\theta_n} + e^{-ip\pi\cos\theta_n}\right) + \mathcal{O}(\epsilon)\right) \Bigg] \int_{\pi}^{2\pi} d\theta \\
= \frac{-1}{(2\pi i)(p\pi)} \Bigg[& \lim_{\epsilon\to 0} \frac{e^{-ip\pi t\frac{c_0}{L_n}}(1+\mathcal{O}(\epsilon))}{1+\mathcal{O}(\epsilon)} \\
& \times \left(\cos\left(p\pi\frac{L_m}{L_n}\right) - \cos\left(p\pi\frac{L_m}{L_n}\cos\theta_m\right) + \mathcal{O}(\epsilon)\right) \\
& \times \left(1 - (-1)^p\cos\left(p\pi\cos\theta_n\right) + \mathcal{O}(\epsilon)\right) \Bigg] \int_{\pi}^{2\pi} d\theta
\end{aligned}$$

$$= \frac{-1}{2\pi \mathrm{i}} \frac{1}{p} \, \mathrm{e}^{-\mathrm{i}p\pi t \frac{c_0}{L_n}} \Bigg[(1 - (-1)^p \cos(p\pi \cos\theta_n)) \times \left(\cos\left(p\pi \frac{L_m}{L_n} \right) - \cos\left(p\pi \frac{L_m}{L_n} \cos\theta_m \right) \right) \Bigg]. \tag{C.8}$$

It follows that the desired inverse Fourier transform has the form

$$\begin{aligned} f(t)_L &= - \sum_{p=-\infty}^{\infty} f(t)_{\gamma_p} \\ &= - \sum_{\substack{p=-\infty \\ p\neq 0}}^{\infty} \frac{-1}{2\pi \mathrm{i}} \frac{1}{p} \, \mathrm{e}^{-\mathrm{i}p\pi t \frac{c_0}{L_n}} \Bigg[(1 - (-1)^p \cos(p\pi \cos\theta_n)) \\ &\qquad \times \left(\cos\left(p\pi \frac{L_m}{L_n} \right) - \cos\left(p\pi \frac{L_m}{L_n} \cos\theta_m \right) \right) \Bigg] \\ &= \frac{1}{2\pi \mathrm{i}} \sum_{\substack{p=-\infty \\ p\neq 0}}^{\infty} \frac{1}{p} \, \mathrm{e}^{-\mathrm{i}p\pi t \frac{c_0}{L_n}} \Bigg[(1 - (-1)^p \cos(p\pi \cos\theta_n)) \\ &\qquad \times \left(\cos\left(p\pi \frac{L_m}{L_n} \right) - \cos\left(p\pi \frac{L_m}{L_n} \cos\theta_m \right) \right) \Bigg] \end{aligned} \tag{C.9}$$

and we have obtained (3.128).

APPENDIX D
Scattering from a Perfectly Electrically Conducting Flat Rectangular Plate

In this appendix we will briefly derive the scattering behavior of a perfectly electrically conducting flat rectangular plate under the physical optics approximation as discussed in [37, 50, 64]. We wish to derive the FSA and BSA scattering matrices, $[\boldsymbol{S}]^{\text{FSA}}_{\text{plate}}$ and $[\boldsymbol{S}]^{\text{BSA}}_{\text{plate}}$, for the general bistatic case and specifically $[\boldsymbol{S}]^{\text{BSA}}_{\text{plate}}$, which is used in simulations presented in Section 3.6.

D.1 Problem Set-up

As discussed in Section 3.2.3, the standard scattering matrix $[\boldsymbol{S}]^{\text{FSA}}$ as given by Sinclair [40] is derived for the forward scattering case and so we will use the coordinate system in Figure D.1 where

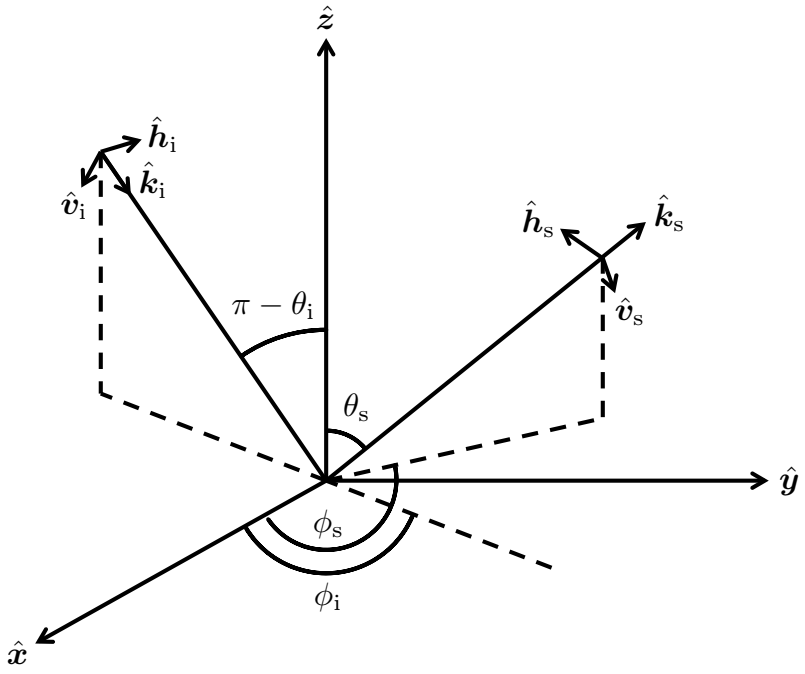

Figure D.1: Forward scatter approximation (FSA) coordinate system.

$$\hat{\boldsymbol{k}}_{\mathrm{i}} = \cos\phi_{\mathrm{i}} \sin\theta_{\mathrm{i}} \hat{\boldsymbol{x}} + \sin\phi_{\mathrm{i}} \sin\theta_{\mathrm{i}} \hat{\boldsymbol{y}} + \cos\theta_{\mathrm{i}} \hat{\boldsymbol{z}}$$
$$\hat{\boldsymbol{h}}_{\mathrm{i}} = -\sin\phi_{\mathrm{i}} \hat{\boldsymbol{x}} + \cos\phi_{\mathrm{i}} \hat{\boldsymbol{y}}$$
$$\hat{\boldsymbol{v}}_{\mathrm{i}} = \cos\phi_{\mathrm{i}} \cos\theta_{\mathrm{i}} \hat{\boldsymbol{x}} + \sin\phi_{\mathrm{i}} \cos\theta_{\mathrm{i}} \hat{\boldsymbol{y}} - \sin\theta_{\mathrm{i}} \hat{\boldsymbol{z}}$$

and

$$\hat{\boldsymbol{k}}_{\mathrm{s}} = \cos\phi_{\mathrm{s}} \sin\theta_{\mathrm{s}} \hat{\boldsymbol{x}} + \sin\phi_{\mathrm{s}} \sin\theta_{\mathrm{s}} \hat{\boldsymbol{y}} + \cos\theta_{\mathrm{s}} \hat{\boldsymbol{z}}$$
$$\hat{\boldsymbol{h}}_{\mathrm{s}} = -\sin\phi_{\mathrm{s}} \hat{\boldsymbol{x}} + \cos\phi_{\mathrm{s}} \hat{\boldsymbol{y}}$$
$$\hat{\boldsymbol{v}}_{\mathrm{s}} = \cos\phi_{\mathrm{s}} \cos\theta_{\mathrm{s}} \hat{\boldsymbol{x}} + \sin\phi_{\mathrm{s}} \cos\theta_{\mathrm{s}} \hat{\boldsymbol{y}} - \sin\theta_{\mathrm{s}} \hat{\boldsymbol{z}}$$

[37].

We will derive the scattering matrices for a PEC flat rectangular plate that is oriented along the $\boldsymbol{x}$-$\boldsymbol{z}$ plane with the normal pointing out of the page in the $\hat{\boldsymbol{y}}$ direction such that $\hat{\boldsymbol{n}} = \hat{\boldsymbol{y}}$ as shown in Figure D.2.

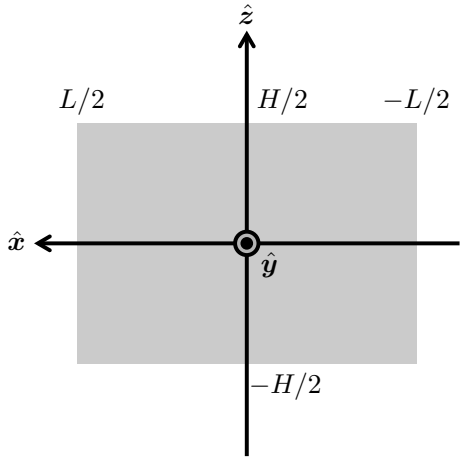

Figure D.2: A flat rectangular plate oriented along the $\boldsymbol{x}$-$\boldsymbol{z}$ plane with normal pointing out of the page in the $\hat{\boldsymbol{y}}$ direction.

D.2 Physical Optics Approximation

Physical optics is a high-frequency technique that holds when the wavelength of the incident field is much smaller that the length of the scattering body. At these higher frequencies the scatterer can be treated as a collection of independent scattering centers [64]. Physical optics specifically eliminates the infinities of flat and singly curved surfaces by approximating the induced surface fields and integrating to obtain the scattered field. Determining the scattered field reduces to a local boundary problem of a plane wave incident on a perfectly conducting plane and it is known that the scattered field is a reflected plane wave satisfying

$$E^{\mathrm{r}}_{\tan} = -E^{\mathrm{i}}_{\tan}, \quad H^{\mathrm{r}}_{\tan} = H^{\mathrm{i}}_{\tan}.$$

It follows that

$$\hat{\boldsymbol{n}} \times \boldsymbol{E} = \hat{\boldsymbol{n}} \times (\boldsymbol{E}^{\mathrm{i}} + \boldsymbol{E}^{\mathrm{r}}) = 0 \tag{D.1}$$

and

$$\hat{\boldsymbol{n}} \times \boldsymbol{H} = \hat{\boldsymbol{n}} \times (\boldsymbol{H}^{\mathrm{i}} + \boldsymbol{H}^{\mathrm{r}}) = 2\hat{\boldsymbol{n}} \times \boldsymbol{H}^{\mathrm{i}} \tag{D.2}$$

within the illuminated region S and

$$\hat{\boldsymbol{n}} \times \boldsymbol{H} = 0 \tag{D.3}$$

elsewhere. The resulting Hertz vectors satisfying the boundary conditions (D.1), (D.2), and (D.3) are given by

$$\boldsymbol{\Pi}_{\mathrm{e}}(\boldsymbol{r}) = \frac{\mathrm{i}\eta_0}{2\pi k} \int_S \hat{\boldsymbol{n}} \times \boldsymbol{H}^{\mathrm{i}} \frac{\mathrm{e}^{\mathrm{i}k|\boldsymbol{r}-\boldsymbol{r}'|}}{|\boldsymbol{r}-\boldsymbol{r}'|} \mathrm{d}S' \tag{D.4}$$

$$\boldsymbol{\Pi}_{\mathrm{m}}(\boldsymbol{r}) = 0 \tag{D.5}$$

where η_0 is the impedance of free space, $\boldsymbol{r}' = \boldsymbol{r}_0 + x'\hat{\boldsymbol{x}} + y'\hat{\boldsymbol{y}} + z'\hat{\boldsymbol{z}}$ is point on the surface of the scattering body, and $\boldsymbol{r}_0$ is the origin of the coordinate system that for simplicity we assume to be $(0, 0, 0)$ [37, 64]. We observe that $\boldsymbol{H}^{\mathrm{i}}$ is a plane wave that can be expressed as

$$\boldsymbol{H}^{\mathrm{i}} = \boldsymbol{H}_0 \mathrm{e}^{\mathrm{i}k\hat{\boldsymbol{k}}_{\mathrm{i}} \cdot \hat{\boldsymbol{r}}}$$

and so

$$\begin{aligned}\boldsymbol{\Pi}_{\mathrm{e}}(\boldsymbol{r}) &= \frac{\mathrm{i}\eta_0}{2\pi k}\left\{\hat{\boldsymbol{n}}\times\boldsymbol{H}_0\right\}\int_S \mathrm{e}^{\mathrm{i}k\hat{\boldsymbol{k}}_{\mathrm{i}}\cdot\boldsymbol{r}'}\frac{\mathrm{e}^{\mathrm{i}k|\boldsymbol{r}-\boldsymbol{r}'|}}{|\boldsymbol{r}-\boldsymbol{r}'|}\mathrm{d}S' \\ &= \frac{\mathrm{i}\eta_0}{2\pi k}\frac{\mathrm{e}^{\mathrm{i}k|\boldsymbol{r}|}}{|\boldsymbol{r}|}\left\{\hat{\boldsymbol{n}}\times\boldsymbol{H}_0\right\}\int_S \mathrm{e}^{\mathrm{i}k\left(\hat{\boldsymbol{k}}_{\mathrm{i}}-\hat{\boldsymbol{k}}_{\mathrm{s}}\right)\cdot\boldsymbol{r}'}\mathrm{d}S'\end{aligned}$$

for an observation in direction $\hat{\boldsymbol{k}}_{\mathrm{s}}$ in the far field. We next break up $\boldsymbol{H}_0$ into $\hat{\boldsymbol{h}}_{\mathrm{i}}$ and $\hat{\boldsymbol{v}}_{\mathrm{i}}$ components and we recall that

$$\boldsymbol{H}_0 = \eta_0^{-1}\hat{\boldsymbol{k}}_{\mathrm{i}}\times\boldsymbol{E}_0$$

so that

$$\begin{aligned}\boldsymbol{\Pi}_{\mathrm{e}}(\boldsymbol{r}) &= \frac{\mathrm{i}\eta_0}{2\pi k}\frac{\mathrm{e}^{\mathrm{i}k|\boldsymbol{r}|}}{|\boldsymbol{r}|}\left\{\hat{\boldsymbol{n}}\times\left(H_{\mathrm{h}}^{\mathrm{i}}\hat{\boldsymbol{h}}_{\mathrm{i}}+H_{\mathrm{v}}^{\mathrm{i}}\hat{\boldsymbol{v}}_{\mathrm{i}}\right)\right\}\int_S \mathrm{e}^{\mathrm{i}k\left(\hat{\boldsymbol{k}}_{\mathrm{i}}-\hat{\boldsymbol{k}}_{\mathrm{s}}\right)\cdot\boldsymbol{r}'}\mathrm{d}S' \\ &= \frac{\mathrm{i}\eta_0}{2\pi k}\frac{\mathrm{e}^{\mathrm{i}k|\boldsymbol{r}|}}{|\boldsymbol{r}|}M\left\{\hat{\boldsymbol{n}}\times\left(-\eta_0^{-1}E_{\mathrm{h}}^{\mathrm{i}}\hat{\boldsymbol{v}}_{\mathrm{i}}+\eta_0^{-1}E_{\mathrm{v}}^{\mathrm{i}}\hat{\boldsymbol{h}}_{\mathrm{i}}\right)\right\} \qquad \text{(D.6)}\end{aligned}$$

where

$$M = \int_S \mathrm{e}^{\mathrm{i}k\left(\hat{\boldsymbol{k}}_{\mathrm{i}}-\hat{\boldsymbol{k}}_{\mathrm{s}}\right)\cdot\boldsymbol{r}'}\mathrm{d}S'. \qquad \text{(D.7)}$$

In the next section we will derive M for our specific scattering body.

D.3 Derivation of the Scattered Electric Field $\boldsymbol{E}^{\mathrm{s}}(\boldsymbol{r})$

The scattered electric field can be expressed in terms of the Hertz vectors as

$$\boldsymbol{E}^{\mathrm{s}}(\boldsymbol{r}) = \nabla\times\nabla\times\boldsymbol{\Pi}_{\mathrm{e}}(\boldsymbol{r}) + \mathrm{i}k\eta_0\nabla\times\boldsymbol{\Pi}_{\mathrm{m}}(\boldsymbol{r})$$

and at larges distances away from the scattering body $\nabla\times(\cdot)\approx\mathrm{i}k\hat{\boldsymbol{r}}\times(\cdot)$ and so

$$\boldsymbol{E}^{\mathrm{s}}(\boldsymbol{r}) = -k^2\left\{\hat{\boldsymbol{r}}\times\hat{\boldsymbol{r}}\times\boldsymbol{\Pi}_{\mathrm{e}}(\boldsymbol{r}) + \hat{\boldsymbol{r}}\times\eta_0\boldsymbol{\Pi}_{\mathrm{m}}(\boldsymbol{r})\right\}. \qquad \text{(D.8)}$$

We obtain the scattered field in the direction $\hat{\boldsymbol{r}} = \hat{\boldsymbol{k}}_\mathrm{s}$ by substituting (D.6) and (D.5) into (D.8)

$$\boldsymbol{E}^\mathrm{s}(\boldsymbol{r}) = -\frac{\mathrm{i}k}{2\pi}\frac{\mathrm{e}^{\mathrm{i}k|\boldsymbol{r}|}}{|\boldsymbol{r}|}M\left\{\hat{\boldsymbol{k}}_\mathrm{s}\times\hat{\boldsymbol{k}}_\mathrm{s}\times\hat{\boldsymbol{n}}\times\left(-E^\mathrm{i}_\mathrm{h}\hat{\boldsymbol{v}}_\mathrm{i}+E^\mathrm{i}_\mathrm{v}\hat{\boldsymbol{h}}_\mathrm{i}\right)\right\}. \tag{D.9}$$

It is at this point that we choose our scattering body and coordinate system. Using the FSA coordinate system in Figure D.1 we obtain

$$\begin{aligned}\hat{\boldsymbol{k}}_\mathrm{s}\times\hat{\boldsymbol{k}}_\mathrm{s}\times\hat{\boldsymbol{n}}\times\hat{\boldsymbol{v}}_\mathrm{i} =&(-\sin\phi_\mathrm{s}\hat{\boldsymbol{x}}+\cos\phi_\mathrm{s}\hat{\boldsymbol{y}})(-\sin\phi_\mathrm{s}\sin\theta_\mathrm{i})\\ &+(\cos\phi_\mathrm{s}\cos\theta_\mathrm{s}\hat{\boldsymbol{x}}+\sin\phi_\mathrm{s}\cos\theta_\mathrm{s}\hat{\boldsymbol{y}}-\sin\theta_\mathrm{s}\hat{\boldsymbol{z}})\\ &\times(\cos\phi_\mathrm{s}\cos\theta_\mathrm{s}\sin\theta_\mathrm{i}-\cos\phi_\mathrm{i}\cos\theta_\mathrm{i}\sin\theta_\mathrm{s})\\ =&\hat{\boldsymbol{h}}_\mathrm{s}(-\sin\phi_\mathrm{s}\sin\theta_\mathrm{i})+\hat{\boldsymbol{v}}_\mathrm{s}(\cos\phi_\mathrm{s}\cos\theta_\mathrm{s}\sin\theta_\mathrm{i}-\cos\phi_\mathrm{i}\cos\theta_\mathrm{i}\sin\theta_\mathrm{s})\end{aligned} \tag{D.10}$$

and

$$\begin{aligned}\hat{\boldsymbol{k}}_\mathrm{s}\times\hat{\boldsymbol{k}}_\mathrm{s}\times\hat{\boldsymbol{n}}\times\hat{\boldsymbol{h}}_\mathrm{i} =&(\cos\phi_\mathrm{s}\cos\theta_\mathrm{s}\hat{\boldsymbol{x}}+\sin\phi_\mathrm{s}\cos\theta_\mathrm{s}\hat{\boldsymbol{y}}-\sin\theta_\mathrm{s}\hat{\boldsymbol{z}})(\sin\phi_\mathrm{i}\sin\theta_\mathrm{s})\\ =&\hat{\boldsymbol{v}}_\mathrm{s}(\sin\phi_\mathrm{i}\sin\theta_\mathrm{s})\end{aligned} \tag{D.11}$$

and substituting (D.10) and (D.11) into (D.9)

$$\begin{aligned}\boldsymbol{E}^\mathrm{s}_\mathrm{plate}(\boldsymbol{r}) = -\frac{\mathrm{i}k}{2\pi}\frac{\mathrm{e}^{\mathrm{i}k|\boldsymbol{r}|}}{|\boldsymbol{r}|}M_\mathrm{plate}\Big\{&E^\mathrm{i}_\mathrm{h}\hat{\boldsymbol{h}}_\mathrm{s}(\sin\phi_\mathrm{s}\sin\theta_\mathrm{i})\\ &+E^\mathrm{i}_\mathrm{h}\hat{\boldsymbol{v}}_\mathrm{s}(\cos\phi_\mathrm{i}\cos\theta_\mathrm{i}\sin\theta_\mathrm{s}-\cos\phi_\mathrm{s}\cos\theta_\mathrm{s}\sin\theta_\mathrm{i})+E^\mathrm{i}_\mathrm{v}\hat{\boldsymbol{v}}_\mathrm{s}(\sin\phi_\mathrm{i}\sin\theta_\mathrm{s})\Big\}.\end{aligned} \tag{D.12}$$

To find M_plate we observe that $\boldsymbol{r}' = x'\hat{\boldsymbol{x}} + z'\hat{\boldsymbol{z}}$ on the surface of the plate oriented along the $\boldsymbol{x}$-$\boldsymbol{z}$ plane and so

$$(\hat{\boldsymbol{k}}_\mathrm{i}-\hat{\boldsymbol{k}}_\mathrm{s})\cdot\boldsymbol{r}' = (\cos\phi_\mathrm{i}\sin\theta_\mathrm{i}-\cos\phi_\mathrm{s}\sin\theta_\mathrm{s})x' + (\cos\theta_\mathrm{i}-\cos\theta_\mathrm{s})z' \tag{D.13}$$

and substituting (D.13) into (D.7) we obtain M for the perfectly conducting flat

rectangular plate

$$\begin{aligned} M_{\text{plate}} =& \int_{-H/2}^{H/2}\int_{-L/2}^{L/2} \mathrm{e}^{\mathrm{i}k((\cos\phi_\mathrm{i}\sin\theta_\mathrm{i}-\cos\phi_\mathrm{s}\sin\theta_\mathrm{s})x'+(\cos\theta_\mathrm{i}-\cos\theta_\mathrm{s})z')}\mathrm{d}x'\mathrm{d}z' \\ =& LH\frac{\sin\left(k\frac{L}{2}(\cos\phi_\mathrm{i}\sin\theta_\mathrm{i}-\cos\phi_\mathrm{s}\sin\theta_\mathrm{s})\right)}{k\frac{L}{2}(\cos\phi_\mathrm{i}\sin\theta_\mathrm{i}-\cos\phi_\mathrm{s}\sin\theta_\mathrm{s})}\frac{\sin\left(k\frac{H}{2}(\cos\theta_\mathrm{i}-\cos\theta_\mathrm{s})\right)}{k\frac{H}{2}(\cos\theta_\mathrm{i}-\cos\theta_\mathrm{s})} \\ =& LH\mathrm{sinc}\left(k\frac{L}{2}(\cos\phi_\mathrm{i}\sin\theta_\mathrm{i}-\cos\phi_\mathrm{s}\sin\theta_\mathrm{s})\right)\mathrm{sinc}\left(k\frac{H}{2}(\cos\theta_\mathrm{i}-\cos\theta_\mathrm{s})\right) \end{aligned} \tag{D.14}$$

where

$$\mathrm{sinc}(x) \equiv \begin{cases} 1 & \text{for } x = 0 \\ \frac{\sin(x)}{x} & \text{otherwise} \end{cases}.$$

Substituting (D.14) into (D.12) we obtain the scattered electric field from a PEC flat rectangular plate

$$\begin{aligned} \boldsymbol{E}^\mathrm{s}_{\text{plate}}(\boldsymbol{r}) =& -\frac{\mathrm{i}k}{2\pi}\frac{\mathrm{e}^{\mathrm{i}k|\boldsymbol{r}|}}{|\boldsymbol{r}|}LH\mathrm{sinc}\left(k\frac{L}{2}(\cos\phi_\mathrm{i}\sin\theta_\mathrm{i}-\cos\phi_\mathrm{s}\sin\theta_\mathrm{s})\right) \\ &\times \mathrm{sinc}\left(k\frac{H}{2}(\cos\theta_\mathrm{i}-\cos\theta_\mathrm{s})\right)\Big\{E^\mathrm{i}_\mathrm{h}\hat{\boldsymbol{h}}_\mathrm{s}(\sin\phi_\mathrm{s}\sin\theta_\mathrm{i}) \\ &+ E^\mathrm{i}_\mathrm{h}\hat{\boldsymbol{v}}_\mathrm{s}(\cos\phi_\mathrm{i}\cos\theta_\mathrm{i}\sin\theta_\mathrm{s}-\cos\phi_\mathrm{s}\cos\theta_\mathrm{s}\sin\theta_\mathrm{i}) + E^\mathrm{i}_\mathrm{v}\hat{\boldsymbol{v}}_\mathrm{s}(\sin\phi_\mathrm{i}\sin\theta_\mathrm{s})\Big\}. \end{aligned} \tag{D.15}$$

D.4 Derivation of the Scattering Matrices

We recall that the scattering matrix $[\boldsymbol{S}]^{\text{FSA}}$ is defined by

$$\boldsymbol{E}^\mathrm{s} = \frac{\mathrm{e}^{\mathrm{i}k|\boldsymbol{r}|}}{|\boldsymbol{r}|}[\boldsymbol{S}]^{\text{FSA}}\boldsymbol{E}^\mathrm{i}$$

or

$$\begin{bmatrix} E^\mathrm{s}_{\mathrm{h_s}} \\ E^\mathrm{s}_{\mathrm{v_s}} \end{bmatrix} = \frac{\mathrm{e}^{\mathrm{i}k|\boldsymbol{r}|}}{|\boldsymbol{r}|}\begin{bmatrix} S_{\mathrm{h_s h_i}} & S_{\mathrm{h_s v_i}} \\ S_{\mathrm{v_s h_i}} & S_{\mathrm{v_s v_i}} \end{bmatrix}^{\text{FSA}}\begin{bmatrix} E^\mathrm{i}_{\mathrm{h_i}} \\ E^\mathrm{i}_{\mathrm{v_i}} \end{bmatrix}$$

where the polarization of the incident field is in the basis associated with the transmitter $(\hat{\boldsymbol{k}}_\mathrm{i}, \hat{\boldsymbol{h}}_\mathrm{i}, \hat{\boldsymbol{v}}_\mathrm{i})$ and the polarization of the scattered field is in the basis associated with the receiver $(\hat{\boldsymbol{k}}_\mathrm{s}, \hat{\boldsymbol{h}}_\mathrm{s}, \hat{\boldsymbol{v}}_\mathrm{s})$.

As in [51] we can extract the scattering matrix from (D.15) so that

$$
\begin{aligned}
[\boldsymbol{S}]^{\mathrm{FSA}}_{\mathrm{plate}} &= -\frac{\mathrm{i}k}{2\pi} M \left[\begin{array}{cc} S_{\mathrm{h_s h_i}} & S_{\mathrm{h_s v_i}} \\ S_{\mathrm{v_s h_i}} & S_{\mathrm{v_s v_i}} \end{array} \right]^{\mathrm{FSA}}_{\mathrm{plate}} \\
&= -\frac{\mathrm{i}k}{2\pi} LH \mathrm{sinc}\left(k\frac{L}{2}(\cos\phi_{\mathrm{i}} \sin\theta_{\mathrm{i}} - \cos\phi_{\mathrm{s}} \sin\theta_{\mathrm{s}}) \right) \\
&\quad \times \mathrm{sinc}\left(k\frac{H}{2}(\cos\theta_{\mathrm{i}} - \cos\theta_{\mathrm{s}}) \right) \\
&\quad \times \left[\begin{array}{cc} \sin\phi_{\mathrm{s}} \sin\theta_{\mathrm{i}} & 0 \\ \cos\phi_{\mathrm{i}} \cos\theta_{\mathrm{i}} \sin\theta_{\mathrm{s}} - \cos\phi_{\mathrm{s}} \cos\theta_{\mathrm{s}} \sin\theta_{\mathrm{i}} & \sin\phi_{\mathrm{i}} \sin\theta_{\mathrm{s}} \end{array} \right].
\end{aligned} \tag{D.16}
$$

Under the FSA convention monostatic backscatter occurs when $\theta \equiv \theta_{\mathrm{s}} = \pi - \theta_{\mathrm{i}}$ and $\phi \equiv \phi_{\mathrm{s}} = \pi + \phi_{\mathrm{i}}$ and the scattering matrix reduces to

$$
\begin{aligned}
[\boldsymbol{S}]^{\mathrm{FSA}}_{\mathrm{plate}} &= -\frac{\mathrm{i}k}{2\pi} LH \mathrm{sinc}\left(kL\cos\phi\sin\theta\right) \mathrm{sinc}\left(kH\cos\theta\right) \\
&\quad \times \left[\begin{array}{cc} \sin\phi\sin\theta & 0 \\ 0 & -\sin\phi\sin\theta \end{array} \right].
\end{aligned} \tag{D.17}
$$

We recall $\boldsymbol{E}^{\mathrm{i}} = \boldsymbol{E}^{\mathrm{t}}$ and

$$
\boldsymbol{E}^{\mathrm{s}} = \left[\begin{array}{cc} -1 & 0 \\ 0 & 1 \end{array} \right] \boldsymbol{E}^{\mathrm{r}}
$$

relate the electric field in the BSA and FSA conventions as discussed in Section 3.2.3 and so it follows that

$$
[\boldsymbol{S}]^{\mathrm{FSA}} = \left[\begin{array}{cc} -1 & 0 \\ 0 & 1 \end{array} \right] [\boldsymbol{S}]^{\mathrm{BSA}}
$$

or

$$
[\boldsymbol{S}]^{\mathrm{BSA}} = \left[\begin{array}{cc} -1 & 0 \\ 0 & 1 \end{array} \right] [\boldsymbol{S}]^{\mathrm{FSA}}.
$$

The scattering matrix under the BSA convention takes the form

$$
\begin{aligned}
[\boldsymbol{S}]^{\mathrm{BSA}}_{\mathrm{plate}} = &- \frac{\mathrm{i}k}{2\pi} LH \mathrm{sinc}\left(k\frac{L}{2}(\cos\phi_{\mathrm{i}}\sin\theta_{\mathrm{i}} - \cos\phi_{\mathrm{s}}\sin\theta_{\mathrm{s}})\right) \\
&\times \mathrm{sinc}\left(k\frac{H}{2}(\cos\theta_{\mathrm{i}} - \cos\theta_{\mathrm{s}})\right) \\
&\times \begin{bmatrix} -\sin\phi_{\mathrm{s}}\sin\theta_{\mathrm{i}} & 0 \\ \cos\phi_{\mathrm{i}}\cos\theta_{\mathrm{i}}\sin\theta_{\mathrm{s}} - \cos\phi_{\mathrm{s}}\cos\theta_{\mathrm{s}}\sin\theta_{\mathrm{i}} & \sin\phi_{\mathrm{i}}\sin\theta_{\mathrm{s}} \end{bmatrix}. \qquad \text{(D.18)}
\end{aligned}
$$

Monostatic backscatter again occurs when $\theta \equiv \theta_{\mathrm{s}} = \pi - \theta_{\mathrm{i}}$ and $\phi \equiv \phi_{\mathrm{s}} = \pi + \phi_{\mathrm{i}}$ and the scattering matrix reduces to

$$
\begin{aligned}
[\boldsymbol{S}]^{\mathrm{BSA}}_{\mathrm{plate}} = &\frac{\mathrm{i}k}{2\pi} LH \mathrm{sinc}\left(kL\cos\phi\sin\theta\right)\mathrm{sinc}\left(kH\cos\theta\right) \\
&\times \begin{bmatrix} \sin\phi\sin\theta & 0 \\ 0 & \sin\phi\sin\theta \end{bmatrix}. \qquad \text{(D.19)}
\end{aligned}
$$

For normal incidence monostatic backscatter with $\theta = \pi/2$ and $\phi = \pi/2$ we obtain the desired scattering matrix

$$
[\boldsymbol{S}]^{\mathrm{BSA}}_{\mathrm{plate}} = \frac{\mathrm{i}k}{2\pi} LH \begin{bmatrix} 1 & 0 \\ 0 & 1 \end{bmatrix} \qquad \text{(D.20)}
$$

that is found in the literature [37, 38, 42, 51, 64].

In Chapter 3 we have adopted the BSA convention and so for ease of notation we let $[\boldsymbol{S}] \equiv [\boldsymbol{S}]^{\mathrm{BSA}}$ denote the general scattering matrix and similarly $[\boldsymbol{S}]_{\mathrm{plate}} \equiv [\boldsymbol{S}]^{\mathrm{BSA}}_{\mathrm{plate}}$.